Ofshore Wind Park Control Assessment Methodologies to Assure Robustness

Gryning, Mikkel Peter Sidoroff

Publication date:
2015

Document Version
Publisher's PDF, also known as Version of record

Technical University of Denmark

Mikkel P.S. Gryning

Offshore Wind Park Control Assessment Methodologies to Assure Robustness

PhD Thesis, November 2015

DTU Electrical Engineering
Department of Electrical Engineering

Offshore Wind Park Control Assessment Methodologies to Assure Robustness

Mikkel P.S. Gryning

DTU Elektro - PhD Thesis
Kongens Lyngby November 2015

www.elektro.dtu.dk
Department of Electrical Engineering
Automation and Control (AUT)
Technical University of Denmark
Elektrovej
Building 326
DK-2800, Kgs. Lyngby
Denmark
Tel: (+45) 45 25 35 76
Email: info@elektro.dtu.dk

Summary

The transition from fossil fuels to renewable energy is an expensive but necessary process to ensure a habitable world for future generations. Renewable energy sources such as hydro-, solar- and wind energy continues to increase their share of the total power production. With national goals set by the Renewable Energy Directive of the European Commission to decrease carbon dioxide emission, the demand for renewable energy is increasing. Wind energy has been harnessed since 1887 [1] and has seen a large growth since the first multi-megawatt turbine in 1978. Gradually the wind energy technology has matured to a point where turbines are reaching a production capability exceeding 6 megawatt and the turbines have moved offshore due to stronger wind, and to avoid proximity to populated areas. The placement of wind power plants (WPP) with a typical size of 60 large turbines in remote locations with a weak grid interconnection point, is a challenge with respect to power system stability. This dissertation considers the interaction between the offshore grid and the control of power electronic devices (PED), its effect on system stability and challenges with respect to unwanted interaction between controllers in the rather complex control hierarchy on an offshore WPP.

The output waveform of modern turbines utilizing PEDs is distorted at high frequencies, and the stability of the control system is affected by resonances and harmonics present in the weak offshore grid. These phenomena pose a risk to drive the system to instability, as they exist within the bandwidth of the turbine controllers. The resonances and the number of turbines in operation are characteristics of the grid, which are partly unknown at the controller design stage. The uncertainty and the unwanted interaction in the grid are difficult challenges for control designers.

This project deals with these challenges and provides insight in root causes to phenomena that have been issues during wind power plant commissioning in the past. This is done through development of design and validation methods for controllers, by analyzing turbine interaction with the grid and suggestion of design guidelines to ensure proper operation of stacked controllers. Two specific faults serve as basis for the analysis and development, a rotor blade deformation and an unwanted oscillation in the reactive power, both of which experienced at a WPP.

The low frequency reactive power oscillations observed were suspected to be

caused by the voltage control at the point of common coupling. The fault was thought to involve the interaction between the static synchronous compensator (STATCOM), the wind turbine voltage control and the power plant control (PPC). By establishing bounds on the sets of possible parameters of all involved controllers, the thesis replicates the phenomena by simulation and a method is proposed that analytically finds the set of control parameters, which ensure stable operation. The method enables DONG Energy to calculate bounds on controller parameters based on network parameters and the thesis contributes by ensuring proper operation before energization.

The analysis of the voltage control philosophy related to the reactive power oscillations showed the need for proper handling of the resonances introduced by the offshore grid in the turbine control structure. The dissertation contributes to this area with the development of a robust $\mathcal{H}_\infty$ converter controller employing notch filters in the performance specification to suppress harmonics of the grid frequency. This method combines attenuation of selected resonance frequencies with system stability and performance within the defined envelope of uncertainty of the grid. The controller is tested in a model of the WPP, and is shown to improve performance, control effort and output disturbance rejection compared to standard PI control.

The second fault was that a turbine rotor blade was observed to deform in a WPP. This severe fault was suspected to have contributory causes from both mechanical- and electrical systems. A preceding investigation was conducted which ruled out physical generator phenomena such as cogging torque, as well as network voltage disturbances and delays in the converter control system. The investigation indicated that the problem was an insufficient implementation of the rotor speed controller. The thesis addresses the problem by the development of control methods to limit the shaft stress, and thereby the rotor blade vibration. The contributions include a feedback linerization controller and an observer based backstepping controller for a wind turbine.

The thesis consists of an introduction part that briefly describes the field, the investigations conducted in the study, the models developed and the controller designs suggested to deal with the challenges described above. The main results of the research are highlighted in the introduction and the detailed results are described in four papers, which are enclosed in the last part of the thesis.

Resume

Overgangen fra fossile brændstoffer til vedvarende energi er en bekostelig men nødvendig proces for a sikre en beboelig verden for fremtidige generationer. Andelen af den totale effekt produceret af vedvarende energikilder såsom hydro-, sol- og vindenergi fortsætter med at forøges. De nationale mål sat af den Europæiske Kommission i Direktivet om Vedvarende Energi om at formindske udledningen af kuldioxid har skabt en stigende efterspørgsel efter vedvarende energi. Vindenergi er blevet udnyttet siden 1887 [1], og har set en stor vækst siden den første multi-megawatt turbine blev udviklet i 1978. Gradvist er vindenergiteknologien modnet til et punkt hvor turbinerne har nået en produktionsevne der overstiger 6 megawatt og de er derfor flyttet offshore pga. stærkere vind, og for at undgå befolkede områder. Placeringen af vindparker med en typisk størrelse på 60 store turbiner i afsides lokalisationer med en svag netforbindelse er en udfordring med hensyn til stabiliteten i parken. Denne afhandling betragter interaktionen mellem det offshore netværk og styringen af den brugte effektelektronik (PED), dens effekt på systemets stabilitet og udfordringerne med hensyn til uønsket interaktion mellem styringer i det komplekse kontrol hierarki.

Udgangsssignalet af moderne turbiner der benytter PEDs er forvrænget ved høje frekvenser, og kontrolsystemets stabilitet bliver påvirket af resonanser og overtoner til stede i et svagt netværk. Eftersom disse fænomener eksisterer inden for båndbredden af turbinens kontrolsystemer, udgør de en risiko for kontrolsystemets stabilitet. Resonanserne og antallet af operationelle turbiner er delvist ukendte karakteristika af nettet i kontroldesign stadiet, hvilket gør usikkerheden og den uønskede interaktion i nettet til svære udfordringer for kontroldesignere.

Dette projekt behandler disse udfordringer og giver en indsigt i grundliggende årsager til fænomener, der tidligere har været problemer ved vindpark komissionering. Dette er udført gennem udvikling af design og validationsmetoder for styringer, ved at analysere turbineinteraktion med nettet og ved at foreslå designretningslinjer for at sikre behørig drift af flere styringer i vindparken. To specifikke fejl ligger til grund for analysen og udviklingen, en deformation af et rotorblad og en uønsket svingning i den reaktive effekt. Begge fejl er observeret i en vindpark.

De observerede lavfrekvente svingninger i reaktiv effekt blev mistænkt for at være

forårsaget af spændingsstyringen i det fælles koblingspunkt. Interaktionen mellem den statiske synkron kompensator (STATCOM), vindturbinens spændingsstyring og vindparkens overordnede styring (PPC) var tænkt værende involveret i fejlen. Ved at etablere grænser for sættet af mulige parametre for all involverede styringer, genskaber afhandlingen det observerede fænomen via simulation, og en metode til analytisk at finde sættet af kontrolparametre der sikrer behørig drift foreslås. Metoden giver DONG Energy muligheden for på forhånd at udregne grænser for kontrolparametrene, baseret på netværksparametre, og afhandlingen bidrager med at sikre behørig drift inden idriftsættelse.

Analysen af spændingskontrolfilosofien relateret til svingningerne i reaktive effekt viste et behov for at håndtere resonanserne introduceret af nettet. Afhandlingen bidrager til dette område med udviklingen af en robust $\mathcal{H}_\infty$ PED styring, der udnytter notch filtre i dens ydelsesspecfikation for at undertrykke overtoner af netfrekvensen. Denne metode kombinerer dæmpning af udvalgte resonansfrekvenser med stabilitet og ydelse inden for det definerede usikkerhedsområde. Styringen er efterprøvet i en model af vindparken, og det er vist at styringen giver en forbedring i ydelse, aktuatorindsats og forstyrrelsesundertrykkelse sammenlignet med standard PI styring.

Den anden fejl var at et turbinerotorblad blev ødelagt i en vindpark. Denne alvorlige fejl var mistænkt for at have bidragende årsager fra både mekaniske såvel som elektriske systemer. En undersøgelse blev udført som udelukkede fysiske generatorfænomener som cogging moment, såvel som spændingsforstyrrelser fra netværket og forsinkelser i PED styringen. Undersøgelsen indikerede at problemet stammede fra en ufuldstændig implementering af rotorhastighedsstyringen. Afhandlingen adresserer dette problem ved at udvikle kontrolmetoder til at begrænse drivakselstress, og derved mindske rotorblad vibrationerne. Bidragene inkluderer en linearisererende tilbagekoblingsstyring og en observer baseret backstepping styring for en vindturbine.

Afhandlingen består af en introduktionsdel der kort beskriver området, undersøgelserne foretaget i studiet, de udviklede modeller og styringsdesignsne foreslået til at håndtere de ovenover beskrevne udfordringer. Hovedresultaterne af forskningen er fremhævet i introduktionen og de detaljerede resultater er beskrevet i fire artikler som er vedlagt i den sidste del af afhandlingen.

Preface

This thesis was prepared at Automation and Control, the Technical University of Denmark in collaboration with DONG Energy in partial fulfillment of the requirements for acquiring the Ph.D. degree in engineering.

The thesis deals with different aspects of mathematical modeling of power systems for control synthesis and verification. The main focus is on development of advanced control methods for wind power plant and turbine components, but also parameter limitations in systems with a predefined control topology.

The content include a real-life data driven fault identification part, and a theoretical controller synthesis part. The thesis consists of a summary report and a collection of four research papers written during the period 2012-2015, that were published or submitted for publication.

Lyngby, November 2015

Mikkel Peter Sidoroff Gryning

Acknowledgements

I would like to thank my main university supervisor Professor Mogens Blanke for the time, guidance and support he has given me during this PhD project. Professor Mogens Blanke has a positive, humorous and inspiring approach to research and its challenges which is highly contagious. Through discussion and understanding he has always inspired me to handle the challenges faced. Even in what seemed the darkest time, he never lost faith in my ability to complete the project, and that kind of support is invaluable.

I would also like to thank my main company supervisor Dr. Karsten Hvalkof Andersen for a tremendous effort in guiding me in the right direction. Through his technical knowledge combined with a managerial know how of the internal workings of a busy company, he has time and time again proved a person whom you could trust to help no matter what.

My co-supervisor team consisting of Associate Professor Qiuwei Wu and Associate Professor Hans Henrik Niemann has been a valuable resource to not only shape the project, but also facilitate the writing of papers and helping me through the entire process from idea to completion. A special thanks goes to Dr. Łukasz Kocewiak of DONG Energy for his knowledge of industrial control systems and for providing critical feedback.

Everybody at the DONG Energy SCADA department deserves a huge acknowledgment for their work in making me feel at home, appreciated and being interested in my work, even though it is far from their area. They have made the time spent doing research fun and exciting. My colleagues at the Technical University of Denmark in Lyngby at the Automation and Control Group at DTU-Elektro deserve acknowledgment for their help in developing ideas and sharing insight which has helped me through rough patches.

I would also like to thank Dr. Troels Stybe Sørensen of DONG Energy Electrical Systems for setting up the funding and framework of the project.

In the end I would like to thank my family for their support and showing an interest in my research.

Table of Contents

List of Acronyms and Abbreviations

AC	Alternating Current
APC	Active Power Control
AS	Asymptotic Stability
B2B	Back-To-Back
BEM	Blade Element Momentum
CLF	Candidate Lyapunov Function
DC	Direct Current
DEWP	Dong Energy Wind Power
DTU	The Technical University of Denmark
EMT	Electromagnetic Transient
EU	European Union
HVAC	High-Voltage Alternating Current
HVDC	High-Voltage Direct Current
IAE	Integrated Absolute Error
IGBT	Insulated Gate Bipolar Transistors
IMC	Internal Mode Control
LCC	Line Commutated Converter
LCL	Inductor-Capacitor-Inductor
LCM	Lowest Common Factor
LFT	Lower Fractional Transformation
LIDAR	Light Detection and Ranging

LQE	Linear Quadratic Regulator
LTI	Linear Time Invariant
MIMO	Multiple-Input Multiple-Output
MISO	Multiple-Input Single-Output
MMCC	Modular Multilevel Cascaded Converter
MO	Modulus Optimum
NREL	National Renewable Energy Laboratory
OWPP	Offshore Wind Power Plant
P	Active Power
P2P	Point To Point
PCC	Point of Common Coupling
PED	Power Electronic Device
PI	Proportional-Integral
PMSG	Permanent Magnet Synchronous Generator
PPC	Power Plant Control
PR	Proportional Resonant
PSL	Power Synchronization Loop
PWM	Pulse Width Modulation
Q	Reactive Power
RC	Repetitive Control
RRF	Rotating Reference Frame
SIMC	Skogestad Internal Mode Control
SISO	Single-Input Single-Output
SO	Symmetrical Optimum
SS	State Space
STATCOM	Static Synchronous Compensator
SVC	Static Var Compensator

SWT	Siemens Wind Turbine
THD	Total Harmonic Distortion
TIP	Transmission Interface Point
TSO	Transmission System Operator
VRPC	Voltage and Reactive Power Control
VSC	Voltage Source Converter
VSI	Voltage Source Inverter
WPCC	Wind Power Plant Control
WPP	Wind Power Plant
WT	Wind Turbine
WTG	Wind Turbine Generator

Chapter 1

Introduction

The Renewable Energy Directive of the European Commission promotes energy from renewable sources in the EU and has, by implementation of national action plans, expanded the already growing market of WPPs [2]. The goals are national and given the shoreline of many European countries, namely The United Kingdom, Denmark, France and partly Germany, it is in many cases the optimal compromise of noise pollution versus performance to place the wind turbines (WTs) offshore. Wind energy is a sustainable clean energy source with high capacity. The electrical power can be generated from clusters of WTs as a WPP. Both on- and offshore WTs are heavy and complex machinery that consist of mechanical and electrical parts. Offshore WTs are bound together by a widespread medium-voltage submarine cable system and connected to an uncertain grid using long high-voltage alternating current cables. Connecting high power WPPs to the transmission grid requires appropriate interconnection and robust control systems to ensure high power quality and stability, while handling the related challenges such as harmonic resonances and disturbances.

The WTs, park controllers and other hard- and software are delivered by a range of suppliers each protecting their intellectual properties, making verification close to impossible before the construction phase. DONG Energy invests large amounts of capital in high risk entrepreneur projects where the final responsibility is with DONG Energy as project owners. The uncertainty of having many suppliers, unknown conditions and no comparable knowledge of possible performance and stability issues pose a great risk. Throughout a project, uncertainty adds to the final cost, and thereby raises the end cost of electricity, which must be lowered to make wind power competitive. To be competitive in the electricity market, WTs must produce electricity at a cost comparable to fossil fuel. The cost of wind energy is dominated by the initial investment. Maintenance and operation are large expenses in the offshore business and the money spent in the lifetime of a WT must be minimized. DONG Energy has invested significant funds in structural research, WPP layout and deployment.

A step in the direction of a lower cost of energy is up-front assessment of perfor-

mance and stability of the equipment. Modern WPPs use power electronic devices (PEDs) in the output stage that support real and reactive power control, but distort the grid. The high-frequency harmonics require complex passive filters or active filtering to limit the distortion. Research has focused on stability, distortion and disturbance rejection of power electronic device systems but does not consider the interplay of multiple WPP controllers. Multiple power electronic devices in the transmission system require technical knowledge of the involved controllers for all operating conditions. The controllers are designed without full system knowledge or coordination amongst suppliers. This thesis has by its unique insight into the industry and the inner workings of supplied controllers currently used in WPPs, the possibility to lower the risk in current WPP iterations and thereby the cost of energy.

1.1 Background

The project described in this thesis was started on the basis on DONG Energy foreseeing potential issues arising with the construction of larger WPPs. Internal research conducted prior to this project highlighted issues with both mechanical and power system control supplied by external manufacturers. Both electrical and mechanical component level control are delegated to external suppliers while the overall control philosophy is designed in-house. Correct operation of deployed systems is tested alongside construction using the parameters supplied. A question of risk and liability exist in case of erroneous operation due to controllers or due to interaction between systems delivered by different suppliers - e.g. static synchronous compensator and WT voltage control. Having access to both turbines and electrical infrastructure, the need for guidelines and tests to validate the supplied hard- and software was born.

1.2 Objectives

The objective of this research project is to provide methods and controller designs which are capable of coping with the challenges and remedy the faults that were observed in existing offshore WPPs. The project has focus on two critical faults, a deformation of rotor blades in a structural sound construction, and reactive power oscillations observed at the point of common coupling to the grid.

The first objective of the project is to develop drive train control methods to limit drive train stress. The motivation was that a preliminary investigation of the rotor blade fault suggested that the rotor speed controller was flawed, and blade vibrations could be associated with a lack of shaft vibration damping.

The second objective is to develop a design method for robust turbine current control this is able to operate in the uncertain offshore grid, and also includes notch filters which are present to suppress harmonics. The objective was motivated by a study compiled by DONG Energy that showed the existence of power system harmonics and resonances in offshore WPPs, with negative effects on output waveform quality.

The third objective of the project is to investigate the root causes of the observed reactive power oscillation fault, to develop a method for design and find a way to validate the controller parameters for such design. The validation method should include the effects of network parameters and show the bounds there exists for controller parameters to remain in stable operation, thereby clarify the limitations of the voltage control philosophy used.

1.3 Contributions

The main contributions of this project are the controllers developed in response to the focused faults, the analytical stabilizing set method, and the use of said method to investigate the influence between controllers and system parameters in the used voltage control philosophy. The preliminary investigation of causes for the blade oscillations both with respect to cogging torque, structural design and electrical network was completed successfully but could not verify the oscillations, and suggested that the cause was a flawed controller (*Unpublished*). The investigation contributes with a two turbine network model with standardized current and voltage control to analyze electromechanical interaction and grid disturbances (*Idea published - paper A*). The follow-up objective to reduce drive train stress was fulfilled by the development of an advanced non-linear back-stepping control in region two of a two-mass WT drive train (*Published - paper B*). This method of control shows promise in fully utilizing the region of operation where maximum power capture is possible, and an adaptive version was proposed [3]. A feedback linearization control of a two-mass drive train using generator torque was developed as a baseline.(*Unpublished*).

An $\mathcal{H}_\infty$ optimal robust controller was developed to provide selective filtering of grid voltage disturbances while guaranteeing stability and performance under uncertain grid conditions (*Published - paper C*). The uncertain system was modeled from the studied WPP to provide realistic grid effects. The original $\mathcal{H}_\infty$ controller was furthermore extended in a theoretical study to include a performance enhancement controller for optimal disturbance rejection (*Unpublished*).

The project additionally contributes with an analysis of the effect of a used distributed voltage control scheme on individual controller parameters and its limitations. A method to determine analytical stability bounds of the PI-based cascade controllers and the power plant control (PPC) as a function of system parameters using signature functions was developed (*Submitted - paper D*). This analysis enables entrepreneurs to validate the parameters of the supplied systems ahead of testing. The sampling time, cable length and droop characteristics of the PPC were shown to be correlated. The stabilizing sets method was used on the faulty WPP to generate the set of control parameters which provided a stable system. As the observed oscillations in reactive power were stable, the envelope served as basis for the analysis, and the oscillation were recreated. Furthermore, the effects of parameters on the generalized stabilizing set were identified.

The published contributions are listed as follows:

- Paper A provides an outline of possible research areas within industrial WPPs. The concept of multiple-input single-output system voltage control and robustness issues are highlighted, and a work-flow for future development is presented.

- Paper B suggests a back-stepping controller operating in the partial load region of a non-linear two-mass drive train model. The rotor speed is fed back while torsion angle and generator speed are estimated using a reduced order observer.

- Paper C presents a model of the studied WPP together with an uncertainty description. It is shown how a perturbation of grid impedance influences the inductor-capacitor-inductor (LCL) filter resonance damping. A $\mathcal{H}_\infty$ optimal controller is formulated using notch filters in the frequency dependent weighting functions. Three PI-based controllers are designed as a baseline. The active filtering and system stability is shown to be guaranteed within the component uncertainty range and has improved performance relative to the proportional integral (PI) controllers.

- Paper D investigates reactive power oscillations at the point of common coupling (PCC) in the studied WPP. Guidelines for WT and STATCOM current control design with respect to the studied WPP implementation is provided. Stability of the local voltage control is related to component values and a stabilizing envelope of controller parameter pairs is developed. A relation between WT, STATCOM and power plant control (PPC) parameter and component values are provided to enable up-front assessment of stability. A relation joining control parameters and system-wide oscillations is finally achieved, and reproduction of the observed oscillatory response is shown to be possible.

1.4 Structure and Outline of the Thesis

The remaining part of the thesis presents a study of two observed issues in a wind power plant, possible causes, and solutions. First an introduction to the field of wind energy is presented with respect to physical limitations and control challenges. Chapter 2 continues with a description of the studied WPP and general modelling of a wind turbine with focus on the electrical subsystem including generator, STATCOM, voltage source converter and an uncertain representation of the connected network. Furthermore, common control principles for voltage source converters are shown. The end of chapter two contains a short literature survey of the research fields touched upon in the thesis.

Chapter 3 presents the mechanical rotor and drivetrain models used for vibration analysis and the development and choice of models is motivated. Two drivetrain models are introduced with respect to the mechanical input torque and the effect on rotor blade vibrations. Chapter 3 ends with an analysis of the observed rotor blade vibrations with respect to actuator delay, parameter variation and network interaction.

Chapter 4 investigates the common current control principles and presents guidelines for parameter tuning aligned with performance and disturbance rejection. The phenomena of power system harmonics and their effect on the current control is shown, and a robust controller with active filtering is developed to enhance the disturbance response. An addition to the current feedback approach is proposed based on residual control, which shows to improve disturbance attenuation. The chapter then focuses on establishing controller parameter stability bounds for voltage controllers using the Hurwitz signature, and the bounds are extended to include the power plant controller. Finally an analysis of the observed reactive power oscillations is presented which identifies plausible causes and recreates the phenomena.

Chapter 5 presents feedback linearization and backstepping control for the two-mass drivetrain to reduce shaft stress and thereby rotor blade vibrations. It is shown that the shaft stress can be minimized for different levels of system information.

Chapter 6 provides perspectives and a conclusion of the presented subjects. Appendices A to D contain papers in which the publishable results obtained in the project have been disseminated.

1.5 Papers included in the thesis

Paper A J. Glasdam, L. Zeni, M. Gryning , C.L. Bak, J. Hjerrild, P.E. Sørensen, A.D. Hansen, P.C Kjær, M. Blanke, K. Andersen, T.S. Sørensen and B. Hesselbæk. "HVDC Connected Offshore Wind Power Plants: Review and Outlook of Current Research." Proc. of the 12th International Workshop on Large-Scale Integration of Wind Power into Power Systems as well as on Transmission Networks for Offshore Wind Power Plants, 2013. **Published.**

Paper B R. Galeazzi, M. Gryning and M. Blanke. "Observer backstepping control for variable speed wind turbine." Proceedings of the American Control Conference — 2013, pp. 1036-1043. **Published**

Paper C M. Gryning, Q. Wu, M. Blanke, H.H. Niemann and K. Andersen. "Wind turbine inverter robust loop-shaping control subject to grid interaction effects." IEEE Transactions on Sustainable Energy, 2015, Issue 99. **Published.**

Paper D M. Gryning, Q. Wu, Ł. Kocewiak, M. Blanke , H.H. Niemann and K. Andersen. "Stability Boundaries and Robust Design for Offshore Wind Park Distributed Voltage Control." IEEE Transactions on Control Systems Technology, 2015. **Submitted.**

Chapter 2

Wind Energy

Wind energy in its simplest form is conversion of kinetic energy from the wind to mechanical energy in the drive train. A WT captures the kinetic energy from the wind and this energy can be used to for instance pump water or converted to electrical energy by a generator. Figure 2.1 shows the crucial components of a Siemens Wind Power SWT-2.3-93. The kinetic energy of the wind drives the blades of the WT which though their hub spins the generator shaft. This shaft can either be connected to the generator through a gearbox or as seen in newer turbines, directly to a multipole generator. The electrical energy is then exported to either the utility grid or a WPP network. Distribution in the connected network requires higher voltage for loss

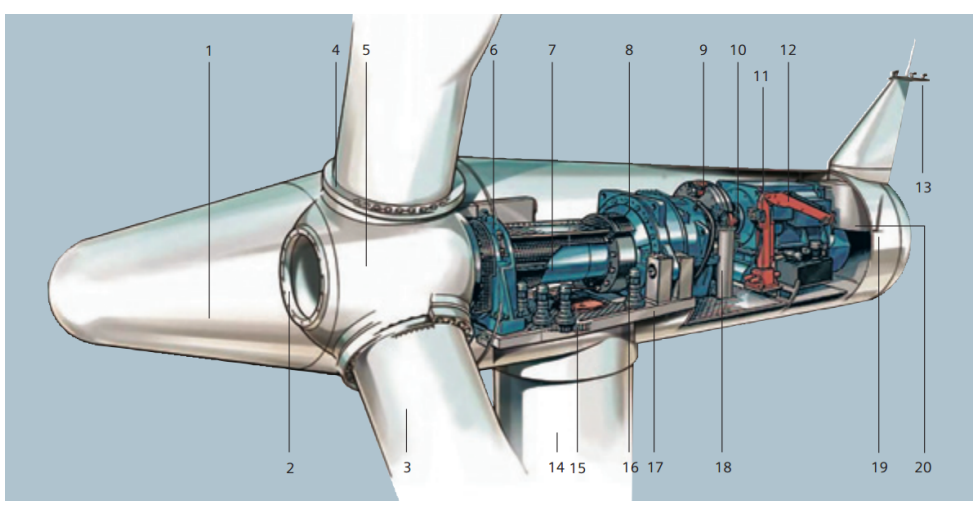

Figure 2.1: Siemens Wind Power SWT-2.3-93. Major components: **3.** Blades, **5.** Rotor hub, **7.** Main shaft, **8.** Gearbox, **11.** Generator. [4]. By permission from Siemens Wind Power.

reduction. Low voltage output power is transmitted to a transformer at the base through a cable in the tower. The transformer steps up the voltage from $690V$ to $33kV$.

The wind energy capture potential is a function of air pressure difference creating a flowing air mass m with the velocity v_w. The kinetic energy of the air mass is,

$$E_{kin} = \frac{1}{2}mv_w^2. \tag{2.1}$$

With a mass density of the flowing air, ρ, the instantaneous power of the wind flowing through the swept area of the blades A,

$$P_m = \frac{dE_{kin}}{dt} = \frac{1}{2}\rho A v_w^3. \tag{2.2}$$

The maximum power obtainable from a cylinder of fluid with cross sectional area A is limited by Betz's law, and thus independent of turbine blade configuration. Betz's law defines the power coefficient C_p as the ratio of extracted power P_t to maximum power P_m, limited to 0.593 by calculation using the Actuator Disc Concept [5]. The actual power capture depends on turbine rotor power efficiency,

$$P_t = \frac{1}{2}C_p(\lambda,\beta)\rho A v_w^3, \quad \lambda = \omega R_b v_w^{-1}, \tag{2.3}$$

where λ is the blade tip speed ratio, β is the blade pitch angle and ω is the angular velocity of the rotor. The $C_p(\lambda,\beta)$ surface is for industrial purposes estimated from measurements or approximated as [6],

$$C_p(\lambda,\beta) = 0.73(\frac{151}{\lambda_i} - 0.58\beta - 0.002\beta^{2.14} - 13.2)e^{-18.4/\lambda_i}, \tag{2.4}$$

$$\lambda_i \triangleq \frac{1}{\frac{1}{\lambda - 0.02\beta} - \frac{0.003}{\beta^3+1}}. \tag{2.5}$$

The $C_p(\lambda,\beta)$ surface of (2.5) obtains a global maximum for $\beta = 0, \beta \in \mathbb{R}^+$. The optimum value of λ vary between rotors.

2.1 Wind Power Plants

WTs are gathered in clusters to utilize common infrastructure such as transformers, cables and compensation devices. Offshore wind power plants (OWPP) are projected to generate 14 percent of the power consumed in the European Union by 2030. The wind speed offshore is on average higher and consistently returns the increased capital investment [7].

2.1.1 Offshore Plants

The clustered WTs make great demands on network sizing, transformers, protection and control systems. OWPPs are connected to shore by high-voltage alternating

current (HVAC) or high-voltage direct current (HVDC) export systems. The alternating current connected utility grid has the potential to be weak as the location of the WPP shore connection could be remote. A weak grid results in a need for precise controller specifications to limit voltage flicker and harmonic pollution in the utility grid. This makes direct current an attractive solution for OWPP grid connection. A typical alternating current connection is shown in Figure 2.2, and emphasizes that the high charging currents in the cables require reactive compensation at cable ends, in order to have a very long export cable, using for instance a STATCOM or a SVC [8]. Direct current export connections utilize converters to reduce the reactive compensation needed, but they have a higher initial cost [9]. One upcoming idea is to use matrix or series interconnected topology for direct current collector systems to reduce losses [10]. Meshing high power direct current systems is still a challenge, but the needed breakers are in focus in the research [11],[12]. Multi-terminal direct current systems suffer from the inability to clear faults quickly and solutions so far include multi-WT connected converters and master/slave control methods [13],[14].

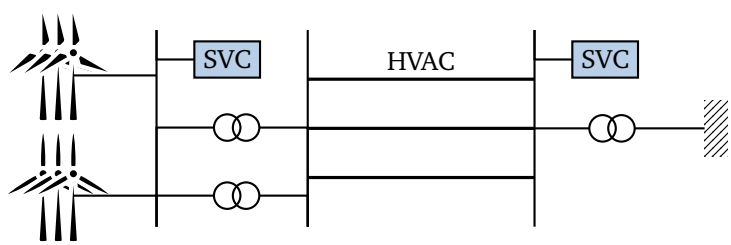

Figure 2.2: High-Voltage Alternation Current generic connection diagram with reactive power support.

Operating clusters of WTs require control on a park level to sustain production and stability. WPPs in general utilize layers of control to achieve maximum production while providing reactive power compensation to maintain the voltage level. With larger WPPs, the effect of multiple power electronic devices may result in unacceptable interaction between controllers and cause reduced efficiency and stress on both mechanical and electrical components [15]. The large submarine cable network external to the WT generator can cause resonances within the power electronic device controller bandwidth. This could lead to loss of production from overcompensation or disconnection of WTs [16].

2.1.2 Grid Codes

The technical specification at the point of connection is commonly called the grid code. The national document facilitates services, parameters and limitations from the perspective of the transmission system operator. The regulating body in collaboration with the transmission system operator determine communication,

metering and electrical standards. The grid code determines the tests needed to achieve final operation notice. In addition to control modes, the code defines the total harmonic distortion and clearing periods for voltage and frequency in case of network disturbances and transients.

The Nordic Grid Code seeks to harmonize the rules that govern the various national grid standards. Standardized requirements across country borders must be established to create the best possible conditions for development of a functioning and effectively integrated Nordic power market [17].

2.2 Wind Power Plant Control

The control of wind turbines is a complex problem and spans multiple fields of research, materials, aerodynamics, and power systems [18]. Standards by IEC define default communication and control practices used in modern WPP. This section presents an overview of WPP control on the wind plant level. The challenges, purpose and objectives of wind power plant control will be introduced with focus on distributed voltage control and power electronic device control with respect to the voltage quality in the utility grid.

2.2.1 Primary Control Objective

Ignoring ancillary services such as balancing power and frequency support, the overall control objective of a WPP is to maximize energy production at the lowest possible cost. Optimal power production with respect to cost requires synchronization of control techniques, minimization of fatigue loading and component stress while maintaining low running costs and complying with the grid code. The objective of high-level control is to *improve* the total energy production [19]. The definition of *improve* is only valid in the sense of WT location and wake effects. Given a certain layout, placement and technical specifications, the objective of wind power plant control is to *minimize* losses relative to the theoretical maximum wind power capture. A hot topic in WPP research is turbine wake interactions. Extraction of energy from the wind by the WT rotor create wakes that propagate downstream [20]. The flow in wakes has lower speed and higher turbulence compared to the surrounding wind. The wake mixes with the free stream of surrounding air and given enough distance regains its previous flow properties [21]. Placement of turbines offshore are limited by geographical properties of the seabed and the distance between WTs are often far from optimal. The WTs thus have less available energy to extract from the wind, see the study WPP layout in section 2.3.

Wind power plant control is a diverse challenge and can be divided into two key areas: Power electronic device engineering and mechanical engineering. Power electronic device engineering and control employ detailed electrical but simplified mechanical models. The range of frequencies from $0.1 - 200$ Hz are of interest in the control design. Electromagnetic transient analysis includes switching, and for both filter design and harmonic analysis, the range of frequencies must include the switching frequencies. The mechanical aspect includes drive train, generator and

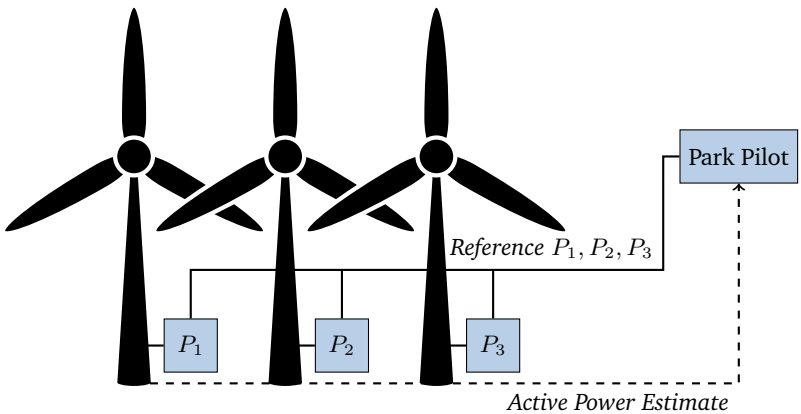

Figure 2.3: Power plant control centralized active power distribution.

aerodynamic parts which have their modes in the sub 5 Hz frequency range. The next section presents a summary of the control challenges faced.

2.2.2 Control Challenges

Wind power plant control challenges follow from the stochastic nature of the captured energy. The growing power rating of WPPs and the weakness of the upstream power grid at the transmission interface point pose a threat to voltage and transient stability. Power injected into the upstream grid influences the system operation point and multiple inertia less WPPs requires fast control to maintain frequency stability. The reactive power consumption is related to the real power production and must be regulated. Control interaction, actuator usage, structural loading, and wind variability are challenges in WPP control performance optimization. Current technology allows WPPs to meet industry expectations such as low voltage ride through and system reactive power support by controlling the terminal voltage [22]. The high-level control areas include: Active Power Control, Voltage and Reactive Power Control, Power Factor Control and Grid Protection.

Active Power Control

The active power output of the WPP follows a time-varying reference generated from estimated available power, external limit, delta control or ancillary services. Maximum power capture is handled by the individual WT and is achieved with pitch angle- and rotor speed control [23]. The extent of the individual regulation capabilities provided is a function of the parameters used to determine the limiting power. In modern WPPs the power plant controller schedules the power to be produced based on anemometer measurements fitted to an optimal power trajectory. If no measurements are available, the wind speed is estimated from pitch angle

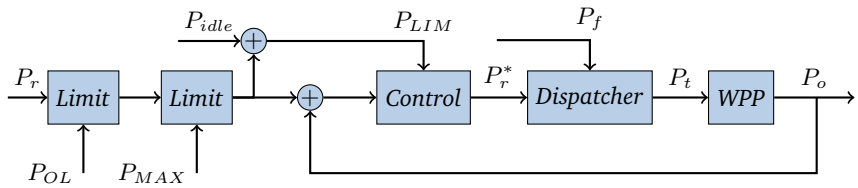

Figure 2.4: Power plant control cascade active power control with dispatcher. WPP point of common coupling external reference P_r, internal reference P_r^*, estimated power P_f, turbine power P_t, output power at the point of common coupling P_o and limits P_{MAX} and P_{OL} for maximum reference and overload.

and angular velocity using rotor C_p tables. Disregarding primary frequency support, synthetic inertia and power oscillation damping, the main challenge in active power control is the distribution of active power set-points.

Power reference dispatch methods are widely researched. Standard methods include feed forward [19], open loop [24] and feedback control [18]. Optimal control for minimization of WT mechanical fatigue or drivetrain backlash exist in the literature but is to the best of the authors knowledge not implemented at a large scale [25].

The complexity of power distribution is determined by the structure of the WPP information pathways. Active power distribution reference signals are shown in Figure 2.3 for a centralized power plant controller based on the estimated active power. Static models are commonly used for optimization of power plant control design to reduce complexity, neglecting signal delay. A recent development in active power control is power derating. Power derating methods seek to provide a lower than rated active power reference to upwind WTs to minimize the wake impact on downstream WTs. Derating minimize the potential losses inflicted by suboptimal WPP layout. Power derating is shown to increase the output in systems with perfect knowledge of the wind direction, but has a negative impact under time-varying conditions [26]. The typical WPP studied in section 2.3 has a power plant controller operating at $5 - 10$ Hz with feed-forward of the available power and feedback of the power output at the point of common coupling, as shown in Figure 2.4.

Voltage and Reactive Power Control

The goal of voltage and reactive power control is to keep voltages at all terminals in the network within acceptable limits using least possible reactive power injection or absorption to reduce RI^2 and XI^2 losses [27]. Voltage control in WPPs is achieved by balancing the reactive power injection and absorption, and WPPs are designed to be able to maintain zero reactive power transfer between the WPP and the grid. The reactive power transfer is proportional to the difference in voltage magnitude, making local compensation a requirement. Static compensation such as filters, shunt

capacitors and reactors are placed at the substation and are characteristics of the designed network. Optimal placement of static components with respect to minimum power loss, installation cost, voltage profiles and more is reviewed in [28],[29]. Dynamic reactive compensation are controllable active sources of reactive power compensation. The voltage regulating capabilities of WTs vary with generator technology and manufacturer. Fixed speed induction generator based WTs have no direct voltage control and require reactive power compensation [30]. The doubly-fed induction generator type-3 WT employs converters in the rotor circuit and can control active and reactive power independently. Full-converter type-4 WTs use converters as the only connection and have the ability to perform voltage or reactive power control. Common control modes are constant power factor, coordinated constant interconnection point voltage, and constant reactive power control [31].

The difficulties in OWPP voltage control include:

- Weak grids. WPPs are often connected at remote locations and with large amounts of wind generation, the short circuit ratio can be very low causing slow fault recovery and operation on the limit of the power-voltage curve of the WTs.

- Weak grid high voltage sensitivity dV/dQ. A challenge for distributed voltage control as the WTs cannot inject adequate reactive power to support the voltage level at the point of common coupling.

- Lack of synchronous generators in full-converter based WPPs. The collective inertia of the system is very low causing faults to propagate quickly.

The OWPP voltage control is summarized in section 2.2.3.

2.2.3 Plant Level Voltage Control

The structure of WPP voltage control depends mainly on production unit capability and plant topology. The methods are divided into distributed voltage- and voltage/reactive power control. The method employed in the studied WPP is distributed voltage control, illustrated in Figure 2.5, where the local production unit regulate the terminal voltage, similar to automatic voltage regulation in synchronous generators. The reference voltage is generated by a power plant controller sustaining the voltage at the point of common coupling, utilizing a STATCOM and the WT reactive power capabilities. For a reactive power error, Q^e_{pcc}, at the point of common coupling and the output of the WT, Q_{wt} in the rotating reference frame,

$$Q^e_{pcc} = (3/2)(-u^{d_e}_{pcc} i^q_{pcc}),\ Q_{wt} = (3/2)(-u^d_t i^q_{wt}), \tag{2.6}$$

where i_{pcc^q}, i^q_{wt}, $u^{d_e}_{pcc}$ and u^d_t are the quadrature axis current at the PCC and WT terminals, direct axis PCC voltage error and direct axis WT terminal voltage respectively.

The required WT quadrature axis current neglecting losses and electrical distance is,

$$i_{wt}^{q} = \frac{u_{pcc}^{d_e} i_{pcc}^{q}}{n i_{wt}^{q}}, \tag{2.7}$$

where n is the number of connected turbines. The reactive power injected is similar for each WT independent of location which can cause saturation. Combined voltage/reactive power control regulates the local unit interface voltage, but determine the reactive power output as a function of both the electrical distance and the active power production. The device injects a reactive current proportional to the distance to the point of common coupling to compensate for the array cables.

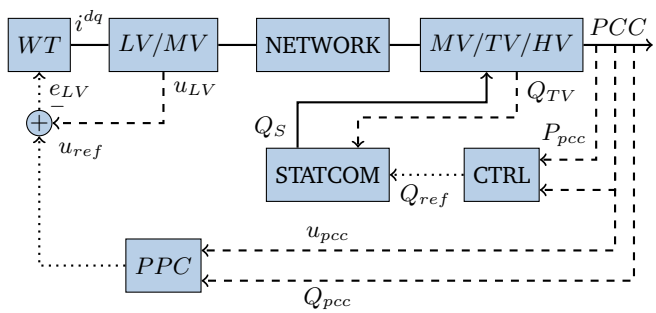

Figure 2.5: Schematic wind farm voltage control. Plants *WT* and *STATCOM* include current controllers in the blocks. $- - -$ Measurement, $\cdots$ Command, $\rightarrow$ Physical connection

Maintaining terminal voltage levels within operational limits in a distributed production environment requires a reactive power injection control philosophy. A schematic of WPP voltage control is illustrated in Figure 2.5. In networks dominated by power electronic devices, the unit adjusts the output within the operational power range to achieve voltage stability. The reactive power supplied by the WTs compensate for the consumption in steady state, while the STATCOM, connected at the point of common coupling, is responsible for the transient supply. Manually switched reactors are added at the point of common coupling and the onshore substation to extend the operational envelope of the STATCOM. The STATCOM is also used for additional compensation in case of lacking WT reactive power capability.

The power plant controller operates through two cascade control loops and constitutes a multiple-input single-output system. As part of the multiple-input single-output system, the power plant controller is operated at a low bandwidth to prevent stability problems. Fast voltage control is dependent on the STATCOM connected directly at the tertiary winding of the high voltage transformer. A case of multiple-input single-output system reactive power oscillations at the point of common coupling is presented in section 2.3.

2.3 Case: Study Wind Power Plant

The particular WPP that is the object for study in this research, abbreviated SWPP, was commissioned for power production in the early 2010s. The WPP has more than 50 turbines connected to the offshore substations by more than 100 km 33kV array cables, and further connected to an onshore substation by 150 kV subsea export cables. The layout of turbines and substations is shown in Figure 2.7. Measured by

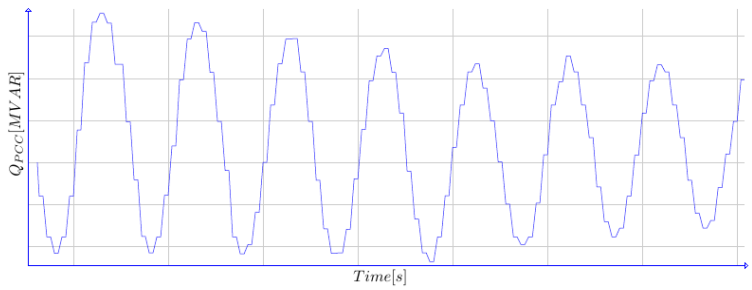

Figure 2.6: Reactive power measurements at the point of common coupling from an operational WPP.

capacity, the WPP was at the point of construction one of the largest offshore WPP in Europe. Due to its massive size and a variety of problems, the research in this thesis is mainly based on component values, control methods and the topology used in this WPP. Observations prior to the initiation of full production indicated a problem with the initial tuning of the voltage controllers. Poorly damped reactive power oscillations were observed at the point of common coupling, as shown in Figure 2.6. A cause was sought through disconnection of WTs from the power plant controller, which attenuated the oscillation amplitude. Adjustment of controller gains partly remedied the problem, but the origin was not fully clarified. These observations are used as basis for the investigation in section 4.3.

2.4 Modelling and Functionality of Main Components

This section introduces the overall principles and modelling of components that are essential to this study, and refers to the literature where detailed models are available.

2.4.1 Small Signal Modelling

System dynamics can be modeled with various levels of complexity depending on the wanted accuracy or available measurements. Consider a system modeled by a

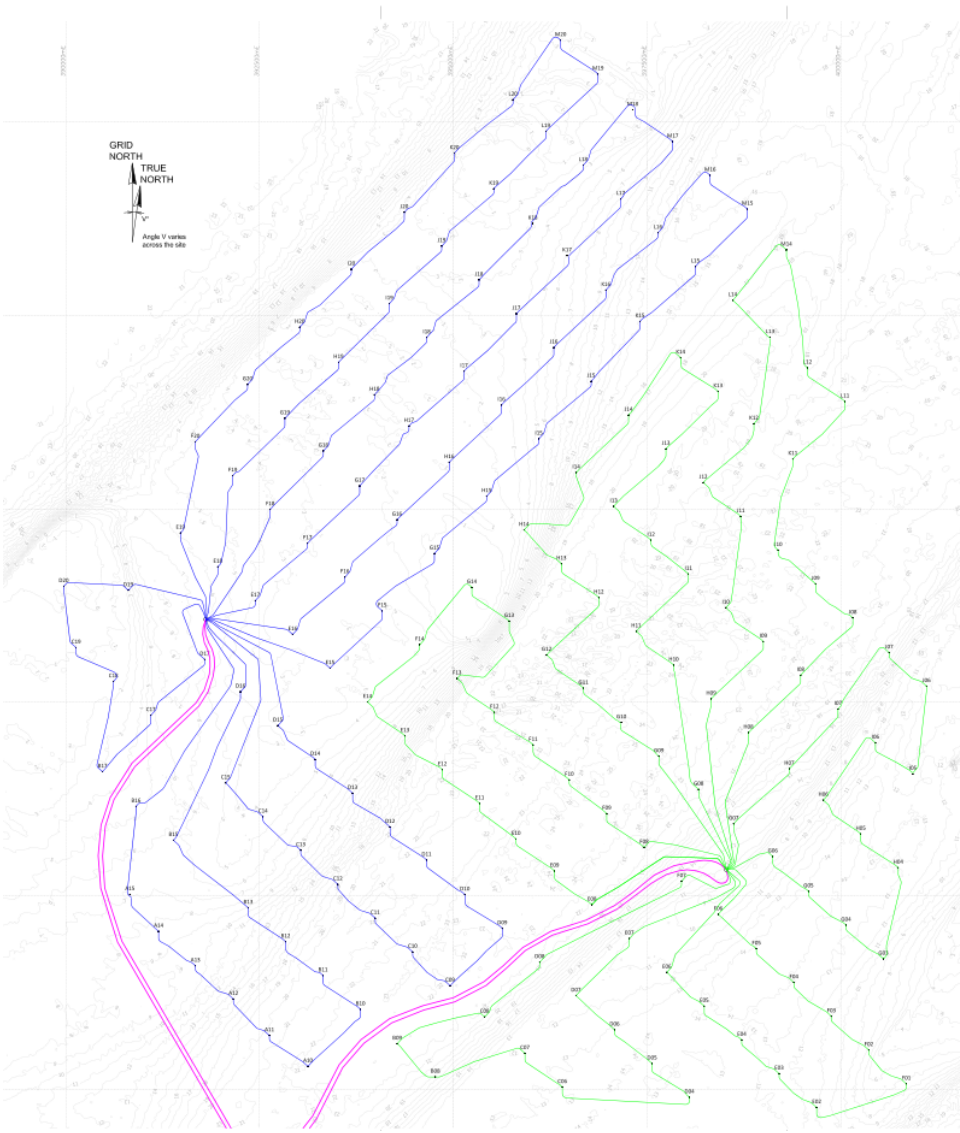

Figure 2.7: Physical layout of the studied wind power plant.

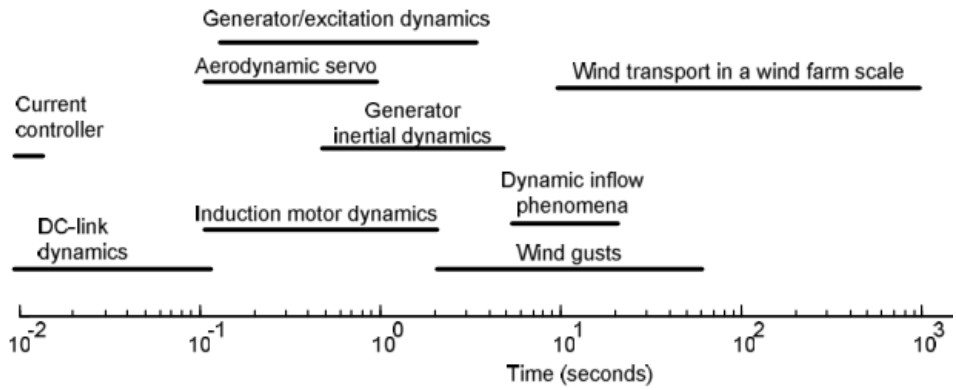

Figure 2.8: Frequency intervals of dynamics [27].

finite number of coupled first-order differential equations,

$$dx_1/dt = f_1(t, x_1, \ldots, x_n, u_1, \ldots, u_p),$$
$$dx_2/dt = f_2(t, x_1, \ldots, x_n, u_1, \ldots, u_p),$$
$$dx_n/dt = f_n(t, x_1, \ldots, x_n, u_1, \ldots, u_p),$$

where $\boldsymbol{x}$ is a vector of system states, and $\boldsymbol{u}$ is the input. The differential equations are expressed as a n-dimensional vector differential equation $\boldsymbol{f}$ and an q-dimensional output vector $\boldsymbol{y}$ which are states that physically can be measured,

$$\boldsymbol{dx}/dt = \boldsymbol{f}(t, \boldsymbol{x}, \boldsymbol{u}), \tag{2.8}$$
$$\boldsymbol{y} = \boldsymbol{h}(t, \boldsymbol{x}, \boldsymbol{u}). \tag{2.9}$$

A system which does not explicitly depend on time, i.e. $dx/dt = f(x)$, is time invariant. For linear time invariant systems, the state, input and output model is represented in the simplest form,

$$\dot{\boldsymbol{x}} = \boldsymbol{A}\boldsymbol{x} + \boldsymbol{B}\boldsymbol{u}, \tag{2.10}$$
$$\boldsymbol{y} = \boldsymbol{C}\boldsymbol{x} + \boldsymbol{D}\boldsymbol{u}, \tag{2.11}$$

called state-space form. The small-signal model describes the state trajectories of the system from any initial condition $\boldsymbol{x_0}$. The eigenvalues of $\boldsymbol{A}$ evaluated at an initial value $\boldsymbol{x_0}$ show the dynamic behavior of the system at the initiation point.

2.4.2 Wind Turbine

Multiple small signal models of WTs are available in the literature. Standardized techniques for modelling of the main components exist in IEC 61400 for power

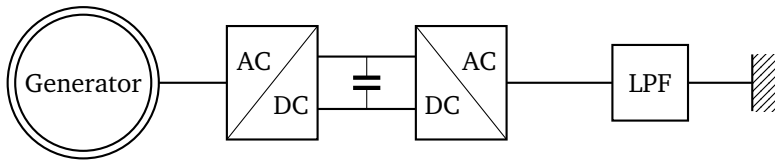

Figure 2.9: Type-4 WT with filter at the output.

system stability studies [32]. The time range of dynamics that should be considered when modelling specific phenomena is shown in Figure 2.8. A widely used model is the National Renewable Energy Laboratory wind turbine aero-hydro-servo-elastic tool FAST [33] when considering mechanical simulations and coupled dynamic responses. FAST utilizes blade element momentum theory to numerically simulate the response, which limits the analytical purpose. Robustness and fault seeking methodologies consider simple worst-case models that aim to bound parameter values. Existing WT models are commonly either purely mechanical or electrical. In this project, a WT model representing mechanical and electrical phenomena and its control was developed to investigate network effects on rotor vibration.

The mechanical torsional torque transferred by the main shaft through the drive-train is interfaced by the generator which converts the mechanical energy to electrical energy. A variable speed type-4 WT is decoupled from the grid-frequency through an AC/DC/AC converter and can operate at an optimal rotational speed for wind power capture. The wind turbine system is often split into an electrical and mechanical part, as the dynamics are in different frequency intervals.

2.4.3 Wind Model

The wind model used is a part of the wind turbine block-set developed by RISØ DTU and Aalborg University based on the Kaimal spectra. The SB-2 model [34] uses the Matlab white noise generator and a seed specifier for accurate reproduction of results. The basic edition used in this thesis takes the tower shadow and the rotational turbulence into account. The inputs are:

- Rotor Diameter [m] - To simulate rotational turbulence.
- Average Wind Speed [m/s].
- Length Scale [m] - Not used in simple version.
- Turbulence Intensity [%].
- Sample Time [s].

An overview is found in [34].

2.4.4 Reference frames

The large-scale components are shown in Figure 2.9 and consist of a generator, two voltage source converters (VSC), an intermittent storage device and an output filter. The electrical systems are represented in the $dq0$ rotating reference frame (RRF). The phases in a balanced three phase abc system are separated by $2\pi/3$ radians and the sum of their individual voltage components, the vectors $\boldsymbol{u_a}$, $\boldsymbol{u_b}$ and $\boldsymbol{u_c}$ can be expressed as the sum, $\boldsymbol{u_s}$,

$$\boldsymbol{u_s} = \boldsymbol{u_a} + \boldsymbol{u_b} + \boldsymbol{u_c} = u_a e^{j0} + u_b e^{j\frac{2}{3}\pi} + u_c e^{j\frac{4}{3}\pi}. \tag{2.12}$$

Using that $e^{j\alpha} = \cos\alpha + j\sin\alpha$,

$$\boldsymbol{u_s} = k_t(u_a + a u_b + a^2 u_c),\ a = e^{j\frac{2}{3}\pi}, \tag{2.13}$$

where k_t is a constant. The space vector transformation of three phase time domain signals into balanced two-phased time varying quadrature quantities is known as the Clarke ($\alpha\beta0$) transformation [35]. The time varying nature of the abc phases are conserved as the Clarke transformation utilizes a stationary reference frame. The Park ($dq0$) transformation additionally rotates the reference frame with an angular velocity selected as the angular velocity of the projected sinusoidal phase quantities. The resulting reference system is time invariant and the phases are DC signals which makes linear control theory an often used approach and reduces simulation time significantly [36]. The drawback is the requirement of an accurate and fast measurement of the phase angle of the utility voltage.

The transformation is instantaneous and can be applied to arbitrary three-phase time dependent signals. For $\theta_d = \omega_d t + \phi$ with ω_d being the angular velocity, t the time and ϕ the initial angle, the transformation is given by,

$$\boldsymbol{x_{dq0}} = \boldsymbol{T_{dq0}}(\boldsymbol{\theta_d})\boldsymbol{x_{abc}}, \tag{2.14}$$

where,

$$\boldsymbol{x_{dq0}} = \begin{bmatrix} x_d & x_q & x_0 \end{bmatrix}^\mathsf{T},\ \boldsymbol{x_{abc}} = \begin{bmatrix} x_a & x_b & x_c \end{bmatrix}^\mathsf{T}, \tag{2.15}$$

with the abc to $dq0$ transformation matrix $\boldsymbol{T_{dq0}}$ defined as,

$$\boldsymbol{T_{dq0}}(\boldsymbol{\theta_d}) = \kappa \begin{bmatrix} \cos\theta_d & \cos(\theta_d - \frac{2\pi}{3}) & \cos(\theta_d + \frac{2\pi}{3}) \\ -\sin\theta_d & -\sin(\theta_d - \frac{2\pi}{3}) & -\sin(\theta_d + \frac{2\pi}{3}) \\ \gamma & \gamma & \gamma \end{bmatrix}, \tag{2.16}$$

with γ being the zero component constant, and the inverse transformation given by,

$$\boldsymbol{T_{dq0}}(\boldsymbol{\theta_d})^{-1} = \frac{2}{3\kappa} \begin{bmatrix} \cos\theta_d & -\sin\theta_d & \gamma \\ \cos(\theta_d - \frac{2\pi}{3}) & -\sin(\theta_d - \frac{2\pi}{3}) & \gamma \\ \cos(\theta_d + \frac{2\pi}{3}) & -\sin(\theta_d + \frac{2\pi}{3}) & \gamma \end{bmatrix}. \tag{2.17}$$

The instantaneous active power, P, and reactive power, Q, are,

$$P = \kappa_p(u_q i_q + u_d i_d + 2u_0 i_0), \tag{2.18}$$

$$Q = \kappa_p(u_q i_d - u_d i_q), \tag{2.19}$$

assuming a balanced and harmonic free system. As the frame rotates with ω_d, the synchronized signal is a constant in steady state, but any non-fundamental harmonics with frequency ω_h will have a frequency of $\omega_h - \omega_d$. The standard for modelling electrical machines is κ set to $2/3$, using the amplitude invariant property of the transformation, and this choice of constant is used throughout the thesis unless otherwise mentioned.

2.4.5 Generator

The decoupling of line and machine side frequencies in type-4 WTs enables use of synchronous generators where the rotor and the magnetic field rotates with the same speed. Either the excitation field in the synchronous generator is provided by a permanent magnet or a coil on the armature side connected to the AC/DC converter. A magnet mounted on the rotor shaft induces currents in the armature, opposing the mechanical torque. In synchronous generators, the frequency of the induced currents is proportional to the amount of pole-pairs passing the armature windings. The gearing in a drivetrain is responsible for maintaining an adequate angular speed of the generator shaft as the rotor shaft revolves in sync with the rotor. A similar change in frequency is achieved by adding multiple pole-pairs to the generator, adding weight and complexity but removing the need for gearing.

The machine used in this thesis is the permanent magnet synchronous generator. Denoting rotor and stator with superscript r and s respectively, the voltage at the stator windings is,

$$\boldsymbol{v}^s_{abc} = r^s \boldsymbol{i}^s_{abc} + \frac{d\boldsymbol{\lambda}_{abc}}{dt}, \tag{2.20}$$

where r^s is the stator winding resistance per phase and $\boldsymbol{v}^s_{abc}$ and $\boldsymbol{i}^s_{abc}$ are the voltage and current vectors for the stator phases. The winding flux linkage matrix $\boldsymbol{\lambda}_{abc}$ is,

$$\boldsymbol{\lambda}_{abc} = \begin{bmatrix} L_{aas} & L_{abs} & L_{acs} \\ L_{bas} & L_{bbs} & L_{bcs} \\ L_{cas} & L_{cbs} & L_{ccs} \end{bmatrix} \boldsymbol{i}^s_{abc} + \lambda_m \begin{bmatrix} \sin\theta_r \\ \sin\theta_r - \frac{2\pi}{3} \\ \sin\theta_r + \frac{2\pi}{3} \end{bmatrix}, \tag{2.21}$$

where subscripts L_{xx} represent the self and mutual inductance of the windings and λ_m is the flux linkage by the permanent magnets on the rotor seen from the stator phase windings. Due to rotor saliency, the air gap is not uniform and the self and mutual inductance of the stator windings are a function of the rotor position. Representing the generator dynamics in the rotating reference frame eliminates the rotor angle dependency as,

$$v^r_{ds} = r_s i^r_{ds} + \frac{d\lambda^r_{ds}}{dt} - \omega_e \lambda^r_{qs}, \tag{2.22}$$

$$v^r_{qs} = r_s i^r_{qs} + \frac{d\lambda^r_{qs}}{dt} + \omega_e \lambda^r_{ds}, \tag{2.23}$$

where ω_e is the electrical rotor angular velocity of the machine. Representing the winding fluxes in the rotating reference frame and assuming a constant magnet flux,

$d\lambda_m/dt = 0$,

$$\boldsymbol{L_{dq}}\frac{\boldsymbol{di_{dq}}}{dt} + \boldsymbol{R_{dq}}\boldsymbol{i_{dq}} = \boldsymbol{v_{dq}} + \boldsymbol{DL_{dq}}\boldsymbol{D\omega i_{dq}}, \tag{2.24}$$

$$\boldsymbol{\omega} = \begin{bmatrix} 0 & \omega_g \\ -\omega_g & 0 \end{bmatrix} \quad \boldsymbol{D} = \begin{bmatrix} 0 & 1 \\ 1 & 0 \end{bmatrix}, \tag{2.25}$$

where $\boldsymbol{L_{dq}}$ and $\boldsymbol{R_{dq}}$ are diagonal matrices with the dimensions $2 \times 2 \in \Re^+$. The output waveforms of the generator is fed to an AC/DC/AC full-converter system. A model of the generator with a non-constant magnet flux is presented in section 3.3.4.

2.4.6 Voltage Source Converter

The decoupling of frequencies between machine and grid is achieved by interfacing the generator and the line AC sides by an intermediate DC-link. Power electronic devices were introduced in the interface between machine and grid to change the WT from an energy source to an active power source [37]. They enable systems to mimic power plants, providing ancillary services necessary in remote locations. A converter interface enables bidirectional power flow, reactive power control and reduces wear on the drivetrain [38]. The converter technology has developed from partial scale converters for rotor frequency control in type-3 WTs, to full-rated application in type-4 WTs. AC/DC converters (rectifier) take sinusoidal input voltages and rectifies

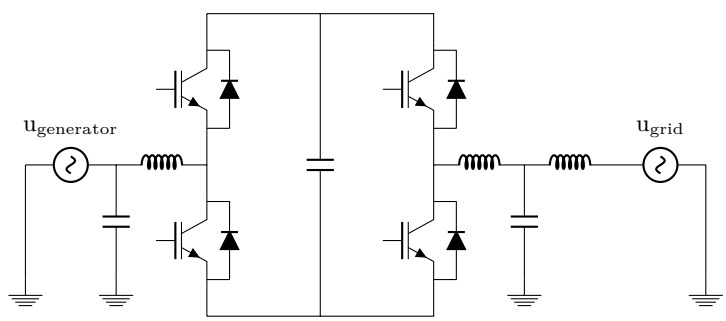

Figure 2.10: Single phase diagram of a generator interfaced to the grid by a full-converter with input inductor-capacitor filter, and output LCL filter.

it into a unidirectional DC voltage, whereas the DC/AC (inverter) converter takes a DC input voltage and converts it to a sinusoidal AC output. Fundamentally, the aim of an AC/DC - DC/AC converter system is to accurately create multilevel voltages with good spectral quality.

The physical configuration of converter systems depends on the power level. The simplest full-converter type uses a diode full-wave bridge rectifier. The n pulse passive rectifier output DC voltage is boosted to an adequate DC level by a DC/DC converter. The DC/DC booster is used as actuator to control the DC-link voltage. In

diode-rectifier configurations, the stator currents are commonly controlled as one which could cause torque ripple, and can reduce the lifetime of the drivetrain [39]. The diode-bridge is often used in permanent magnet applications where there is no reactive power need in the generator and the drivetrain system is gear-less, minimizing the effect of torque ripple. Modular multilevel converter configurations are preferred in high power turbines for independent phase control, bidirectional power flow and their spectral quality [40].

Figure 2.10 shows a back to back voltage source converter with two output voltage levels common in many industrial WTs due to costs and reliability [41]. The drawbacks of a two-level converter are a large DC-link capacitor, higher harmonic amplitude levels and the voltage change rate. Modular multilevel converters alleviate the drawbacks of the two-level converter using additional output voltage levels. The switching devices used e.g. insulated gate bipolar transistors or thyristors, influence the transient properties of the system. These fully controlled switches can be turned-on and off using the control terminal. For a comprehensive review of converter technology, see [37],[41] and [42]. The output waveform quality is a function

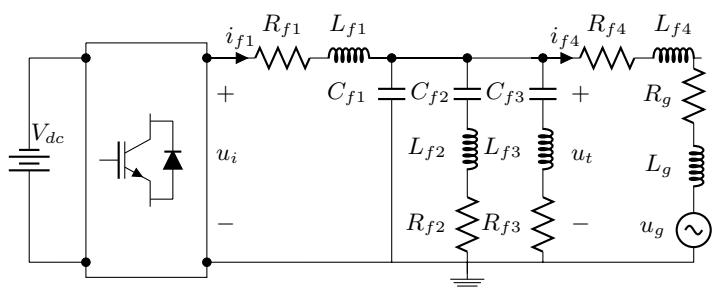

Figure 2.11: Single line diagram of power electronic device with LCL and trap filters for 1^{st} and 2^{nd} switching frequency group connected to grid.

of voltage levels and gate signal control of the switching devices. The switched devices are controlled by variations of pulse width modulation. With a switching frequency of f_s and modulating frequency f_m, the resulting output waveform contains harmonics centered around $f_s - f_m$ as sidebands [42]. This non-sinusoidal behavior of pulse width modulation based power electronic devices causes injection of current harmonics into the grid. LCL-filters, as shown in Figure 2.10, is the classic solution to attenuate pulse width modulation harmonics [43], but trap filters or a combination hereof is readily seen in the industry for grids with tight harmonic requirements. Figure 2.11 shows a single phase converter connected to the grid using LCL and trap filters for 1^{st} and 2^{nd} switching group harmonics, used in paper D.

Given a state vector $\boldsymbol{x_v}$ and input vector $\boldsymbol{u_v}$ as,

$$\begin{aligned} \boldsymbol{x_v} &= \begin{bmatrix} i_{f1} & i_{f2} & i_{f3} & i_{f4} & u_{cf1} & u_{cf2} & u_{cf3} \end{bmatrix}^\intercal, \\ \boldsymbol{u_v} &= \begin{bmatrix} u_i & u_g \end{bmatrix}^\intercal, \end{aligned} \tag{2.26}$$

where the currents and voltages are as defined in Figure 2.11, the small-signal model is,

$$\boldsymbol{A} = \begin{bmatrix} \frac{-R_1}{L_1} & 0 & 0 & 0 & \frac{-1}{L_1} & 0 & 0 \\ 0 & \frac{-R_2}{L_2} & 0 & 0 & \frac{1}{L_2} & \frac{-1}{L_2} & 0 \\ 0 & 0 & \frac{-R_3}{L_3} & 0 & \frac{1}{L_3} & 0 & \frac{-1}{L_3} \\ 0 & 0 & 0 & \frac{-R_4-R_g}{L_4+L_g} & \frac{1}{L_4+L_g} & 0 & 0 \\ \frac{1}{C_1} & -\frac{1}{C_1} & -\frac{1}{C_1} & -\frac{1}{C_1} & 0 & 0 & 0 \\ 0 & \frac{1}{C_2} & 0 & 0 & 0 & 0 & 0 \\ 0 & 0 & \frac{1}{C_3} & 0 & 0 & 0 & 0 \end{bmatrix}, \tag{2.27}$$

$$\boldsymbol{B} = \begin{bmatrix} \frac{1}{L_1} & 0 & 0 & 0 & 0 & 0 & 0 \\ 0 & 0 & 0 & \frac{-1}{L_4+L_g} & 0 & 0 & 0 \end{bmatrix}^{\mathsf{T}},$$

and $\boldsymbol{C} = I$. The LCL filter output stage contains a resonance peak at,

$$\omega_{res} = \sqrt{(L + L_g)/(LL_gC_f)}, \tag{2.28}$$

where L is the direct output inductance of the filter. The system of (2.27) compared to the system of Figure 2.10 contains additional resonant frequencies. The dominating resonant frequency must be included in analysis as it can cause instability. The resonant characteristic is often attenuated by insertion of a resistor in series with the filter capacitor. A consequence of the physical resistor is active power loss, and it is common to introduce an augmented control signal with a damping term proportional to the capacitor current instead [44],[45],[46].

Adequate damping of the resonance frequency and control bandwidth selection enables the multiple-input multiple-output system of (2.27) to be represented by two identical single-input single-output systems for control synthesis by neglecting the filter capacitor(s) and approximating the LCL filter with an inductor-filter for low frequencies [43]. The inner current loop dynamics are,

$$\boldsymbol{L_f}\frac{\boldsymbol{di_f^{dq}}}{dt} + \boldsymbol{R_f i_f^{dq}} = \boldsymbol{u_i^{dq}} - \boldsymbol{E^{dq}} + \boldsymbol{DL_f D\omega_g i_f^{dq}}, \tag{2.29}$$

where $E(s)$ is the grid voltage, ω_g is the grid frequency and,

$$\boldsymbol{\omega_g} = \begin{bmatrix} 0 & \omega_g \\ -\omega_g & 0 \end{bmatrix}, \quad \boldsymbol{D} = \begin{bmatrix} 0 & 1 \\ 1 & 0 \end{bmatrix}, \tag{2.30}$$

$$\boldsymbol{L_f} = \boldsymbol{L_{f1}} + \boldsymbol{L_{f4}} + \boldsymbol{L_g}, \ \boldsymbol{R_f} = \boldsymbol{R_{f1}} + \boldsymbol{R_{f4}} + \boldsymbol{R_g}. \tag{2.31}$$

2.4.7 Static Synchronous Compensator

A static synchronous compensator (STATCOM) is a voltage source converter based device used to provide reactive power compensation. The unit contains a DC energy storage device, usually a capacitor, which is connected to the three phase output

voltages through a DC/AC converter. The output voltage is controlled in phase with the coupled AC system and by varying the amplitude of the output voltage, the reactive power exchange is controlled. The system is commonly connected to the AC system through a reactance, often supplied by the coupling transformer leakage inductance. The STATCOM reactive power rating is determined by the DC energy storage device, but can supply its maximum rating even at decreased AC side voltage. The STATCOM can from a control perspective be seen as a controllable synchronous voltage source able to inject or absorb reactive power. The control challenges are thus similar to the voltage source converter presented in section 2.4.6. A full review of static var compensators and STATCOM technology can be found in [47].

2.4.8 Full-Converter Network Interaction and System Uncertainty

The system matrix of (2.27) shows that the governing dynamics of the system is a function of the impedance seen from the terminals of the converter. The impedance is only partially known at the design state, leading to decreased damping under uncertain conditions [48]. The connected transmission system is uncertain as multiple-WT systems with power electronic devices each represent an impedance depending on their control topology. Furthermore, the converter output current causes distortion of the system voltage. The details of converter-network interaction with respect to harmonics and the change in overall system impedance as a function of the number of WTs in operation was investigated by [49]. The national grid code specify performance criteria, and it is paramount that the overall system can operate within the specifications. With focus on control synthesis, a WT supplier must comply with specifications and be robust again system changes - which implies a performance tradeoff.

Given an uncertain set of system parameters describing the possible WPP configurations, Π_R, parametric uncertainty can represent the set of plants, G_Π, a control system should stabilize with a defined performance. Π_R should accurately represent component uncertainty and operating scenarios including the number of connected WTs. System aggregation is used in electromagnetic transient simulations and various methods exist, for instance the technique used to model the studied WPP in section C.4. The frequency dependency of the system components requires complex perturbations, which has the added advantage of being able to represent umodelled dynamics. For a nominal transfer function $G_0(s) \in G_\Pi$ there exist a bounding radius $L_O(\omega)$ such that $G_\Pi = (I + L_O)G_0(s)$,

$$L_O(\omega) = \underset{G \in G_\Pi}{max} \left| \frac{G_p(j\omega) - G_0(j\omega)}{G_0(j\omega)} \right|, \tag{2.32}$$

and a rational weight $|W_o(j\omega)| > L_O(\omega) \forall \omega$. Any plant, $G_p(s)$, in the set G_Π can then be characterized by,

$$G_p(s) = G_0(s)(1 + W_O(s)\Delta(s)), \tag{2.33}$$

for $|\Delta(j\omega)| \leq 1, \forall \omega$. Unstructured complex uncertainty represents the set of plants as disc-shaped regions in the complex plane. The representation, illustrated in

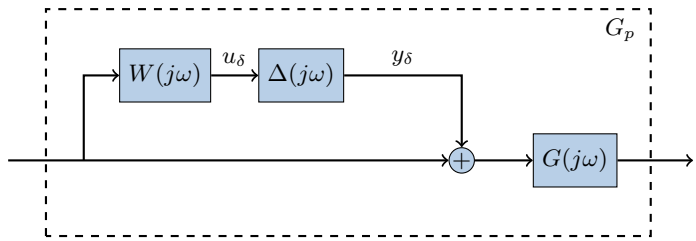

Figure 2.12: Plant with multiplicative input uncertainty, inspired by [50].

Figure C.4, includes plants outside of G_Π and is considered conservative for controller synthesis. An illustration of multiplicative input uncertainty is shown in Figure 2.12. $L_O(\omega)$ and the uncertainty weight $W_O(j\omega)$ with $|\Delta(j\omega)| < 1$ in the frequency domain are found by adequate sampling of random plants in the set G_Π and mapping the relative error. The complex uncertainty description $W_O(j\omega)$ is lumped for the studied WPP using a 15% variation of the filter coefficients and a 75% variation of the system components from nominal using a third order filter, shown in Figure C.6. The uncertain representation is used for $\mathcal{H}_\infty$ control synthesis with respect to robust control in paper C.

The parameter set Π_R provides valuable information. Another aspect of robust analysis is that given a fixed-structure controller and a set of nominal parameters, how is the choice of control parameter affected by a change in component values. From an entrepreneur point of view, this operational envelope of a system is of interest as it can guarantee stability given a range of parameters. This is investigated in section 4.2.1.

2.4.9 Control methodologies

The bidirectional converter topology utilized in modern WT regulates both the inflow current from the generator and the outflow current from the intermittent storage system. Converter control is a well-studied area as rectifiers and inverters are often used equipment outside of back to back systems. The focus of this thesis is on linear control techniques such as rotating frame PI controllers due to their standardized implementation in industrial systems. In the rotating reference frame, the converters are controlled independently through decoupled vector control. The separation of the direct and quadrature axis components enable achievement of individual control goals by use of inner current control loops. This method is called the decoupled vector control method. The reference frame is commonly oriented along the stator or supply voltage vector position. The control scheme enables use of advanced pulse width modulation strategies, but uses the dq transformation, which require phase locked loops. An illustration of the decoupled control concept is shown in Figure 2.13

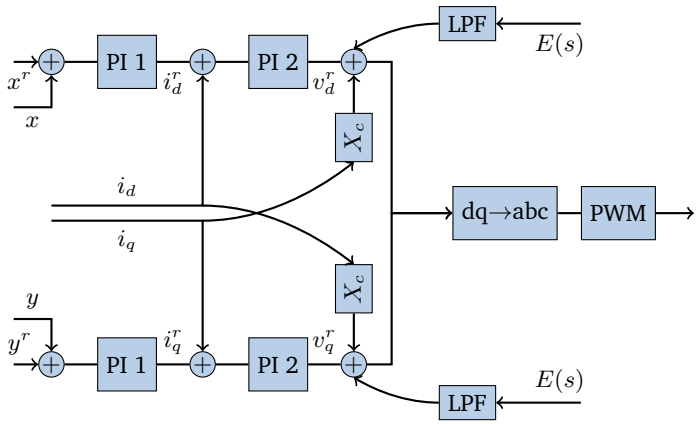

Figure 2.13: Decoupled dq-vector control with low pass filtered grid voltage feed forward. The outer loop controlled variables are denoted x and y. $E(s)$ is the grid voltage and X_c is the system reactance.

2.4.10 Machine Control

Common machine control methods are constant torque angle, unity power factor, constant stator flux control and maximum torque per ampere control. A full comparison of each technique can be found in surveys [51],[52]. The constant torque angle method used in the WT model keeps the angle between the stator current space vector, and the direct-axis of the rotor, known as the torque angle α, constant at 90 degrees to obtain maximal torque with minimum quadrature current [53],[54]. The direct and quadrature currents are functions of the stator current space vector, $i_s = |\boldsymbol{i_{dq}}|_2$,

$$i_d = |i_s| \cos \alpha, \; i_q = |i_s| \sin \alpha. \tag{2.34}$$

The electrical torque of the permanent magnet synchronous generator is,

$$T_e = (3/2) P \lambda i_q, \tag{2.35}$$

where P is the number of generator pole pairs and λ is the flux linkage. Controlling the direct axis current i_d to zero, making $\alpha = 90$ degrees,

$$i_q = |i_s|, \text{ for } i_d = 0. \tag{2.36}$$

An important advantage of the constant torque angle method is the direct proportionality between torque and current. This proportionality is used to implement the synthesized controllers in sections 5.3 and 5.4. For an extensive explanation of the machine control properties, see [55],[56].

2.4.11 Line Control

The main objective of the line side controller is the transfer of the active power to the grid. The active power produced by the generator is delivered to the DC-link capacitor and the tracking of active power simplifies to tracking an output current reference generated from the DC-link voltage error. The line side controller is further responsible for adjusting the level of reactive power. Using the converter terminal voltage as actuator, the current control is disturbed by the grid voltage. The current waveform produced by the converter should in theory be a perfect sinusoidal for various supply disturbances. The grid voltage in a resonant grid contains multiples of the power system fundamental and switching harmonics [57]. The total harmonic distortion of the output current is lowered by passive or active filtering, or compensation. Passive filters are tuned to attenuate specific harmonics and have diminishing effect if the topology of the system changes. Furthermore, they could introduce resonances in the power system [58]. Active filtering attenuate select harmonics in the control system bandwidth by modifying properties of the closed loop system, while active compensation generates voltage/current waveforms which cancel the harmonics. The research area of active filtering and compensation is reviewed in the literature survey, and section 4.1.2 introduces the synthesized $\mathcal{H}_\infty$ controller for power system harmonic attenuation in uncertain power systems.

2.5 Literature Survey

Robustness in offshore WPP control and assessment hereof is considered a multi-disciplinary field of research which have ties to both electrical and mechanical control. Robust control of technical processes has been an active research area since the 1980s. The fundamental concept of stability in case of bounded system uncertainty was already known in the 1960s based on the work of Bode, represented by gain and phase margin for single-input single-output systems. The analysis was extended to include multiple-input multiple-output systems in the modern control era. Robust control is often directly associated with $\mathcal{H}_\infty$ based loop shaping, of which the foundation was laid in [59]. The formulation of robustness and system sensitivity to uncertainty expanded into the field of single-input single-output control as new methods to asses robustness and stability envelopes [60]. Countless textbooks exist in the field of robust control and analysis. Highlights amongst single-input single-output analysis includes Tay [61] and Vilanova [60]. With regard to multiple-input multiple-output and robust control, textbooks from Skogestad and Postlethwaite [50] and Zhou [62] is among the top candidates.

Power System Robustness Definition

Power system robustness can be defined as the ability of a system to function despite possible faults and system uncertainty [63]. This definition in regard to WPPs defines the capability and effectiveness of a system to handle varying generation,

load and parameters. Systematic analysis of varying load with respect to power flow in a system with high wind power penetration is shown in [64] using probabilistic turbine models. Probabilistic power flow is closely tied to the response of wind turbine control systems in weak grids [65]. The particular field of WT control in weak grids has been researched vastly and is in constant development as the technology has yet to reach maturation.

Converter Technology

Authors such as Blaabjerg, Teodorescu, Liserre and Kazmierkowski have in [51], [66] and [38] reviewed state of the art converter based technology in wind turbines. Modern converter topologies such as matrix converters and modular multi-level converters are reviewed in [67] and [68]. Given an adequate high converter switching frequency, the output waveform can be represented by an averaged model with a current source on the DC-side or a three phase controllable voltage source on the AC-side. A method for developing averaged models is proposed and it is shown that the nonlinearities and cross couplings do not have any significant effect on the small-signal response [69]. The switching devices are often neglected in the literature as they operate outside the bandwidth of the converter control. The advantages of using different variations of pulse width modulation is reflected in a change in the spread of generated harmonics and total harmonic distortion [70]. Weak grids, as defined by a low short circuit ratio, combined with a wide subsea network can contain both power system harmonics as well as series and parallel resonant frequencies of considerable magnitudes [16]. The distortion is sought attenuated by both filter design and control. A recent overview highlights the advances made in the field of converter control from a high-level perspective [71] . A full representation of converter dynamics requires both non-linear and switching functions. The non-linear components are primarily related to blanking time and non-ideal valves and are often neglected in control analysis. The influence of non-linear phenomena on converter control is investigated in [72].

Converter Control

Control of converters has generally been developed as an extension of electrical motors. In [66], current controllers are analyzed with respect to tracking properties and disturbance rejection. The book splits the reference tracking methods into linear such as stationary reference frame types and rotating reference types and non-linear. The most popular rotating reference frame type is the decoupled PI control with grid voltage feed forward, which is easy to dimension but in practice impossible to fully decouple. An attempt to improve axis decoupling is the pseudo-continuous multivariable-PI current controller, but the improvement is minor [73]. In the stationary frame, the proportional resonant type controller is common. The resonant controller can track AC references in the stationary reference frame with no steady-state error, but are sensitive to grid variations and has a larger phase lag than PI

controllers. The proportional-resonant method can be implemented in the stationary frame as second order generalized integrators and provides similar tracking to PI-based methods but offer selective filtering. Repetitive control is an addition to existing feedback controllers as a specialized feed forward control adjusting the control input based on previous errors [74]. Predictive control, in which model predictive control is dominant, shows promise but clearly depends on the model. A comparison of PI-based control and model predictive control [75], shows that the PI control has the lowest current ripple but a slower transient response. The predictive controller is efficient in limiting peak current but has stability problems for parameter mismatch [66]. Non-linear methods e.g. passivity and hysteresis [76], are commonly applied when subject to unbalanced and nonlinear loads in micro grids. The nonlinear methods commonly apply varying switching frequencies. Several papers consider synthesis of non-linear methods, notably gain scheduling [77] and non-linear predictive control [78]. An excellent review of micro grid converter control is found in [73].

Robust Converter Control

Robust control methods such as gain-scheduling [73], sliding mode control [79] and $\mathcal{H}_\infty$ are seen in the literature. Gain-scheduling was shown to have improved performance relative to PI and resonant based methods using inductance estimation at the connection point [73]. A Youla-Kucera gain-scheduling method was implemented in [80]. In [81], a loop shaping $\mathcal{H}_\infty$ controller is designed for tracking with good performance. The design is improved to include admittance control by [82], and be robust without influencing the global power system stability. A new method is adaptive sliding mode control which reduces oscillations during disturbances for uncertain systems [83].

Harmonic Filtering and Compensation

The interest in system harmonic capabilities for full-converter WTs overlaps with the control system design for the STATCOM and grid connected components such as photovoltaic systems. A recent survey highlights the established methods for mitigation of power system and switching harmonics [42]. The book focuses on elimination and filtering of both positive and negative sequence harmonics in type-3 and type-4 WT systems. Multiple phase locked loops synchronized to frames rotating with angular speeds similar to the wanted harmonics are used to isolate the positive and negative sequence harmonics in the rotating reference frame. Extraction of the negative sequence components is shown to require high order low-pass filters for proper isolation. The isolated harmonic components are fed to individual controllers with a zero reference and transformed back to the abc frame. The system can be operated at both the machine and the grid side, but introduces electromagnetic torque ripple when applied on the machine. Both selective harmonic compensation and filtering using the proportional-resonant filter structure is proposed [84]. Harmonic compensation is comparable to the PI-based control, but with the added advantage

of individual adjustment of resonant peaks and most importantly simultaneous compensation of positive and negative sequence. Hybrid designs such as a combination of resonant control with odd harmonic repetitive control were proposed by [85].

Voltage control

The converter is used to control the active and the reactive power output. If a network is primarily inductive, reactive power is used to control terminal voltage. The autonomous control strategy of a power system for voltage stability is distributed reactive power and switchable reactive sources. In [86], the devices are grouped into static compensation devices and control devices e.g. synchronous generators, STATCOMs and power flow control. The static compensation devices provide the bulk of reactive power while the dynamic reactive compensation is used to maintain terminal voltages for all load levels. The simplest approach to voltage level management is based on using local measurements to avoid data transfer. Local voltage control could cause an unnecessary high flow of reactive power between units [87]. This has recently evolved to optimal tracking of the voltage in regional pilot nodes [88]. In WPPs with communication readily available, centralized supervisory control at a pilot node such as the point of common coupling combined with distributed generators tracking an external voltage or reactive power set-point is possible. The distributed reactive power supply is augmented with a static var compensator (SVC) or a STATCOM at the point of common coupling to comply with grid code specifications [89]. The impact of communication delay on centralized control is analyzed in [90], and shown to influence system performance during faults. Voltage control in WPPs is comparable to voltage control in distribution networks with weak grids and a review of methods for distribution networks can be found in [91]. A traditional method for analyzing static voltage stability in power systems is modal analysis based on the power flow Jacobian matrix [27]. In [92] a method based on system topology and unit capability curves is proposed to analyze voltage stability. Considering the power system as a state space multiple-input multiple-output model with controllers, a singular value decomposition approach is proposed by [93]. Inclusion of the controllers is a challenge as the structure is intellectual property. Given system topology and controller layout, the fragility and stabilizing parameter set is of interest. In [60], the signature function of linear systems in used to quantify the parameter space in which a system is stable.

System Aggregation

Control methods are often analyzed on aggregated systems. Aggregation techniques for WPPs and WTs are vastly important in studies of control system robustness. In [94], common WPP aggregation techniques are compared with respect to accurately representing the power system dynamics. Common WPP aggregation techniques include (N-1) models in which the WT impedance is seen from a single WT in the grid, with the rest of the N turbines connected in parallel, and (1/N)

where all the wind turbines are lumped together to a single turbine equivalent and the stability is evaluated from this equivalent WT. The (1/N) approach for WPPs with multiple types of WTs is studied in [95]. Splitting of the WPP into multiple sections and the consequence wrt. accurate dynamic representation is studied in [96].

Mechanical Control

The mechanical control strategies for wind turbines depend on the region of operation. The main regions are partial load where the power capture must be maximized, and full-load where the structural load should be minimized while production is maintained. Given a certain pitch angle, the optimal point on the power production surface depends on the rotor angular velocity. Methods such as tip speed ratio, power signal feedback and hill climbing methods are introduced as possible maximum power point tracking candidates in [71]. The partial load region is dominated by tracking of the optimal tip speed ratio of the turbine [97]. The tip speed ratio is tracked by using the generator torque as actuator, indirectly using the rectifier to control output current. The mechanical torque can be seen as a nonlinear disturbance, and advanced methods such as adaptive control and linear parameter variation methods have been developed [98]. Given tip speed ratio tracking, the wind is a disturbance and could be canceled by feed forward. Recent methods seeks to eliminate the wind disturbance by the use of light detection and ranging (LIDAR) equipment, measuring the wind before it interacts with the blades [99]. The area of drivetrain control spans an impressive amount of methods. Great reviews of recent control methods of the partial region can be found in [97] and [100]. Wind turbines exhibit nonlinear dynamics and are exposed to periodic disturbances that may excite the poorly damped modes of the drivetrain and tower. There are two groups of control strategies widely used, passive and active. Active methods refer to control, and passive is a change of the structure of the drivetrain and the tower. The classic physical vibration absorber is presented in [101] and an extension of the idea is using virtual inertia by [102]. In [103], the mechanical stresses on the rotor shaft is analyzed with respect to network disturbances. It is found that electrical faults can reduce the lifetime of the drivetrain and a damping controller should be implemented. Active oscillation damping can be achieved by both pitch and torque control. In [104] a link between turbine pitch angle and drivetrain oscillation magnitude is found. A torque damping controller is proposed by injecting an additional electrical torque component proportional to the generator speed. A review article by [105] from 2015 highlights innovative drivetrain designs that can minimize vibrations. Load reduction methods such as pitch and torque joint control and nacelle accelerometer implementation to reduce tower vibration is introduced as competing schemes. A promising control method is individual pitch control of blades to reduce asymmetric loading. A full review is found in [105].

Chapter 3

Mechanical Modelling

This chapter presents the rotor and drivetrain models and the motivation for their development. A combined model of the rotor-drivetrain system is introduced to study the plausible interaction between two wind turbines in a weak offshore network. The mechanical system is scrutinized with respect to parameter variation and the maximum flap-wise displacement of the rotor blade is estimated. Furthermore, the inclusion of electrical components and control is introduced to study the effect of actuator delay and periodic disturbances in the electrical torque. The effect of parameter variation, interaction and disturbances are shown to be negligible which suggests flawed drivetrain control. Advanced methods designed to reduce drivetrain stress and thereby rotor vibrations through control of the electrical torque are shown in chapter 5.

3.1 Motivation: Blade-Shaft Torsional Oscillation

DONG Energy has multiple times observed damaged WT blades in a structural sound construction. An investigation revealed that the blades were experiencing unusual vibrations, but the origin of the vibrations was not found. The vibrations excited the flap-wise bending modes and in the end destroyed the blade. Designing a rotor blade for WT operation is a challenging task. The objectives of blade design include aerodynamic performance, light weight and structural integrity versus cost. A long light-weight blade build as a composite sandwich structure can have low damping properties both flap-wise and edgewise [103]. The material does not weaken by low amplitude shear stress, but will break at high forces.

Excitation of blade-shaft modes is expected due to torque transients from turbulent wind capture, blade tip vortexes, inadequate drive-train damping controller or network faults. The faulty WTs were distributed randomly across the WPP, which excludes wind-induced vibration as root cause since the incidents would then be expected to be clustered. Every WT in the WPP had similar software implementation which might point to network disturbances as the cause. Tripping a three-phase short circuit or a switching circuit breaker could produce network changes large enough to

excite the blade-shaft modes.

Shaft mode excitation in type-2 generators from network faults was analyzed and found to cause high shaft stress [106]. The shaft-mode electrical disturbance excitation was extended to fixed-speed WTs, and it was shown that activation of circuit breakers near the WT can provoke extreme torque spikes [103]. The fixed-speed WT contained a gearbox which provided a damping effect which is not present in modern gear-less turbines. WT blade and shaft torsional stress during a network disturbance using a six degree of freedom mechanical drivetrain model in a system using a STATCOM was found to require extensive damping [107]. The grid-side and machine-side is assumed electrically decoupled in type-4 and most type-3 WTs. The coupling present is a function of the control system architecture and the communication delays. The analysis is presented in section 3.3.

3.2 Mechanical Models

The mechanical models in this thesis are developed with the objective of establishing a simple framework for recreating the blade vibrations. The models are kept of low order as the introduction of higher order modes in mechanical systems can provide additional damping, and the first modes are of highest energy. Furthermore, the data needed to fully exploit advanced models was not available such that application of detailed existing models would require additional parameter estimation.

3.2.1 Rotor

The WT rotor consists of three identical blades mounted at the rotor hub. The subsequent analysis incorporates multiple rotor models and the aim is to keep the methods and models simple. The WT rotor and blade assembly model must accurately represent blade stiffness and damping of high energy modes. The complexity of the rotor model depends on the structural representation of the blades [30]. The blade-shaft torsional oscillation problem indicates resonant modes with adequately high energy to result in deformed blades. The deformity was observed in the flap-wise directions of the blade and only on selected blades, which indicates a structural sound blade. Modelling of the rotor is based on a single mass equivalent system representing the first mode of oscillation [108].

Given an angular position θ of a rigid body rotating blade with linear velocity $\dot{\theta}L$ at distance L from the shaft and a deformation u from the rigid-body axis, for small deformations the mass m will have a velocity of $v = \dot{u} + L\dot{\theta}$. The kinetic, E_k, and potential energy, E_p, for a three blade system attached to a rigid body with inertia J_0,

$$E_k = (1/2)J_0\dot{\theta}^2 + 3(\frac{1}{2}mv^2), \tag{3.1}$$

$$E_k = (1/2)J_0\dot{\theta}^2 + \frac{3}{2}m(\dot{u} + L\dot{\theta})^2, \tag{3.2}$$

and,

$$E_p = 3(\frac{u^2}{2}K), \tag{3.3}$$

where K is the blade kinetic constant. The dissipation function D is defined as,

$$D = 2(\frac{\dot{u}^2}{2}K_d), \tag{3.4}$$

with K_d being the blade dissipation constant. The most general form of the Lagrange equations representing the energy equilibrium is [108],

$$\frac{d}{dt}(\frac{\partial E_k}{\partial \dot{q}_i}) - \frac{\partial E_k}{\partial q_i} + \frac{\partial E_p}{\partial q_i} + \frac{\partial D}{\partial \dot{q}_i} = Q_i, \quad (i = 1, ..., n), \tag{3.5}$$

where $q_i = [\theta, u]$ and Q_i is the torque about the axis of rotation. Partial evaluation of (3.5) for coordinate θ,

$$\frac{\partial E_k}{\partial \dot{\theta}} = J_0\dot{\theta} + 3mL^2\dot{\theta} + 3m\dot{u}L = J_0\dot{\theta} + 3mL(L\dot{\theta} + \dot{u}), \tag{3.6}$$

$$\frac{d}{dt}(\frac{\partial E_k}{\partial \dot{\theta}}) = J_0\ddot{\theta} + 3mL^2\ddot{\theta} + 3\ddot{u}L = (J_0 + 3mL^2)\ddot{\theta} + 3mL\ddot{u}, \tag{3.7}$$

$$\frac{\partial E_k}{\partial \theta} = 0, \quad \frac{\partial E_p}{\partial \theta} = 0, \quad \frac{\partial D}{\partial \dot{\theta}} = 0. \tag{3.8}$$

and for u,

$$\frac{\partial E_k}{\partial \dot{u}} = 3m(\dot{u} + L\dot{\theta}), \tag{3.9}$$

$$\frac{d}{dt}(\frac{\partial E_k}{\partial \dot{u}}) = 3m(\ddot{u} + L\ddot{\theta}), \tag{3.10}$$

$$\frac{\partial E_k}{\partial u} = 0, \quad \frac{\partial E_p}{\partial u} = 3uK, \quad \frac{\partial D}{\partial \dot{u}} = 3\dot{u}K_d. \tag{3.11}$$

Defining the resulting torque T affecting the rigid-body as the difference between mechanical and electrical torque, it follows that

$$(J_0 + 3mL^2)\ddot{\theta} + 3mL\ddot{u} = T, \tag{3.12}$$

$$m\ddot{u} + K_d\dot{u} + Ku = -mL\ddot{\theta}. \tag{3.13}$$

The moment of inertia of one blade about the hub center of mass is defined as $J_b = mL^2$, the total inertia around the hub center of mass is,

$$J = J_0 + 3J_b, \tag{3.14}$$

and (3.12) simplifies to,

$$J\ddot{\theta} + 3mL\ddot{u} = T. \tag{3.15}$$

Transformation of (3.12) and (3.13) to the Laplace domain yields,

$$T = J\theta s^2 + 3mLus^2, \tag{3.16}$$
$$-mL\theta s^2 = mus^2 + K_d us + Ku. \tag{3.17}$$

Viscous friction B is added to (3.16) for additional damping. The mechanical position θ is converted to the electrical position θ_e as $\theta = \theta_e/P$ where P is the number of generator pole pairs,

$$T = (J/P)\theta_e s^2 + (J/P)B\theta_e s + 3mLus^2, \tag{3.18}$$
$$-(mL/P)\theta_e s^2 = mus^2 + K_d us + Ku. \tag{3.19}$$

The electrical angle and rotor blade displacement are isolated,

$$\theta_e s^2 = \frac{PT}{J} - B\theta_e s - \frac{3PmLus^2}{J}, \tag{3.20}$$
$$us^2 = -(L/P)\theta_e s^2 - \frac{K_d}{m}us - \frac{K}{m}u, \tag{3.21}$$

and rearranged as,

$$\theta_e s^2 + J^{-1}3mLPus = -B\theta_e s + J^{-1}TP, \tag{3.22}$$
$$\frac{L}{P}\theta_e s^2 + us^2 = \frac{-K}{m}u - \frac{K_d}{m}us, \tag{3.23}$$

such that choosing the state and input vectors,

$$\begin{aligned} \boldsymbol{x} &= \begin{bmatrix} \dot{\theta} & u & \dot{u} \end{bmatrix}^\intercal, \\ u &= T, \end{aligned} \tag{3.24}$$

the system is given as $\boldsymbol{F}\dot{\boldsymbol{x}} = \boldsymbol{A'}\boldsymbol{x} + \boldsymbol{B}u$,

$$\boldsymbol{F} = \begin{bmatrix} 1 & 0 & 3mLPJ^{-1} \\ 0 & 1 & 0 \\ \frac{L}{P} & 0 & 1 \end{bmatrix}, \qquad \boldsymbol{A'} = \begin{bmatrix} -B & 0 & 0 \\ 0 & 0 & 1 \\ 0 & \frac{-K}{m} & \frac{-K_d}{m} \end{bmatrix}. \tag{3.25}$$

The standard state-space form $\dot{\boldsymbol{x}} = \boldsymbol{A}\boldsymbol{x} + \boldsymbol{B}\boldsymbol{u}$ is achieved by evaluating $\boldsymbol{A} = \boldsymbol{F^{-1}A'}$ and $\boldsymbol{B} = \boldsymbol{F^{-1}B'}$,

$$\boldsymbol{A} = \frac{1}{J_0}\begin{bmatrix} -JB & 3LKP & 3LK_dP \\ 0 & 0 & J_0 \\ \frac{LJB}{P} & \frac{-JK}{m} & \frac{-JK_d}{m} \end{bmatrix}, \qquad \boldsymbol{B} = \frac{1}{J_0}\begin{bmatrix} P \\ 0 \\ -L \end{bmatrix}, \tag{3.26}$$

with $T = T_m - T_e$ where $T_e = (3/2)\lambda_m P i_{qs}$.

The rotor is mechanically coupled to the drivetrain which is introduced in the next section.

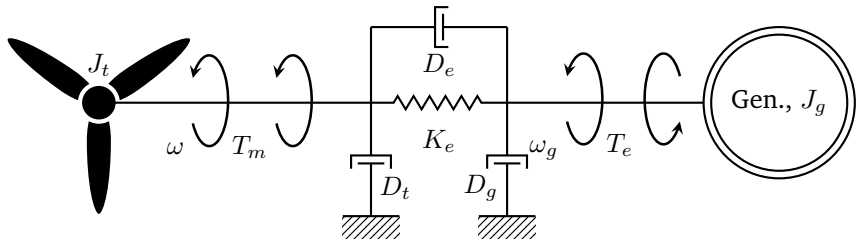

Figure 3.1: 2-mass drivetrain.

3.2.2 Drivetrain

The drivetrain receives mechanical energy from the rotor hub. Drivetrain models are generally divided into three types: Purely torsional models, rigid multibody models and flexible multibody models. Multibody models include non-torsional modes obtained by extending the dynamic models with non-torque based information. The non-torsional modes are of interest in gear design and load simulation [109]. The component of interest in this thesis is the controllable resulting torque transferred by the drivetrain shaft to the generator. Various drivetrain configurations transfer the non-torque components such as bending moments towards the tower and provide a damping effect.

A mechanical model describing the physical relation as a spring-mass-damper system focusing on torsional vibrations is used for the dynamic analysis of the torque in the drivetrain. Structural models commonly use either six, three or only one masses to represent the dynamics. The six mass model includes the blades, main shaft, gear and generator shaft. Considering a gear-less system extending the rotor model of section 3.2.1, the original six mass system is reduced to a lumped two mass system assuming that the aerodynamic torques acting on the hub are zero. The gear-less equivalent shaft stiffness is determined from the parallel shaft stiffness of rotor and generator. The model is composed of the equivalent torsional stiffness of the shaft K_e, the flexibility damping D_e and the torsional inertia of the rigid bodies J_t and J_g. The influence of other sources of flexibility is estimated by lumped parameters which results in a reduction of shaft stiffness coefficient [110].

The system of equations for a lumped two-mass model, shown in Figure 3.1, is given as [111],

$$\begin{aligned} J_t \frac{d\omega}{dt} &= T_m - K_e\theta - D_e(\omega - \omega_g) - D_t\omega, \\ J_g \frac{d\omega_g}{dt} &= -T_e + K_e\theta + D_e(\omega - \omega_g) - D_g\omega, \\ \frac{d\theta}{dt} &= \omega - \omega_g, \end{aligned} \tag{3.27}$$

where D_t and D_g represent the lumped viscous damping. The blade-shaft torsional

interaction model interfaces the two-mass model shown in Figure 3.1 and (3.27) with the rotor model (3.23) through the rotor angular velocity ω converted to electrical angular velocity,

$$\begin{aligned} J_t\theta_e s^2 + D_t\theta_e s &= T_m P - D_e(\theta_e s - \theta_g s) - K_e(\theta_e - \theta_g) - 3mLuPs^2, \\ J_g\theta_g s^2 + D_g\theta_g s &= -T_e P + D_e(\theta_e s - \theta_g s) + K_e(\theta_e - \theta_g), \\ (\theta_e - \theta_g)s &= \theta_e s - \theta_g s, \\ us^2 + \frac{L}{P}\theta_e s^2 &= \frac{-K_d}{m}us - \frac{K}{m}u. \end{aligned} \tag{3.28}$$

Defining the state and input vectors,

$$\begin{aligned} \boldsymbol{x_{dt}} &= \begin{bmatrix} \omega & \omega_g & \theta_{km} & u & \dot{u} \end{bmatrix}^\intercal, \\ \boldsymbol{u_{dt}} &= \begin{bmatrix} T_m & T_e \end{bmatrix}, \end{aligned} \tag{3.29}$$

results in the state space matrices,

$$\boldsymbol{A_{dt}} = J_0^{-1} \begin{bmatrix} -D_e - D_t & D_e & -K_e & 3LPK_b & 3LPK_{bd} \\ \frac{J_0}{J_g}D_e & \frac{J_0}{J_g}(-D_e - D_g) & \frac{J_0}{J_g}K_e & 0 & 0 \\ J_0 & -J_0 & 0 & 0 & 0 \\ 0 & 0 & 0 & 0 & J_0 \\ \frac{L}{P}(D_e + D_t) & -\frac{L}{P}D_e & \frac{L}{P}K_e & \frac{-J_t K_b}{m} & \frac{-J_t K_{bd}}{m} \end{bmatrix}, \tag{3.30}$$

where J_0 is the rigid body inertia of the rotor, s.t. $J_t = J_0 + 3J_b$ where $J_b = 3mL^2$ is the rigid body inertia of the blade and,

$$\boldsymbol{B_{dt}} = J_0^{-1} \begin{bmatrix} P & 0 \\ 0 & -\frac{J_0 P}{J_g} \\ 0 & 0 \\ 0 & 0 \\ -L & 0 \end{bmatrix}. \tag{3.31}$$

The combined rotor and drivetrain model represents a linear five-mass model. The drivetrain interfaces the electrical system through the controllable electrical generator torque T_e. The interface provides the opportunity to analyze the possible interaction between wind turbines in an electrical network which was thought to contribute to the vibration issues.

The model is extended by considering the mechanical torque as a nonlinear disturbance. By considering the mechanical torque as a state dependent nonlinear disturbance contrary to a fixed input, the exposure of the effect of generator torque variation on the rotor angular velocity and thereby rotor blade vibrations is enhanced. The mechanical torsional torque input can be expressed as a nonlinear term combining (2.2) and (2.3),

$$T_m = \frac{P_m}{\omega} = \frac{1}{2}C_p(\lambda, \beta)\rho\pi\frac{R^5}{\lambda_3}\omega^2 = k_w\omega^2, \tag{3.32}$$

where k_ω is a constant optimal value of $C_p(\lambda_{opt}, \beta_{opt})$ and R is the blade length. Inserting (3.32) in (3.27) equates,

$$J_t \frac{d\omega}{dt} = k_\omega \omega^2 - K_e \theta - D_e(\omega - \omega_g) - D_t \omega, \tag{3.33}$$

and the system (3.27) can be transformed to the standard form,

$$\begin{aligned} \dot{x} &= f(x) + g(x)u, \\ y &= h(x). \end{aligned} \tag{3.34}$$

The system is not in any easy controllable form as the nonlinear state dependent disturbance $k_\omega \omega^2$ is unmatched. The nonlinear system is transformed to an equivalent linear system in normal form using feedback linearizaition. The technique enables linear control theory to be used on challenging nonlinear problems, but it requires full knowledge of the nonlinearties. Defining the shorthand notation state and input vectors,

$$\begin{bmatrix} x_2 & x_3 & x_1 \end{bmatrix} = \begin{bmatrix} \omega & \omega_g & \theta_{km} \end{bmatrix}, \tag{3.35}$$

$$u = T_e. \tag{3.36}$$

The system is sought transformed to the normal form,

$$\begin{aligned} \dot{\eta} &= f_0(\eta, \boldsymbol{\xi}), \\ \dot{\boldsymbol{\xi}} &= \mathbf{A}_c \boldsymbol{\xi} + \mathbf{b}_c \gamma(\eta, \boldsymbol{\xi}) \left[u - \alpha(\eta, \boldsymbol{\xi}) \right], \\ y &= \mathbf{c}_c \boldsymbol{\xi}, \end{aligned} \tag{3.37}$$

where $\eta \in \mathbb{R}$, $\boldsymbol{\xi} \in \mathbb{R}^2$, $f_0 : \mathbb{R}^3 \to \mathbb{R}$ is a smooth function of its arguments, and $(\mathbf{A}_c, \mathbf{b}_c, \mathbf{c}_c)$ is a canonical form representation of a chain of integrators. Input-to-state feedback linearization finds a transformation which makes the relative degree ρ equal to the system order n but results in a nonproper diffomorphism with polynomials of degree larger than one. The system with output $y = h(x) = x_2$ has relative degree $\rho = 2$, in fact by using the Lie derivative,

$$L_g h(\mathbf{x}) = 0, \tag{3.38}$$

$$L_g L_f h(\mathbf{x}) = -\frac{D_e}{J_g J_r}. \tag{3.39}$$

The first two new state variables are,

$$\xi_1 \triangleq h(\mathbf{x}) = x_2, \tag{3.40}$$

$$\xi_2 \triangleq L_f h(\mathbf{x}) = J_r^{-1} \left(-K_d x_1 + k_w x_2^2 - (D_e + D_t) x_2 + D_e x_3 \right). \tag{3.41}$$

Since the relative degree $\rho = 2$ and the state space is three dimensional, it is possible to find another function $\eta(\mathbf{x})$ such that the mapping $\mathbf{T}(\mathbf{x}) = [\eta, \xi_1, \xi_2]^{\mathrm{T}}$ is a global diffeomorphism. The zero-dynamics, Z^*, of the system is defined to be the internal

dynamics of the system when the system output is kept at zero by the input. The zero dynamics can be characterized by restricting $\mathbf{x} \in \mathbb{R}^3$ to,

$$\begin{aligned} Z^* &= \{x_2 = 0 \wedge -K_d x_1 + k_\omega x_2^2 - (D_e + D_t)x_2 + D_e x_3 = 0\}, \\ &= \{x_1 = x_2 = x_3 = 0 \vee x_2 = 0 \wedge D_e x_3 - K_d x_1 = 0\}. \end{aligned} \tag{3.42}$$

Forcing all states to zero provides no information about the zero dynamics of the system. Inserting $x_3 = K_d x_1 / D_e$ in the original state equations,

$$\begin{bmatrix} \dot{x_1} \\ \dot{x_2} \\ \dot{x_3} \end{bmatrix} = \begin{bmatrix} -x_1(K_d/D_e) \\ 0 \\ \frac{K_d - (D_e)K_d/D_e}{J_g} x_1 \end{bmatrix} = \begin{bmatrix} -x_1(K_d/D_e) \\ 0 \\ 0 \end{bmatrix}. \tag{3.43}$$

The only zero dynamics is,

$$\dot{x_1} = -x_1(K_d/D_e)\ ,\ K_d/D_e > 0, \tag{3.44}$$

which shows that the system is minimum phase.

The change of variables needed to transform the original drive train system into normal form can be taken as $n - \rho$ smoothing transformation functions $\boldsymbol{\phi}(\boldsymbol{x})$ which maps the internal dynamics η s.t. they are uncontrollable by the input and a $\boldsymbol{\psi}(\boldsymbol{x})$ function which maps the states which will be put in controllable canonical form $\boldsymbol{\xi}$. The functions $\boldsymbol{\phi}(\boldsymbol{x})$ must be chosen s.t. $\boldsymbol{T}(\boldsymbol{x})$ is a diffeomorphism on a domain D and,

$$\frac{\partial \phi_i}{\partial x} g(x) = 0,\ 1 \leq i \leq n - \rho,\ \forall x \in D, \tag{3.45}$$

which ensures that the input cannot affect the internal dynamics. The internal dynamics are then defined as,

$$f_0(\eta, \boldsymbol{\xi}) = \frac{\partial \boldsymbol{\phi}}{\partial x} \boldsymbol{f}(\boldsymbol{x}). \tag{3.46}$$

To transfer the system to normal form, the vector function $\boldsymbol{\phi}(\boldsymbol{x})$ must satisfy criteria (3.45),

$$\frac{\partial \phi}{\partial x} g(x) = \frac{\partial \phi}{\partial x_3}(-1/J_g) = 0, \tag{3.47}$$

which is true for $x_3 \notin \boldsymbol{\phi}(\boldsymbol{x})$. Choosing,

$$\phi(x) = x_1, \tag{3.48}$$

is the obvious choice as the torsion angle x_1 is a challenge to measure. The internal dynamics described in (3.46) results in,

$$\dot{\eta} = \frac{\partial \phi}{\partial x} f(x) = \frac{\partial \phi}{\partial x_1} f(x) = x_2 - x_3. \tag{3.49}$$

The resulting change of variables is,

$$\mathbf{z} = \begin{bmatrix} \eta \\ \boldsymbol{\xi} \end{bmatrix} = \mathbf{T}(\mathbf{x}) = \begin{bmatrix} x_1 \\ x_2 \\ J_r^{-1}\left(-K_d x_1 + k_\omega x_2^2 - (D_e + D_t)x_2 + D_e x_3\right) \end{bmatrix}, \tag{3.50}$$

and the internal dynamics follows an inverse change of variables as (3.50),

$$\dot{\eta} = \xi_1 - D_e^{-1}\left((D_e + D_t)\xi_1 - k_\omega \xi_1^2 + J_r \xi_2 + K_d \eta\right). \tag{3.51}$$

The full input-output linearized system in normal form is given by,

$$\begin{aligned} \dot{\eta} &= \xi_1 - D_e^{-1}\left((D_e + D_t)\xi_1 - k_\omega \xi_1^2 + J_r \xi_2 + K_d \eta\right), \\ \dot{\xi}_1 &= \xi_2, \\ \dot{\xi}_2 &= \kappa_1 \eta + \kappa_2 \xi_1 + \kappa_3 \xi_2 + \kappa_4 T_e, \\ y &= \xi_1, \end{aligned} \tag{3.52}$$

where the output $y = \xi_1$ has a physical meaning being the rotor speed ω and,

$$\begin{aligned} \kappa_1 &= \frac{K_d^2}{J_r D_e} + \frac{D_e K_d}{J_g J_r} - \frac{(D_g + D_e)K_d}{J_g J_r},\ \kappa_3 = \frac{K_d}{D_e} + \frac{k_\omega}{J_r}\xi_1 - \frac{D_e + D_t}{J_r} - \frac{D_g + D_e}{J_g}, \\ \kappa_2 &= \frac{-K_d}{J_r} + \frac{K_d(D_e + D_t)}{J_r D_e} - \frac{K_d k_\omega}{J_r D_e}\xi_1 + \frac{k_\omega}{J_r}\xi_2 + \frac{D_e^2}{J_g J_r} + \frac{D_e + D_g}{J_g J_r}\xi_1, \\ &\quad - \frac{(D_g + D_e)(D_t + D_e)}{J_g J_r},\ \kappa_4 = \frac{-D_e}{J_g J_r}. \end{aligned}$$

The system is thus given by (3.37) with,

$$\gamma(x) = -\frac{D_e}{J_g J_r}, \tag{3.53}$$

$$\begin{aligned} \alpha(x) = D_e^{-2}&((k_\omega {\xi_1}^2 + (-D_g - D_t)\xi_1 - \xi_2(J_g + J_r)){D_e}^2 \\ &+ ({\xi_1}^2 D_g k_\omega + (2J_g k_\omega \xi_2 - D_g D_t)\xi_1 - \xi_2 D_t J_g - D_g(\xi_2 J_r + K_d \eta))D_e \\ &+ J_g K_d(-k_\omega {\xi_1}^2 + D_t \xi_1 + \xi_2 J_r + K_d \eta)), \end{aligned} \tag{3.54}$$

which are uniquely determined in terms of $\boldsymbol{f}$, $\boldsymbol{g}$ and $\boldsymbol{h}$ in the x domain. The system matrices are,

$$\boldsymbol{A_c} = \begin{bmatrix} 0 & 1 \\ 0 & 0 \end{bmatrix},\ \boldsymbol{b_c} = \begin{bmatrix} 0 \\ 1 \end{bmatrix}. \tag{3.55}$$

The devised model represents the non-linear system with unmatched disturbances using a linear model in the ξ, η variable space. The change of variables enables linear analysis of the original non-linear model and thereby the influence of the electrical torque on the rotor angular velocity. The model in normal form has through the transformation mapped the disturbances as matched such that they can be canceled by control and minimize drivetrain stress. The model is furthermore used for development of the feedback linearization control and compared to the non-linear advanced observer backstepping control with respect to drivetrain stress.

3.3 Blade-Shaft Torsional Oscillation Analysis

This section presents a short summary of the analysis motivated by the vibration issue. The vibration data was not available for processing and the nature and origin was at the time of investigation unknown. Proprietary rights limit the access to the data collection systems and no logs were available for processing by DONG Energy. The supplier argued that the cause was in fact not due to controller tuning, but could be:

- Structurally frail rotor blade delivery.
- Network interaction with nearby turbine.
- Delay in single WT converter system.
- Periodic mechanical excitation of rotor blade dynamics.

The dimensions of the rotor blade is known but the airfoil and structural properties are not available. No information was disclosed from the supplier investigation. The following sections focus on analysis of electrical transients and mechanical periodic disturbances.

3.3.1 Blade & Data

A mathematical model of the WT rotor blade and drivetrain system is presented in section 3.2.1. Based on the dutch offshore wind energy converter 6MW study [112] and the NREL 5MW study [113], the blade data is shown in Table 3.1. The WT

Mass	**Length**	**Center of Mass**	**Damping(ζ_b)**
17.7 Mg	61m	20.45m	0.47%
1^{st} mode (σ_b)	**Kinetic constant**	**Dissipation constant**	
0.62 Hz	$2\zeta_b\sigma_b m$	$\sigma_b^2 m$	

Table 3.1: Generic rotor blade parameters

drivetrain system parameters are based on the NREL 5MW study with the additional damping factor B estimated from collected data. The mechanical friction coefficient B is estimated assuming a loss coefficient, a, converting from mechanical to electrical energy. Given the rotor-model of section 3.2.1, the steady state angular velocity is,

$$\omega_{e0} = \frac{PT}{JB} = \frac{P(T_m - T_e)}{JB}, \tag{3.56}$$

such that for $T_e = aT_m$,

$$B = \frac{P(T_m - aT_m)}{J\omega_{e0}} = \frac{aT_m P}{J\omega_{e0}} = \frac{aT_m}{J\omega_{m0}}. \tag{3.57}$$

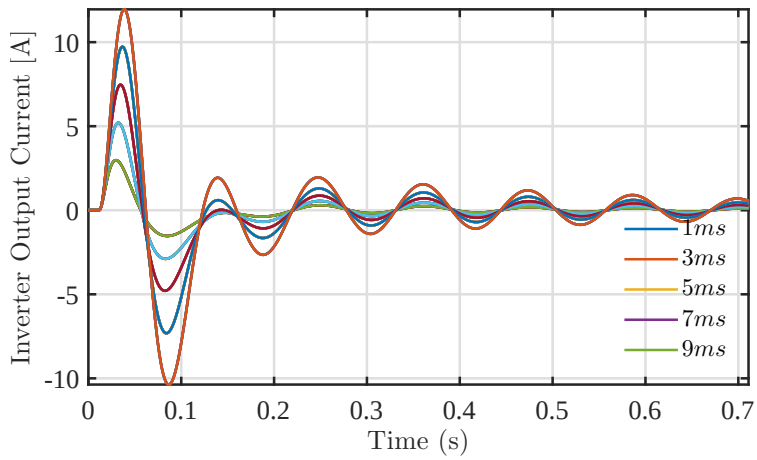

Figure 3.2: Inverter output current response to network voltage disturbance with variation in modulation delay.

The conversion coefficient a is estimated as 0.95 from NREL sample data. For the NREL 5MW turbine, this results in a damping factor,

$$B = 0.0052\text{Nms}. \tag{3.58}$$

The mechanical control is designed according to the constant torque angle method and the line side controllers are tuned using the internal mode control design to maintain the DC-link voltage. The controllers are designed according to the specifications outlined in section 2.4.9 with controllers tuned according to the UK grid code standard.

3.3.2 Single Wind Turbine: Actuator Modulation Delay

Active power transfer from a type-4 WT to the grid is handled by inverter control. The output current reference, and thereby the inverter voltage reference, is generated from the DC-link voltage error, as described in section 2.4.11. Given $W = v_{dc}^2$, the power balance is,

$$\frac{1}{2}C\dot{W} = \frac{3}{2}(P_s - P_g), \tag{3.59}$$

where C is the DC-link capacitance, P_s is the supplied active power and P_g is the active power grid injection. A PI-based controller with active conductance feedback is dimensioned [114]. The delay from controller input to switch actuation is commonly modeled as half a switching cycle. Large WTs use a lower switching frequency to reduce losses. A consequence of the modulation and communication delay is a mismatch in the DC-link voltage reference and the output power. Given a sequence of small network voltage dips, it is possible that the time-delay could introduce

oscillatory behavior. Figure 3.2 shows the response of a rotor-drivetrain plus full-converter model with the grid modeled by constant impedances. The figure shows a variation of the modulation delay from $1ms$ to $10ms$. The switching frequency is normally multiple times faster than $1kHz$, making the contribution of this effect negligible.

3.3.3 Dual Wind Turbines: Network Interaction

The interaction between electrically close WTs were proposed as a possible cause of the vibrations. A previous DONG project investigated the effect of multiple full-converter turbines in a weak grid with focus on stability, and concluded that an effect was present [49]. A simple dual WT system is shown in Figure 3.3 with impedances Z_{t1}, Z_{t2} and Z_{t3} representing the two cables and a coupling respectively. Each WT is of type-4 with standard PI-based machine and line control. The dual wind turbine

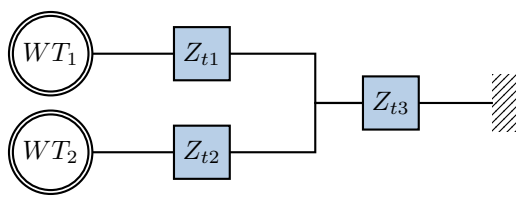

Figure 3.3: Simple dual wind turbine network.

system and its associated controllers is analyzed by deriving the state matrices from the system dynamics. The participation matrix is then found for an operating point using a constant mechanical torque.

The participation matrix shows the coupling between system states and modes. Every system mode had a damping ratio greater than 0.6 which indicated adequate controller design. The matrix revealed that the turbines had mutual participation factors with magnitudes of 1.001, which are very minor. One turbine output current state had a negligible effect on the DC-link voltage and output current of another, even for very weak systems. The dual WT system is simplified to investigate possible direct interaction assuming ideal converters and control. Given a mechanical input torque $T_m = 2MNm$ for both WTs, the system eigenvalues evaluated at the operating point are,

$$\boldsymbol{\lambda} = \begin{bmatrix} -22.74 \pm 48.96I & -0.07 \pm 0.4I & -0.09 \pm 0.4I & -0.21 \end{bmatrix}^{\mathsf{T}}. \tag{3.60}$$

With $\boldsymbol{\zeta} = -\Re(\boldsymbol{\lambda})/|\boldsymbol{\lambda}|$ and $\boldsymbol{\omega_n} = |\boldsymbol{\lambda}|$,

$$\boldsymbol{\omega_n} = \begin{bmatrix} 54 & 54 & 54 & 54 & 0.08 & 0.08 & 0.10 & 0.10 & 0.21 & 0.21 \end{bmatrix}, \tag{3.61}$$

$$\boldsymbol{\zeta} = \begin{bmatrix} 0.42 & 0.42 & 0.42 & 0.42 & 0.88 & 0.88 & 0.93 & 0.93 & 1 & 1 \end{bmatrix}. \tag{3.62}$$

The system modes are well damped with frequencies as shown in Figure 3.4. Figure 3.4 presents the frequency magnitude response from the mechanical input torque

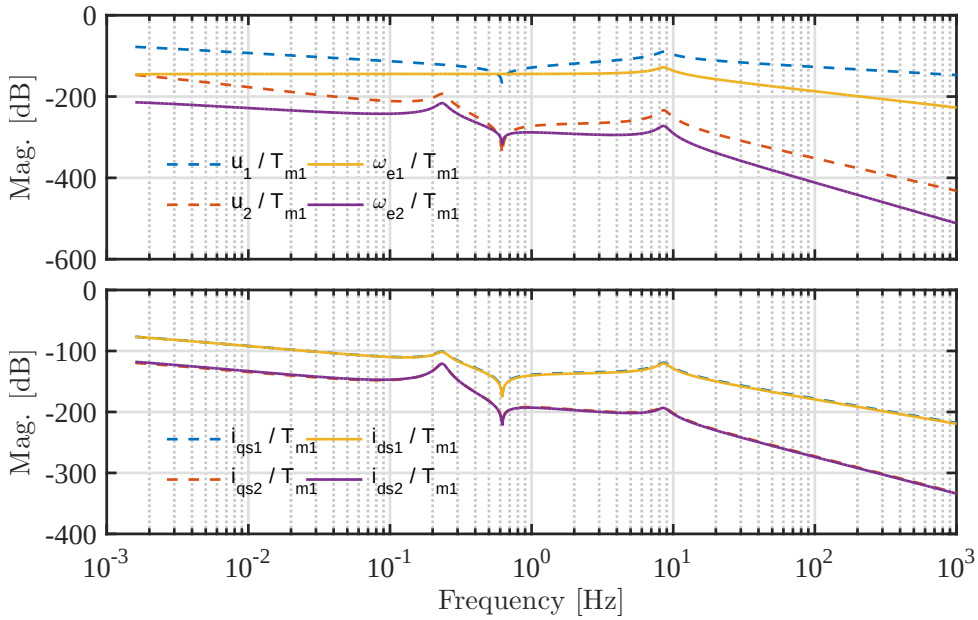

Figure 3.4: Effect of mechanical torque on rotor blade flap-wise position, u, angular velocity ω_e, and output currents i_{qs}, i_{ds} in the rotating refrence frame for dual turbine system employing ideal converters connected in a weak grid.

to key physical states. The maximum response magnitude regarding turbine interaction is linked to the rotor blade flap wise position at -180dB. It can be concluded that the system even for large disturbances in mechanical torque cannot provoke blade deformation. It should be noted that a change in the electrical torque will produce an identical effect for this system.

3.3.4 Periodic Disturbance

A periodic disturbance in the rotor-generator system can originate from either changes in the electrical or the mechanical torque. The electrical torque is for control purposes used as actuator and the mechanical torque is a disturbance. The system is further subject to external and internal disturbances. Internally the generator and rotor system can generate periodic disturbances due to mechanical imbalances. Cogging torque and non-static generator flux linkage are plausible causes of the electrical torque disturbances.

Cogging torque is the interaction between the stator teeth and the permanent magnet. It is a derivative of the stator, magnet and teeth design compared to the number of poles. The torque ripple originates from imperfect magnet production,

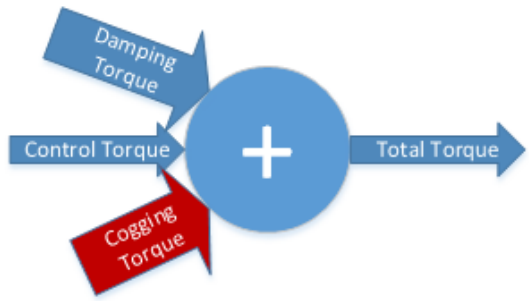

Figure 3.5: Resulting torque in drivetrain-generator system.

mutual torque and radial attractive force variation between the rotor and the stator. The electromagnetic vibrations can excite structural modes which causes resonance. Cogging torque can be seen as a zero average periodic varying component with the frequency ω_c relative to the number of stator teeth. Given a rotor position θ and the mechanical rotor angular velocity $\omega_m = \dot{\theta_m}$,

$$\omega_c = (LCM(N_s, P)/(rev))\omega_m, \tag{3.63}$$

where LCM is the lowest common factor, P is the number of poles and N_s is the number of slots. The instantaneous electromagnetic torque in the abc frame is [115],

$$T_e(\theta_m) = \sum_{x=a,b,c} \frac{u_x i_x}{\dot{\theta_m}} + \frac{1}{2}\lambda_m^2 \frac{d\mathcal{R}}{d\theta_m}, \tag{3.64}$$

where λ_m is the permanent magnet flux and $\mathcal{R}$ is the airgap reluctance. The cogging torque can thus be expressed as the change in stored energy in the air-gap W as a function of rotor position,

$$T_{cog}(\theta_m) = -\frac{d(-\frac{1}{2}F_m\phi_r)}{d\theta_m} = \frac{1}{2}\phi_r \frac{dF}{d\theta_m}, \tag{3.65}$$

where F_m is the magnetomotive force and ϕ_r is the component of remanent flux inside the airgap [116]. Treating the air-gap reluctance variation as a Fourier series, the torque can be expressed as a sum of harmonic sinusoidals [117],

$$T_{cog} = \sum_{k=1}^{\infty} T_{mk} \sin\left(LCM(N_s, P)k\theta_m\right), \tag{3.66}$$

where k is the harmonic type, and T_{mk} is a Fourier coefficient. The equation for the fundamental cogging torque component is,

$$T_{cog}(\theta_m) = \frac{1}{2}\lambda_m^2 \sin\left(\theta_m\right), \tag{3.67}$$

where the average cogging torque component is assumed to be 0.02 percent of the maximum possible torque [118].

In section 2.4.5 the permanent magnet flux linkage λ_m was assumed constant. The flux is a function of the rotor mechanical angle s.t. the electromechanical torque assuming a salient generator is,

$$T_e = 3/2 \left(P i_{qs}^r \lambda_m(\theta_m) + \frac{i_{ds}^r}{\omega_m} \frac{d\lambda_m(\theta_m)}{dt} \right) + T_c \sin\left(\omega_c(\omega_m)t\right), \tag{3.68}$$

with T_c being the average cogging torque,

$$T_e = \frac{3}{2} \left(P i_{qs}^r \lambda_m(\theta_m) + \frac{i_{ds}^r}{\omega_m} \frac{d\lambda_m(\theta_m)}{dt} \right) + \frac{1}{2} \lambda_m(\theta_m)^2 \sin\left(\omega_c(\omega_m)t\right). \tag{3.69}$$

Omitting the change in flux linkage per time,

$$T_e = \frac{3}{2} P i_{qs}^r \lambda_m(\theta_m) + \frac{1}{2} \lambda_m(\theta_m)^2 \sin\left(\omega_c(\omega_m)t\right). \tag{3.70}$$

The magnitude of the periodic electrical torque disturbance is a function of rotor position and the frequency is thus proportional to the angular velocity of the machine. The generator torque is,

$$T_e = \frac{P_o}{N_{gear}\omega_g}. \tag{3.71}$$

For the NREL turbine with gear ratio, $N_{gear} = 1/97$, active power $P_o = 5MW$ and $\omega_g = 122.9 rad/s$, the resulting maximum torque is,

$$T_e^{max} = \frac{P_o}{N_{gear}\omega_g} = 4.16 MNm. \tag{3.72}$$

The cogging torque disturbance T_d is thus,

$$T_d = 0.02\% T_e^{max} = 832 Nm. \tag{3.73}$$

The following section establishes the maximum gain of the rotor-blade system subject to parameter variations to investigate if a disturbance of magnitude T_d can provoke blade deformation.

3.3.5 Electrical Torque Disturbance Gain

The rotor-shaft open-loop system minimum attenuation is primarily a function of stiffness and damping coefficients, K_e, K_d,K, D_e, D_t and D_g. The system inertia is assumed fixed but the vibrations could be explained by a manufacturing fault such that the stiffness or the damping is lower than anticipated. The uncertain parameters are varied from 1 pct. to 300 pct. of their nominal values and the resulting minimum attenuation and frequency is shown in Table 3.3.5. The parameters are varied in pairs to reflect a flawed construction of either subsystem. The worst possible attenuation frequency is located at the resonance frequencies of the system.

		D_e,K_e	D_t, K_e,	D_g, K_e	K_d, K	$f[Hz]$
$\lvert\omega_e/T_e\rvert$	$[rad/Ns]$	0.31μ	0.33μ	0.34μ	211μ	8.09
$\lvert\omega_g/T_e\rvert$	$[rad/Ns]$	0.32μ	0.15μ	0.37μ	215μ	8.09
$\lvert u/T_e\rvert$	$[m/N]$	0.41μ	0.45μ	0.4μ	56.4μ	$5.64m$
$\lvert\omega_e/T_m\rvert$	$[rad/Ns]$	0.33μ	0.30μ	0.34μ	213μ	8.09
$\lvert\omega_g/T_m\rvert$	$[rad/Ns]$	0.31μ	0.32μ	0.34μ	212μ	8.09
$\lvert u/T_m\rvert$	$[m/N]$	0.41μ	0.45μ	0.4μ	56.2μ	$5.64m$

Table 3.2: Minimum attenuation of electrical and mechanical torque disturbances to rotor angular velocity ω_e, generator angular velocity ω_g and rotor blade position u.

The data obtained and shown in Table 3.3.5 illustrates that for a flawed blade construction, a flap-wise deflection of $4.7cm$ at the far point of the blade is possible when the cogging torque has a frequency component of $8.09Hz$. The tip speed of the blades do not approach a dangerous velocity even for large disturbances. It is evident that a variation of the blade characteristics has the greatest impact on system deformation. The blade is modeled as a one-mass system and lowering the power dissipation constant will as a consequence be impactful.

3.4 Chapter Conclusion

The study of the effect of disturbances on rotor blade flap-wise bending through network interaction, actuator delay and parameter variation transpired no cause for concern. The rotor and drivetrain models have thus successfully disproven the causes presented. The analysis exhibited that the reason must be hidden in the umodelled part of the drivetrain-rotor system. It was later uncovered by the supplier that the specific cause was a flawed tuning of the torque damping controller. No non-commonly known problem areas in multiple-WT systems were discovered in the investigations, although many of the assumptions that are taken for granted were proven true and led to a better understanding of the underlying system. Unfortunately, the vibration issue has recently re-appeared in another WPP, which could commence further examination. The fact that the vibrations could not be replicated, facilitated the design of the drivetrain control methods presented in chapter 3.

Chapter 4

Control of Electrical Systems

This chapter builds on the common current control methodologies used in power electronic device based wind turbines presented in section 2.4. A robust $\mathcal{H}_\infty$ controller achieving current tracking in an uncertain power system based on the studied WPP is presented. The controller provides active filtering using frequency dependent performance criteria. Guidelines for rotating reference frame PI current control design are shown and the voltage control philosophy of the studied WPP is analyzed with respect to controller interaction. The local controllers are shown to participate in the reactive power oscillations and an explanation involving the centralized power plant control is shown. A method to establish analytical stability envelopes for controller parameters is introduced, and the method is used to show the effect of network component values and other controllers operating in the network on the boundaries of controller parameters.

4.1 Current Control

4.1.1 Converter Current Control Design

Consider the system of Figure 2.11 represented for current controller synthesis by (2.29). Given a bounded trajectory $i_f^r(s)$, the output current $i_f(s)$ is sought controlled by actuation of the converter terminal voltage $u_i(s)$. An averaging model of a converter is modeled in the time domain as a delay τ_s,

$$u_i(t) = e^{-s\tau_s} u_i^r(t), \rightarrow u_i(s) = \frac{u_i^r(s)}{\tau_s s + 1}, \tag{4.1}$$

where $\tau_s = 0.5/f_s$ with f_s being the converter switching frequency. A generic PI-based current control design structure for balanced operation is,

$$u_i^r = (k_p + \frac{k_i}{s})(i_f^r - i_f N(s)) + C(s)E(s) \pm j\omega_g L_f i_f \tag{4.2}$$

$$N(s) = \frac{s^2 + (\omega_N/Q_n)s + \omega_N^2}{s^2 + (\omega_N/Q_d)s + \omega_N^2}, \tag{4.3}$$

where ω_N is the feedback notch filter frequency, Q_n and Q_d are filter quality factors and $j\omega_g L_f i_f$ is the decoupling. The feed-forward filter $C(s)$ cancels the network disturbance $E(s)$ within its bandwidth. The closed loop transfer functions from reference $i_f^r(s)$ to output $i_f(s)$ and from disturbance $E(s)$ to $i_f(s)$ are,

$$\begin{aligned} i_f(s) &= \frac{(k_p s + k_i) i_f^r(s)}{D(s)} - \frac{(s\tau_s + 1)s^2 E(s)}{(s + \alpha_f) D(s)}, \\ D(s) &= L_f \tau_s s^3 + (R_f \tau_s + L_f) s^2 + (N k_p + R_f) s + N k_i. \end{aligned} \tag{4.4}$$

The open loop system $i_f(s)/u_i(s)$ is represented as a first-order plus time delay model,

$$\widetilde{G_1}(s) = \frac{1}{R_f} \frac{1}{(L_f/R_f + \tau_s/2)s + 1} e^{-\tau_s/2s}, \tag{4.5}$$

for internal mode control tuning. The considered output stage is similar to the STATCOM connection of the studied WPP depicted in Figure D.9 with constants as (D.69). The Skogestad internal mode control PI tuning rules are derived from the method of direct synthesis, which specifies the desired closed-loop response and solves for the corresponding controller. The resulting controller is a function of the system order, and for a first order system $\widetilde{G_1}(s)$ [60],

$$k_p = \frac{L_f + R_f(\tau_s/2)}{\tau_c + \tau_s/2}, \; k_i = \frac{k_p}{\min\left(L_f/R_f + \tau_s/2, 4(\tau_c + \tau_s/2)\right)}, \tag{4.6}$$

where τ_c is a tuning parameter. The choice of τ_c is based on minimization of the integrated absolute error (IAE),

$$IAE = \int_0^\infty |i_f(t) - i_f^r(t)| dt, \tag{4.7}$$

which is favored by a small τ_c for a fast response and good disturbance rejection, or robustness quantified by the peak values of the sensitivity function, favored by a large τ_c. The choice of τ_c is a multiobjective optimization problem. The closed-loop system bandwidth ω_b is limited by the switching frequency ω_s to ensure proper attenuation of the switching harmonics. Bandwidth limiting (4.5) to $\omega_s/5$ or by the maximum proportional gain K_{max}, τ_c is lower bounded as,

$$\tau_c \geq \begin{cases} \dfrac{-50(\kappa_2 + L_f)R_f - \tau_s \kappa_1 + 5\kappa_2 \kappa_3 + 10 L_f \kappa_3}{50 R_f^2 + 2\kappa_1}, \omega_b \leq \omega_s/5 \\ \dfrac{(\tau_s/2)(R_f - K_{max}) + L_f}{K_{max}}, k_p \leq K_{max}, \end{cases} \tag{4.8}$$

where κ represent functions of system components given in the appendix of paper D. The lower bound of k_i for τ_c bounded by ω_b is found by insertion of k_p in τ_c. The feed-forward control problem for output disturbance rejection seeks to minimize the effect of $E(s)$ on $i_f(s)$ using a compensator $C(s)$. Given the control-law (4.2), $C(s)$

must reflect a compromise between converter over-current protection for network disturbances and disturbance rejection specifications. $C(s)$ is parametrized as,

$$C(s) = \alpha_f/(s + \alpha_f), \tag{4.9}$$

with respect to the tuning parameter α_f, deciding the filter bandwidth. The load disturbance response $i_f(s)/E(s)$ is characterized by its maximum output current magnitude i_f^{max} and time t_{max}. The system response is given by (D.24) which for large α_f obtains a global maximum at,

$$t_{max} = \ln(\frac{-2\kappa_5}{\kappa_2 - \kappa_3})/\left(\alpha_f - \kappa_4 - \kappa_7\right). \tag{4.10}$$

The maximum output current i_f^{max} as a function of α_f and system components at t_{max} is shown in the contour-plot of Figure D.5. Combining the developed design procedure for performance, filter and disturbance rejection using converter specifications provides a valuable way of designing a generic current controller based on system component data.

4.1.2 $\mathcal{H}_\infty$ Current Control Design with Active Filtering

Consider the following general system,

$$\begin{aligned} \dot{\boldsymbol{x}} &= \boldsymbol{Ax} + \boldsymbol{B_1 w} + \boldsymbol{B_2 u}, \\ \boldsymbol{z} &= \boldsymbol{C_1 x} + \boldsymbol{D_{11} w} + \boldsymbol{D_{12} u}, \\ \boldsymbol{v} &= \boldsymbol{C_2 x} + \boldsymbol{D_{21} w} + \boldsymbol{D_{22} u}, \end{aligned} \tag{4.11}$$

where $\boldsymbol{x} \in \mathbb{R}^n$, $\boldsymbol{u} \in \mathbb{R}^m$, $\boldsymbol{w} \in \mathbb{R}^q$, $\boldsymbol{v} \in \mathbb{R}^p$ and $\boldsymbol{z} \in \mathbb{R}^v$ are the states, control inputs, exogenous disturbances, internal outputs and exogenous outputs respectively. The system (4.11) is cast into the general formulation,

$$\begin{bmatrix} \boldsymbol{z} \\ \boldsymbol{v} \end{bmatrix} = \boldsymbol{P}(\boldsymbol{s}) \begin{bmatrix} \boldsymbol{w} \\ \boldsymbol{u} \end{bmatrix} = \left[\begin{array}{c|c} \boldsymbol{P_{11}(s)} & \boldsymbol{P_{12}(s)} \\ \hline \boldsymbol{P_{21}(s)} & \boldsymbol{P_{22}(s)} \end{array}\right] \begin{bmatrix} \boldsymbol{w} \\ \boldsymbol{u} \end{bmatrix}, \tag{4.12}$$

with $\boldsymbol{u} = \boldsymbol{K}(\boldsymbol{s})\boldsymbol{v}$. $\mathcal{H}_\infty$ algorithms minimize the $\mathcal{H}$-infinity norm of the lower fractional transformation, $\boldsymbol{N}$, of the generalized plant $\boldsymbol{P}$,

$$\boldsymbol{N} = F_l(\boldsymbol{P}, \boldsymbol{K}) = \boldsymbol{P_{11}} + \boldsymbol{P_{12}K}(\boldsymbol{I} - \boldsymbol{P_{22}K})^{-1}\boldsymbol{P_{21}}, \tag{4.13}$$

with the output feedback controller $\boldsymbol{K}$ as a parameter. The lower fractional transformation describes the transfer function from exogenous inputs $\boldsymbol{w}$ to exogenous outputs $\boldsymbol{z}$, such that an $\mathcal{H}_\infty$ output feedback controller generates a control signal $\boldsymbol{u}$ that minimizes the influence from $\boldsymbol{w}$ to $\boldsymbol{z}$. The $\mathcal{H}_\infty$ algorithms solve a suboptimal controller design problem, formulated as finding a controller achieving a closed loop gain $||\boldsymbol{N}||_\infty < \gamma$ for a given $\gamma > 0$. The output vector $\boldsymbol{z}$ is shaped by frequency dependent weighting functions to reflect the desired control objectives. Parametric uncertainty is represented in $\boldsymbol{P}$ by augmenting the input and output vectors as,

$$\left[\begin{array}{cccc} \boldsymbol{y_\delta} & \boldsymbol{z} & \boldsymbol{v} \end{array}\right]^\intercal = \boldsymbol{P}(\boldsymbol{s}) \left[\begin{array}{cccc} \boldsymbol{u_\delta} & \boldsymbol{w} & \boldsymbol{u} \end{array}\right]^\intercal, \tag{4.14}$$

where $\boldsymbol{u_\delta}$ and $\boldsymbol{y_\delta}$ are the open loop input and output signals of the system perturbation, defined in Figure 2.12. The LCL plus network system model from converter terminal voltage u_i to output current i_{f2} with multiplicative uncertainty, subject to network and grid disturbances u_c and u_g, is represented for balanced operation by two identical decoupled single-input single-output systems,

$$i_{f2}(s) = \begin{bmatrix} (1 + W_O(s)\Delta)G_{i_{f2}v_{inv}}(s) \\ G_{i_{f2}v_g}(s) \\ G_{i_{f2}v_{col}}(s) \end{bmatrix}^{\mathsf{T}} \begin{bmatrix} v_{inv}(s) \\ v_g(s) \\ v_c(s) \end{bmatrix}. \tag{4.15}$$

with the closed loop definitions omitting the Laplace operator,

$$i_{f2} = \underbrace{\frac{GK}{I + GK}}_{T} i^*_{f2} + \underbrace{\frac{1}{I + GK}}_{S}(G_{i_{f2}v_g}v_g + G_{i_{f2}v_c}v_c) - \underbrace{\frac{GK}{I + GK}}_{T} n, \tag{4.16}$$

for a bounded reference trajectory i^*_{f2}. The passive LCL filter ensures an attenuation of 60 dB/dec for frequencies outside the control bandwidth. A tradeoff between disturbance rejection and reference tracking is $\omega_s/5$ [119]. High power converters must minimize the amount of switching, and a switching frequency of $1 - 2kHz$ is required to minimize losses [120]. Denoting ω_h the odd power system harmonics within the controller bandwidth, the desired control objectives are:

- Attenuation of the power system harmonics within the control bandwidth. Sensitivity function gain of $1 - \epsilon,\ \epsilon \in [0.1; 0.2]\ \forall\omega \in \omega_h$.
- Tracking of the fundamental frequency component in the rotating reference frame with a bandwidth of $0.4kHz$.
- Maximum overshoot of 20%.
- Roll-off of output disturbance to control signal of $40dB$ from the closed-loop bandwidth.

Objective one through three is achieved by shaping the sensitivity function S and the complementary sensitivity function T, while the control effort is limited by KS. The stacked $S/T/KS$ problem,

$$\min_K \|\boldsymbol{N}(\boldsymbol{K})\|_\infty,\ \boldsymbol{N} = \begin{bmatrix} W_u KS \\ W_t T \\ W_p S \end{bmatrix}, \tag{4.17}$$

is shown in Figure C.5. The standard control configuration for the studied WPP with the shaping weights W_p, W_t and W_u is,

$$P(s) = \left[\begin{array}{cccc|c} 0 & 0 & 0 & 0 & G_{i_{f2}v_i}W_o \\ W_p & W_pG_{i_{f2}v_c} & W_pG_{i_{f2}v_g} & -W_p & W_pG_{i_{f2}v_i} \\ 0 & 0 & 0 & 0 & W_u \\ W_t & 0 & 0 & 0 & W_tG_{i_{f2}v_i} \\ \hline -I & -G_{i_{f2}v_c} & -G_{i_{f2}v_g} & 1 & -G_{i_{f2}v_i} \end{array}\right], \tag{4.18}$$

with input and output vectors,

$$\begin{bmatrix} \boldsymbol{w} & \boldsymbol{u} \end{bmatrix} = \begin{bmatrix} u_\delta & u_c & u_g & i^*_{f2} & u_i \end{bmatrix}, \tag{4.19}$$

$$\begin{bmatrix} \boldsymbol{z} & \boldsymbol{v} \end{bmatrix} = \begin{bmatrix} y_\delta & z_1 & z_2 & z_3 & e_{i_{f2}} \end{bmatrix}. \tag{4.20}$$

The system response to power system harmonic frequencies ω_h, is shaped by the sensitivity function S. Comparable to proportional-resonant control, the response is augmented by insertion of n non-ideal notch/trap filters,

$$W_p(s) = \frac{s/A_p + \omega_{ph}}{s + \omega_{pl}\tau_i} \prod_{k=1}^{n} \left(1/(\frac{s^2 + 2kg_p\omega_{bn}\omega_0 s + (\omega_0 k)^2}{s^2 + 2k\omega_{bn}\omega_0 s + (\omega_0 k)^2}) \right), \tag{4.21}$$

where ω_{bn}, ω_{ph} and ω_{pl} determine the bandwidth of the filters, g_k is the gain of the k^{th} notch filter, τ_i provides approximate integral action and A_t determines the allowed overshoot. Shaping S for a specific range of frequencies necessarily implies an arbitrarily large change at other frequencies, as per evaluation of the Bode sensitivity integrals. The complementary constraint $S + T = 1$ represents a trade-off as S and T cannot be minimized for the same frequency, thus for $W_p(s)$ given in (4.21), the complementary sensitivity function T must be shaped accordingly as,

$$W_t(s) = \frac{s/A_t + \omega_{th}}{s + \omega_{tl}} \prod_{k=1}^{n} \left(\frac{s^2 + 2kg_t\omega_{bn}\omega_0 s + (\omega_0 k)^2}{s^2 + 2k\omega_{bn}\omega_0 s + (\omega_0 k)^2} \right), \tag{4.22}$$

to facilitate an $\mathcal{H}_\infty$ minimization for $\gamma < 1$ and meet the robust performance and stability demands. The control signal $\boldsymbol{u}$ is shaped by $W_u(j\omega)$ to allow control effort while ensuring roll-off of KS for high frequencies,

$$W_u(s) = \frac{(s/g_u^{1/2} + \omega_h)^2}{(s + \omega_l)^2}, \tag{4.23}$$

where ω_h and ω_l are frequency limits, and g_u is the attenuation of the filter. The notch filter gain values are found by a numerical local search method to achieve a nominal closed-loop sensitivity of unity for every $\omega \in \omega_h$. Performance and stability for all plants in the set described by $W_o(s)\Delta$ is achieved for,

$$||W_p(s)S(s)||_\infty + ||W_o(s)T(s)||_\infty < 1, \tag{4.24}$$

$$||T(s)||_\infty < ||1/W_o(s)||_\infty, \tag{4.25}$$

which is obtained for the parameters in Table C.2 and visualized in Figure C.10. The bounded reference trajectory i^*_{f2} is filtered to avoid excitation of the under damped notch filter dynamics.

The performance of the designed $\mathcal{H}_\infty$ output feedback controller is measured by the ability to obtain the desired control effort and sensitivity attenuation. With S_{v_g} being the spectrum of the harmonics, the metrics J_{d1} and J_{d2} quantify the desired

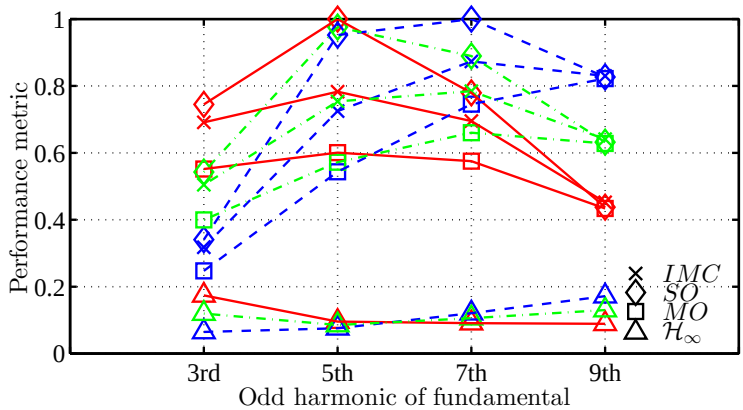

Figure 4.1: Normalized $J_d(\omega_h)/|(J_d(\omega_h))|_\infty$, performance metric $J_d(\omega_h)$ for internal mode control, symmetrical optimum, modulus optimum and $\mathcal{H}_\infty$ controllers. Disturbance to control input $J_{d1}(solid)$, sensitivity $J_{d2}(stipple)$ and combined $J_d(dashdot)$.

performance for all $\omega \in \omega_h$,

$$\begin{aligned} J_{d1}(\omega_h) &= \frac{1}{2}\int_{\omega_h-\omega_d}^{\omega_h+\omega_d} \left(|H_{i_{v_{inv}}v_g}(\omega)|^2\right) S_{v_g} d\omega, \\ J_{d2}(\omega_h) &= \frac{1}{2}\int_{\omega_h-\omega_d}^{\omega_h+\omega_d} \left(|1-|H_{i_{f2}v_g}(\omega)||^2\right) S_{v_g} d\omega, \end{aligned} \tag{4.26}$$

where ω_d is the bandwidth of the notch filters. Evaluation of the metrics for the $\mathcal{H}_\infty$ controller and the PI-based controllers is shown in Figure 4.1. The $\mathcal{H}_\infty$ controller shows a performance metric J_d in Figure 4.1 close to 0.1 for all $\omega_h \pm \omega_d$, improving J_{d1} and J_{d2} by a minimum of 75% compared to the internal mode control, symmetrical optimum and modulus optimum designs.

The system is tested in a SimPower Systems model of the studied WPP using the (N+1) model shown in Figure C.9. System reference tracking is shown in Figure 4.2 and the disturbance response to an input signal with frequency components of,

$$\omega = [100Hz, 200Hz, 300Hz, 400Hz], \tag{4.27}$$

is shown in Figure 4.3. The systems obtains a bandwidth of $0.27kHz$ which is lower than anticipated but a consequence of the $\mathcal{H}_\infty$ design conservatism. The settling time is improved compared to the PI-controllers with less control effort. The desired power system harmonic sensitivity is achieved for the harmonic frequencies and complements the passive filters. The system furthermore shows an attenuation of 90% from noise to output.

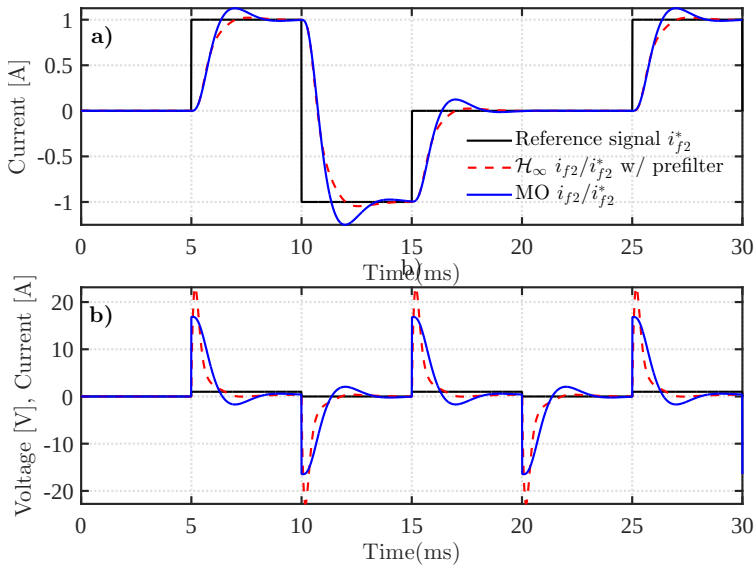

Figure 4.2: Reference tracking. **a)** Output current, $\mathcal{H}_\infty$ compared to best PI controller. $\mathcal{H}_\infty$ shows faster tracking with no overshoot and within specifications. **b)** Control effort.

4.1.3 Observer Based $\mathcal{H}_\infty$ Current Control Design with Performance Enhancement Controller

A $\mathcal{H}_\infty$ output feedback controller was designed in section 4.1.2 for the LCL output filter shown in Figure 2.10. The $\mathcal{H}_\infty$ controller achieved active filtering of power system harmonic disturbances in a system subject to parametric uncertainty. An optimal control condition is to have constant output power while rejecting the grid voltage disturbance during both ramp and step disturbances. This section presents a state estimate feedback controller with a residual based performance enhancement controller for disturbance response minimization. Consider a single phase LCL-converter system with state input, disturbance and output vectors,

$$\begin{aligned} \boldsymbol{x} &= \begin{bmatrix} i_1 & i_g & i_c & v_{c1} \end{bmatrix}^\intercal, \\ u &= [u_i],\ e_x = [u_g],\ y = [i_g], \end{aligned} \tag{4.28}$$

the system dynamics are,

$$\frac{di_1}{dt} = L_1^{-1}(u_i - u_{c1} - R_1 i_1) \tag{4.29}$$

$$\frac{di_g}{dt} = L_g^{-1}(u_{c1} - u_g - R_g i_g) \tag{4.30}$$

$$\frac{dv_{c1}}{dt} = C_1^{-1}(i_1 - i_g) \tag{4.31}$$

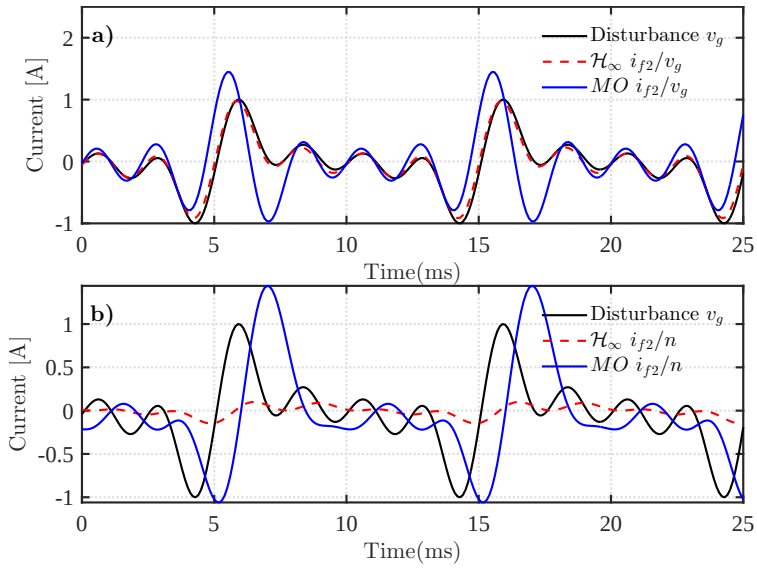

Figure 4.3: Disturbance v_g and i_{f2} measurement noise composed of normalized harmonic signal, $\omega = [100Hz, 200Hz, 300Hz, 400Hz]$ **a)** Disturbance attenuation. Output current, $\mathcal{H}_\infty$ compared to best PI controller for harmonic grid disturbance. **b)** Noise rejection.

$$\frac{di_c}{dt} = L_g^{-1}(u_g - u_{c1} + R_g(i_1 - i_c)) + L_1^{-1}(u_i - u_{c1} - R_1 i_1), \tag{4.32}$$

where u_i is the controllable inverter voltage, u_g is the grid voltage, and i_g is the output current at the low voltage side of the transformer. The capacitance C_1 and inductances L_1 and L_g make up the combined LCL filter plus grid inductance. The resistances R_1 and R_g are the snubber resistance and grid resistance respectively. Checking the observability and controllability of the system defined by (4.29), it is found that the capacitor current i_c is neither observable nor controllable. The modes associated with i_c are located in the left half plane and decay exponentially from any initial set of values. As the mode is not controllable and exponentially stable, the system is simplified by neglecting the dynamics of i_c. Given the reduced state, input, disturbance and output vectors,

$$\boldsymbol{x} = \begin{bmatrix} i_1 & i_g & v_{c1} \end{bmatrix}^\intercal, \tag{4.33}$$

$$u = [u_i],\ e_x = [u_g],\ y = [i_g], \tag{4.34}$$

the system in state-space form is,

$$\begin{aligned}
\boldsymbol{A} &= \begin{bmatrix} -R_1/L_1 & 0 & -1/L_1 \\ 0 & -R_g/L_g & 1/L_g \\ 1/C_1 & -1/C_1 & 0 \end{bmatrix} \\
\boldsymbol{B} &= \begin{bmatrix} 1/L_1 & 0 & 0 \end{bmatrix}^\intercal, \boldsymbol{E_x} = \begin{bmatrix} 0 & -1/L_g & 0 \end{bmatrix}^\intercal \\
\boldsymbol{C} &= \begin{bmatrix} 0 & 1 & 0 \end{bmatrix},
\end{aligned} \tag{4.35}$$

which is fully observable and controllable. The system is cast into the generalized formulation (4.12). Denoting $G(s) = i_g(s)/u_i(s)$ and $H(s) = i_g(s)/u_g(s)$, setting $w = [e_x]$, $v = i_g$ and the weighted error signals $\boldsymbol{e} = \begin{bmatrix} W_1(s)i_g & W_2(s)u \end{bmatrix}$,

$$\begin{bmatrix} e \\ v \end{bmatrix} = \begin{bmatrix} W_1(s)H(s) & W_1(s)G(s) \\ 0 & W_2(s) \\ H(s) & G(s) \end{bmatrix} \begin{bmatrix} w \\ u \end{bmatrix}, \tag{4.36}$$

with,

$$\begin{aligned}
\boldsymbol{P_{11}} &= \begin{bmatrix} W_1(s)H(s) & 0 \end{bmatrix}^\intercal, \boldsymbol{P_{12}} = \begin{bmatrix} W_1(s)G(s) & W_2(s) \end{bmatrix}^\intercal \\
\boldsymbol{P_{21}} &= H(s), P_{22} = G(s).
\end{aligned} \tag{4.37}$$

The state estimate feedback gain $\boldsymbol{K}$ is computed using a linear quadratic regulator design which seeks to minimize the performance index,

$$\boldsymbol{J} = \int_0^\infty \boldsymbol{x(t)}^\intercal \boldsymbol{R_1 x(t)} + u(t)\boldsymbol{R_2}u(t)dt, \tag{4.38}$$

where $\boldsymbol{R_1}$ and $\boldsymbol{R_2}$ are matrices of appropriate dimensions penalizing state and input magnitude. The performance index is minimized for,

$$\boldsymbol{J_{min}} = \frac{1}{2}\boldsymbol{x_0}^\intercal \boldsymbol{P_\infty x_0}, \tag{4.39}$$

where $\boldsymbol{P_\infty}$ is the solution to the algebraic Ricatti equation [121]. The observer is designed as a Luenberger state observer with state estimate $\bar{\boldsymbol{x}}$,

$$\dot{\bar{\boldsymbol{x}}} = \boldsymbol{A}\bar{\boldsymbol{x}} + \boldsymbol{B}u + \boldsymbol{H}(y - \boldsymbol{C}\bar{x}) \tag{4.40}$$

with the observer state dynamics $\boldsymbol{H}$ and the estimation error, $\boldsymbol{e} = \boldsymbol{x} - \bar{\boldsymbol{x}}$,

$$\dot{\boldsymbol{e}} = (\boldsymbol{A} - \boldsymbol{HC})\boldsymbol{e}, \tag{4.41}$$

which is Hurwitz for the characteristic polynomial $|(\boldsymbol{A} - \boldsymbol{HC}) - \lambda \boldsymbol{I}|$ for $\Re\lambda \leq 0$. The eigenvalues are chosen three times faster than the original system, such that for ω_i being the natural frequency of the i'th eigenvalue of A_i, the observer eigenvalues are placed at,

$$\lambda_{oi} = -\omega_i\zeta + \sqrt{(2\omega_i\zeta)^2 - 4\omega_i^2}/2, \tag{4.42}$$

and results in a stabilizing pair $\boldsymbol{A}$ and $\boldsymbol{H}$. The system $\boldsymbol{A}$, $\boldsymbol{B}$, $\boldsymbol{C}$, $\boldsymbol{K}$ and $\boldsymbol{H}$ is factored into left and right coprimes for which the Bezout equation holds, i.e $\boldsymbol{A}$ and $\boldsymbol{K}$ is a stabilizing pair [61]. The stable coprime factorizations of the plant $G(s)$ and controller $K(s)$ are,

$$\boldsymbol{K} = \boldsymbol{U}\boldsymbol{V}^{-1} = \bar{\boldsymbol{V}}^{-1}\bar{\boldsymbol{U}}, \tag{4.43}$$

$$\boldsymbol{G} = \boldsymbol{N}\boldsymbol{M}^{-1} = \bar{\boldsymbol{M}}^{-1}\bar{\boldsymbol{N}}. \tag{4.44}$$

The class of controllers $\boldsymbol{K}(\boldsymbol{Q})$, parametrized in terms of $\boldsymbol{Q}$ can be expressed as,

$$\boldsymbol{K}(\boldsymbol{Q}) = \boldsymbol{U}(\boldsymbol{Q}) + \boldsymbol{V}(\boldsymbol{Q})^{-1}, \tag{4.45}$$

with $\boldsymbol{U}(\boldsymbol{Q}) = \boldsymbol{U} + \boldsymbol{M}\boldsymbol{Q}$ and $\boldsymbol{V}(\boldsymbol{Q}) = \boldsymbol{V} + \boldsymbol{N}\boldsymbol{Q}$. The $\boldsymbol{P}, \boldsymbol{K}, \boldsymbol{Q}$ interconnection is formulated into the compact form,

$$\boldsymbol{J} = \begin{bmatrix} \boldsymbol{U}\boldsymbol{V}^{-1} & \bar{\boldsymbol{V}}^{-1} \\ \boldsymbol{V}^{-1} & -\boldsymbol{V}^{-1}\boldsymbol{N} \end{bmatrix}, \tag{4.46}$$

representing the open loop system,

$$\begin{bmatrix} \boldsymbol{u} \\ \boldsymbol{r} \end{bmatrix} = \boldsymbol{J}\begin{bmatrix} \boldsymbol{y} \\ \boldsymbol{s} \end{bmatrix}, \boldsymbol{s} = \boldsymbol{Q}\boldsymbol{r}, \tag{4.47}$$

where r is the residual of the estimation,

$$\boldsymbol{r} = \bar{\boldsymbol{M}}\boldsymbol{y} - \bar{\boldsymbol{N}}\boldsymbol{u}. \tag{4.48}$$

The closed loop matrix transfer function with $\boldsymbol{K}(\boldsymbol{Q})$ as the internal feedback controller is,

$$\begin{bmatrix} \boldsymbol{e} \\ \boldsymbol{r} \end{bmatrix} = \boldsymbol{T}\begin{bmatrix} \boldsymbol{w} \\ \boldsymbol{s} \end{bmatrix}, \boldsymbol{T} = \begin{bmatrix} \boldsymbol{T_{11}} & \boldsymbol{T_{12}} \\ \boldsymbol{T_{21}} & \boldsymbol{T_{22}} \end{bmatrix} = \begin{bmatrix} \boldsymbol{P_{11}} + \boldsymbol{P_{12}}\boldsymbol{U}\bar{\boldsymbol{M}}\boldsymbol{P_{21}} & \boldsymbol{P_{12}}\boldsymbol{M} \\ \bar{\boldsymbol{M}}\boldsymbol{P_{21}} & \boldsymbol{0} \end{bmatrix}, \tag{4.49}$$

and the transfer function from exogenous disturbance $\boldsymbol{w}$ to disturbance performance signal $\boldsymbol{e}$ is given by the lower fractional transformation of $\boldsymbol{T}$ and $\boldsymbol{Q}\boldsymbol{r}$,

$$\boldsymbol{e} = \boldsymbol{F_Q}\boldsymbol{w}, \ \boldsymbol{F_Q} = \boldsymbol{T_{11}} + \boldsymbol{T_{12}}\boldsymbol{Q}\boldsymbol{T_{21}}, \tag{4.50}$$

which is affine in $\boldsymbol{Q}$. It is possible to choose $\boldsymbol{Q}$ such that some performance index is minimized. The control objective of disturbance rejection can be achieved by proper scaling of the performance signal $\boldsymbol{e}$. The selection of performance index for Q optimization is chosen to achieve optimal worst-case 2-norm of the bounded disturbance performance signals. In the frequency domain, this optimization can be formulated as a generalized $\mathcal{H}_\infty$ control problem,

$$\min_{Q} ||\boldsymbol{F_Q}||_\infty^2, \tag{4.51}$$

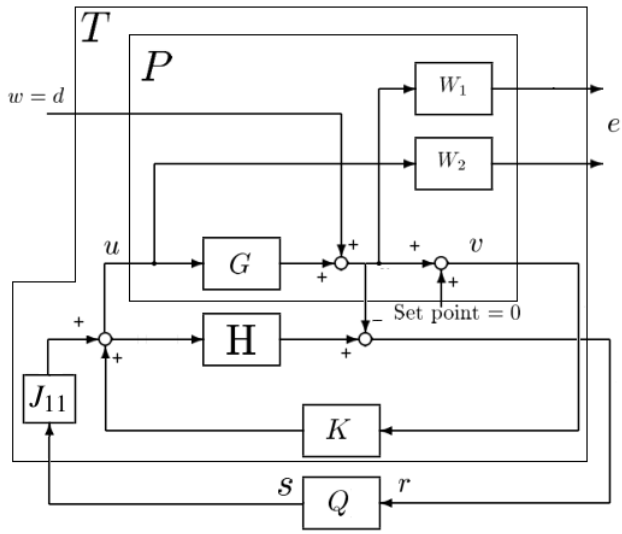

Figure 4.4: $\mathcal{H}_\infty$ S/KS mixed-sensitivity optimization in standard form with added observer and Q design - Regulation.

where,

$$||\boldsymbol{F_Q}||_\infty^2 = \sup_{\theta\in[-\pi,\pi]} \sigma_{max}(\boldsymbol{F_Q}(e^{j\theta})). \tag{4.52}$$

The disturbance frequency contents consist of power system harmonics, i.e. integer multiples of $50Hz$. The objective is to minimize $i_g(s)/e_x(s)$ for a step change in voltage which could occur at fault or tap-changer activation. The setup is shown in Figure 4.4. The shaping filters $W_1(s)$ and $W_2(s)$ shape the control effort and the output of the system. Using (4.49) as the plant to be optimized, and $\boldsymbol{F_Q(s)}$ given in (4.50), the optimization problem (4.52) is solved by γ iteration using Matlab such that the residual is minimized by fitting $\boldsymbol{Q}$. The weighting functions,

$$W_1(s) = \frac{s/M + \omega_b}{s + \omega_b A}, \;\; W_2(s) = 1, \tag{4.53}$$

are used for the scaled system such that $\boldsymbol{w}$ and $\boldsymbol{u}$ are bounded signals with a worst-case magnitude of one. The parameters of weighing function $W_1(s)$ are chosen to achieve approximate integral action and a roll-off in the sensitivity function. The parameters are,

$$M = 1,\; A = 10^{-4},\; \omega_b = 10. \tag{4.54}$$

The system is subjected to a sequence of grid voltage disturbances which ramp from $-0.5pu$ to $0.5pu$ in 5 seconds and then step down to $-0.5pu$ again. Figure 4.5 shows the system response to the disturbance. The linear quadratic plus residual control

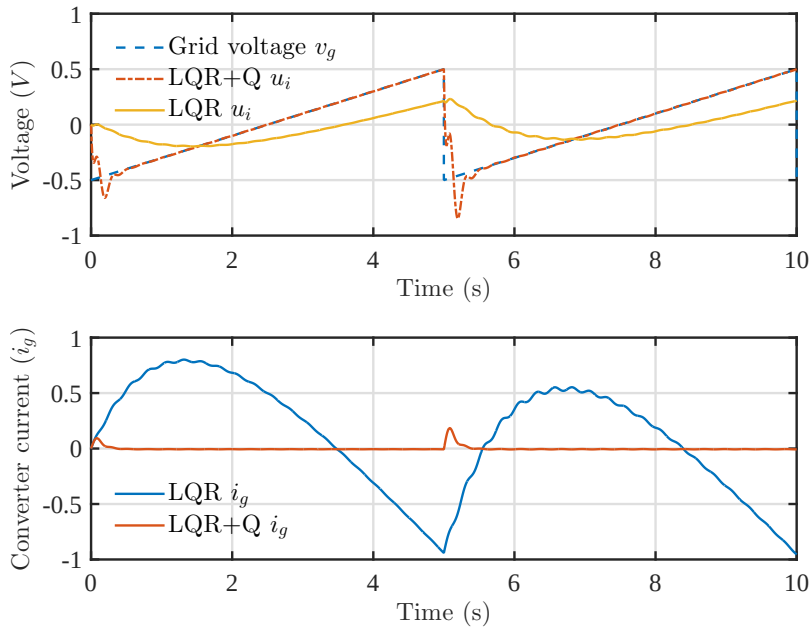

Figure 4.5: Current response for sequential steps in grid voltage, v_g, with linear quadratic regulator and linear quadratic regulator plus residual feedback.

is able to track the slope of v_g and reject the step change within $300ms$ while the linear quadratic regulator controller never obtains a steady state in the 5 seconds available. The control effort is used more aggressively by the linear quadratic plus residual control, but stays within the defined boundaries. An improvement using linear-quadratic gaussian control to create the residual signal on which $\boldsymbol{Q}$ is optimized against is possible. The work shows a clear proof of concept and research is ongoing.

4.2 Voltage Control

This section presents the main findings of paper D. A method to validate the supplied controller parameters is developed and used for the chosen voltage control philosophy. The observed reactive power oscillations are recreated by varying the controller parameters within their stabilizing envelope and a possible cause is found.

4.2.1 Stability Envelopes of PI Based Converter Voltage Control

Dynamic voltage control at the interface point is a feature of many industrial turbines. Automatic voltage control in systems employing power electronic devices is achieved by controlling the terminal voltage of the converter. Given the voltage control scheme of the studied WPP introduced in section 2.2.3, effective local voltage

control is paramount in maintaining system-wide terminal voltage levels. A generic voltage control structure of a STATCOM and a WT is shown in Figure D.4. Applying the current control design methods of section 4.1.1, the stabilizing envelope of the outer voltage controller is determined based on the Hurwitz signature.

The plant from output current $i_f(s)$ to terminal voltage $v_t(s)$ with damping resistance R_d is given in (D.12). The stabilizing envelope $\Omega(k_{pv}, k_{iv})$ of a plant $P(s) = D(s)/N(s)$ with degrees n and m respectively, a local voltage PI-controller $K_1(s) = k_{pv} + k_{iv}/s$ and a fixed current controller $K_2(s) = k_{pc} + k_{ic}/s$, is defined from the characteristic polynomial $\delta(s)$,

$$\delta(s) \triangleq D(s)s + (k_{pv}s + k_{iv})N(s) \tag{4.55}$$

$$\begin{aligned}\delta(s) = {} & C_pL_fL_v\tau_s s^6 + C_p\left(L_fR_d\tau_s + L_fR_v\tau_s + L_vR_f\tau_s + L_fL_v\right)s^5 \\ & + C_p\left(R_dR_f\tau_s + R_fR_v\tau_s + L_fR_d + L_fR_v + L_vR_f + L_vk_{pc} + L_f\tau_s/C_p\right)s^4 \\ & + \left(C_p(L_vk_{ic} + R_d(R_f + k_{pc}) + R_fR_v + R_vk_{pc}) - L_vk_{pc}k_{pv} + R_f\tau_s + L_f\right)s^3 \\ & + \left(C_pR_dk_{ic} + C_pR_vk_{ic} - L_vk_{ic}k_{pv} - L_vk_{iv}k_{pc} - R_vk_{pc}k_{pv} + R_f + k_{pc}\right)s^2 \\ & + \left(-L_vk_{ic}k_{iv} - R_vk_{ic}k_{pv} - R_vk_{iv}k_{pc} + k_{ic}\right)s - R_vk_{ic}k_{iv}.\end{aligned} \tag{4.56}$$

In traditional methods the characteristic polynomial is solved with respect to its parameters to constrain the poles to the left half plane. An analytical relation requires the formation of the polynomial,

$$\nu(s) = \delta(s)N(-s), \tag{4.57}$$

which can be factorized as,

$$\nu(s) = \nu_r(s^2, k_{iv}) + s\nu_i(s^2, k_{pv}), \tag{4.58}$$

$$\nu(j\omega) = (p_1(\omega) + k_{iv}p_2(\omega)) + j(q_1(\omega) + k_{pv}q_2(\omega)), \tag{4.59}$$

separating stability bounds for k_{pv} and k_{iv}. The signature formula for a rational function with real coefficients $P(j\omega)$ describing the total phase change when the frequency runs from 0 to $+\infty$ is [60],

$$\Delta_0^{\infty}\angle P(j\omega) = \frac{\pi}{2}[z_r^- - z_r^+ - (p_r^- - p_r^+)], \tag{4.60}$$

$$\sigma(P) \triangleq z_r^- - z_r^+ - (p_r^- - p_r^+), \tag{4.61}$$

where $z_r^{\pm}$ and $p_r^{\pm}$ denote the number of zeroes and poles in $P(s)$ in the left half plane and right half plane respectively. The Hurwitz signature σ for $P(j\omega)$ with $w_0, \ldots, \omega_{l-1}$ denoting the real nonnegative zeroes of $p_i(\omega)$ with odd multiplicities is computed as [122],

$$\begin{aligned}\sigma(P) = {} & \left(sgn[P_r(\omega_0)] + 2\sum_{j=1}^{l-1}(-1)^j sgn[P_r(\omega_j)] + (-1)^l sgn[P_r(\omega_j)]\right) \\ & \cdot (-1)^{l-1} sgn[P_i(\infty^-)], \text{ for } n-m \text{ even},\end{aligned} \tag{4.62}$$

$$\sigma(P) = \left(sgn[P_r(\omega_0)] + 2\sum_{j=1}^{l-1} (-1)^j sgn[P_r(\omega_j)] \right) \cdot (-1)^{l-1} sgn[P_i(\infty^-)], \text{ for } n-m \text{ odd}, \tag{4.63}$$

for any $P(s)$ factorized as (4.58). With the controller $K_1(s)$ having one free pole, closed loop stability is guaranteed for $n+1$ zeroes of the characteristic polynomial in the open left half plane, equivalent to $\sigma(\nu) = n+2$,

$$\sigma(\nu) = n + 1 + z^+ - z^- = (n-m) + 1 + 2z^+. \tag{4.64}$$

For a fixed $k_{pv} \in \Omega(k_{pv}, k_{iv})$ with $j = sgn[\nu_i(0^+, k_{pv})]$ and the real positive finite zeroes $0 < \omega_1 < \omega_{l-1}$ with odd multiplicities of $\nu_i(-\omega^2, k_{pv})$, stability is guaranteed for the distinct strings of integers, $I_j = \{i_0, i_1, \ldots, i_l\}$ satisfying,

$$j(i_0 - 2i_1 + 2i_2 + \cdots + (-1)^{l-1} 2i_{l-1} + (-1)^l i_l) = \sigma(\nu), \text{ for } n+m \text{ even}, \tag{4.65}$$

$$j(i_0 - 2i_1 + 2i_2 + \cdots + (-1)^{l-1} 2i_{l-1}) = \sigma(\nu), \text{ for } n+m \text{ odd}. \tag{4.66}$$

The stabilizing sets in (k_{pv}, k_{iv}) space for fixed k_{pv} are given by the linear inequalities,

$$\nu_r(-\omega_t^2, k_{iv}) i_t > 0, \; i_t \in I_j, \tag{4.67}$$

with each string I_j generating a convex stability set $S_j(k_{pv})$ such that the complete stabilizing set is the union of these sets,

$$S(k_{pv}) = \underset{j}{\cup} S_j(k_{pv}). \tag{4.68}$$

The full stabilizing set can be obtained by iteration through all k_{pv} satisfying (4.64). The range of k_{pv} can be restricted to the set Ω, satisfying (4.65) and (4.66) for (4.64) with a number of roots $l-1$ such that,

$$\begin{aligned} l - 1 &\geq (n - m + 2z^+ - 1)/2, \text{ for } n+m \text{ even}, \\ l - 1 &\geq (n - m + 2z^+ + 1)/2 - 1, \text{ for } n+m \text{ odd}. \end{aligned} \tag{4.69}$$

The Stabilizing Sets method developed by L.H. Keel and S.P. Bhattacharyya does not consider an analytical way to find Ω.

Several methods to upper bound the amount of roots in univariate polynomials exist. The classic method of Budan-Fourier provides the maximum number of roots in an univariate polynomial as a function of the variation in coefficient signs. A method to lower bound the number of real roots is Sturm's theorem. Sturm's theorem states that given an univariate polynomial f and two real numbers $a, b \in \mathbb{R}$ with $a < b$ and $f(a), f(b) \neq 0$, the number of zeroes of f in the interval (a, b) is the difference,

$$var(F, a) - var(F, b), \tag{4.70}$$

where F is the Sturm sequence of f and the var function returns the number of sign changes. Sturm's theorem expresses the amount of distinct non-negative real

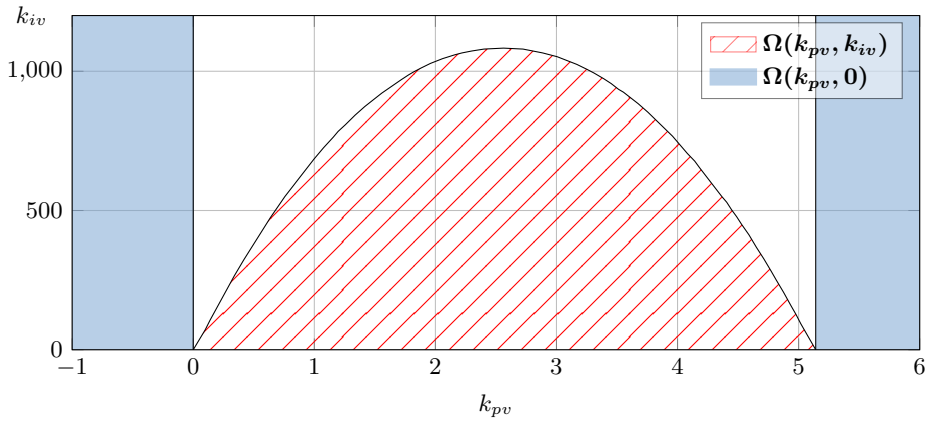

Figure 4.6: Stabilizing set $\boldsymbol{\Omega}(k_{pv}, k_{iv})$ for WT local voltage control in the studied WPP.

roots in a frequency interval of f using sign change counting in the associated Sturm sequence. The method is traditionally used to numerically isolate roots in arbitrary small intervals, but is readily able to provide an analytical method to find Ω. The Sturm sequence of an univariate polynominal f is the Sylvester sequence of f and $\dot{f}$. For f_k being the greatest common divisor of f and $\dot{f}$, the Sturm sequence is obtained by application of Euclid's algorithm,

$$\begin{aligned} f_0 &= f,\ f_1 = df/dt, \\ f_i &= f_{i-1}q_{i-2} - f_{i-2}, \\ &\vdots \\ 0 &= f_{k-1}q_{k-2} - f_{k-2}, \end{aligned} \tag{4.71}$$

with q_i being the long division quotient of f_{i-1}, f_i. Denoting $\boldsymbol{\Xi(F)_\omega}$ the Sturm sequence evaluated at ω, the sign of the individual vector components can be manipulated to provided a bound on k_{pv} for $\omega \in (0^+, \infty)$ such that the number of real roots is greater than or equal to $l-1$,

$$var(\boldsymbol{\Xi(\nu_i(k_{pv}))_0}) - var(\boldsymbol{\Xi(\nu_i(k_{pv}))_\infty}) \geq l - 1. \tag{4.72}$$

From the evolution (4.71) it is seen as $i \to k$ the order of f_i decreases at the cost of expression complexity. Assuming the existence of a set Ω satisfying (4.72), the $l-1$ distinctive non-negative roots of $\nu_i(k_{pv})$ can be isolated by factorization or a change of variables for simple polynomials. Insertion of the resulting expression for the root(s) in (4.67) provides the full stabilizing set $\Omega(k_{pv}, k_{iv})$.

Application of the developed theory to the characteristic polynomial of (4.55) result in parameter bounds (D.39) and (D.47). The STATCOM dynamics of (D.70)

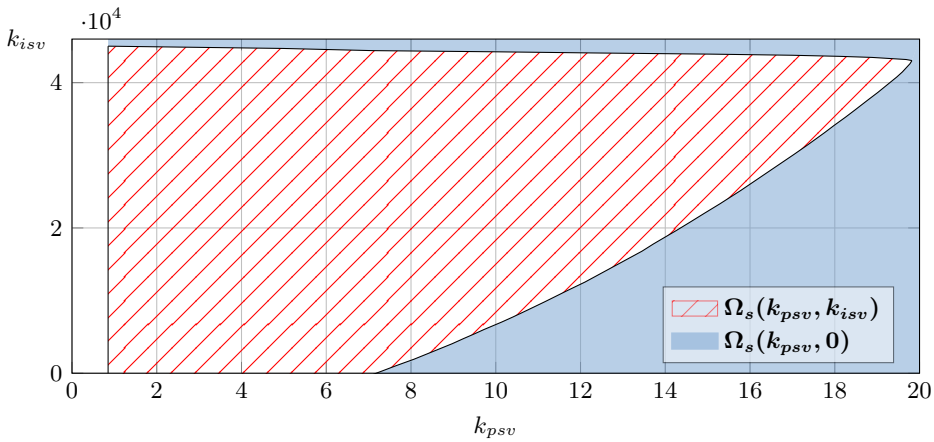

Figure 4.7: Stabilizing set $\Omega_s(k_{psv}, k_{isv})$ for the STATCOM voltage control. White area has less than two real roots of $\nu(s)$. Hatched area $\Omega_s(k_{psv}, k_{isv})$ and blue area $\Omega_s(k_{psv}, 0)$.

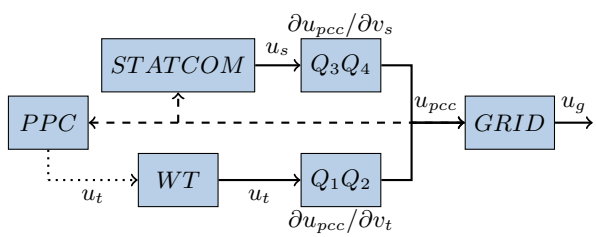

Figure 4.8: Conceptional diagram of the WPP voltage control. Q_2 and Q_3 represent the shunt admittance and series impedance of the transformer and network respectively. – – – Measurement, $\cdots$ Command, $\rightarrow$ Physical connection

result in the PI-controller limits of (D.74). The bounds are visualized for component parameters from the studied WPP in Figure 4.6 and Figure 4.7. A stabilizing sets analysis of the studied power plant controller is presented in section 4.2.2.

4.2.2 High Level Cascade Voltage Control Stability Envelope

The voltage control philosophy shown in Figure 2.5 is modeled for power plant controller analysis using power flow equations. A linearized version is obtained by considering operation at a steady state power flow solution and using the resulting voltage sensitivities. The model is shown in Figure 4.8. The power plant controller acts on the local turbine voltage control, and constitutes a cascaded closed loop control. This fixed-structure system delivered by an external supplier is implemented

as a digital PI controller with a sample time of $T_s = 100ms$. The response of the inner dynamics of the current and voltage control can be considered of first order for power plant control analysis.

An interesting phenomenon is how the system stability is affected by cascade delay, voltage sensitivity and sampling time. Denoting T_v the effective rise-time of the voltage and current control cascade, Q_c the voltage sensitivity from turbine terminals to the point of common coupling and $\alpha = T_s/T_v$ the ratio between sampling time and inner delay, the open-loop response is,

$$u_{pcc}(s) = Q_c / \left((T_v s + 1)(\alpha T_v/2s + 1)\right). \tag{4.73}$$

Using the method of Stabilizing Sets presented in section 4.2.1, the following bounds on the control are found,

$$\begin{aligned} k_{pu} &\geq -\frac{1}{Q_c(SQ_4+1)},\ 2Q_c^2(SQ_4+1) > 0, \\ k_{iu} &< \underbrace{\frac{\alpha+2}{\alpha T_v}}_{a_k} k_{pu} + \underbrace{\frac{\alpha+2}{\alpha T_v}\frac{1}{Q_c(SQ_4+1)}}_{b_k}, \end{aligned} \tag{4.74}$$

where S is the power plant controller droop and Q_4 is the effect on the voltage at the point of common coupling for a change in terminal reactive power. The limits of (4.74) has a linear dependence of k_{iu} on k_{pu} and shows a clear relation between the sampling time and the inner process rise time.

4.3 Analysis of the Reactive Power Oscillations

WPP voltage levels are controlled by regulating the injection or absorption of reactive power. The reactive power oscillations described in section 2.3 can as a consequence be linked with local or global voltage control. The voltage control scheme utilized in the studied WPP is shown in Figure 4.8. The reactive power is supplied by the WT(s), a STATCOM and a manually switched reactor. Steady state reactive power levels are supported by shunt components and the WT(s). The STATCOM, connected at the tertiary winding of the point of common coupling transformer, is used for fast compensation.

The oscillations were observed at the WT terminals and at the point of common coupling. Given the electrical distance separating the WTs and the STATCOM, the problem could be of a distributed nature. In paper D, the following propositions are sought proved or disproved:

- Proposition 1: Inadequate controller bandwidth separation in the cascade voltage control configuration and interaction with the grid dynamics.
- Proposition 2: Similar regulation objective of the power plant controller and the STATCOM using one feedback signal.

The current control design developed in section 4.1.1 combined with the voltage controller design and stability envelope assessment in section 4.2.1 provide the foundation for the analysis.

4.3.1 Proposition 1

The nature of voltage control requires careful selection of controller parameters. The inner current controller should be designed towards a maximum bandwidth specification. The outer voltage controller sees the plant $P_2(s)G_i(s)$ with G_i being the inner loop and $P_2(s)$ an approximate representation of the grid dynamics. Given a current controller dimensioned according to section 4.1.1, the outer voltage controller should be of lower bandwidth for the inner loop to be able to track the generated reference. Industrial systems often employ rate and output limits that can lead to limit cycles in case of incorrectly tuned loops. Disconnection of turbines from the power plant controller attenuated the oscillations, indicating that this is a contributing mechanism.

It was shown in paper D that both inner and outer loop control parameter bounds depends on the system impedance. Using component parameters from the studied WPP, a root locus plot of the voltage cascade control, Figure D.6, shows the effect of perturbing the PI-controller parameters. Having a low integration parameter or a high proportional parameter result in poorly damped local oscillations. The electrical distance separating the contributing converter systems indicates that while local oscillation is indeed possible for flawed tuning, the nature of the phenomenon points to a centralized control cause.

4.3.2 Proposition 2

The multiple-input single-output system of Figure 4.8 is studied in paper D by simulation. Using the identified envelopes of stability from proposition one, the system is simulated for every parameter pair defined in (D.7). A change in impedance is introduced by varying the cable length. Every simulation is represented by the amplitude weighted dominating oscillation and associated damping, shown in Figures 4.9 and 4.11. The findings show an inter-area network frequency component around 2Hz.

The effect of increasing the electrical distance separating the power plant controller and the local control is observed in Figure 4.11. An increase in cable length, equal to a larger impedance, decreases the possible interval of power plant control integral parameters resulting in well-damped conditions. Having a nominal power plant controller coupled with a short cable, an increase of the local WT integration parameter enhances the oscillation damping. As the cable length is increased, the integration constant must follow proportionally to reduce oscillation and increase damping. It can be seen that at very long cable lengths, the WT integral parameter cannot be increased without causing further oscillatory behavior and decrease the damping. This indicates that the grid code specification cannot be met given a certain

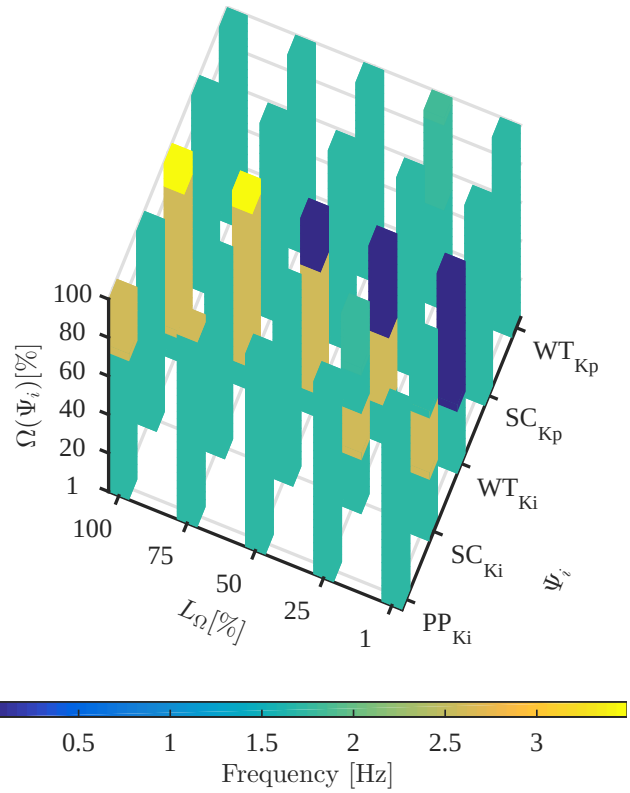

Figure 4.9: Amplitude weighted mode frequency from variation of cable length versus controller parameters.

cable length and control philosophy.

The oscillations were recreated, with better damping, for cable lengths within the defined set using the nominal power plant controller and a flawed WT tuning. Assuming a WT control tuned to grid code compliance, a method to achieve the desired reactive power response at the point of common coupling is a large power plant control integrator gain. As shown in Figure 4.11 the power plant controller response is dependent on the system impedance and thus cable length. Figure 4.10 shows the observed oscillations compared to a simulation of a WPP with very long cables and a power plant control integral gain increased to fulfill the grid code. The oscillations can in fact be caused by the described mechanism and be very poorly damped when having long cables.

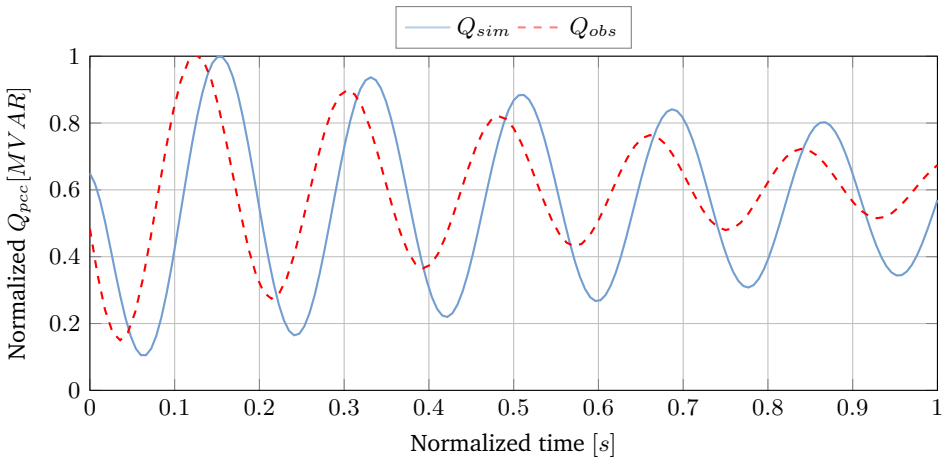

Figure 4.10: Reactive power oscillations at the point of common coupling with a long cable and a large power plant controller integral gain.

4.3.3 Analysis Conclusion

The analysis of the reactive power oscillations at the point of common coupling points to three plausible causes,

1. Flawed WT tuning for long cables (impedance).
2. Adequate WT tuning for long cables (impedance), output and rate limits.
3. Adequate WT tuning for long cables and a flawed power plant controller.

Tests have not been conducted to rule out any combination of the causes. Given that the cause is either 2 or 3, the grid code specification may be difficult to achieve with the applied strategy for voltage control. The studied WPP with modified converter control parameters is on the limit of grid code compliance. The main-result, highlighted in paper D, is that given a stable combination of WT and STATCOM cascade control, the most plausible cause is a too aggressive power plant control setting for the studied system.

4.4 Chapter Conclusion

This chapter has provided an overview of the results obtained in paper C and paper D. First, a current control design method based on internal mode control and fulfillment of both bandwidth and disturbance rejection properties was proposed. Using this as a baseline, the $\mathcal{H}_\infty$ current controller with active filtering properties was introduced. The $\mathcal{H}_\infty$ design proved that disturbance attenuation for specific frequencies can be obtained in uncertain systems such as OWPPs. The current control

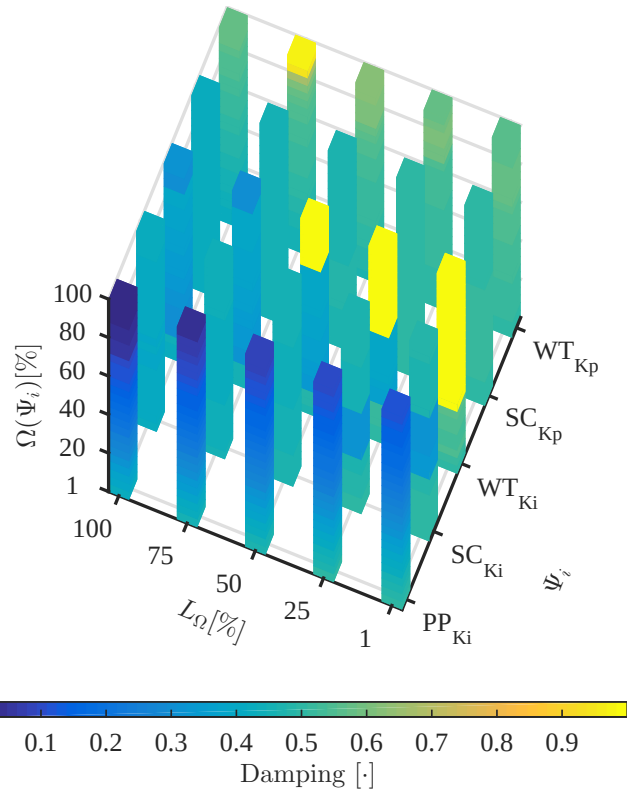

Figure 4.11: Amplitude weighed damping from variation of cable length versus controller parameters.

problem was additionally approached using full state estimation and feedback with added residual control. The approach showed $\mathcal{H}_\infty$ shaping of an outer loop could be used to improve disturbance rejection.

Finally, the voltage control stability envelopes were established analytically using the designed current control and WPP components. The voltage stability envelopes were used to rule out possible contributory causes for the observed reactive power oscillations, and through simulation of the studied WPP, three plausible causes were found.

Chapter 5

Control of Mechanical Systems

The objectives and operating regions of wind turbine control seen from a mechanical point of view are introduced in this chapter. The vibration analysis of chapter 3 unveiled that a plausible cause was inadequate drivetrain damping. The designed controllers should as a consequence achieve low stress of the drivetrain system. A feedback linearization controller is presented which enables the use of standard linear control and analysis methods by cancellation of the system nonlinearities. The controller shows promising results in reducing shaft stress. Furthermore, a backstepping controller is designed for tip speed ratio tracking which does not require extensive system knowledge. The backstepping controller is shown to achieve enhanced drivetrain stress reduction.

5.1 Control Regions

Optimization and limitation of power production are achieved by control of the generator speed, blade angle adjustments and rotating the WT away from the dominant wind direction. The objective of WT control is commonly divided in three operating regions, shown in Figure 5.1. Given a wind speed v_w, the regions are:

1. No load, $v_w \leq v_{min}$.
2. Partial load $v_{min} < v_w \leq v_{max}$.
3. Full load $v_w \geq v_{max}$.

Region one is distinguished by having wind-speeds lower than cut-in, and the system must reduce structural stress by yaw and pitch actuation. The partial load region is defined as the system operating between minimum and rated wind speed and seeks to maximize wind power capture through maintaining optimal tip speed ratio and limit generated noise, stress and vibrations on mechanical and structural components. The full-load region concerns minimizing structural stress and maintaining an optimal tip speed ratio at high wind speeds. Pitch and yaw control is predominantly used

to enable maximum wind power capture in the partial load region, and limit the load in the full-load region. A comprehensive review of control regions is found in [123],[124].

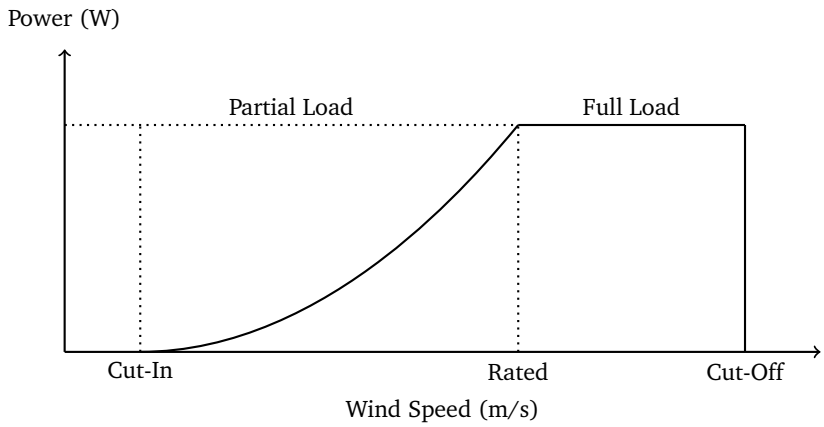

Figure 5.1: Wind turbine operating regions.

5.2 Objectives

The mechanical control presented focus on rotor angular velocity tracking using generator torque in the partial load region. Given a rotor yawed into the dominating wind direction and a pitch of $\beta = 0$, the $C_p(\lambda, \beta)|_{\beta=0}$ curve has a global maximum for some λ_{opt}. Given a reference trajectory ω_r^* and recalling the definition of the tip speed ratio,

$$\lambda = \omega_r R_b v_w^{-1}, \tag{5.1}$$

it shows that for non-constant wind speeds v_w, the tracking error $\omega_r^* - \omega_r$ of the drivetrain is subject to a fluctuating disturbance from the wind. Achieving an optimal tip speed ratio simplifies to keeping the rotor blades spinning at a rotational frequency related to that of the incoming wind.

The control objectives are:

- Minimize rotor angular velocity tracking error, $e_d = \omega_r^* - \omega_r$.
- Reject wind fluctuation disturbance to minimize torsional stress.

The torsional stress is measured as the total change in shaft torsion angle magnitude,

$$S = \int \dot{\theta_k}(t)^2 dt. \tag{5.2}$$

Fulfillment of the control objectives and controller synthesis method depends on available information. Both the wind speed disturbance v_w and non-linear term k_w acting on the nonlinear drive-train model (3.27) is unmatched and cannot be directly canceled by actuator control. The system is transformed into a chain of integrators by a change of variables using feedback linearization. The input-output map of the system with matched disturbances is linearized by applying a state feedback law such that the tracking problem for the nonlinear system is reduced to a tracking problem for a linear controllable and observable system. The input-output feedback linearized tracking control is presented in section 5.3.

The feedback linearization technique requires full knowledge of the nonlinear terms for perfect cancellation. In the case of imperfect information, a control method for the non-linear drivetrain system is needed. Consider the angular velocity of the rotor ω_r the only measurable quantity, then an observer must be designed to estimate the generator angular velocity and the torsion angle. The non-linear term k_ω exist only in the rotor angular velocity dynamics and the needed quantities can thus be estimated by a reduced order linear observer or a copy of the linear dynamics. Recursive backstepping control for the two-mass drivetrain system is presented in section 5.4.

5.3 Feedback Linearization

The baseline controller is implemented as an input-output linearizing controller that cancels the nonlinearities of the system by feedback, assuming perfect knowledge of the dynamics. The concept is shown in Figure 5.2, where the system inner loop linearizes the system and the outer loop is a regular state feedback in ξ variables.

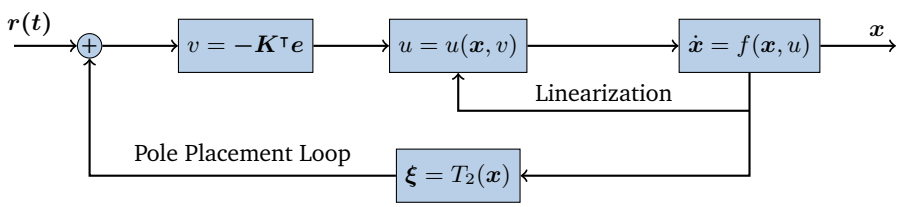

Figure 5.2: Feedback linearization concept

Given a bounded reference trajectory $\boldsymbol{r(t)} \in \boldsymbol{\mathcal{C}^2}$ with bounded derivatives, the error dynamics of (3.52) with state vector $\boldsymbol{\xi} = \begin{bmatrix} \xi_1 & \xi_2 \end{bmatrix}^\intercal$ is,

$$\boldsymbol{R} = \begin{bmatrix} r \\ \dot{r} \end{bmatrix}, \boldsymbol{e} = \begin{bmatrix} \xi_1 - r \\ \xi_2 - \dot{r} \end{bmatrix} = \boldsymbol{\xi} - \boldsymbol{R}. \tag{5.3}$$

Insertion in (3.37) results in,

$$\dot{\eta} = f_0(\eta, \boldsymbol{e} + \boldsymbol{r}), \tag{5.4}$$

$$\dot{\boldsymbol{e}} = A_c\boldsymbol{e} + B_c\{\gamma(x)[u - \alpha(x)] - \dot{r}\}, \tag{5.5}$$

implying that choosing the state feedback control,

$$u = \alpha(x) + \beta(x)[v + \dot{r}], \tag{5.6}$$

where $\beta(x) = 1/\gamma(x)$, reduces the system to a linear cascade system,

$$\dot{\eta} = f_0(\eta, \boldsymbol{e} + \boldsymbol{r}), \tag{5.7}$$
$$\dot{\boldsymbol{e}} = A_c\boldsymbol{e} + B_c v. \tag{5.8}$$

The linear feedback control,

$$v = -\boldsymbol{K}\boldsymbol{e}, \tag{5.9}$$

where $A_c - B_cK$ is Hurwitz, enables arbitrary placement of the poles of the system. Inserting (5.9) in (5.6) results in,

$$u = \alpha(x) + \beta(x)\{-\boldsymbol{K}[T_2(x) - \boldsymbol{R}] + \dot{r}\}, \tag{5.10}$$

where $T_2(\boldsymbol{x})$ is the diffeomorphism that transforms the system into normal form, given in (3.50). The system zero dynamics $\eta(t)$ was shown in (3.44) to be minimum phase, making the origin of $\dot{\eta} = f_0(\eta, 0)$ asymptotically stable.

The state dynamics and output matrix for a chain of integrators (3.55) makes placement of poles trivial. The system poles are placed at,

$$\boldsymbol{P} \triangleq \left[\ -\omega_n\zeta + \omega_n\sqrt{\zeta^2 - 1} \quad -\omega_n\zeta - \omega_n\sqrt{\zeta^2 - 1}\ \right], \tag{5.11}$$

with $\omega_n = 30$ rad/s and $\zeta = \sqrt{2}/2$. Given an optimal power capture tip speed ratio, λ_{opt}, the optimal rotor angular velocity, $\omega_d = \lambda_{opt}v_w/R_b$, provides the bounded reference trajectory $\boldsymbol{r(t)}$. Tracking is tested in a stochastic environment with wind simulated using the wind model with a mean wind of 10.33m/s and 12% turbulence shown in Figure 5.3 and Figure 5.4. The figures highlight the efficiency of linearizaition feedback control in case of known nonlinearities as the system tracks the reference trajectory smoothly with $||e_\omega||_\infty = 356\mu rad/s$ and $S = 23.5mrad^2/s$.

5.4 Recursive Backstepping Control

Backstepping control considers stabilization of the origin of systems in strict feedback form,

$$\begin{aligned} \dot{\boldsymbol{z}} &= \boldsymbol{f(z)} + \boldsymbol{g(z)}\boldsymbol{\xi}, \\ \dot{\boldsymbol{\xi}} &= \boldsymbol{u}. \end{aligned} \tag{5.12}$$

The entire system in strict feedback form is stabilized by recursive application of the backstepping approach using the dependable state as virtual input,

$$\begin{aligned} \dot{x} &= f_0(x) + g_0(x)z_1, \\ \dot{z_1} &= f_1(x, z_1) + g_1(x, z_1)z_2, \\ \dot{z_k} &= f_k(x, z_1, \ldots, z_k) + g(x, z_1, \ldots, x_k)u, \end{aligned} \tag{5.13}$$

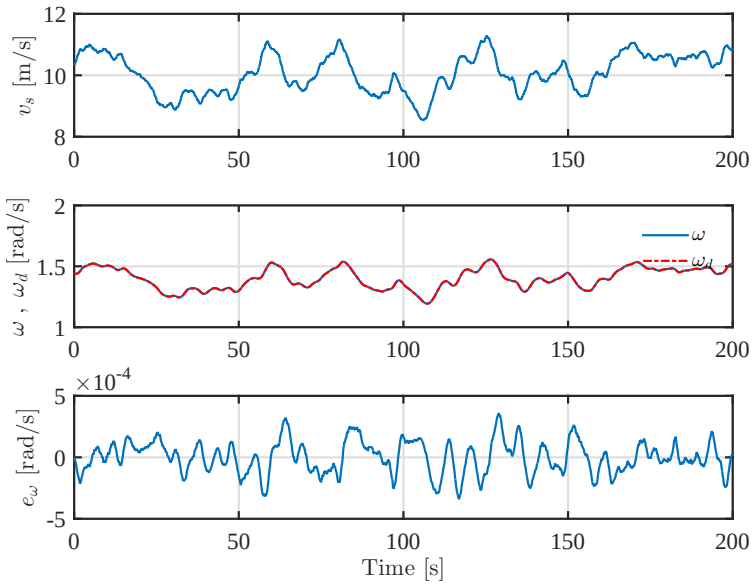

Figure 5.3: Feedback Linearization Control: Tip speed ratio tracking in stochastic environment - 1. Wind speed, 2. Desired and real rotor speed, 3. Tracking error.

where z_1 through z_{k-1} are the inputs to the previous states. Suppose that the simplest scalar system of type (5.12) can be stabilized by the control law,

$$\xi = \phi(z), \phi(0) = 0, \tag{5.14}$$

and a positive definite Lyapunov function $V_1(z)$ with negative definite derivative smaller than some positive definite function $W(z)$ with respect to z exist, the change of variables $y = \xi + \phi(z)$ results in,

$$\begin{aligned} \dot{z} &= [f(z) + g(z)\phi(z)] + g(z)y, \\ \dot{y} &= u - \dot{\phi(z)}. \end{aligned} \tag{5.15}$$

The functions f, g and ϕ are known and letting $v = u - \dot{\phi}$ obtains,

$$\dot{z} = [f(z) + g(z)\phi(z)] + g(z)y, \tag{5.16}$$

$$\dot{y} = v, \tag{5.17}$$

which is similar to the initial system, but with guaranteed asymptotic stability. The stability of the entire system is guaranteed by considering a candidate Lyapunov function ,

$$V_2(z, \xi) = V_1(z) + (1/2)y^2, \tag{5.18}$$

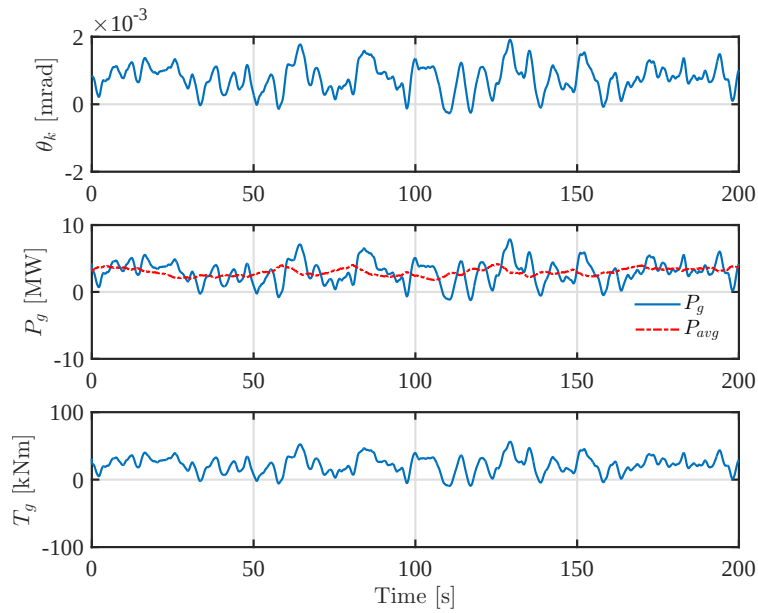

Figure 5.4: Feedback Linearization Control: Tip speed ratio tracking in stochastic environment - 1. Torsion angle, 2. Power generated, 3. Generator torque.

with derivative,

$$\dot{V_2}(z,\xi) \leq -W(z) + \frac{\partial V_1(z)}{\partial z} g(z) y + yv. \tag{5.19}$$

Choosing the internal output as,

$$v = \frac{\partial V_1(z)}{\partial z} g(z) - ky, \tag{5.20}$$

makes $\dot{V_2}(z,\xi)$ negative definite. Given the state vector,

$$\boldsymbol{x} = \begin{bmatrix} \theta_k & \omega & \omega_g \end{bmatrix}^\intercal, \tag{5.21}$$

for (3.27) where ω and ω_g are the angular velocity of the rotor and the generator respectively, and θ_k is the torsion angle. The system is rewritten in terms of the tracking error $e_\omega \triangleq \omega - \omega_d$, where $\omega_d(t) \in \mathcal{C}^2$ is the bounded reference trajectory with bounded derivatives. The outputs θ_k and ω_g are substituted by the linear observer estimates, $\hat{\theta_k}$ and $\hat{\omega_g}$ as,

$$\dot{e}_\omega = \frac{1}{J_r} \Bigg[- K_d \left(\hat{\theta}_k + \tilde{\theta}_k \right) + k_w \left(e_\omega + \omega_d \right)^2$$

$$- \left(B_d + B_r\right)\left(e_\omega + \omega_d\right) + \frac{B_d}{N_g}\left(\hat{\omega}_g + \tilde{\omega}_g\right)\Bigg] - \dot{\omega}_d \tag{5.22}$$

$$\dot{\hat{\omega}}_g = \frac{1}{J_g}\left[\frac{K_d}{N_g}\hat{\theta}_k + \frac{B_d}{N_g}\left(e_\omega + \omega_d\right) - \left(\frac{B_d}{N_g^2} + B_g\right)\hat{\omega}_g - T_g\right], \tag{5.23}$$

with the β functions and system parameters are defined in paper B. The observer dynamics are proven exponential stable, and an output feedback controller based on the observer backstepping control approach is designed for (5.23). The system (5.22)-(5.23) is proven globally asymptotically stable with the output feedback backstepping control law $T_g(\hat{\theta}_k, e_\omega, z, \boldsymbol{\Omega_d})$ and the reference vector $\boldsymbol{\Omega}_d = [\omega_d(t), \dot{\omega}_d(t), \ddot{\omega}_d(t)]^{\mathrm{T}}$ as,

$$\begin{aligned}
T_g\left(\hat{\theta}_k, e_\omega, z, \boldsymbol{\Omega}\right) \triangleq\ & J_g\left(\frac{K_d}{J_g N_g} - \frac{N_g K_d\left(\frac{B_d^3}{N_g^3}\beta_1 + K_d^2\beta_2\right)}{J_r B_d} - \frac{2k_w N_g K_d}{J_r B_d}\left(e_\omega + \omega_d\right)\right)\hat{\theta}_k \\
& + J_g\left(\frac{B_d}{J_g N_g} - \frac{N_g K_d}{B_d} - \frac{N_g\left(\frac{B_d^3}{N_g^3}\beta_1 + K_d^2\beta_2\right)\left(B_d + B_r\right)}{J_r B_d}\right)\left(e_\omega + \omega_d\right) \\
& + J_g\left(\frac{K_d}{B_d} + \frac{2k_w}{J_r}\left(e_\omega + \omega_d\right)\frac{\left(\frac{B_d^3}{N_g^3}\beta_1 + K_d^2\beta_2\right)}{J_r}\right) z + J_g\left(\beta_3 + \beta_4\right)\left(1 + \left(e_\omega + \omega_d\right)^2\right) z \\
& + J_g\left(\frac{K_d}{B_d} - \frac{1}{J_g}\left(\frac{B_d}{N_g^2} + B_g\right) + \frac{\left(\frac{B_d^3}{N_g^3}\beta_1 + K_d^2\beta_2\right)}{J_r} + \frac{2k_w}{J_r}\left(e_\omega + \omega_d\right)\right)\alpha\left(\hat{\theta}_k, e_\omega, \boldsymbol{\Omega}_d\right) \\
& + J_g\left(\frac{2k_w^2 N_g}{J_r B_d}\left(e_\omega + \omega_d\right)^3 - \frac{k_w N_g}{J_r B_d}\left(2\left(B_d + B_r\right) - \left(\frac{B_d^3}{N_g^3}\beta_1 + K_d^2\beta_2\right)\right)\left(e_\omega + \omega_d\right)^2\right) \\
& + J_g\left(-\frac{N_g}{B_d}\left(\frac{B_d^3}{N_g^3}\beta_1 + K_d^2\beta_2 + B_d + B_r\right)\dot{\omega}_d + \frac{N_g J_r}{B_d}\ddot{\omega}_d\right) z
\end{aligned} \tag{5.24}$$

$$\begin{aligned}
\alpha(\hat{\theta}_k, e_\omega, \boldsymbol{\Omega}_d) \triangleq\ & \frac{N_g}{B_d}(-k_w(e_\omega + \omega_d)^2 + (B_d + B_r)\omega_d + K_d\hat{\theta}_k \\
& + J_r\dot{\omega}_d - (\frac{B_d^3}{N_g^3}\beta_1 + K_d^2\beta_2)e_\omega)
\end{aligned} \tag{5.25}$$

The torsional angle $\theta_k(t)$ is shown to be globally uniformly ultimately bounded using the upper bounds,

$$\left|e_\omega\left(t\right)\right| \leq \gamma\left(\left|e_\omega\left(t_0\right)\right|, t - t_0\right), \quad \forall t \geq t_0 \tag{5.26}$$

where $\gamma\left(r, s\right)$ is a class $\mathcal{KL}$ function and

$$\left|\tilde{\theta}_k\left(t\right)\right| \leq k_e\left|\tilde{\theta}_k\left(t_0\right)\right| e^{\lambda_{\max}(\mathbf{A})(t - t_0)}, \quad \forall t \geq t_0, \tag{5.27}$$

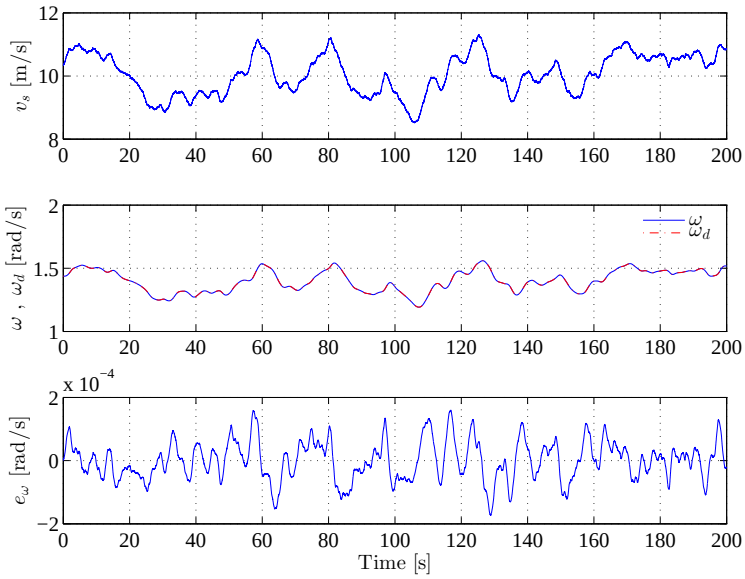

Figure 5.5: Optimal tip speed ratio tracking in stochastic environment - 1. Wind speed, 2. Desired and real rotor speed, 3. Tracking error.

where $\boldsymbol{A}$ is the observer system matrix. The state estimation errors are considered disturbances who must be dominated by the control input. The system tracking is tested in a stochastic environment with wind simulated using the wind model, with a mean wind of 10.33m/s and 12% turbulence shown in Figure 5.5 and Figure 5.6. The simulation shows that the system with control law (5.24) tracks the tip speed ratio reference smoothly with $||e_\omega||_\infty = 324\mu rad/s$, while the torsion angle remains bounded. Evaluation of (5.2) results in a total stress level of $S = 2.08mrad^2/s$.

The novel backstepping control design of a WT two-mass drivetrain system for tip speed ratio tracking subject to wind disturbances creates a baseline non-linear controller for further development in the field of drivetrain stress reduction. An extension to the work was presented at the American Control Conference 2015 [3], including adaptive backstepping control of both electric and tower components.

5.5 Chapter Conclusion

This chapter presented feedback linearization and backstepping as applicable control methods of a two-mass drivetrain. Both methods achieved to keep the torsional oscillation magnitude low. Fulfilment of tracking and shaft stress reduction using full information linear control and non-linear backstepping control was shown to be achievable. The feedback linearization approach is naïve as it relies on an

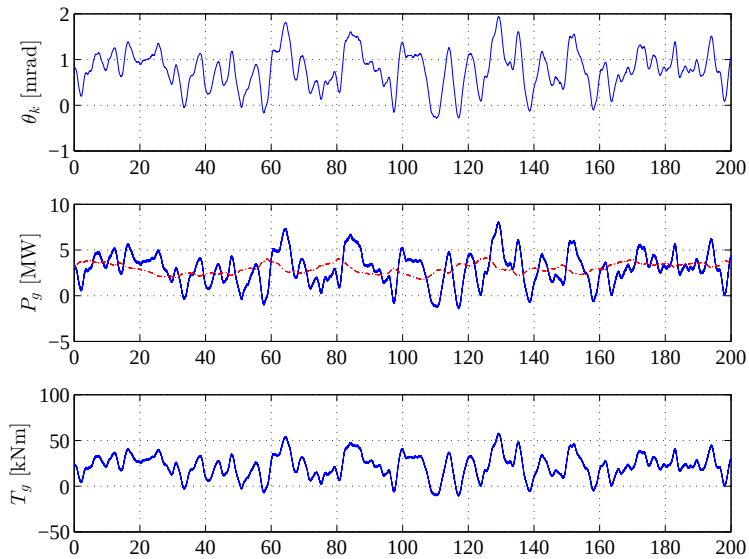

Figure 5.6: Optimal tip speed ratio tracking in stochastic environment - 1. Torsion angle, 2. Power generated, 3. Generator torque.

unrealistic amount of information, while the backstepping approach achieves similar tip speed ratio tracking performance and lower torsional stress with less information. Mechanical disturbances induced by the electrical network are minimized for fast mechanical control, and the designed controllers can help to counteract the vibration issue.

Chapter 6

Conclusion and Perspectives

6.1 Conclusion

In this thesis, control and assessment methods for both entire wind power plants and selected sub-components have been studied. Through a scenario driven approach, the project has spawned several new results, and all results of general nature have been published. The focus has throughout the project been two-fold, equally shared between developing advanced control and defining guidelines for ensuring compliance and functionality in all operational scenarios. The operational scenarios defined through variation in system topology and component values were analyzed with respect to the effect on fixed structure controller parameters. Mathematical electromagnetic transient models of the studied wind power plant including the mechanical and electrical wind turbine dynamics have been developed to provide a baseline for analysis and controller development. The generic structure of the models and associated converter filters ensures that the results can be reused for other output stages.

Two fault scenarios were analyzed to determine plausible root causes. In all cases, the objective has been to identify the issue, the contributory phenomena and if possible establish guidelines to avoid the problem in future wind power plants. The systems investigated in this thesis were all of closed nature and controllers had to be developed to clarify possible interaction mechanisms and the parameter ranges for which undesired interaction could take place.

Initially the project had focus on identification of plausible rotor blade vibration and deformation causes. The cause of the vibration was not known but thought to originate from the electrical subsystem. One of the minor contributions of this research was an analysis of the effects transient disturbances from the network and periodic disturbances in the generator have on the mechanical structure. Periodic generator disturbances such as cogging torque and non-constant magnet flux were shown to have a negligible effect. The network disturbances were analyzed with

respect to voltage dips and the full-converter response, showing that even for large transients the mechanical system appeared to be safe. Finally, a system of two connected wind turbines was investigated numerically for potential controller interaction in the low frequency range; this was shown to be unlikely. That left the black-box mechanical system as the culprit. A baseline feedback linearization controller was developed, and in paper B the developed models were used to design an observer based backstepping controller, able to operate with low drivetrain stress. The research disproved all given causes, which leads to the conclusion that the vibrations could be caused be inadequate drivetrain damping control.

A previous study by DONG showed that harmonics in isolated wind power plant networks could cause a system wide shut down. A scheme for using $\mathcal{H}_\infty$ control to shape the frequency response of the wind turbine current controllers has been suggested in paper C. This scheme utilizes that $\mathcal{H}_\infty$ control is designed through loop shaping and can thus be shaped to mimic an active filter. The active filter properties can easily be adjusted to compensate for harmonics within the controller bandwidth and complement existing filters. The combination of uncertain component values and $\mathcal{H}_\infty$ robust control was proved to guarantee the desired performance and filtering within the set of possible systems. The approach was further extended to include residual based $\mathcal{H}_\infty$ control for systems utilizing state estimation. The scheme of having an inner current controller and a residual based controller for disturbance rejection optimization was shown to be successful.

Reactive power oscillations observed in a wind power plant were also scrutinized. When operating multiple power electronic devices in a distributed network, undesired controller interaction effects were suspected. The detection of reactive power oscillations at the point of common coupling required a course of action due to losses. By identification of the used wind power plant voltage control scheme, an overall model was formed and the implicated controllers were dimensioned based on IEC standards and internal knowledge. An analytical voltage source converter based current control parameter selection method was proposed based on specifications and component values. The local voltage control was investigated in detail and an analytical expression was found for the envelope of operation using the Stabilizing Sets method [60] that was extended to fit the purpose. The power plant controller tuning was linked to the local voltage control and system topology. The studied wind power plant was simulated and three plausible causes were identified while providing a novel way to represent the results and visualizing the effect of controller interaction. The analysis was presented in paper D.

6.2 Perspectives

Wind power is only going to increase its share of the total energy market. Even though the wind power industry is approaching maturity, the engineers of DONG Energy continuously observes and solves new problems. While academia has focus

on development of advanced control methods, the industry is looking for methods to ensure production and lower risk. This project has by its analysis pointed out multiple key areas that should be checked for every turbine and wind power plant. Commissioning algorithms to serve as controller checklists such as in paper D, could be developed for all systems given the needed topological information. Furthermore, the analytical methods of establishing operational envelopes could be expanded to include more systems to lower the risk of failure.

A continuation of this project is testing and application of the developed controllers and stability evaluation methods in a real wind power plant or a real time simulation. The real life testing will show how the nonlinearities and unmodelled dynamics affect the designed methods. Additional to the implementation of robust control, application of fault identification methods is seen as the next step in wind turbine risk management.

Bibliography

[1] N. Nixon. *Timeline: The history of wind power*. English. Newspaper. Oct. 2008. URL: http://www.theguardian.com/environment/2008/oct/17/wind-power-renewable-energy.

[2] E. Comission. *Renewable energy: Moving towards a low carbon economy*. English. European Union. July 2015. URL: https://ec.europa.eu/energy/en/topics/renewable-energy.

[3] R. Galeazzi, K. T. Borup, H. Niemann, N. K. Poulsen, and F. Caponetti. "Adaptive Backstepping Control of Lightweight Tower Wind Turbine". English. *Proceedings of 2015 American Control Conference* (2015), pp. 3058–3065.

[4] Siemens. *Siemens SWT-2.3-93 Product Brochure*. Siemens. July 2015.

[5] T. Burton, D. Sharpe, N. Jenkins, and E. Bossanyi. *Wind Energy Handbook*. Springer New York, 2001.

[6] J. G. Slootweg. "Wind Power: Modelling and Impact on Power System Dynamics". PhD thesis. Technische Universiteit Delft, 2003.

[7] EWEA. *Wind Energy Factsheet*. English. EWEA. July 2015. URL: http://www.ewea.org/uploads/pics/EWEA_Wind_energy_factsheet.png.

[8] G. Guidi and O. B. Fosso. "Investment Cost of HVAC Cable Reactive Power Compensation off-Shore". *IEEE International Energy Conference and Exhibition, Energycon 2012* (2012), pp. 299–304.

[9] O. Vestergaard, B. Westman, G. McKay, P. Jones, J. Fitzgerald, and B. Williams. "HVDC - Enabling the transition to an energy system based on renewables". eng. *IET Conference Publications* 2010.570 (2010), pp. 1–6.

[10] S. Chuangpishet and A. Tabesh. "Matrix interconnected topology for dc collector systems of offshore wind farms". *IET Conference Publications* 2011.579 (2011), P37.

[11] T. Probert. "A DC breaker breakthrough". English. *Materials World* 21.9 (2013), pp. 24–27.

[12] Y. Morishita, T. Koyama, S. Yanabu, I. Yamaguchi, S. Okabe, and G. Ueta. "Development of DC-current-limiting circuit-breaker with superconducting fault current limiter". *17th International Conference on Gas Discharges and Their Applications* (2008), pp. 97–100.

[13] L. Tang and B.-T. Ooi. “Locating and isolating DC faults in multi-terminal DC systems”. English. *IEEE Transactions on Power Delivery* 22.3 (2007), pp. 1877–1884.

[14] R. T. Pinto, S. Rodrigues, P. Bauer, and J. Pierik. “Operation and control of a Multi-terminal DC Network”. English. *IEEE ECCE Asia Downunder* (2013), pp. 474–480.

[15] J. B. Glasdam. “Harmonics in Offshore Wind Power Plants Employing Power Electronic Devices in the Transmission System”. eng. PhD thesis. Aalborg University, 2015.

[16] L. H. Kocewiak. “Harmonics in large offshore wind farms”. eng. PhD thesis. Department of Energy Technology, Aalborg University, 2012.

[17] G. Styrbro, B. Agerholm, T. Toivonen, O. Hoelsæter, J. Magnusson, and Nordel. *Nordic grid code 2004*. Electronic, 2004, 177 s.

[18] J. Aho, A. Buckspan, J. Laks, F. Dunne, L. Pao, P. Fleming, M. Churchfield, Y. Jeong, and K. Johnson. “A tutorial of wind turbine control for supporting grid frequency through active power control”. *Proceedings of the American Control Conference* (2012), pp. 3120–3131.

[19] T. Knudsen, T. Bak, and M. Svenstrup. “Survey of wind farm control-power and fatigue optimization”. *Wind Energy* (2014), n/a.

[20] L. Vermeer, J. Sorensen, and A. Crespo. “Wind turbine wake aerodynamics”. English. *Progress in Aerospace Sciences* 39.6-7 (2003), pp. 467–510.

[21] F. Massouh and I. Dobrev. “Exploration of the vortex wake behind of wind turbine rotor”. English. *Science of Making Torque from Wind* 75.1 (2007).

[22] A. G. Abo-Khalil. *Modeling and Control Aspects of Wind Power Systems*. 2013.

[23] X. Juankorena, I. Esandi, J. Lopez, and L. Marroyo. “Method to enable variable speed wind turbine primary regulation”. English. *Proceedings of the 2nd International Conference on Power Engineering, Energy and Electrical Drives* (2009), pp. 495–500.

[24] T. Ackermann. *Wind Power in power systems*. English. John Wiley, 2011, lxiii, 1049 s.

[25] Y. Mu, Z. Lu, Y. Qiao, and K. L. Lo. “Optimized active power control of DFIG wind farm”. eng. *Proceedings of the Universities Power Engineering Conference* (2012), p. 6398552.

[26] B. Bjarnason and Ö. Sveinsson. “Wind farm concontrol - optimzation of power production”. MA thesis. Technical University of Denmark, 2010.

[27] P. Kundur. *Power System Stability and Control*. Ed. by N. J. Balu. McGaw-Hill Inc., 1993.

[28] M. Aman, G. Jasmon, and A. Bakar. “Optimum shunt capacitor placement in distribution system—A review and comparative study.” *Renewable and Sustainable Energy Reviews* 30 (2014), p. 429.

[29] V. Calderaro, V. Galdi, A. Piccolo, G. Conio, and R. Fusco. “Wind farm power plant: Optimal capacitor placement for reactive power compensation”. eng. *IEEE Innovative Smart Grid Technologies Europe* (2013), p. 6695308.

[30] S. Santoso and M. Singh. *Dynamic Models for Wind Turbines and Wind Power Plants*. NREL/SR-5500-52780. The University of Texas at Austin, 2008-2011.

[31] J. D. Glover, M. S. Sarma, and T. J. Overbye. *Power System Analysis and Design*. Ed. by S. Meherishi. Global Engineering, 2008.

[32] A. Perdana. “Dynamic Models of Wind Turbines, A Contribution towards the Establishment of Standardized, Models of Wind Turbines for Power System Stability Studies”. PhD thesis. Chalmers University of Technology, 2008.

[33] J. Jonkman. *FAST - An aeroelastic computer-aided engineering (CAE) tool for horizontal axis wind turbines*. English. National Renewable Energy Laborator. Nov. 2015. URL: `https://nwtc.nrel.gov/FAST`.

[34] F. Iov, A. D. Hansen, P. Soerensen, and F. Blaabjerg. *Wind Turbine Blockset in Matlab/Simulink. General Overview and Description of the Model*. eng. Institut for Energiteknik, Aalborg Universitet, 2004.

[35] E. Clarke. *Circuit Analysis of A-C Power Systems*. Ed. by E. Clarke. Seventh Printing, 1961.

[36] J. Pierik, J. Morren, E. Wiggelinkhuizen, S. de Haan, T. van Engelen, and J. Bozelie. *Electrical and Control Aspects of Offshore Wind Farms II (Erao II), Volume 1: Dynamic Models of Wind Farms*. Tech. rep. Delft University of Technology, ECN, 2004.

[37] F. Blaabjerg, Z. Chen, R. Teodorescu, and F. Iov. “Power Electronics in Wind Turbine Systems”. *5th International Power Electronics and Motion Control Conferenc* 1 (2006), pp. 1–11.

[38] F. Blaabjerg, M. Liserre, and K. Ma. “Power Electronics Convertrs for Wind Turbine Systems”. eng. *IEEE Energy Conversion Congress and Exposition: Energy Conversion Innovation for a Clean Energy Future* (2011), pp. 6063781, 281–290.

[39] Y. Xia, K. H. Ahmed, and B. W. Williams. “Different torque ripple reduction methods for wind energy conversion systems using diode rectifier and boost converter”. eng. *Proceedings of the IEEE International Electric Machines and Drives Conference* (2011), pp. 5994902, 729–734.

[40] R. Teichmann and S. Bernet. “A comparison of three-level converters versus two-level converters for low-voltage drives, traction, and utility applications”. und. *IEEE Transactions on Industry Applications* 40.6 (2004), pp. 855–865.

[41] L. Pham. “A Review of Full Scale Converter for Wind Turbines”.

[42] S. Chakraborty, M. G. Simões, and W. E. Kramer. “Power Electronics for Renewable and Distributed Energy Systems: A Sourcebook of Topologies, Control and Integration”. eng. *Green Energy and Technology* 59 (2013), pp. 111–149.

[43] M. Liserre, F. Blaabjerg, and S. Hansen. “Design and control of an LCL-filter based three-phase active rectifier”. English. *IEEE Industry Applications Society* 1 (2001), pp. 299–307.

[44] J. Lettl, J. Bauer, and L. Linhart. “Comparison of Different Filter Types for Grid Connected Inverter”. *Proc. PIERS, Marrakesh* (2011).

[45] V. Blasko and V. Kaura. “A novel control to actively damp resonance in input LC filter of a three-phase voltage source converter”. *IEEE Transactions on Industrial Applications* 33 (1997), pp. 542–550.

[46] Y. A.-R. I. Mohamed, M.A.-Rahman, and R. Seethapathy. “Robust Line-Voltage Sensorless Control and Synchronization of LCL-Filtered Distributed Generation Inverters for High Power Quality Grid Connection”. *IEEE Transactions on Power Electronics* 27 (2012).

[47] N. G. Hingorani and L. Gyugyi. *Understanding FACTS : concepts and technology of flexible AC transmission systems*. English. Institute of Electrical and Electronics Engineers, 2000, XIX, 432 p.

[48] A. E. Leon and J. A. Solsona. “Performance Improvement of Full-Converter Wind Turbines Under Distorted Conditions”. *IEEE Transactions on Sustainable Energy* 4 (2013), pp. 652–660.

[49] L. H. Kocewiak, J. Hjerrild, and C. L. Bak. “Wind turbine converter control interaction with complex wind farm systems”. und. *American Institute of Physics Conference Proceedings* 1606.4 (2014), pp. 380–389.

[50] S. Skogestad and I. Posletwaite. *Multivariable Feedback Control: Analysis and Design, Second Edition*. John Wiley & Sons, Ltd., 2009.

[51] M. P. (Kazmierkowski, R. (Krishnan, and F. Blaabjerg. *Control in Power Electronics: Selected Problems*. eng. Academic Press, Incorporated, 2002.

[52] M. P. Kazmierkowski and L. Malesani. “Current control techniques for three-phase voltage-source pwm converters: A survey”. eng. *IEEE Transactions on Industrial Electronics* 45.5 (1998), pp. 691–703.

[53] M. G. Molina and P. E. Mercado. *Modelling and Control Design of Pitch-Controlled Variable Speed Wind Turbines*. Tech. rep. CONICET, Instituto de Energia Electrica, Universidad Nacional de San Juan, 2010.

[54] S. Li, T. Haskew, E. Muljadi, and C. Serrentino. “Characteristic Study of Vector-Controlled Direct-Driven Permanent Magnet Synchronous Generator In Wind Power Generation”. *Electric Power Components and Systems* 37, no. 10 (2009), pp. 1162–1179.

[55] A. Opritescu. “Control of a saturated Permanent Magnet Synchronus Motor”. MA thesis. Department of Energy Tehnology Aalborg University, Denmark, 2010.

[56] P. C. Perera. “Sensorless Control Of Permanent-Magnet Synchronous Motor Driv”. PhD thesis. Institute of Energy Technology, Aalborg University, 2002.

[57] D. Holmes and T. A. Lipo. *Pulse Width Modulation for Power Converters: Principles and Practice*. IEEE Press, 2003.

[58] S. Bhattacharya and P.-T. Cheng. "Hybrid solutions for improving passive filter performance..." *IEEE Transactions on Industry Applications* 33.3 (1997), p. 732.

[59] D. McFarlane and K. Glover. *Robust Controller Design Using Normalized Coprime Factor Plant Descriptions*. Springer-Verlag, 1990, 216 s.

[60] R. Vilanova and A. Visioli. *PID control in the third millennium : lessons learned and new approaches*. English. Springer, 2012, 1 online resource (xiv, 599 p.)

[61] T.-T. Tay. *High Performance Control*. Birkhäuser Boston, 1998, 344 s.

[62] K. Zhou, J. Doyle, and K. Glover. *Robust and optimal control*. Prentice Hall, 1996, 596 s.

[63] C. Battistelli and M. Uccelletti. "Assessing wind power and electrical power systems interconnection: A methodological approach". *IEEE PES Trondheim PowerTech: the Power of Technology for a Sustainable Society* (2011), p. 6019202.

[64] D. Villanueva, J. Luis Pazos, and A. Feijoo. "Probabilistic Load Flow Including Wind Power Generation". und. *IEEE Transactions on Power Systems* 26.3 (2011), pp. 1659–1667.

[65] B. Zaker and M. Mohammadi. "Probabilistic optimal operation of a smart grid including wind power generator units". *2nd Iranian Conference on Smart Grids* (2012), pp. 1–5.

[66] R. Teodorescu, M. Liserre, and P. Rodriguez. *Grid Converters for Photovoltaic and Wind Power Systems*. eng. Wiley-IEEE press, 2011.

[67] L. Empringham, J. W. Kolar, J. Rodriguez, P. W. Wheeler, and J. C. Clare. "Technological Issues and Industrial Application of Matrix Converters: A Review". und. *IEEE Transactions on Industrial Electronics* 60.10 (2013), pp. 4260–4271.

[68] E. N. Abildgaard and M. Molinas. "Modelling and Control of the Modular Multilevel Converter (MMC)". und. *Energy Procedia, Enrgy Proc, Enrgy Proced, Enrgy Procedia* 20 (2012), pp. 227–236.

[69] M. Lindgren. "Modeling and Control of Voltage Source Converters Connected to the Grid". PhD thesis. Chalmers University of Technology, 1998.

[70] K. V. Kumar, P. A. Michael, J. P. John, and S. S. Kumar. "Comparative analysis of SPWM and SVPWM control for three phase inverter". *Journal of Engineering and Applied Sciences* 5.7 (2010), p. 61.

[71] Z. Chen, J. M. Guerrero, and F. Blaabjerg. "A Review of the State of the Art of Power Electronics for Wind Turbines". und. *IEEE Transactions on Power Electronics* 24.8 (2009), pp. 1859–1875.

[72] J. Svensson and M. Lindgren. "Influence of non-linearities on the frequency response of a grid-connected vector-controlled VSC". eng. PhD thesis. 1998.

[73] B. Bahrani. “Advanced Control Strategies for Voltage Source Converters in Microgrids and Traction Networks”. PhD thesis. ÉCOLE POLYTECHNIQUE FÉDÉRALE DE LAUSANNE, 2012.

[74] Y. Ye, K. Zhou, B. Zhang, D. Wang, and J. Wang. “High-Performance Repetitive Control of PWM DC-AC Converters With Real-Time Phase-Lead FIR Filter”. *IEEE Transactions on Circuits and Systems II: Express Briefs* 53.8 (2006), pp. 768–772.

[75] C. S. Lim, E. Levi, M. Jones, N. A. Rahim, and W. P. Hew. “A comparative study of synchronous current control schemes based on FCS-MPC and PI-PWM for a two-motor three-phase drive”. eng. *IEEE Transactions on Industrial Electronics* 61.8 (2014), pp. 6642107, 3867–3878.

[76] A. Fereidouni, M. A. S. Masoum, T. H. Mehr, and M. Moghbel. “Improving performance of shunt active power filter with hysteresis-based direct current control using particle swarm optimisation”. English. *Australian Journal of Electrical and Electronics Engineering* 11.4 (2014), pp. 357–365.

[77] Y. H. Liu, N. R. Watson, K. L. Zhou, and B. F. Yang. “Converter System Nonlinear Modeling and Control for Transmission Applications-Part I: VSC System”. und. *IEEE Transactions on Power Delivery* 28.3 (2013), pp. 1381–1390.

[78] J. Rodriguez, J. Pontt, C. A. Silva, P. Correa, P. Lezana, P. Cortes, and U. Ammann. “Predictive current control of a voltage source inverter”. und. *IEEE Transactions on Industrial Electronics* 54.1 (2007), pp. 495–503.

[79] S. Jena, B. C. Babu, and L. Sahu. “Experimental study on adaptive hysteresis current controller for inverter-interfaced 1-theta grid connected system”. *Ind. Appl., (INDICON)* (2011), pp. 1–6.

[80] M. O. K. Niss, T. Esbensen, C. Sloth, J. Stoustrup, and P. F. Odgaard. “A Youla-Kucera approach to Gain-Scheduling with Application to Wind Turbine Control”. eng. *IEEE Conference on Control Applications. 2009* (2009), pp. 1489–1494.

[81] W. Gong, S. Hu, M. Shan, and H. Xu. “Robust current control design of a three phase voltage source converter”. English. *Journal of Modern Power Systems and Clean Energy* 2.1 (2014), pp. 16–22.

[82] J. Perez, S. Cobreces, F. Javier Rodriguez Sanchez, and R. Grino. “Hinf simultaneous admittance and tracking current controller of three-phase active grid front-ends”. English. *IEEE International Conference on Industrial Technology* (2015), pp. 2092–2097.

[83] P. Dash and N. Nayak. “Nonlinear control of voltage source converters in AC–DC power system”. *ISA Transactions* 53.4 (2014), pp. 1268–1285.

[84] R. Teodorescu, F. Blaabjerg, M. Liserre, and P. C. Loh. “Proportional-resonant controllers and filters for grid-connected voltage-source converters”. und. *Iee Proceedings - Electric Power Applications* 153.5 (2006), pp. 750–762.

[85] Z. Zou, W. Zheng, and M. Cheng. “Modeling, Analysis, and Design of Multi-function Grid-Interfaced Inverters With Output LCL Filter”. *IEEE Transactions on Power Electronics* 29 (2014), pp. 3830–3839.

[86] S. Corsi. *Voltage control and protection in electrical power systems : from system components to wide-area control*. English. 2015, 1 online resource.

[87] P. E. Sørensen, A. D. Hansen, F. Iov, F. Blaabjerg, and M. Donovan. *Wind farm models and control strategies*. eng. Tech. rep. RISØ, 2005.

[88] M. El Moursi and G. Joos. “Optimal tracking secondary voltage control for the DFIG wind turbines and compensator devices”. und. *Electric Power Systems Research, Electr. Power Syst. Res, Elec Pow Sy, Electr Pow Syst Res, Elec Power Syst Res, Electr Power Syst Res* 79.12 (2009), pp. 1705–1716.

[89] L. Wang and D. Truong. “Stability Enhancement of a Power System With a PMSG-Based and a DFIG-Based Offshore Wind Farm Using a SVC With an Adaptive-Network-Based Fuzzy Inference System”. und. *IEEE Transactions on Industrial Electronics* 60.7 (2013), pp. 2799–2807.

[90] Z. Chen, Z. Hao, and S. Qin. “Centralized reactive power control for a wind farm under impact of communication delay”. eng. *International Journal of Control and Automation, Int. J. Control Autom* 7.2 (2014), pp. 85–98.

[91] T. J. T. Hashim, A. Mohamed, and H. Shareef. “A review on voltage control methods for active distribution networks”. und. *Przeglad Elektrotechniczny, Przegląd Elektrotechniczny, Prz. Elektrotechniczny, Prz Elektro, Prz Elektrotechniczn, Prz Elektrotechniczny* 88.5B (2012), pp. 304–312.

[92] E. Muljadi and Y. C. Zhang. “Wind Power Plant Voltage Stability Evaluation”. *International Conference on Wind Energy Grid-Adaptive Technologies* (2014).

[93] L.-J. Cai and I. Erlich. “Power system static voltage stability analysis considering all active and reactive power controls - Singular value approach”. und. *IEEE Lausanne Powertech* 1-5 (2007), pp. 367–373.

[94] A. M. Atallah and M. A. Bayoumii. “Comparison between Wind Farm Aggregation Techniques to Analyze Power System Dynamics”. und. *International Journal of Computer Applications* 88.15 (2014), pp. 1–7.

[95] D. Yang, L. Ban, Z. Xiang, N. Du, B. Zheng, and Z. Wu. “An aggregation method of wind farm model for electromagnetic transient simulation analysis”. *IEEE Transaction on Power Electronics and Machines in Wind Applications* (2012), pp. 1–5.

[96] V. Jalili-Marandi, L.-F. Pak, and V. Dinavahi. “Real-Time Simulation of Grid-Connected Wind Farms Using Physical Aggregation”. und. *IEEE Transactions on Industrial Electronics* 57.9 (2010), pp. 3010–3021.

[97] L. Y. Pao and K. E. Johnson. “A tutorial on the dynamics and control of wind turbines and wind farms”. eng. *Proceedings of the American Control Conference, Proc Am Control Conf, American Control Conference* (2009), pp. 5160195, 2076–2089.

[98] J. B. Freeman and M. J. Balas. “Direct model-reference adaptive control of variable speed horizontal-axis wind turbines”. eng. *Wind Engineering* 22.5 (1998), pp. 209–218.

[99] J. Gieras. “Wind turbine control applications of turbine-mounted LIDAR”. English. *Journal of Physics: Conference Series* 40, no. 5.1 (2014), p. 012011.

[100] J. H. Laks, L. Y. Pao, and A. D. Wright. “Control of Wind Turbines: Past, Present, and Future”. und. *Proceedings of the American Control Conference, Int C Intel, Int C Intell Comp Co, Int C Intell Comp Commun Proc, Proc Am Control Conf, American Control Conference* (2009), pp. 2096–2103.

[101] S. Timoshenko. *Vibration Problems in Engineering*. D. Van Nostrand Company Inc, 1928, 462 s.

[102] W. N. White, Z. Yu, and C. Lucero. “Active damping of torsional resonance in wind turbine drivetrains”. English. *40th Annual Conference of the IEEE Industrial Electronics Society* (2014), pp. 1957–1963.

[103] S. A. Papathanassiou and M. P. Papadopoulos. “Mechanical stresses in fixed-speed wind turbines due to network disturbances”. eng. *IEEE Transactions on Energy Conversion* 16.4 (2001), pp. 361–367.

[104] Z.-x. Xing, L.-z. Liang, H.-y. Guo, and X.-d. Wang. “Damping Control Study of The Drive Train of DFIG Wind Turbine”. und. *International Conference on Energy and Environment Technology* 1 (2009), pp. 576–579.

[105] S. Struggl, V. Berbyuk, and H. Johansson. “Review on wind turbines with focus on drive train system dynamics”. und. *Wind Energy* 18.4 (2015), pp. 567–590.

[106] A. Abolins, D. Lambrecht, J. S. Joyce, and L. T. Rosenberg. “Effect of clearing short circuits and automatic reclosing on torsional stress and life expenditure of turbine-generator shafts”. English. *IEEE Transactions on Power Apparatus and Systems* PAS-95.1 (1976), pp. 14–25.

[107] S. M. Muyeen, M. H. Ali, R. Takahashi, T. Murata, and J. Tamura. “Damping of blade-shaft torsional oscillations of wind turbine generator system”. und. *Electrochemistry Communications, Electrochem. Commun, Electroch C, Electrochem Commun* 9.9 (2007), pp. 195–211.

[108] M. J. Sidi. *Spacecraft Dynamics and Control*. Ed. by M. J. Rycroft and R. F. Stengel. Cambridge University Press, 1997.

[109] J. Helsen, D. Vandepitte, and W. Desmet. “Flexible Modelling Of Wind Turbine Gearboxes with Special Focus on Shaft Flexibilities”. *10th International Conference on Recent Advances in Structural Dynamics* (2010).

[110] J. Peeters. “Simulation of Dynamic Drive Train Loads in a Wind Turbine”. PhD thesis. Katholieke Universiteit Leuven, 2006.

[111] R.-j. Ye, H. Li, Z. Chen, and Q. Gao. “Comparison of Transient Behaviors of Wind Turbines with DFIG Considering the Shaft Flexible Models”. English. *Proceedings of the 11th International Conference on Electrical Machines and Systems* 1-8 (2008), pp. 2585–2590.

[112] H. B. Hendriks, B. H. Bulder, J. J. Heijdra, J. T. G. Pierik, G. J. W. V. Bussel, R. V. Rooij, M. Zaaijer, W. A. A. M. Bierbooms, D. T. D. Hoed, G. J. D. Vilder, F. Goezinne, M. H. Lindo, and R. V. D. Berg. “DOWEC Concept Study. Evaluation of Wind Turbine Concepts for Large Scale Offshore Application”. English (2008).

[113] J. Jonkman, S. Butterfield, W. Musial, and G. Scott. *Definition of a 5-MW Reference Wind Turbine for Offshore System Development*. Tech. rep. National Renewable Energy Laboratory, 2009.

[114] R. Ottersten. “On control of back-to-back converters and sensorless induction machine drives”. English. *Doktorsavhandlingar Vid Chalmers Tekniska Hogskola* 1978 (2003).

[115] K. Lu, P. O. Rasmussen, and E. Ritchie. “An Analytical Equation for Cogging Torque Calculations in Permanent Magnet Motors” (2006).

[116] M. R. Islam. “Cogging Torque, Torque Ripple and Radial Force Analysis of Permanent Magnet Synchronous Machines”. PhD thesis. University of Akron, 2009.

[117] J. Gieras. “Analytical Approach To cogging torque calculation of PM brushless motors”. *IEEE Transactions on Industry Applications* 40, no. 5 (2004), pp. 1310–1316.

[118] D. Svechkarenko. “On Design and Analysis of a Novel Transverse Flux Generator for Direct-driven Wind Application”. PhD thesis. KTH Electrical Engineering, 2010.

[119] M. Monfared, S. Golestan, and J. M. Guerrero. “Analysis, Design, and Experimental Verification of a Synchronous Reference Frame Voltage Control for Single-Phase Inverters”. und. *IEEE Transactions on Industrial Electronics* 61.1 (2014), pp. 258–269.

[120] R. Barrera-Cardenas and M. Molinas. “Multi-objective Optimization of a Modular Power Converter Based on Medium Frequency AC-Link for Offshore DC Wind Park”. *10th Deep Sea Offshore Wind R&D Conference* (2013).

[121] E. Hendricks, O. E. Jannerup, and P. H. Sørenson. *Linear Systems Control: Deterministic and Stochastic Methods*. eng. Springer-Verlag, 2008.

[122] L. H. Keel and S. P. Bhattacharyya. “Controller synthesis free of analytical models: Three term controllers”. und. *IEEE Transactions on Automatic Control* 53.6 (2008), pp. 1353–1369.

[123] T. Burton, D. Sharpe, N. Jenkins, and E. Bossanyi. *Wind energy handbook*. English. John Wiley and Sons Ltd, 2001, 617 s.

[124] I. Munteanu, A. I. Bratcu, N.-A. Cutululis, and E. Ceanga. *Optimal control of wind energy systems : Towards a global approach*. Springer, 2008, 283 s.

[125] J. Glasdam, J. Hjerrild, L. H. Kocewiak, and C. L. Bak. "Review on multi-level voltage source converter based HVDC technologies for grid connection of large offshore wind farms". *2012 IEEE International Conference on Power System Technology, POWERCON 2012* (2012), p. 6401377.

[126] T. C. Estate. "The Crown Estate Round 3 Offshore Wind Farm Connection Study Version 1.0". Version 1.0. 2008.

[127] H. J. Knaak. "Modular multilevel converters and HVDC/FACTS: A success story". eng. *Proceedings of the 2011 14th European Conference on Power Electronics and Applications, Epe 2011, Proc. Eur. Conf. Power Electron. Appl., Epe* (2011), p. 6020674.

[128] Energinet.dk, S. Kraftnät, and V. Transmission. *An Analysis of Offshore Grid Connection at Kriegers Flak in the Baltic Sea*. Tech. rep. 2009.

[129] E. Möllerstedt. "Dynamic Analysis of Harmonics in Electrical Systems". PhD thesis. Department of Automatic Control, Lund Institute of Technology, 2000.

[130] P. Brogan. "The stability of multiple, high power, active front end voltage sourced converters when connected to wind farm collector systems". eng. *Epe Wind Energy Chapter Symposium 2010, Epe Wind Energy Chapter Symp* (2010).

[131] I. Arana Aristi, J. Holbøll, C. L. Bak, L. Kocewiak, A. H. Nielsen, A. Jensen, J. Hjerrild, and T. Sørensen. "How to improve the design of the electrical system in future wind power plants". eng. *Nordic Wind Power Conference Proceedings* (2009).

[132] F. Last, G. Jarrett, K. Huddart, G. Brewer., and W. Watson. "Isolated generator DC link feasability trials". *lEE conference on high voltage dc transmission* ().

[133] J. Ainsworth. "Harmonic instability between controlled static convertors and a.c. networks". *Proceedings of the Institution of Electrical Engineers* 114.7 (1967), pp. 949–957.

[134] N. Flourentzou, V. G. Agelidis, and G. D. Demetriades. "VSC-Based HVDC Power Transmission Systems: An Overview". und. *IEEE Transactions on Power Systems* 29.6 (2014), pp. 592–602.

[135] C. Oates and C. Davidson. "A comparison of two methods of estimating losses in the Modular Multi-Level Converter". *14th European Conference on Power Electronics and Applications* (2011), pp. 1–10.

[136] B. D. Gemmell, J. Dorn, D. Retzmann, and D. Soerangr. "Prospects of multilevel VSC Technologies for power transmission". eng. *Transmission and Distribution Exposition Conference: 2008 Ieee Pes Powering Toward the Future, Pims 2008, Transm. Distrib. Expo. Conf.: Ieee Pes Powering Toward Future, Pims* (2008), p. 4517192.

[137] Lesnicar and Marquardt. “An innovative modular multilevel converter topology suitable for a wide power range”. 3 (2003), 6 pp. Vol.3.

[138] S. Johansson, G. Asplund, E. Jansson, and R. Rudervall. “Power system stability benefits with VSC DC-transmission systems”. *Cigré* (2004).

[139] S. Chaudhary. “Control and Protection of Wind Power Plants with VSC-HVDC Connection”. eng. PhD thesis. 2011.

[140] R. Sharma. “Electrical Structure of Future Off-shore Wind Power Plant with a High Voltage Direct Current Power Transmission”. eng. PhD thesis. 2012.

[141] C. Heising, D. Meyer, R. Bartelt, M. K. Zadeh, T. Lebioda, and J. Jung. “Power electronic asset characteristics for HVDC-connected offshore grids”. *11th International Workshop on Large-Scale Integration of Wind Power into Power Systems* (2010).

[142] L. Zhang, L. Harnefors, and H.-P. Nee. “Modeling and Control of VSC-HVDC Links Connected to Island Systems”. und. *IEEE Transactions on Power Systems* 26.2 (2011), pp. 783–793.

[143] N. Ahmed, A. Haider, L. Angquist, and H.-P. Nee. “M2C-based MTDC system for handling of power fluctuations from offshore wind farms”. English. *IET Conference on Renewable Power Generation (RPG 2011) — 2011* (2011).

[144] Y. Wang, X. Zhu, L. Xu, and H. Li. “Contribution of VSC-HVDC connected wind farms to grid frequency regulation and power damping”. eng. *Iecon Proceedings (industrial Electronics Conference), Iecon Proc* (2010), pp. 5674995, 397–402.

[145] L. Zeni, I. Margaris, A. D. Hansen, P. E. Sørensen, and P. Kjær. “Generic Models of Wind Turbine Generators for Advanced Applications in a VSC-based Offshore HVDC Network”. eng. *10th International Conference on AC and DC Power Transmission* (2012).

[146] B. Silva, C. L. Moreira, L. Seca, Y. Phulpin, and J. A. Pecas Lopes. “Provision of Inertial and Primary Frequency Control Services Using Offshore Multiterminal HVDC Networks”. und. *IEEE Transactions on Sustainable Energy* 3.4 (2012), pp. 800–808.

[147] T. M. Haileselassie and K. Uhlen. “Primary frequency control of remote grids connected by multi-terminal HVDC”. *IEEE Power and Energy Society General Meeting* (2010), pp. 1–6.

[148] Y. Pipelzadeh, B. Chaudhuri, and T. C. Green. “Inertial response from remote offshore wind farms connected through VSC-HVDC links: A Communication-less scheme”. *IEEE Power and Energy Society General Meeting* (2012), p. 6345609.

[149] B. Berggen, R. Majumder, C. Sao, and K. Linden. “Method and control device for controlling power flow within a dc power transmission network”. WO 2012/000 549A1. 2010.

[150] E. Prieto-Araujo, F. D. Bianchi, A. Junyent-Ferre, and O. Gomis-Bellmunt. "Methodology for Droop Control Dynamic Analysis of Multiterminal VSC-HVDC Grids for Offshore Wind Farms". und. *IEEE Transactions on Power Delivery* 26.4 (2011), pp. 2476–2485.

[151] IEC 61400-27-1. *Wind Turbines Part 27-1: Electrical simulation models – Wind turbines*. Tech. rep. IEC, Nov. 2013.

[152] Working Group Joint Report – WECC WGDP & IEEE DPWP Generation. "Description and Technical Specifications for Generic WTG Models – A Status Report". *Proceedings of IEEE PSCE* (2013).

[153] CIGRE Technical Brochure 328. *Modeling and Dynamic Behavior of Wind Generation as it Relates to Power System Control and Dynamic Performance*. Tech. rep. CIGRE WG C4.601, 2007.

[154] S.-T. Cha, Q. Wu, H. Zhao, I. Margaris, P. E. Sørensen, and J. Østergaard. "Implementation of IEC Generic Model Type 1 Wind Turbine Generators using RTDS". eng. *Proceedings of 11th International Workshop on Large-scale Integration of Wind Power Into Power Systems* (2012).

[155] N. Kroutikova, C. A. Hernandez-Aramburo, and T. C. Green. "State-space model of grid-connected inverters under current control mode". und. *IET Electric Power Applications* 1.3 (2007), pp. 329–338.

[156] Y. Guo, W. Wang, C. Y. Tang, J. N. Jiang, and R. G. Ramakumar. "Model Predictive and Adaptive Wind Farm Power Control". und. *Proceedings of the American Control Conference, P Am Contr, P Amer Contr Conf, Proc Am Control Conf, American Control Conference* (2013), pp. 2890–2897.

[157] EWEA. *Generic Grid Code Format for Wind Power Plants*. Tech. rep. EWEA, 2009.

[158] B. Badrzadeh, M. Bradt, N. Castillo, R. Janakiraman, R. Kennedy, S. Klein, T. Smith, and L. Vargas. "Wind power plant SCADA and controls". *IEEE Power and Energy Society General Meeting* (2012), pp. 1–7.

[159] U. Ozbay, E. Zergeroglu, and S. Sivrioglu. "Adaptive backstepping control of variable speed wind turbines". *International Journal of Control* 81:6 (2011), pp. 910–919.

[160] Z. Lu and W. Lin. "Asymptotic Tracking Control of Variable-Speed Wind Turbines". *Proceedings of the 18th IFAC World Congress*. Vol. 18th. 2011.

[161] Y. Song, B. Dhinakaran, and X. Bao. "Variable speed control of wind turbine using nonlinear and adaptive algorithms". *Journal of Wind Engineering and Industrial Aerodynamics* 85 (2000), pp. 293–308.

[162] K. Hammerum. "A fatigue approach to wind turbine control". MA thesis. Technical University of Denmark, 2006.

[163] C. Sloth, T. Esbensen, M. Niss, J. Stoustrup, and P. Odgaard. "Robust LMI-based control of wind turbines with parametric uncertainties". *Proceedings of the 3rd IEEE Multi-conference on Systems and Control*. 2009, pp. 776–81.

[164] C. Sloth, T. Esbensen, and J. Stoustrup. "Robust and fault-tolerant linear parameter-varying control of wind turbines". *Mechatronics* 21 (2011), pp. 645–659.

[165] M. Krstic, I. Kanellakopoulos, and P. Kokotovic. *Nonlinear and Adaptive Control Design*. Ed. by S. Haykin. John Wiley and Sons, 1995.

[166] H. Khalil. *Nonlinear Systems*. Third. Prentice Hall, 2002.

[167] C. Fischer, S. Mariéthoz, and M. Morari. "A model predictive control approach to reducing low order harmonics in grid inverters with LCL filters". *IECON Proceedings* (2013), pp. 3252–3257.

[168] H. A. Pereira, S. Y. Liu, M. C. de Lima Ramos, V. F. Mendes, and S. R. Silva. "A Comparative Analysis of Wind Turbine Technologies in Focus on the Grid Integration". *Ind. Appl., (INDUSCON)* (2010), pp. 1–6.

[169] H. Pinheiro, V. F. Montagner, and I. J. Gabe. "Design and implementation of a robust current controller for VSI connected to the grid through an LCL filter". *IEEE Transactions on Power Electronics* 24 (2009), pp. 1444–1452.

[170] H. Haitao, Q. Shi, Z. He, J. He, and S. Gao. "Potential Harmonic Resonance Impacts of PV Inverter Filters On Distribution Systems". *IEEE Transactions on Sustainable Energy* (2014).

[171] M. Hasan, K. N. Binti, K. Rauma, A. Luna, J. I. Candela, and P. Rodriguez. "Harmonic Compensation Analysis In Offshore Wind Power Plants Using Hybrid Filters". *IEEE Transactions on Industrial Applications* 50.3 (2014).

[172] L. H. Kocewiak, J. Hjerrild, and C. L. Bak. "Harmonic Analysis of Offshore Wind Farms With Full Converter Wind Turbines". *International Conference on Large-Scale Integration of Wind Power into Power Systems* 8 (2009).

[173] M. Lindgren and J. Svensson. "Control of a voltage-source converter connected to the grid through and LCL filter application to active filtering". *Proc. IEEE PESC* 1 (1998), pp. 229–235.

[174] R. Beres, X. Wang, F. Blaabjerg, C. L. Bak, and M. Liserre. "Comparative analysis of the selective resonant LCL and LCL plus trap filters". *Int. Conf. Opt. of Electrical and Electronic Equip.* (2014), pp. 740–747.

[175] S. V. Araujo, A. Engler, and F. L. M. Antunes. "LCL Filter design for grid-connected NPC invertersin offshore wind turbines". *The 7th International Conference on Power Electronics* (2007), pp. 1133–1138.

[176] E. Lightner and S. Widergren. "An orderly transition to a transformed electricity systems". *IEEE Transactions on Smart Grid* 1 (2010), pp. 3–10.

[177] M. L. R. Teodorescu F. Blaabjerg and P. C. Loh. "A New Breed of Proportional-Resonant Controllers and Filters for Grid-Connected Voltage-Source Converters". *Proceedings of IEEE Electric Power Applications* 153 (2006), pp. 750–762.

[178] M. Liserre, F. Blaabjerg, and R. Teodorescu. “Multiple harmonics control for three-phase systems with the use of PI-RES current controller in a rotating frame”. *IEEE Transactions on Power Electronics* 21 (2006).

[179] A. Asbafkan, B. Mirzaeeian, M. Niroomand, and H. A. Zarchi. “Frequency Adaptive Repetitive Control of Grid Connected Inverter for Wind Turbine Applications”. *21st Iran. Conf. Electr. Eng., ICEE* (2013).

[180] G. Weiss, Q. C. Zhong, T. C. Green, and J. Liang. “Hinf repetitive control of DC-AC converters in microgrids”. *IEEE Transactions on Power Electronics* 19 (2004), pp. 219–230.

[181] S. Kim. “Sliding mode controller for the single-phase grid-connected photovoltaic system”. *Applied Energy* 83 (2006), pp. 1101–1115.

[182] J. D. Christian Wessels and F. W. Fuchs. “Active Damping of LCL-Filter Resonance based on Virtual Resistor for PWM Rectifiers – Stability Analysis with Different Filter Parameters”. *Power Electronics Specialists Conference* (2008), pp. 3532–3538.

[183] E. Twinning and D. Holmes. “Grid current regulation of a three-phase voltage source inverter with an LCL input filter”. *IEEE Transactions on Power Electronics* 18 (2003), pp. 888–895.

[184] R. Teodorescu, F. Blaabjerg, U. Borup, and M. Liserre. “A New Control Structure for Grid-Connected LCL PV Inverters with Zero Steady-State Error and Selective Harmonic Compensation”. *IEEE Applied Power Electronics Conference and Exhibition* 1 (2004), pp. 580–586.

[185] E. Muljadi, C. Butterfield, A. Ellis, J. Mechenbier, J. Hocheimer, R. Young, N.Miller, R. Delmerico, R. Zavadil, and J. Smith. “Equivalencing the collector system of a large wind power plant”. *Power Engineering Society General Meeting* (2006).

[186] J. Brochu, R. Gagnon, and C. Larose. “Generic Equivalent Collector System Parameters for Large Wind Power Plant”. *IEEE Transactions on Energy Conversion* 26 , Issue: 2 (2011).

[187] B.-G. Cho and S.-K. Sul. “LCL Filter Design for Grid-connected Voltage-source Converters in High Power Systems”. *IEEE Energy Conv. Cogress and Exp. (ECCE)* (2012), pp. 1548–1555.

[188] J. P. (ECN), S. de Haan (TUD), J. M. (TUD), E. (ECN), T. van Engelen (ECN), and J. B. (Neg-Micon). “Electrical And Control Aspects of Offshore Wind Farms II (Erao II), Volume 1: Dynamic models of wind farms”. *Tech Report* (2004).

[189] J. W. Umland and M. Safiuddin. “Magnitude and Symmetric Optimum Criterion for the Design of Linear Control Systems: What is It and How Does it Compare with the Others”. *IEEE Transactions on Industrial Applications* 26 (1990), pp. 489–197.

[190] C. Bajracharya, M. Molinas, J. A. Suul, and T. M. Undeland. “Understanding of tuning techniques of converter controllers for VSC-HVDC”. *Nordic Workshop on Power and Industrial Electronics* (2008).

[191] K.Åström and T. Hägglund. *PID Controllers: Theory, Design and Tuning - 2nd edition*. Instrument Society of America, 1995.

[192] D. Schröder. *Elektrische Antriebe 2, Regelung von Antriebssystemen, 2nd ed.* Springer-Verlag, 2001.

[193] I. Landau, R. Lozano, M. M’Saad, and A. Karimi. *Adaptive Control: Algorithms, Analysis and Applications*. Springer, 2011.

[194] M. G. Simões and S. Chakraborty. *Power Electronic for Renewable and Distributed Energy Systems: A sourcebook of Topologies, Control and Integration*. Ed. by S. Chakraborty, M. G. Simões, and W. E. Kramer. Springer-Verlag London, 2013.

[195] F. Blaabjerg and M. P. Kazmierkowski. *Control in Power Electronic: Selected Problems*. Ed. by M. P. Kazmierkowski, R. Krishnan, and F. Blaabjerg. Academic Press - Elsevier Science, 2002.

[196] T. Friedli, J. W. Kolar, J. Rodriguez, and P. W. Wheeler. “Comparative Evaluation of Three-Phase AC-AC Matrix Converter and Voltage DC-Link Back-to-Back Converter Systems”. und. *IEEE Transactions on Industrial Electronics* 59.11 (2012), pp. 4487–4510.

[197] P. Guo, W. Y. Liu, a. B. W. W. Wang, and H. S. Jia. “Wind Farm Voltage Control Scheme to Improve Dynamic Voltage Stability”. *Advanced Materials Research* 732-733 (Aug. 2013), pp. 745–75.

[198] M. Hunyar and K. Veszpremi. “Reactive Power Control of Wind Turbines”. und. *International Power Electronics and Motion Control Conference and Exposition* (2014), pp. 348–352.

[199] A. Ghaffari, M. Krstic, and S. Seshagiri. “Power Optimization and Control in Wind Energy Conversion Systems Using Extremum Seeking”. und. *IEEE Transactions on Control Systems Technology* 22.5 (2014), pp. 1684–1695.

[200] A. Berizzi, C. Bovo, V. Ilea, M. Merlo, A. Miotti, and F. Zanellini. “Decentralized reactive power control of wind power plants”. eng. *IEEE International Energy Conference and Exhibition* (2012), pp. 6348237, 674–679.

[201] V. Calderaro, G. Conio, V. Galdi, and A. Piccolo. “Reactive power control for improving voltage profiles: A comparison between two decentralized approaches”. und. *Electric Power Systems Research* 83.1 (2012), pp. 247–254.

[202] D. F. Opila, A. M. Zeynu, and I. A. Hiskens. “Wind Farm Reactive Support and Voltage Control”. *IREP Symposium - Bulk Power System Dynamics and Control* (2010).

[203] C. Zheng and M. Kezunovic. “Distribution system voltage stability analysis with wind farms integration”. *North American Power Symposium (NAPS 2010)* (2010), pp. 1–6.

[204] J. Duan, R. Li, and L. An. “Study of Voltage Stability in Grid-Connected Large Wind Farms”. *Materials Science And Information Technology* (2012), pp. 433–440.

[205] A. Doria-Cerezo, M. Bodson, C. Batlle, and R. Ortega. “Study of the Stability of a Direct Stator Current Controller for a Doubly Fed Induction Machine Using the Complex Hurwitz Test”. und. *IEEE Transactions on Control Systems Technology* 21.6 (2013), pp. 2323–2331.

[206] T. Messo, J. Jokipii, and T. Suntio. “Effect of Conventional Grid-Voltage Feed-forward on the Output Impedance of a Three-Phase Photovoltaic Inverter”. *International Power Electronics Conference, IPEC-Hiroshima* (2014).

[207] J. C. Ramos and R. E. Araujo. “Design considerations on feed-forward and Kalman tracking filters in grid-tied-inverters current-control”. *IEEE 23rd International Symposium on Industrial Electronics (ISIE)* (2014).

[208] L. Harnefors, M. Bongiorno, and S. Lundberg. “Input-Admittance Calculation and Shaping for Controlled Voltage-Source Converters”. *IEEE Transactions on Industrial Electronics* 54 (2007), pp. 3323–3334.

[209] K. Ammous, E. Haouas, and S. Abid. “Averaged modelling of multilevel converters”. und. *International Journal for Computation and Mathematics in Electrical and Electronic Engineering* 29.3 (2010), pp. 626–646.

[210] C. Wessels, J. Dannehl, and F. W. Fuchs. “Active damping of LCL-filter resonance based on virtual resistor for PWM rectifiers - Stability analysis with different filter parameters”. eng. *IEEE Annual Power Electronics Specialists Conference* (2008), pp. 4592502, 3532–3538.

[211] L. Harnefors. “Analysis of Subsynchronous Torsional Interaction with Power Electronic Converters”. *IEEE Transactions on Power Systems* 22.1 (2007), pp. 305–313.

[212] L. Harnefors and H.-P. Nee. “Model based current control of ac drives using the internal model method”. *IEEE Transactions on Industrial Applications* 34 (1998), pp. 133–141.

[213] B. Yang, F. C. Lee, and M. Concannon. “Over current protection methods for LLC resonant converter”. English. *18th Annual Applied Power Electronics Conference - APEC 2003* (2003).

[214] J. Forde and P. Nelson. “Applications of Sturm sequences to bifurcation analysis of delay differential equation models”. *Journal of Mathematical Analysis and Applications* 300.2 (2004), pp. 273–284.

[215] D. G. Hook and P. R. McAree. “Graphics Gems”. In: *Graphics Gems*. Ed. by A. S. Glassner. San Diego, CA, USA: Academic Press Professional, Inc., 1990. Chap. Using Sturm Sequences to Bracket Real Roots of Polynomial Equations, pp. 416–422.

[216] J. M. Amada and M. P. C. Moreno. “Reactive power injection strategies for wind energy regarding its statistical nature”. *6th International Workshop on Large-Scale Integration of Wind Power and Transmission Networks for Offshore Wind Farms* 138 (2006).

[217] P. Zhang, R. Li, J. Shi, and X. He. “An improved reactive power control strategy for inverters in microgrids”. eng. *IEEE International Symposium on Industrial Electronics* (2013).

[218] W. Stevenson. *Elements of Power System Analysis 3rd ed*. McGraw Hill, New York, 1975.

[219] A. Wolfenden and V. K. Kinra. *M3D III: Mechanics and Mechanisms of Material Damping (Special Testing Publications)*. Ed. by A. Wolfenden. American Society for Testing & Materials, 1997.

[220] C. Sourkounis and P. Tourou. “Grid Code Requirements for Wind Power Integration in Europe”. *Conference Papers in Energy* 2013.Article ID 437674 (2013).

[221] P. Anderson, B. Agrawal, and J. V. Ness. *Subsynchronous Resonance in Power Systems*. Ed. by L. Shaw. Wiley-IEEE Press, 1990.

[222] B. Beltram, T. Ahmed-Ali, and M. E. H. Benbouzid. “Sliding Mode Power Control of Variable-Speed Wind Energy Conversion Systems”. *IEEE Transactions on Energy Conversion* 23 (2008), pp. 551–558.

[223] F. Blaabjerg, R. Teodorescu, M. Liserre, and A. Timbus. “Overview of control and grid synchronization for distribusted power generation systems”. *IEEE Transactions on Industrial Electronics* 53 (2006), pp. 1398–1409.

[224] B. Boukhezzar and H. Siguerdidjane. “Nonlinear Control of Variable Speed Wind Turbines without Wind Speed Measurement”. *Proceedings of the 44th IEEE Conference on Decision and Control*. 2005.

[225] A. M. Cantarellas, E. Rakhshani, D. Remon, and P. Rodriguez. “Design of passive trap-LCL filters for two-level grid connected converters”. eng. *European Conference on Power Electronics and Applications* 15 (2013), p. 6634403.

[226] J. Chauvin. “Drivetrain control strategy for wind turbines”. eng. *Proceedings of the IEEE International Conference on Control Applications* (2012), pp. 6402652, 1104–1110.

[227] O. Dordevic, M. Jones, and E. Levi. “A comparison of PWM techniques for three-level five-phase voltage source inverters”. *Proceedings of the 2011 14th European Conference on Power Electronics* (2011), pp. 1–10.

[228] I. Erlich, K. Rensch, and F. Shewarega. “Impact of large wind power generation on frequency stability”. *Power Engineering Society General Meeting, 2006. IEEE*. IEEE. 2006, 8–pp.

[229] M. P. S. Gryning, Q. Wu, M. Blanke, H. H. Niemann, and K. P. H. Andersen. “Wind Turbine Inverter Robust Loop-Shaping Control Subject to Grid Interaction Effects”. und. *IEEE Transactions on Sustainable Energy* (2015), pp. 1–10.

[230] Y. Guo, S. H. Hosseini, C. Y. Tang, J. N. Jiang, and R. G. Ramakumar. “An Approximate Wind Turbine Control System Model for Wind Farm Power Control”. und. *IEEE Transactions on Sustainable Energy* 4.1 (2013), pp. 262–274.

[231] E. Iyasere, M. H. Salah, D. M. Dawson, J. R. Wagner, and E. Tatlicioglu. “Robust nonlinear control strategy to maximize energy capture in a variable speed wind turbine with an internal induction generator”. *Journal of Control Theory and Applications* 10(2) (2012), pp. 184–194.

[232] Y. Jeong, K. Johnson, and P. Fleming. “Comparison and testing of power reserve control strategies for grid-connected wind turbines”. English. *Wind Energy* 17.3 (2014), pp. 343–358.

[233] T. Knudsen, T. Bak, and S. Tabatabaeipour. “Detection of excessive wind turbine tower oscillations fore-aft and sideways”. English. *Proceedings of the American Control Conference* (2012).

[234] M. B. Lindgren. “Analysis and Simulation of Digitally-controlled Grid-connected PWM-converters Using the Space-vector Average Approximation”. *IEEE 5th Workshop on Computers in Power Electronics, Portland, USA* (1996), pp. 157–162.

[235] M. Mirzaei. “Wind Turbine Control: Robust Model Based Approach”. eng. PhD thesis. 2012.

[236] D. Mueller and W. Kuehn. “Full converter wind turbine operating under weak grid conditions”. *IEEE PES Innovative Smart Grid Technologies Conference Europe* (2014), pp. 1–6.

[237] S. Muyeen. *Wind Energy Conversion Systems: Technology and Trends*. Ed. by S. Muyeen. Springer, 2012.

[238] S. M. Muyeen, M. H. Ali, R. Takahashi, T. Murata, J. Tamura, Y. Tomaki, A. Sakahara, and E. Sasano. “Blade-shaft torsional oscillation minimization of wind turbine generator system by using STATCOM/ESS”. eng. *Proceedings of the IEEE Lausanne Powertech* (2007), pp. 4538314, 184–189.

[239] S. M. Muyeen, J. Tamura, and T. Murata. *Stability Augmentation of a Grid-connected Wind Farm*. Springer, 2009.

[240] R. Ottersten. “On Control of Back-to-Back Converters and Sensorless Induction Machine Drives”. PhD thesis. Department of Electric Power Engineering, Chalmers University of Technology, 2003.

[241] S. S. S. Ozbaky and E. Zerge. “Variable Speed Control of Wind Turbines: A Robust Backstepping Approach”. *Proceedings of the 17th IFAC World Congress*. 2008.

[242] M. Peterson, B. N. Singh, and P. Rastgoufard. “Active and passive filtering for harmonic compensation”. eng. *Proceedings of the Annual Southeastern Symposium on System Theory* (2008), pp. 4480217, 188–192.

[243] N. Phankong, N. Yuktanon, and K. Bhumkittipich. “Three-level Back-to-Back Converter Simulation for Wind Turbine Energy Source”. *10th Eco-Energy and Materials Science and Engineering Symposium* 34 (July 2013), pp. 449–458.

[244] Q. Zhang. “Analysis and design of an LCL filter for the three-level grid-connected inverter”. *IEEE 7th Int Power Elect. and Motion Control Conf* 3 (2012), pp. 2023–2027.

[245] S. K. Salman and A. L. J. Teo. “Windmill Modeling Consideration and Factors Influencing the Stability if a Grid-Connected Wind Power-Based Embedded Generator”. *IEEE Transactions on Power Systems* 18(2) (2003), pp. 793–802.

[246] E. R. C. da Silva, E. C. dos Santos, and C. B. Jacobina. “Pulsewidth Modulation Strategies Nonsinusoidal Carrier-Based PWM and Space Vector Modulation Techniques”. und. *IEEE Industrial Electronics Magazine* 5.2 (2011), pp. 37–45.

[247] W. R. Skrzypinski, M. Gaunaa, and C. Bak. “The Effect of Mounting Vortex Generators on the DTU 10MW Reference Wind Turbine Blade”. eng. *Journal of Physics: Conference Series (online), Journal of Physics. Conference Series* 524.1 (2014).

[248] R. Vepa. *Dynamic modeling, simulation and control of energy generation*. English. 2013, 1 online resource (xvi, 373 pages).

[249] H. Wang, C. Yu, and X. C. Jianwen Zhang. “Control of Voltage Source Inverter with an LCL Filter without Voltage Sensors”. *Przeglad Elektrotechniczny* 88 (2012), pp. 119–122.

[250] S. Yang, Q. Lei, F. Z. Peng, and Z. Qian. “A robust control scheme for grid-connected voltage source inverters”. eng. *Proceedings of IEEE Applied Power Electronics* (2010), pp. 5433380, 1002–1009.

Appendix A

HVDC Connected Offshore Wind Power Plants: Review and Outlook of Current Research[1]

Jakob Glasdam[2], Lorenzo Zeni[2], Mikkel Gryning[3], Jesper Hjerrild[2], Łukasz Kocewiak[2], Bo Hesselbaek[2], Karsten Andersen[2], Troels Sørensen[2], Mogens Blanke[4], Poul E. Sørensen[5], Anca D. Hansen[5], Claus L. Bak[6], Philip C. Kjær [6]

A.1 Abstract

This paper presents a state-of-the-art review on grid integration of large offshore wind power plants (OWPPs) using high voltage direct voltage (HVDC) for grid connection. The paper describes in detail selected challenges hereto and presents how DONG Energy Wind Power (DEWP) is addressing these challenges through three coordinated PhD projects in close collaboration with leading academia within the field. The overall goal of these projects is to acquire in-depth knowledge of relevant operating phenomena in the offshore OWPP grid, rich with power electronics devices (PEDs) such as the HVDC and the PED widely used in the wind turbine generators

[1]Proceedings of the 12th International Workshop on Large-Scale Integration of Wind Power into Power Systems as well as on Transmission Networks for Offshore Wind Power Plants

[2]J. Glasdam, L. Zeni, J. Hjerrild, Ł. Kocewiak, B. Hesselbaek, K. Andersen and T. Sørensen are with the Wind Power Electrical Systems, DONG Energy, 2820 Gentofte, Denmark

[3]M. Gryning is with the SCADA Department, DONG Energy, 2820 Gentofte, Denmark, and with DTU Electrical Engineering, Technical University of Denmark, 2800 Kgs. Lyngby, Denmark

[4]M. Blanke is with DTU Electrical Engineering, Technical University of Denmark, 2800 Kgs. Lyngby, Denmark, and is also adjunct prof. at the AMOS Centre of Excellence at Norwegian University of Science and Technology, 7491 Trondheim, Norway

[5]P. Sørensen and A. Hansen are with DTU Electrical Engineering,Technical University of Denmark, 2800 Kgs. Lyngby, Denmark

[6]C. Bak and P. Kjær are with Department of Energy Technology, Aalborg University, 9100 Aalborg, Denmark.

(WTGs), such as the control system interaction (from a stability point of view), quality of vendor supplied control systems and their robustness against e.g. short circuits and load rejection. Furthermore, the outcome of the projects will be developed and validated models of e.g. the HVDC system, methodologies for assessment of control system stability and fault identification in implemented control system.

A.2 Introduction

The fact that future OWPPs are increasing in size and located more remotely from shore poses challenges to the wind power industry [125]. The voltage sourced converter (VSC) based HVDC technology seems to be the obvious solution for transmission of the produced power to shore. The VSC-HVDC technology has therefore become the preferred choice for grid connection of a large number of the planned OWPPs in e.g. the United Kingdom round 3 projects, in Germany and in Denmark [126][127][128] The VSC-HVDC system is associated with a high initial cost, but the marginal cost per MW is relatively low, making it advantageous to connect multiple OWPPs (or clusters) to a common offshore HVDC hub [125]. Figure 1 shows three candidate configurations for grid connection of OWPPs using HVDC. Whereas BorWin1 in Germany is the only operating HVDC connected OWPP using the point-to-point (P2P) in Figure 1a, it is expected that future grid connections will be made by connecting the offshore HVDC terminal either on the AC and/or on the DC side of the converter (Figure 1a and b). As large OWPP clusters are distributed over a large physical area with different wind conditions it is possible to optimize the utilization and loading of the HVDC converters using these configurations. As an example, HVDC 1 can be used to transmit the produced power in case of low wind at OWPP 1 and full production from OWPP 2 in Figure 1b, while HVDC 2 is out of service for maintenance purposes etc. The new system configuration requires in-depth knowledge of all relevant technical aspects, including e.g. the involved control systems performance and robustness for all possible operating conditions. The transmission system operator might impose new control requirements when HVDC is going to be used for OWPP grid connection and the dynamic compliance specifications might change. This sets up a need to develop new strategies for ensuring robustness and adaptability, considering aspects such as fault-handling, ancillary services, congestion management, etc. It is therefore important to analyze and assess all possible control aspects related to the interaction between the OWPP and the HVDC system. The paper will present a review of the state-of-the-art of grid integration of large OWPPs using HVDC for grid connection, on the involved PEDs in the OWPP and in the HVDC system. Furthermore, on the PEDs control capabilities and on how the testing of the control systems is currently being carried out. Based on the review, the paper will give a detailed description on the challenges that need to be addressed in order to ensure robust operation of the OWPP. The paper will present how DEWP, market leader in development and operating of OWPPs, is addressing these challenges through three coordinated PhD projects in close collaboration with leading academia within the field. The paper is organized following the separation between the three PhD

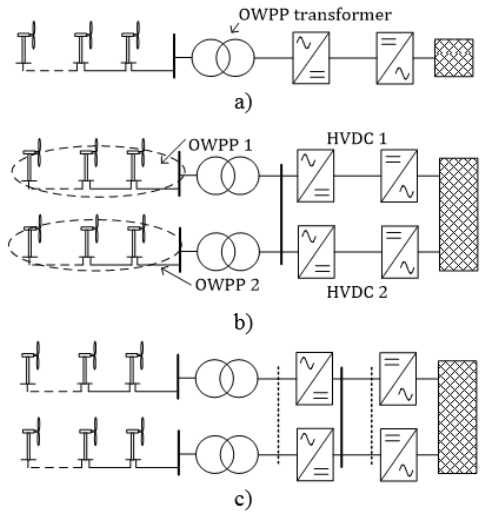

Figure A.1: Simplified single line diagrams of grid connection of OWPP(s) using a) point-to-point (P2P) VSC-HVDC b) parallel P2P connected on the offshore AC side, fed by multiple OWPPSs c) multi-terminal. HVDC converter transformers (if any) have not been included in the figures.

projects: Section A.3 presents the project Harmonics in *Large Offshore Wind Farms, Employing Power Electronics in the Transmission System*, dealing with the harmonics in the OWPP and on how the controllers employed in the respective PEDs interact with each other from a stability perspective in the frequency range above 50 Hz. In Section A.4, a description of the project *Communication and Control in Clusters of Wind Power Plants Connected to HVDC Offshore Grids* is given. The project focuses on the investigation of problems concerning the efficient coordination of HVDC system and OWPPs controllers to properly perform dedicated control features such as the provision of system services (both to the AC and the DC grid), fault-handling, coordination of multiple OWPPs behind HVDC converter(s), etc. Finally, Section A.5 draws the attention to the project *Offshore Wind Park Control Assessment Methodologies*, that investigates the control system architecture top-down of an OWPP and how the complex dynamics can be reduced and compiled into a set of generalized parameter specifications for components in an early stage of planning to minimize design based problems at a later stage.

A.3 Harmonics in Large Offshore Wind Farms, Employing Power Electronics in the Transmission System

Stability assessment and control design in conventional power systems have been carried out on basis of the assumption of sinusoidal excitation at fundamental power system frequency [129]. Although harmonics exist due to non-linear components such as e.g. the line commutated converter (LCC) HVDC, they have been assumed to be negligible with regard to power system stability. However, due to the increasing application of PEDs in e.g. OWPPs this assumption is no longer valid, as harmonics may lead to unpredicted and unwanted interaction between components, which eventually may lead to instability [130]. State-of-the-art full-scale back-to-back power converters are typically used in the WTGs, which are grid-friendly in many aspects, including their relatively low harmonic emission level [131]. However, OWPPs have a significant medium voltage cable network, and depending on the grid connection solution, long HVAC cabling. The distributed cable capacitances are prone to cause resonances within the bandwidth of the closed loop control systems of the PEDs in the WTGs and therefore affect the stability of the closed loop control system. Operating experiences in conventional HVAC grid connected OWPPs have shown that these converters can interact with each other, with the internal OWPP electric system as well as the external network causing so-called harmonic instability problems. Harmonic instabilities involve the interaction between the AC system, the WTG converter itself and its control system and have the adverse effect in OWPPs of voltage oscillations prior to disconnection of the OWPP, leading to lost revenue unless countermeasures are taken. The observation of harmonic instabilities can be traced back to mid-sixties [132][133] for LCC-HVDC schemes. One of the most significant incidents with the application of modern PED was reported in the mid-nineties, where the Swiss railways experienced malfunction of the electric rail vehicles, leading to shutdown of the traction system. The malfunction was explained to be caused by resonance in the Swiss 132 kV network, which was excited by the control systems used in the PEDs of the electric rail vehicles [129]. For high power VSC-HVDC transmission system applications, the three main topologies utilized so far are the two-level, three-level and the modular multilevel cascaded converters (MMCC) [125][134][135][136]. Whereas only the Trans Bay Cable project utilizes the merging MMCC technique [125][127], the two- and three-level topologies have found their application in a number of installations, as outlined in Table A.1 [125]. Table A.1 indicates that the trend in future VSC-HVDC installations is to employ the MMCC for power transmission and grid connection of OWPPs. The MMCC VSC-HVDC, introduced in [137], synthesises a high quality sinusoidal voltage waveform by incrementally switching a high number of voltage levels thus having low harmonic emission and low filter requirements.

A.3.1 Purpose of PhD project

Although the MMCC based VSC-HVDC provides close to sinusoidal fundamental voltage and current waveforms into the system, it is still of high importance to the

Installation	Year	Manufacturer	$P[MW]$	Topology
Gotland	1999	ABB	50	2-level
Murraylink	2002	ABB	220	3-level
Estlink	2006	ABB	350	2-level
BorWin1 (OWPP)	2009	ABB	400	2-level
Trans Bay Cable Project	2010	Siemens	400	MMCC
BorWin2 (OWPP)	2013	Siemens	800	MMCC
HelWin1 (OWPP)	2013	Siemens	576	MMCC
DolWin1 (OWPP)	2013	ABB	800	MMCC
SylWin1 (OWPP)	2014	Siemens	864	MMCC
South-West Link	2014	Alstom	1440	MMCC
HelWin2 (OWPP)	2015	Siemens	800	MMCC
Dolwin2 (OWPP)	2015	ABB	900	MMCC

Table A.1: Overview of Selected VSC-HVDC Projects

wind power industry to investigate and acquire detailed knowledge on the possible interaction (from a harmonic perspective) between the control systems used in the PEDs in the WTGs and in the offshore VSC-HVDC terminal in order to design a robust system. This industrial PhD project will mainly focus on investigating the best possible way(s) to perform harmonic studies in VSC-HVDC grid connected OWPPs. The project is aimed at gaining new methods and models, which will contribute to achieve a high degree of reliability of future OWPPs mainly based on the VSC-HVDC grid connection. The project will investigate the possibility of developing detailed models, which are independent of manufacturer provided data, as this is normally confidential. By achieving a better understanding of the complexity of how such PED systems interact with each other, seen from a harmonic perspective, it will be possible to optimize design of harmonic filters, reactive compensation etc. Furthermore, the increased know-how will also enable DEWP to give relevant input during the compliance assessment of an OWPP. The PhD project will also enable DEWP to ask for the right information for the VSC-HVDC system in due time during the design of an OWPP and will lead to improvement in the reliability of future OWPPs.

A.3.2 Project Objectives

The following list summarizes the main expected deliverables from the PhD project:

- Obtain detailed knowledge of MMCC technologies for wind power integration (VSC-HVDC and static synchronous compensator (STATCOM)).
- Develop and validate appropriate models of the MMCCs. In time, frequency and harmonic (modulator) domain, where found applicable.
- Conduct field measurement campaign for model validation.

- Investigate wind farm stability issues for frequencies above the fundamental frequency with widespread use of PEDs.
- Compare different stability assessment methods in time and frequency domain.
- Develop a best-practice for harmonic stability assessment in offshore wind farms.
- Investigate involved parameters influence on the stability margins.

  Sensitivity analysis of e.g. HVDC control parameters, grid strength etc.
- Develop a best-practice for harmonic stability assessment in OWPPs.

  Deliver different assessment methods.

A.4 Communication and Control in Clusters of Wind Power Plants Connected to HVDC Offshore Grids

Along with technical issues related to harmonics, the wide-spread utilization of PEDs poses, on the one hand, new challenges related to more classical control facets, such as normal operation or delivery of system services, while offering, on the other hand, more opportunities for tackling them. This is obviously true also for VSC-HVDC [138]. When the picture involves OWPPs (e.g. future HVDC projects indicated with OWPP in Table I), additional coordination may be necessary to guarantee the optimal operation of the OWPP and the HVDC transmission system. New dynamic requirements are brought about by the introduction of the VSC-HVDC connection, the behavior of which is substantially different from that of a classical power system. One direction of research is related to the excitation of the offshore AC islands (left parts of Figure 1), where, at least initially, single HVDC converters will have to shoulder the main control burden to guarantee evacuation of the power, by fixing the voltage magnitude and angle (so called U/f control), and the OWPP will synchronize in the usual way [139][140]. However, more advanced and generalized approaches have also been proposed, and are expected to offer a more robust and flexible solution when the number of HVDC converters feeding the same island will increase [141][142][143]. The other focus area is the coordination of HVDC converter and OWPP controllers during normal operation [139][140], delivery of ancillary services [139][144][145] and faults of various nature [139][140]. Further research is directed to address the same challenges, but is considering more complex multi-terminal DC networks, e.g. [146][147]. However, further room for research is left, in particular directed towards:

- A more detailed investigation of the aspects touched upon by the cited references, with careful assessment of dynamic requirements and control and coordination issues when considering real OWPPs and their relatively slow controller.

- Handling of events that so far, to the authors' knowledge, have not been touched upon, such as for instance the response to HVDC converter tripping or a thorough theoretical analysis of short circuit in offshore AC islands.

The control challenges to be solved come along with the utilization of an appropriate level of communication. Studies have been initiated, for example, on simple networks [148][145] and with focus on frequency control, where communication seems to offer satisfying performance. However, more complex grid layouts might suffer robustness lack when relying heavily on real-time fast communication and solutions have been proposed, e.g. in [149][150].

A.4.1 Purpose of PhD project

In order to facilitate the deployment of very remote OWPPs through VSC-HVDC transmission, it is important to provide a contribution to fill the research gaps outlined above. Issues concerning the excitation of offshore islands should be looked at, by comparing techniques proposed to date or suggesting new improvements. As an example, a simple comparison between a simple master-slave approach (U/f control [139]) and the power synchronization loop (PSL) [142] is depicted in Figure 2, where voltage and frequency steps have been tested at the offshore station of a point-to-point HVDC connection for OWPP. It can be seen that the schemes offer similar performance. Future work will more thoroughly assess the similarities and differences. The steady-state differences in direct and quadrature current are due to the different reference for the angle, which is the grid side of the converter transformer for the U/f and the converter internal voltage for the PSL. On the other hand, control coordination between VSC-HVDC networks and OWPPs should be further investigated, with special attention drawn upon the actual need for fast communication. In [145], a frequency control scheme based on communication proved to perform equivalently to a coordinated control involving offshore frequency and DC voltage. Further work is needed in the area, expanding it to other services such as power oscillation damping and HVDC voltage control.

A.4.2 Project Objectives

The main objectives of the study are the following:

- Developing and comparing solutions for the connection of OWPPs through HVDC network with respect to normal operation (delivery of scheduled energy).
- Investigation of alternatives for provision of currently required system services.
- Investigation of new possible services and requirements and characterization in terms of their direct influence on the OWPP's operation and control and analyze solutions thereto.
- Investigate other control problems such as fault-handling (e.g. short circuit and load rejection), robustness against communication faults.

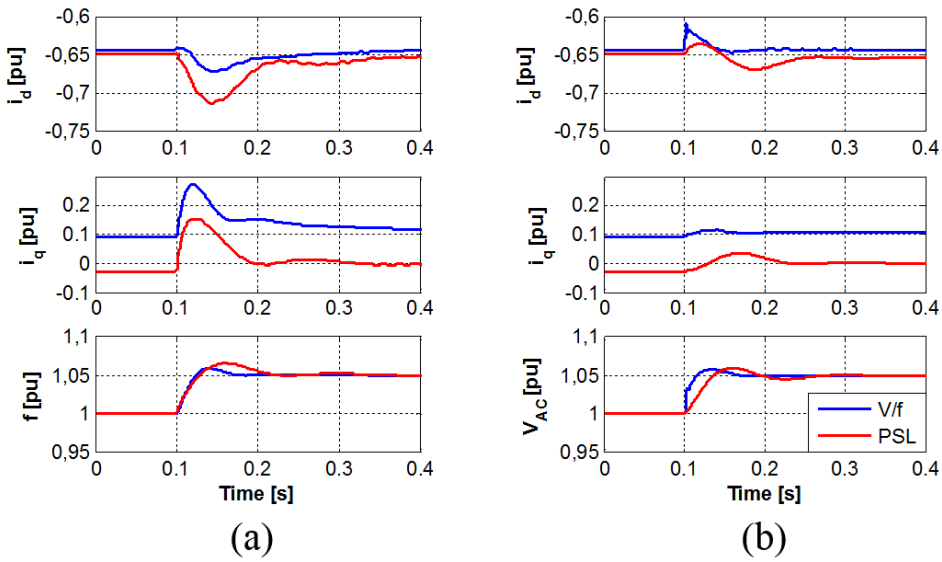

Figure A.2: Offshore converter control: comparison between current vector control (U/f) based scheme and power synchronisation loop (PSL) based scheme. (a) frequency reference step, (b) AC voltage reference step.

- Assessment of communication needs for all the above items.

A.5 Offshore Wind Park Control Assessment Methodologies

Every aspect of control design is a trade-off between performance and stability, and the OWPP relies on its suppliers to deliver systems that conform with the performance specifications as set by the national grid code. Although the suppliers deliver the subsystems, the OWPP developer is liable for any delay or unforeseen situations, even if the situation is caused by a malfunction in the delivered subsystem. One of the challenges in minimizing the risk of malfunction is to validate the implementation of the control systems without having direct access to the mathematical models used. In order to conform with the Intellectual Property Right (IPR) of the industry, generic models of the most used WTG structures have been developed to provide a baseline for stability and transient analysis by IEEE, IEC and CIGRE [151][152][153]. Various PhDs have also investigated the representation of type 1-4 WTG's, notably[32]. The use of generic models is shown to represent the dynamics of a WTG during steady state operation and fault precisely [154]. A challenge in WTG modelling is adequate level of detail in the component descriptions to represent the interactions and dynamics of interest. One focus area of the project is the dynamic interaction between controllers associated with the individual type 4 permanent magnet synchronous generator (PMSG) WTGs in a small scale OWPP and the risk of having oscillations

and unforeseen dynamics which eventually can lead to instability. The generic models developed include unwanted simplifications with respect to generators and critical components such as the PEDs to minimize simulation requirements, and are often represented in the frequency domain and not in a form suitable for control system analysis. Work has been done on restructuring and expressing both the physical and the control systems in a non-linear state-space model [155], but further research is needed to include dynamics of interest. Another focus area is the analysis of the park level control systems such as the STATCOM and power distribution. The second-to-minute timescale of the problem dictates a low-level of detail in the WTG modelling which must represent the used WTG in the OWPP. A power control system identification approach is suggested by [156] and was followed up by a simplified overall park control design [156]. As mentioned in the previous sections, experiences from existing OWPPs have led to a renewed interest in investigating the maturity and interaction between control systems both in the WTGs but also on a park level. Currently the specifications set for the operation of an OWPP vary nationally even though work has been done on harmonizing grid code requirements [157]. Commissioning tests are performed to just ensure compliance with grid code in order to achieve operation notice, but it does not convey a precise picture of the limitations of the OWPP. To the author's best knowledge, no research has been conducted with regards to worst-case excitation and testing methodologies. The research done on modelling of OWPPs and WTGs is primarily focused on standardization due to industry IPR, but every research objective requires another level of detail and a well-defined structure for the study of WTG control system interaction and its key parameters is needed to lower the risk of investing in OWPPs.

A.5.1 Purpose of PhD project

The main challenge approached in this project is modifying and combining generic models as to generate a structure suitable for estimating key parameters in both WTG and OWPP control system interaction using in-house knowledge concerning the underlying dynamic systems. This effort can be split into two sub-objectives:

1. Interaction between the control systems operating on the WTGs and complications in a small scale 2-WTG system.

2. Stability and performance of the OWPP with regard to high-level control system loops such as the STATCOM local voltage, reactive power control and distribution of set points from the park pilot.

The model distinction required for the analysis of (1) and (2) is significant and the frequency range of interest is diverse. In (2), the model is proposed to be a power source parametrized as a modified Hammerstein model due to the non-linearity, i.e. a static non-linearity combined with linear dynamics, which can represent the steady state and transient properties [156]. This split structure is repeated in the WTG modelling of (2), which will be described as a nonlinear state-space model using state-space averaging techniques to represent the switching systems. The purpose is

not to design new control systems, but apply robust control theory on the generated structure in order to assess challenging operation areas of the system, i.e. operation and stability bounds given a conservative control structure, and design methods to excite and test real-life OWPPs in order to minimize risk. Another aspect of the project is the study of physical points of measurement used in the feedback control laws in the WTG and on a park controller level in order to optimize SCADA design which is the backbone of the OWPP [158]. The objective of the project as a whole is to put emphasis on the critical aspect of ensuring compatibility, robustness and having control system specifications to complement the load-flow and dynamic simulations conducted by the OWPP developer.

A.5.2 Project Objectives

The objectives are summarized as follows:

- Design an appropriately structured WTG and system model top-down to investigate OWPP excitation and feedback loops using data from field measurements in one of DEWP's parks.
- Design adequately detailed model for small scale system control interaction based on a conservative control scheme.
- Investigation of key sensitivity parameters in both high-level and low-level models using non-linear robust analysis.
- Determine worst-case excitation as an amendment to the commissioning testing to minimize risk and guarantee operation.
- Generate a minimum requirement for WTG and OWPP control systems in order to ensure robustness with on-par performance.

A.6 Summary

The purpose of the paper has been to review the state-of-the-art of grid integration of large OWPPs using HVDC for grid connection. Furthermore, the paper has outlined some of the selected challenges, which are being addressed in three related PhD projects in close collaboration between DEWP and leading academia within the field. The state-of-the-art within the different research areas has been pictured in the paper and an outlook for future research has been proposed. The three projects described in the paper are aimed at gaining an overall understanding of OWPP operation in connection with HVDC networks, focusing on modelling, communication and control and spanning over a wide dynamic range, going from power system frequency control (several seconds range) to harmonic stability (few milliseconds range). The main challenges to be addressed have been pointed out:

- Assessment of harmonics and harmonic stability in OWPPs with substantial amount of PED (Section A.3).

- Control coordination and communication in HVDC connected OWPPs (Section A.4).
- Provision of simple but reliable models for more thorough assessment of control performance of OWPPs (Section A.5).

Harmoniously coordinating the research in the three areas will help the OWPP developer obtain an as holistic as possible picture of challenges related to OWPPs with HVDC connection. The projects aim at providing tools for addressing these possible challenges in due time in the design phase of a future OWPP.

A.7 Acknowledgments

The PhD projects described in Section A.3 and Section A.5 are financed by DEWP with support from Danish Ministry of Science, Innovation and Higher Education. The project described in Section A.4 lies within the OffshoreDC project (www.offshoredc.dk) which belongs to the Top-level Research Initiative funded by Nordic Energy Research under project no. TFI PK-int 02.

Appendix B

Observer Backstepping Control for Variable Speed Wind Turbine[1]

Roberto Galeazzi[2], Mikkel P. S. Gryning[3] and Mogens Blanke[4]

B.1 Abstract

This paper presents an observer backstepping approach to the variable speed control of wind turbines for maximizing wind power capture when operating between cut-in and rated wind speeds. The wind turbine is modeled as a two-mass drive-train system controlled by generator torque. The nonlinear controller relies on output feedback backstepping to regulate the generator torque such that a constant tip-speed-ratio can be obtained. The rotor speed is fed back while torsion angle and generator speed are estimated using a linear observer based on the dynamics of the system. The proposed scheme shows smooth and asymptotic tracking of the rotor speed as illustrated by simulation results.

B.2 Introduction

In order for wind energy to gain further attention by governments worldwide, the cost of the produced energy must match other competing sources, e.g. coal and gas power. The environmental awareness has only increased, and many countries

[1]Proceedings of the American Control Conference — 2013

[2]R. Galeazzi is with DTU Electrical Engineering,Technical University of Denmark, 2800 Kgs. Lyngby, Denmark rg@elektro.dtu.dk

[3]M. P. S. Gryning is with the SCADA Department, DONG Energy, 2820 Gentofte, Denmark, and with DTU Electrical Engineering, Technical University of Denmark, 2800 Kgs. Lyngby, Denmark migry@dongenergy.dk

[4]M. Blanke is with DTU Electrical Engineering, Technical University of Denmark, 2800 Kgs. Lyngby, Denmark, and is also adjunct prof. at the AMOS Centre of Excellence at Norwegian University of Science and Technology, 7491 Trondheim, Norway, mb@elektro.dtu.dk

are showing a large interest in deploying offshore wind power plants. Due to the high risk and capital investment needed to build offshore wind power, the energy produced is supported locally through various regulations, often subsidiaries. When the deployment of offshore wind parks reach an industrialized state, the subsidiaries will be out phased, but the maintenance cost will not be reduced. The challenging task of controlling wind turbines for maximum energy output while minimizing drive train stress is therefore of high interest.

The complexity of wind turbine models is a great challenge due to the many degrees of freedom needed to include the most important dynamic effects. The main focus in this article is controlling the drive-train as it is the part which has the most wear, and is a limiting factor in maximizing wind energy capture. The focus of wind turbine control is divided into two regions as a function of the wind speed as shown in Figure B.1. The goal in the region between cut-in and rated is to maximize energy capture. In case of wind speeds in the operational range between rated and cut-out, the goal is to keep a constant angular velocity to limit generated noise, stress and vibrations on mechanical and structural components while maintaining the maximum rated power generation. When the power is below rated value, the system should maintain its pitch angle at the optimal value and control the generator torque to achieve optimal tip-speed ratio (TSR) which is a function of the pitch angle. The pitch angle of the rotor blades determine the relative angle with respect to wind direction and thereby turbine speed, and is assumed kept constant such that the turbine speed solely is regulated indirectly by opposing the aerodynamic torque using generator torque control. Achieving optimal tip-speed ratio then simplifies to keeping the rotor blades spinning at a rotational frequency related to that of the incoming wind. The choice of operating at the optimal wind tip speed ratio is based on the turbulent wake a blade makes when passing through an air stream. Extracting power from turbulent wind is less efficient and will subject the blades to high vibration stress, i.e. the angular speed of the rotor must match the settling time of the wind for optimum power capture.

The modeling of drive-trains varies with regard to assumptions of stiffness in the shafts, damping, inertia assessment and efficiency. The drive-train used is modeled as a two-mass system which compared to the traditional one-mass model includes torsional effects. Further increasing model complexity adds an unnecessary level of detail, and there is a major consensus that a two-mass model is sufficient for representing the important dynamics in power system stability studies from which this study originates. The aerodynamic torque affecting the high-speed shaft is nonlinear, thus making the resulting system nonlinear and challenging to control in an optimum manner.

The control strategies proposed for variable speed wind turbines in literature includes adaptive back-stepping control [159], feedback linearization [160], non-linear control using exact model knowledge and one adaptive type [161]. The conservative nature of the industry and commercial aspect of wind turbines have limited the implementation of advanced non-linear control, and methods such as gain-scheduling for classical controllers [162] and bump-less transfer in between local robust controllers [163] have been favored. Wind turbines are time varying with

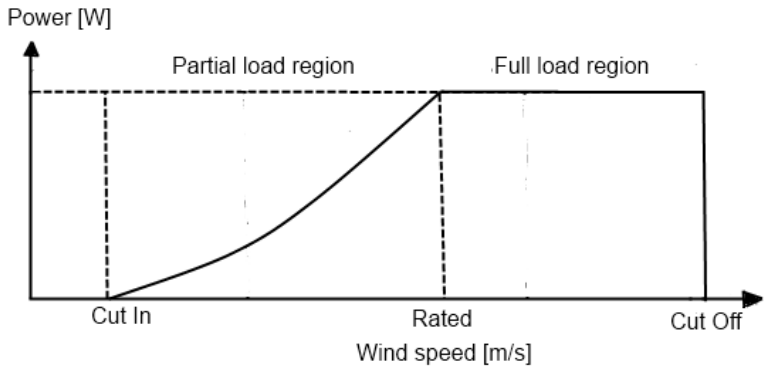

Figure B.1: Output power in different operating regions

respect to efficiency, mechanical and electrical systems, making LPV based control [164] and adaptive robust methods viable as they guarantee stability in a large range of model perturbations.

This paper proposes an observer backstepping controller for the variable speed wind turbine in order to maximize wind power capture. The output backstepping controller fully exploits the nonlinear two-mass drive-train model of the wind turbine through the combination of a globally exponentially stable (GES) observer for the estimate of the torsion angle and of the generator shaft speed, and a globally asymptotically stable (GAS) controller that guarantees asymptotic tracking of the desired rotor speed and uniform ultimate boundedness (UUB) of the torsion angle.

B.3 Model

B.3.1 Wind Power Capture

The efficiency of a wind turbine is described using a power curve which is taken as a function of the pitch angle β and tip-speed-ratio λ. The power coefficient C_p is the ratio between aerodynamic rotor power P and the power available from the wind P_w, defining the ratio of power possible of capturing,

$$C_p = \frac{P}{P_w} \tag{B.1}$$

The power available is

$$P_w = \frac{1}{2}\rho A v^3 \tag{B.2}$$

where ρ is the air density, v is the wind speed and A is the swept area of the rotor which is given by πR_r^2, where R_r is the blade tip radius. From the definition of the

power coefficient, the power captured by the wind turbine is,

$$P_m = \frac{1}{2} C_p(\lambda, \beta) \rho A v^3. \tag{B.3}$$

The tip-speed ratio λ is defined as

$$\lambda = \frac{R_r \omega}{v} \tag{B.4}$$

and it can be seen from (B.3) that operating at a fixed pitch angle makes the power coefficient C_p a function of only λ such that an optimal point on the power curve can be obtained by keeping λ constant. From the definition in (B.4) it is clear that λ is a function of the non controllable wind speed v, but also of the controllable rotor speed ω. In order to sustain maximum power output, the rotor speed must as a consequence be adjusted according to wind speed variation. The relationship between captured wind power, rotor speed and rotor torque is derived from (B.3) and (B.4) [161]

$$P(\omega) = k_w \omega^3 \tag{B.5}$$

$$T_a = \frac{P}{\omega} = k_w \omega^2 \tag{B.6}$$

where the constant k_w is given from the optimal value of C_p and λ

$$k_w = \frac{1}{2} C_p \rho \pi \frac{R_r^5}{\lambda^3}. \tag{B.7}$$

The rotor torque is applied to the low-speed shaft of the drive-train and the dynamics of the two-mass drive train system can now be set up.

B.3.2 Two-mass Drive-train Model

The two-mass drive-train model consists of two shafts interconnected by a gearbox. The aerodynamic torque drives the low-speed shaft at the rotor speed ω, while the gearbox increases the angular speed of the high speed shaft to w_g while lowering the torque. The drive-train thereby converts wind energy to mechanical energy and through the generator to electrical energy.

The inertia of the rotor and generator is respectively lumped into J_r and J_g, and T_{ls}, T_{hs} and T_g denote low speed shaft torque, high speed shaft torque and generator torque. The stiffness of the shafts are modeled through damping and torsional coefficients B_r,B_g, K_d and B_d. The inertia of the low speed shaft includes the inertia of the rotor, while the friction component includes bearing frictions. The dynamics of the low speed shaft is

$$J_r \dot{\omega} = T_a - T_{ls} - B_r \omega \tag{B.8}$$

while the high speed shaft has similar dynamics which includes the inertia of the gearbox and generator and adds the friction from bearing and gears,

$$J_g\dot{\omega_g} = T_{hs} - T_g - B_g\omega_g. \tag{B.9}$$

The drive train torsion is modeled by a torsion spring and a friction coefficient,

$$T_{ls} = K_d\theta_k + B_d\dot{\theta_k} \tag{B.10}$$

$$\theta_k = \theta_r - \theta_g/N_g \tag{B.11}$$

where N_g is the drive train gear ratio. The low speed and high speed shaft are interconnected by the gearbox such that

$$N_g = \frac{T_{ls}}{T_{hs}} = \frac{\omega_g}{\omega_{ls}}. \tag{B.12}$$

Combining equations (B.8) to (B.12) results in the following ODEs for the dynamics of the two-mass drive-train model

$$\dot{\theta}_k = \omega - \frac{1}{N_g}\omega_g \tag{B.13}$$

$$\dot{\omega} = \frac{1}{J_r}\left(-K_d\theta_k + k_w\omega^2 - (B_d + B_r)\,\omega + \frac{B_d}{N_g}\omega_g\right) \tag{B.14}$$

$$\dot{\omega}_g = \frac{1}{J_g}\left(\frac{K_d}{N_g}\theta_k + \frac{B_d}{N_g}\omega - \left(\frac{B_d}{N_g^2} + B_g\right)\omega_g - T_g\right) \tag{B.15}$$

B.4 Observer Backstepping Control

Given the third order nonlinear system (B.13)-(B.15) the control objective is to design a controller capable of dynamically varying the rotor angular velocity ω such that a desired speed reference can be tracked. This must be achieved assuming that the only available measurement is ω.

The strategy chosen is an output feedback controller based on the observer backstepping control [165]. First an observer is designed for the subsystem (θ_k, ω_g), which has an exponentially stable estimation error dynamics. Then, a new system is considered where the unmeasured states dynamics is replaced with the observer dynamics. Hence backstepping is applied using the state estimates as virtual control inputs and considering the estimation errors as disturbances whose behavior must be dominated.

Since the control objective is reference tracking the system (B.13)-(B.15) is rewritten in terms of the tracking error $e_\omega \triangleq \omega - \omega_d$ where $\omega_d(t) \in \mathcal{C}^2$ is the bounded reference trajectory with bounded derivatives. By inserting e_ω into Eqs. (B.13)-(B.15)

the following dynamics is obtained

$$\dot{\theta}_k = e_\omega + \omega_d - \frac{1}{N_g}\omega_g \tag{B.16}$$

$$\dot{e}_\omega = \frac{1}{J_r}\left(- K_d\theta_k + k_w\left(e_\omega + \omega_d\right)^2 + \frac{B_d}{N_g}\omega_g - \left(B_d + B_r\right)\left(e_\omega + \omega_d\right)\right) \tag{B.17}$$

$$\dot{\omega}_g = \frac{1}{J_g}\left(\frac{K_d}{N_g}\theta_k + \frac{B_d}{N_g}\left(e_\omega + \omega_d\right) - \left(\frac{B_d}{N_g^2} + B_g\right)\omega_g - T_g\right) \tag{B.18}$$

B.4.1 Observer Design

The observer is built as a copy of the (θ_k, ω_g) dynamics, that is

$$\dot{\hat{\theta}}_k = e_\omega + \omega_d - \frac{1}{N_g}\hat{\omega}_g \tag{B.19}$$

$$\dot{\hat{\omega}}_g = \frac{1}{J_g}\left(\frac{K_d}{N_g}\hat{\theta}_k + \frac{B_d}{N_g}\left(e_\omega + \omega_d\right) - \left(\frac{B_d}{N_g^2} + B_g\right)\hat{\omega}_g - T_g\right). \tag{B.20}$$

The estimation error dynamics is hence given by the following linear system

$$\begin{aligned}\dot{\mathbf{e}}_o &= \mathbf{A}\mathbf{e}_o \\ &= \begin{bmatrix} 0 & -\frac{1}{N_g} \\ \frac{K_d}{J_g N_g} & -\frac{1}{J_g}\left(\frac{B_d}{N_g^2} + B_g\right)\end{bmatrix}\mathbf{e}_o\end{aligned} \tag{B.21}$$

where $\mathbf{e}_0 = \left[\tilde{\theta}_k, \tilde{\omega}_g\right]^{\mathrm{T}}$. Due to linearity, exponential stability of the estimation error can be easily assessed by checking if the matrix $\mathbf{A}$ is Hurwitz; however the Lyapunov based analysis is here preferred.

Proposition 1 *The origin of the estimation error dynamics* (B.21) *is GES.*

Proof: Consider the Lyapunov function candidate

$$V_o(\mathbf{e}_o) = \mathbf{e}_o^{\mathrm{T}}\mathbf{P}_o\mathbf{e}_o \tag{B.22}$$

where

$$\mathbf{P} = \begin{bmatrix} \frac{N_g^2 B_g + B_d}{2K_d\beta_1} + \frac{\beta_1 K_d + \beta_2 J_g}{2\beta_1\beta_2\left(B_g + \frac{B_d}{N_g^2}\right)} & -\frac{J_g N_g}{2\beta_1 K_d} \\ -\frac{J_g N_g}{2\beta_1 K_d} & \frac{\beta_2 J_g^2 + \beta_1 J_g K_d}{2\beta_1\beta_2 K_d\left(B_g + \frac{B_d}{N_g^2}\right)}\end{bmatrix},$$

$\mathbf{P}_o = \mathbf{P}_o^{\mathrm{T}} > 0$, is the solution of the Lyapunov equation $\mathbf{P_o M} + \mathbf{M}^{\mathrm{T}}\mathbf{P_o} = -\mathbf{Q}$, with $\mathbf{Q} = \mathrm{diag}\{1/\beta_1, 1/\beta_2\}$ and $\beta_i > 0$. The derivative along the trajectories of (B.21)

results in

$$\begin{aligned}\dot{V}_o(\mathbf{e}_o) &= \mathbf{e}_o^{\mathrm{T}}\left(\mathbf{P_o}\mathbf{A} + \mathbf{A}^{\mathrm{T}}\mathbf{P_o}\right)\mathbf{e}_o \\ &= -\mathbf{e}_o^{\mathrm{T}}\mathbf{Q}\mathbf{e}_o \\ &\leq -\lambda_{\min}(\mathbf{Q})\left\|\mathbf{e}_o\right\|_2^2 \end{aligned} \tag{B.23}$$

Hence the origin $\mathbf{e}_o = (0,0)^{\mathrm{T}}$ is GES [166, Theorem 4.10], and the estimation error is always bounded

$$\|\mathbf{e}_o(t)\| \leq \kappa_e \left\|\mathbf{e}_o(t_0)\right\| e^{\lambda_{\max}(\mathbf{M})(t-t_0)}, \quad \forall\, t \geq t_0 \tag{B.24}$$

where $\kappa_e > 0$ and $\Re\{\lambda_{\max}(\mathbf{M})\} < 0$. ■

Remark 2 *It is worth noting that if a faster observer dynamics is needed then a standard reduced order observer could be used instead*

$$\hat{\mathbf{x}}_2 = \mathbf{w} + \mathbf{L}y \tag{B.25}$$

$$\dot{\mathbf{w}} = \mathbf{M}\mathbf{w} + \mathbf{N}T_g + \mathbf{R}y \tag{B.26}$$

where $\hat{\mathbf{x}}_2 = [\hat{\theta}_k, \hat{\omega}_g]^{\mathrm{T}}$*,* $y = x_1 = \omega$ *is the measured output, the matrices* $\mathbf{M}$*,* $\mathbf{N}$*, and* $\mathbf{R}$ *are design parameters, and* $\mathbf{L}$ *is the observer gain matrix.*

B.4.2 Output Feedback Backstepping Controller

An output feedback backstepping controller is now designed for the system

$$\begin{aligned}\dot{e}_\omega = \frac{1}{J_r}\Bigg[&- K_d\left(\hat{\theta}_k + \tilde{\theta}_k\right) + k_w\left(e_\omega + \omega_d\right)^2 \\ &- \left(B_d + B_r\right)\left(e_\omega + \omega_d\right) + \frac{B_d}{N_g}\left(\hat{\omega}_g + \tilde{\omega}_g\right)\Bigg] - \dot{\omega}_d \end{aligned} \tag{B.27}$$

$$\dot{\hat{\omega}}_g = \frac{1}{J_g}\left[\frac{K_d}{N_g}\hat{\theta}_k + \frac{B_d}{N_g}\left(e_\omega + \omega_d\right) - \left(\frac{B_d}{N_g^2} + B_g\right)\hat{\omega}_g - T_g\right] \tag{B.28}$$

where the estimate $\hat{\omega}_g$ is used as virtual control to stabilize (B.27), and T_g is the physical control input.

Proposition 3 *Consider the system* (B.27)-(B.28)*, and the reference vector* $\mathbf{\Omega}_d = [\omega_d(t), \dot{\omega}_d(t), \ddot{\omega}_d(t)]^{\mathrm{T}}$*. The output feedback backstepping control law*

$$T_g = T_g\left(\hat{\theta}_k, e_\omega, z, \mathbf{\Omega}_d\right)$$

with

$$\beta_1 > 0,\ \beta_2 > 0 \tag{B.29}$$

$$\beta_3 > \frac{4k_w^2 N_g^2 K_d^2 + N_g^2 K_d^2 \left(\frac{B_d^3}{N_g^3}\beta_1 + K_d^2\beta_2\right)^2}{4J_r^2 B_d^2} \tag{B.30}$$

$$\beta_4 > \frac{4k_w^2 + \left(\frac{B_d^3}{N_g^3}\beta_1 + K_d^2\beta_2\right)^2}{4J_r^2} \tag{B.31}$$

where

$$\begin{aligned}
T_g\left(\hat{\theta}_k, e_\omega, z, \mathbf{\Omega}\right) \triangleq\ & J_g\left(\frac{K_d}{J_g N_g} - \frac{N_g K_d\left(\frac{B_d^3}{N_g^3}\beta_1 + K_d^2\beta_2\right)}{J_r B_d} - \frac{2k_w N_g K_d}{J_r B_d}\left(e_\omega + \omega_d\right)\right)\hat{\theta}_k \\
& + J_g\left(\frac{B_d}{J_g N_g} - \frac{N_g K_d}{B_d} - \frac{N_g\left(\frac{B_d^3}{N_g^3}\beta_1 + K_d^2\beta_2\right)\left(B_d + B_r\right)}{J_r B_d}\right)\left(e_\omega + \omega_d\right) \\
& + J_g\left(\frac{K_d}{B_d} + \frac{2k_w}{J_r}\left(e_\omega + \omega_d\right)\frac{\left(\frac{B_d^3}{N_g^3}\beta_1 + K_d^2\beta_2\right)}{J_r}\right) z + J_g\left(\beta_3 + \beta_4\right)\left(1 + \left(e_\omega + \omega_d\right)^2\right) z \\
& + J_g\left(\frac{K_d}{B_d} - \frac{1}{J_g}\left(\frac{B_d}{N_g^2} + B_g\right) + \frac{\left(\frac{B_d^3}{N_g^3}\beta_1 + K_d^2\beta_2\right)}{J_r} + \frac{2k_w}{J_r}\left(e_\omega + \omega_d\right)\right)\alpha\left(\hat{\theta}_k, e_\omega, \mathbf{\Omega}_d\right) \\
& + J_g\left(\frac{2k_w^2 N_g}{J_r B_d}\left(e_\omega + \omega_d\right)^3 - \frac{k_w N_g}{J_r B_d}\left(2\left(B_d + B_r\right) - \left(\frac{B_d^3}{N_g^3}\beta_1 + K_d^2\beta_2\right)\right)\left(e_\omega + \omega_d\right)^2\right) \\
& + J_g\left(-\frac{N_g}{B_d}\left(\frac{B_d^3}{N_g^3}\beta_1 + K_d^2\beta_2 + B_d + B_r\right)\dot{\omega}_d + \frac{N_g J_r}{B_d}\ddot{\omega}_d\right) z
\end{aligned} \tag{B.32}$$

and

$$\begin{aligned}
\alpha(\hat{\theta}_k, e_\omega, \mathbf{\Omega}_d) \triangleq\ & \frac{N_g}{B_d}(-k_w(e_\omega + \omega_d)^2 + (B_d + B_r)\omega_d + K_d\hat{\theta}_k \\
& + J_r\dot{\omega}_d - (\frac{B_d^3}{N_g^3}\beta_1 + K_d^2\beta_2)e_\omega)
\end{aligned} \tag{B.33}$$

renders GAS the origin of the $(e_\omega, z, \mathbf{e}_o)$ *system, where* $T_g\left(\hat{\theta}_k, e_\omega, z, \mathbf{\Omega}_d\right)$ *is shown in* (B.32)*,*

$$z \triangleq \hat{\omega}_g - \alpha\left(\hat{\theta}_k, e_\omega, \mathbf{\Omega}_d\right) \tag{B.34}$$

and $\alpha\left(\hat{\theta}_k, e_\omega, \mathbf{\Omega}_d\right)$ *is shown in* (B.33)*.*

Proof: The first step is to stabilize the tracking error dynamics (B.27) through the virtual control $\hat{\omega}_g$. Consider the control Lyapunov function (CLF) candidate

$$V_1\left(e_\omega, \mathbf{e}_o\right) = \frac{J_r}{2} e_\omega^2 + V_o\left(\mathbf{e}_o\right) \tag{B.35}$$

whose derivative along the trajectories is given by

$$\begin{aligned}\dot{V}_1 = e_\omega \Bigg(& - K_d \left(\hat{\theta}_k + \tilde{\theta}_k\right) - \left(B_d + B_r\right)\left(e_\omega + \omega_d\right) \\ & + k_w \left(e_\omega + \omega_d\right)^2 + \frac{B_d}{N_g}\left(\hat{\omega}_g + \tilde{\omega}_g\right) - J_r \dot{\omega}_d \Bigg) - \frac{1}{\beta_1}\tilde{\theta}_k^2 - \frac{1}{\beta_2}\tilde{\omega}_g^2.\end{aligned} \tag{B.36}$$

The virtual control $\hat{\omega}_g = \alpha\left(\hat{\theta}_k, e_\omega, \mathbf{\Omega}_d\right)$ renders GAS the origin of the $(e_\omega, \mathbf{e}_o)$ system. In fact by inserting (B.33) into (B.36) $\dot{V}_1\left(e_\omega, \mathbf{e}_o\right)$ reads

$$\begin{aligned}\dot{V}_1 &= -\left(B_d + B_r\right) e_\omega^2 - K_d e_\omega \tilde{\theta}_k + \frac{B_d}{N_g} e_\omega \tilde{\omega}_g - \left(\frac{B_d^2}{N_g^2}\beta_1 + K_d^2 \beta_2\right) e_\omega^2 - \frac{1}{\beta_1}\tilde{\theta}_k^2 - \frac{1}{\beta_2}\tilde{\omega}_g^2 \\ &\leq -\left(B_d + B_r\right) e_\omega^2 - \beta_1 \left(\frac{B_d}{N_g}\left|e_\omega\right| - \frac{1}{2\beta_1}\left|\tilde{\omega}_g\right|\right)^2 \qquad \text{(B.37)} \\ &\quad - \beta_2 \left(K_d \left|e_\omega\right| - \frac{1}{2\beta_2}\left|\tilde{\theta}_k\right|\right)^2 - \kappa_1 \left\|\mathbf{e}_o\right\|_2^2 \qquad \text{(B.38)}\end{aligned}$$

which is negative definite for (β_1, β_2) as in (B.29), and where $\kappa_1 = \max\left\{-\frac{3}{4\beta_1}, -\frac{3}{4\beta_2}\right\}$.

Introducing the error variable z as in (B.34) the design of the real control input T_g is undertaken. The z-dynamics reads

$$\dot{z} = \dot{\hat{\omega}}_g - \frac{\partial \alpha}{\partial \hat{\theta}_k}\dot{\hat{\theta}}_k - \frac{\partial \alpha}{\partial e_\omega}\dot{e}_\omega - \frac{\partial \alpha}{\partial \mathbf{\Omega}_d}\dot{\mathbf{\Omega}}_d \tag{B.39}$$

and the detailed expression can be found in Appendix A. Then consider the following CLF

$$V_2\left(z, e_\omega, \mathbf{e}_o\right) = V_1\left(e_\omega, \mathbf{e}_o\right) + \frac{1}{2} z^2 + V_o\left(\mathbf{e}_o\right) \tag{B.40}$$

whose derivative along the trajectories reads as

$$\begin{aligned}\dot{V}_2 \leq & -\left(B_d + B_r\right) e_\omega^2 - \beta_1 \left(\frac{B_d}{N_g}\left|e_\omega\right| - \frac{1}{2\beta_1}\left|\tilde{\omega}_g\right|\right)^2 \\ & - \beta_2 \left(K_d \left|e_\omega\right| - \frac{1}{2\beta_2}\left|\tilde{\theta}_k\right|\right)^2 - \kappa_1 \left\|\mathbf{e}_o\right\|_2^2 - \frac{1}{\beta_3}\tilde{\omega}_g^2 - \frac{1}{\beta_4}\tilde{\theta}_k^2 + z\dot{z}\end{aligned} \tag{B.41}$$

The control input $T_g = T_g\left(\hat{\theta}_k, e_\omega, z, \mathbf{\Omega}\right)$ renders GAS the origin of the $(e_\omega, z, \mathbf{e}_o)$ system; in fact by inserting (B.32) into (B.41) $\dot{V}_2\left(z, e_\omega, \mathbf{e}_o\right)$ reads

$$\begin{aligned}\dot{V}_2 \leq \dot{V}_1 &- \frac{1}{J_g}\left(\frac{B_d}{N_g^2} + B_g\right) z^2 - \beta_3 \left(\left|\left(e_\omega + \omega_d\right) z\right| - \frac{k_w N_g K_d}{J_r B_d \beta_3}\left|\tilde{\theta}_k\right|\right)^2 \\ &- \beta_3 \left(|z| - \frac{N_g K_d \left(\frac{B_d^3}{N_g^3}\beta_1 + K_d^2 \beta_2\right)}{2 J_r B_d \beta_3}\left|\tilde{\theta}_k\right|\right)^2 - \beta_4 \left(\left|\left(e_\omega + \omega_d\right) z\right| - \frac{k_w}{J_r \beta_4}\left|\tilde{\omega}_g\right|\right)^2 \\ &- \beta_4 \left(|z| - \frac{\frac{B_d^3}{N_g^3}\beta_1 + K_d^2 \beta_2}{2 J_r \beta_4}\left|\tilde{\omega}_g\right|\right)^2 - \left(1 - \frac{k_w^2 N_g^2 K_d^2}{J_r^2 B_d^2 \beta_3} - \frac{N_g^2 K_d^2 \left(\frac{B_d^3}{N_g^3}\beta_1 + K_d^2 \beta_2\right)^2}{4 J_r^2 B_d^2 \beta_3}\right) \tilde{\theta}_k^2 \\ &- \left(1 - \frac{k_w^2}{J_r^2 \beta_4} - \frac{\left(\frac{B_d^3}{N_g^3}\beta_1 + K_d^2 \beta_2\right)^2}{4 J_r^2 \beta_4}\right) \tilde{\omega}_g^2 \end{aligned} \tag{B.42}$$

■

which is negative definite for (β_3, β_4) as in (B.30)-(B.31).

B.4.3 Boundedness of the θ_k Dynamics

As last step in the design of the output tracking controller it is important to prove that the dynamics of the torsion angle θ_k remains bounded. Towards this end consider the candidate Lyapunov function

$$V_3\left(\theta_k\right) = \frac{1}{2}\theta_k^2 \tag{B.43}$$

whose derivative along the trajectory of (B.13) is

$$\begin{aligned}\dot{V}_3 &= \theta_k \Big[e_\omega + \omega_d - \frac{1}{B_d}\big(- k_w \left(e_\omega + \omega_d\right)^2 + \left(B_d + B_r\right)\omega_d \\ &\quad + K_d\left(\theta_k + \tilde{\theta}_k\right) + J_r \dot{\omega}_d - \left(\beta_1 + \beta_2\right) e_\omega\big)\Big] \qquad \text{(B.44)} \\ &\leq -\frac{K_d}{B_d}\theta_k^2 + \left|\left(e_\omega + \omega_d\right)\right|\left|\theta_k\right| + \frac{k_w}{B_d}\left(e_\omega + \omega_d\right)^2 \left|\theta_k\right| \\ &\quad + \frac{B_d + B_r}{B_d}\left|\omega_d\right|\left|\theta_k\right| + \frac{K_d}{B_d}\left|\tilde{\theta}_k\right|\left|\theta_k\right| + \frac{J_r}{B_d}\left|\dot{\omega}_d\right|\left|\theta_k\right| + \frac{\beta_1 + \beta_2}{B_d}\left|e_\omega\right|\left|\theta_k\right|. \qquad \text{(B.45)}\end{aligned}$$

The desired trajectory $\omega_d\left(t\right)$ is a class $\mathcal{C}^2$ bounded function with bounded first derivative, that is

$$\left|\omega_d\left(t\right)\right| \leq \omega_{d,\max} < \infty \tag{B.46}$$

$$\left|\dot{\omega}_d\left(t\right)\right| \leq \dot{\omega}_{d,\max} < \infty \tag{B.47}$$

Moreover the dynamics of the tracking error $e_\omega(t)$ was shown to be asymptotically stable hence

$$|e_\omega(t)| \leq \gamma\left(|e_\omega(t_0)|, t - t_0\right), \quad \forall t \geq t_0 \tag{B.48}$$

where $\gamma(r, s)$ is a class $\mathcal{KL}$ function; whereas the dynamics of the estimation error $\mathbf{e}_{\text{obs}}$ was shown to be exponentially stable therefore

$$\left|\tilde{\theta}_k(t)\right| \leq k_e \left|\tilde{\theta}_k(t_0)\right| e^{\lambda_{\max}(\mathbf{A})(t-t_0)}, \quad \forall t \geq t_0. \tag{B.49}$$

By replacing these upper bounds into (B.45) we obtain

$$\begin{aligned}\dot{V}_3 \leq & -(1-\delta)\frac{K_d}{B_d}\theta_k^2 - \delta\frac{K_d}{B_d}\theta_k^2 + \left(\left(1 + \frac{\beta_1+\beta_2}{B_d}\right)\gamma\left(|e_\omega(t_0)|, 0\right)\right. \\ & + \left(1 + \frac{B_d + B_r}{B_d}\right)\omega_{d,\max}\Bigg)|\theta_k| + \left(\frac{k_w}{B_d}\left(\gamma\left(|e_\omega(t_0)|, 0\right) + \omega_{d,\max}\right)^2\right. \\ & \left. + \frac{K_d}{B_d}k_e\left|\tilde{\theta}_k(t_0)\right| + \frac{J_r}{B_d}\dot{\omega}_{d,\max}\right)|\theta_k| \leq -(1-\delta)\frac{K_d}{B_d}\theta_k^2\end{aligned} \tag{B.50}$$

for all $|\theta_k| > \mu$

$$\begin{aligned}\mu = \frac{B_d}{\delta K_d}\Bigg(&\left(1 + \frac{\beta_1+\beta_2}{B_d}\right)\gamma\left(|e_\omega(t_0)|, 0\right) + \left(1 + \frac{B_d + B_r}{B_d}\right)\omega_{d,\max} \\ &+ \frac{k_w}{B_d}\left(\gamma\left(|e_\omega(t_0)|, 0\right) + \omega_{d,\max}\right)^2 + \frac{K_d}{B_d}k_e\left|\tilde{\theta}_k(t_0)\right| + \frac{J_r}{B_d}\dot{\omega}_{d,\max}\Bigg)\end{aligned} \tag{B.51}$$

whit $0 < \delta < 1$. Hence $\theta_k(t)$ is globally uniformly ultimately bounded.

B.5 Control Strategy Testing

B.5.1 Operating point

The system is designed to operate in the partial load region, i.e the the interval of wind speeds ranging $5m/s$ to $12.3m/s$ for this particular wind turbine. A wind-speed ($\bar{v}$) and a tip-speed ratio ($\bar{\lambda}$) is selected and the state of the system is calculated. Using (B.4) the angular velocity of the rotor can be calculated and through (B.12) the angular velocity of the generator shaft ω_g can be found. Inserting (B.4) into (B.6) yields

$$\bar{T_a} = \frac{1}{2\bar{\omega}}\rho A\bar{v}^3 C_p(\bar{\lambda}, \bar{\beta}) \tag{B.52}$$

and utilizing (B.12) gives

$$\bar{T_g} = \frac{1}{N_g}\bar{T_a}. \tag{B.53}$$

Table B.1: Simulation parameters

$\bar{v}[m/s]$	$\bar{\lambda}$	$\bar{\beta}[^\circ]$	$\bar{T}_a[MNm]$
10.33	8.00	0.00	2.17
$\bar{T}_g[kNm]$	$\bar{\theta}_k[m^\circ]$	$C_p(\bar{\lambda}, \bar{\beta})$	
22.86	80.42	0.46	

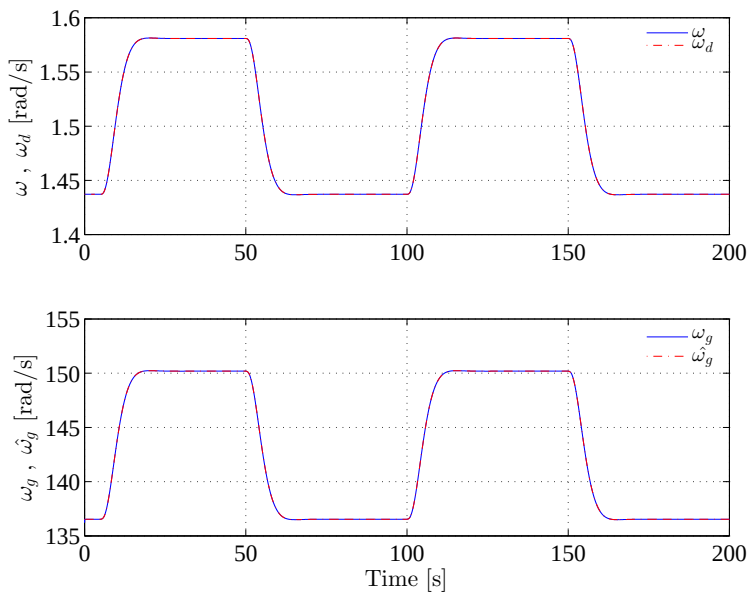

Figure B.2: Rotor speed tracking - 1. Desired and real rotor speed, 2. Generator angular velocity and estimate.

The steady state torsion angle $\bar{\theta_k}$ can be found by inserting (B.10) into (B.8) which gives the following

$$\bar{\theta_k} = \frac{\bar{T_a} - B_r\bar{\omega}}{K_d}. \tag{B.54}$$

Equations (B.52)-(B.54) enables the non-linear simulation model to be initiated in an operating point. The tip-speed-ratio value selected for simulations reflects an initial condition of being in an position for maximum power generation. The values used in simulation are shown in Table B.1.

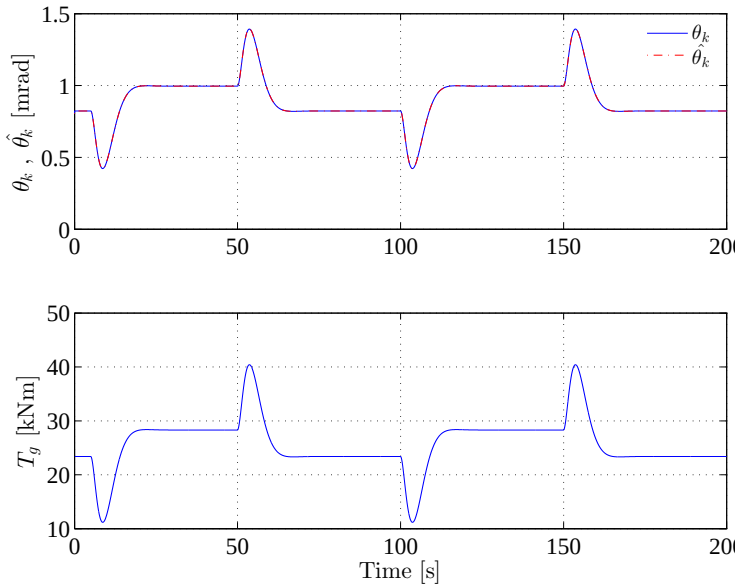

Figure B.3: Rotor speed tracking - 1. Torsion angle and estimate, 2. Generator torque.

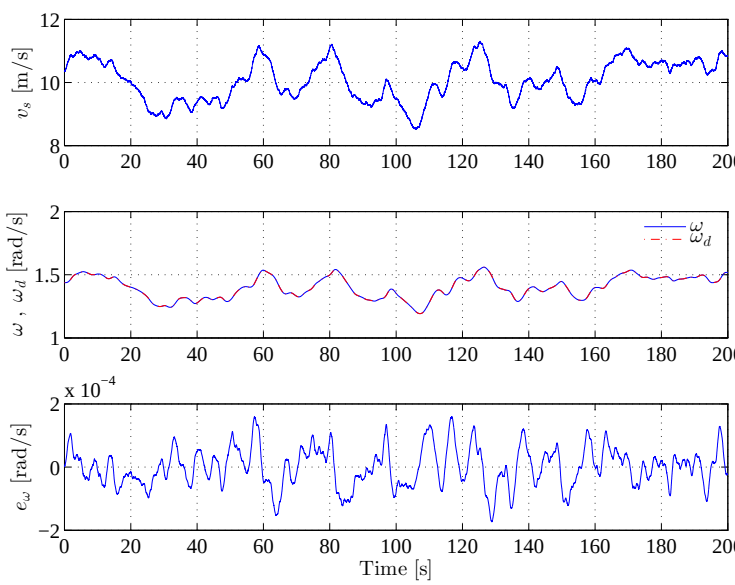

Figure B.4: Optimal TSR tracking in stochastic environment - 1. Wind speed, 2. Desired and real rotor speed, 3. Tracking error.

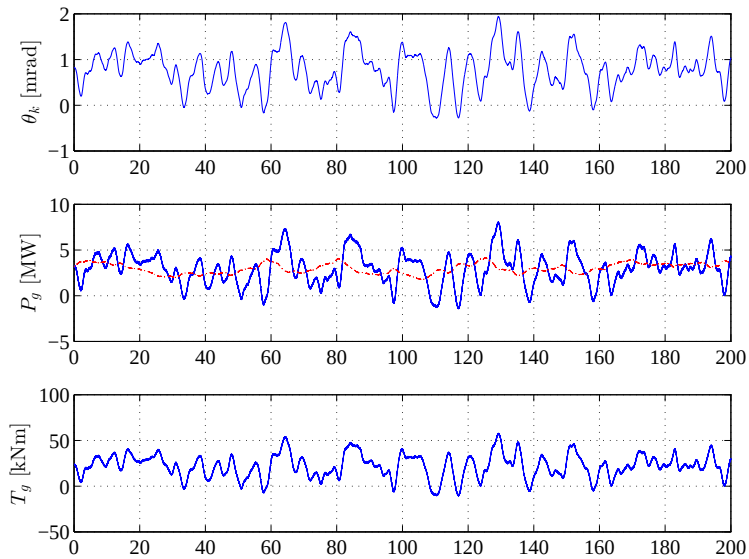

Figure B.5: Optimal TSR tracking in stochastic environment - 1. Torsion angle, 2. Power generated, 3. Generator torque.

B.5.2 Testing

The rotor speed tracking of a square wave with a frequency of 0.06 radians per second and an amplitude of 10 percent of the operation point is shown in Figure B.2 and B.3. It is clear that the proposed control scheme achieves smooth and precise asymptotic speed tracking while the observer estimates the unmeasured states perfectly. The system is tested in a stochastic environment in which the wind is simulated using RISØ DTU SB-2 wind model with a mean wind of $10.33m/s$ and 12% turbulence. Given an optimal tip-speed ratio and the measured wind speed, the optimal rotor speed with respect to wind power capture can be calculated from (B.4). Simulation of the wind speed and tracking of the optimal rotor angular velocity is shown in Figure B.4. The system tracks the desired rotor speed nicely, having $||e_\omega||_\infty = 324\mu rad/s$. The power generated and control effort is shown in Figure B.5. The system drive train stress during the simulation period is measured as the magnitude of the change in torsion angle:

$$S = \int \dot{\theta_k}(t)^2 dt. \tag{B.55}$$

The stress affecting the system during stochastic simulation is $2.08mrad^2/s$ which is comparable to similar systems.

B.6 Conclusions

Maximizing wind power capture in wind turbines is a major challenge given the constant evolution of the technologies involved and measurements available. In this work an output feedback backstepping approach has been proposed for the variable speed control of the wind turbine. Due to the challenges in measuring the torsion angle and generator speed a linear observer was designed and the estimation error dynamics was shown to be globally exponentially stable. Then an output feedback backstepping controller was designed exploiting the measured and estimated states and the closed-loop system was shown to be globally asymptotically stable. Finally, it was also proven that the dynamics of the torsion angle remains bounded under the action of the controller; in particular it was shown that it is uniformly ultimately bounded. Simulation results have confirmed the effectiveness of the proposed approach.

Appendix

B.6.1 Dynamics of the Error Variable z

The error variable dynamics is given by

$$
\begin{aligned}
\dot{z} &= \dot{\hat{\omega}}_g - \frac{\partial \alpha}{\partial \hat{\theta}_k}\dot{\hat{\theta}}_k - \frac{\partial \alpha}{\partial e_\omega}\dot{e}_\omega - \frac{\partial \alpha}{\partial \mathbf{\Omega}_d}\dot{\mathbf{\Omega}}_d \\
&= \left(\frac{K_d}{J_g N_g} + \frac{N_g K_d\left(\beta_1+\beta_2\right)}{J_r B_d} - \frac{2k_w N_g K_d}{J_r B_d}\left(e_\omega+\omega_d\right)\right)\hat{\theta}_k \\
&\quad + \left(\frac{B_d}{J_g N_g} - \frac{N_g K_d}{B_d}\right)\left(e_\omega+\omega_d\right) + \left[\frac{K_d}{B_d} - \frac{1}{J_g}\left(\frac{B_d}{N_g^2}+B_g\right)\right] \\
&\quad \times \left[z + \alpha\left(\hat{\theta}_k, e_\omega, \omega_d, \dot{\omega}_d\right)\right] - \frac{N_g}{B_d}\left[\left(\frac{B_d^3}{N_g^3}\beta_1 + K_d^2\beta_2\right) + B_d + B_r\right]\dot{\omega}_d \\
&\quad + \frac{N_g J_r}{B_d}\ddot{\omega}_d - \frac{N_g}{J_r B_d}\left[-2k_w\left(e_\omega+\omega_d\right) - \left(\frac{B_d^3}{N_g^3}\beta_1 + K_d^2\beta_2\right)\right] \\
&\quad \times \left[k_w\left(e_\omega+\omega_d\right)^2 - \left(B_d+B_r\right)\left(e_\omega+\omega_d\right)\right] \\
&\quad - \frac{1}{J_r}\left[-2k_w\left(e_\omega+\omega_d\right) - \left(\frac{B_d^3}{N_g^3}\beta_1 + K_d^2\beta_2\right)\right] \\
&\quad \times \left[z + \alpha\left(\hat{\theta}_k, e_\omega, \omega_d, \dot{\omega}_d\right)\right] - \frac{2k_w N_g K_d}{J_r B_d}\left(e_\omega+\omega_d\right)\tilde{\theta}_k \\
&\quad - \frac{N_g K_d\left(\frac{B_d^3}{N_g^3}\beta_1 + K_d^2\beta_2\right)}{J_r B_d}\tilde{\theta}_k \\
&\quad + \frac{2k_w}{J_r}\left(e_\omega+\omega_d\right)\tilde{\omega}_g + \frac{\left(\frac{B_d^3}{N_g^3}\beta_1 + K_d^2\beta_2\right)}{J_r}\tilde{\omega}_g - \frac{1}{J_g}T_g
\end{aligned}
\tag{B.56}
$$

Appendix C

Wind turbine inverter robust loop-shaping control subject to grid interaction effects[1]

Mikkel P.S. Gryning[2], Qiuwei Wu[3], Mogens Blanke[3], Hans Henrik Niemann[3] and Karsten P.H. Andersen[4]

C.1 Abstract

An $\mathcal{H}_\infty$ robust control of wind turbine inverters employing an LCL filter is proposed in this paper. The controller dynamics are designed for selective harmonic filtering in an offshore transmission network subject to parameter perturbations. Parameter uncertainty in the network originates from the grid and the number of wind turbines connected. Power converter based turbines inject harmonic currents, which are attenuated by passive filters. A robust high order active filter controller is proposed to complement the passive filtering. The $\mathcal{H}_\infty$ design of the control loop enables desired tracking with integral effect while bounding the induced change. The design was tested in an aggregated model of the London Array offshore wind power plant and compared with traditional PI controller designs. Robust stability and performance and a reduction of control effort by 25% are obtained over the full envelope of operation.

[1]IEEE Transactions on Sustainable Energy, 2015

[2]M. Gryning is with DONG Energy and Department of Electrical Engineering, Technical University of Denmark, e-mail: migry@dongenergy.dk

[3]Q. Wu, M. Blanke and H.H. Niemann are with Department of Electrical Engineering, Technical University of Denmark, 2800 Kgs. Lyngby, Denmark, e-mail: qw@elektro.dtu.dk, mb@elektro.dtu.dk and hhn@elektro.dtu.dk

[4]K. Andersen is with DONG Energy, 2820 Gentofte, Denmark, e-mail: kahan@dongenergy.dk

C.2 Introduction

Offshore wind turbines (WT) are increasing in power rating. Turbine output control requirements have been extended as the power rating has increased. The requirements have been further extended by the move to a power electronic interface. Modern type-4 wind turbines are interfaced to the point of common coupling (PCC) by current-controlled voltage source inverter (VSI) systems [167],[168]. VSIs have fast dynamic response and high quality of the power injection [169]. The current contains components at switching frequency caused by the pulse-width modulation (PWM) switching process [170],[171]. Additionally, the controlled output current is disturbed by polluted PCC voltage due to harmonics of the fundamental power frequency and harmonic resonance in the offshore transmission network [172].

Damping of switching frequency components by L, LC or LCL ac-side filter improves attenuation [173]. L filters require high frequency switching and in high power applications, such as wind turbines, the switching frequency is kept low to reduce losses [43]. The LCL filter provides ideally $60dB$ per decade harmonic rejection compared with $20dB$ of the L filter at lower inductance values hence makes lower switching frequencies possible [43]. The LCL filter attenuates the harmonics within the first carrier group, and additional damping of 2^{nd} and 3^{rd} order harmonics is achieved using trap filters [174].

A challenge in the LCL filter design is the resonance characteristic [44]. Active converter resonance damping was proposed for an LC filter by injecting a damping voltage proportional to the filter capacitance [45]. This virtual resistor control loop was extended to LCL filters to damp resonance peaks [46]. An optimal virtual resistor value was found to be a function of the LCL filter resonance frequency and capacitance [175]. However, impedance seen from the inverter is only partially known at the design state, leading to suboptimal resistor values and decreased damping under uncertain conditions [48]. The sideband harmonics in a resonant grid contains multiples of the power system fundamental and will excite undamped system dynamics [57]. Transmission system uncertainty extends the envelope of parameters, and control must encapsulate both uncertainty and power system harmonics [176].

This can be achieved by using grid voltage feed forward to suppress induced current distortion with proportional-resonant (PR) control. PR control introduces an infinite gain at a selected resonant frequency [177]. Repetitive control (RC) extends the idea to a a parallel combination of PI and many resonant controllers [178]. Hybrid designs such as a combination of PR with odd harmonic RC were proposed by [85]. The RC theory was extended to an adaptive solution by [179], and robust RC control wrt. grid frequency change was introduced by [180]. Multiple PI controllers in the $dq0$ were introduced as a variation of PR in the $\alpha\beta\gamma$ reference frame in [178]. Hysteresis Band and nonlinear sliding mode control strategies were suggested in [79] and [181].

This paper takes another route by suggesting a control design that combines robust performance and selective filtering. A single repetitive $\mathcal{H}_\infty$ design is introduced by cascading notch filters in the synthesis. This enables a wide bandwidth of the notch filters without sacrificing performance while guaranteeing stability in the full envelope

of operation. A major contribution is the novel idea of ensuring low attenuation of system frequency harmonics to minimize cascade-controller interaction. The network is aggregated and the WTs are a controllable voltage source with harmonic distortion. This enables a study of the interaction between the network, grid and VSI dynamics for varying parameters.

The paper is organized as follows. After a discussion on control requirements, an analytical model is introduced and uncertainty is discussed. Evaluation criteria are then defined and an $\mathcal{H}_\infty$ controller is designed and compared with the traditional controllers in simulation, followed by conclusions.

C.3 Control Requirements

Using an LCL filter requires damping of the grid-converter resonance with robustness against perturbations of system parameters. The resonance frequency of an LCL filter with known grid inductance L_g is

$$\omega_{res} = \sqrt{\frac{L_{f1} + L_{f2} + L_g}{L_{f1}(L_{f2} + L_g)C_f}}, \tag{C.1}$$

which determines the amount of damping needed in the control system [182]. If L_g is uncertain, there exists a large envelope of operation which opts for a robust control design. The system harmonics of other WTs acts as a disturbance on the inverter control through the voltage at the PCC. The attenuation of a voltage disturbance at the grid to a net change in injected current from the inverter is *harmonic admittance* [183].

Figure C.1 shows the harmonic admittance of the system with two distinct resonance frequencies. The resonant frequency of the LCL filter given by equation C.1 is located at $965Hz$ and its effect must be damped by the control system. The topology

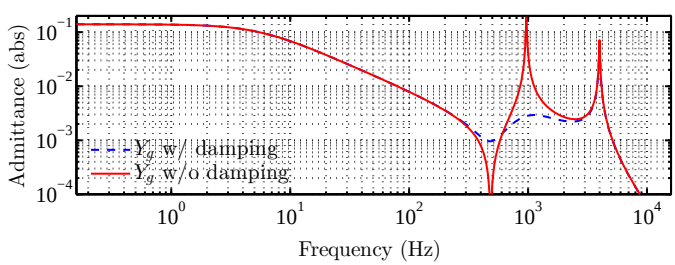

Figure C.1: Open loop sensitivity function of equation C.5. Harmonic admittance w/ damping, i_{f2}/v_g, is adequate. Control design must minimize control effort while not attenuating the power system spectra.

of the VSI and the voltage modulator switching frequency f_s sets the maximum obtainable bandwidth of the control system. A compromise between disturbance rejection and reference tracking is $f_{bi} = f_s/5$ [119]. For $5MW$ class converters,

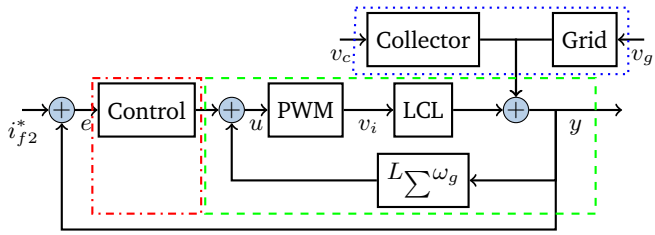

Figure C.2: Certain system model of closed loop control. Control($dashdot$), plant($stipple$) and disturbances($dotted$).

switching losses dictate a low frequency of $1 - 2kHz$ [120]. The crossover frequency for control then needs to be located around $f_{bi} = 2kHz/5 = 0.4kHz$ to ensure proper attenuation of switching harmonics.

The control structure and decoupling feedback is shown in Figure C.2. The current injection due to potential changes in the grid and collector system is shown as output disturbances. The reference current is an externally generated signal, normally from a DC-link controller. The ideal control requirements for the system are:

- Low attenuation of odd harmonics of the fundamental power system frequency as they are the most prominent harmonics in the current spectrum [184], i.e. sensitivity function gain of $1 - \epsilon,\ \epsilon \in [0.1; 0.2]\ \forall\omega \in \omega_h$.
- Tracking of abc $50Hz$ fundamental, steady state in dq with bandwidth $f_{bi} = 0.4kHz$.
- Maximum overshoot of 20%.
- Roll-off of output disturbance to control signal of $40dB$ at f_{bi}.

The Measurement noise of the transformer inductor currents is attenuated by the notch filter characteristic for the selected power system harmonics. Outside of the controller bandwidth, the LCL filter ensures an attenuation of 60 dB/dec. These requirements must be met for uncertainties in the range specified in Table C.1.

C.4 Three-Phase Current-Controlled VSI with LCL Filter

The system topology of a VSI with a LCL filter is shown in Figure C.3, where L_{f1} and L_{f2} are the filter inductance. R_{f1} represents the inverter switching losses, R_{f2} is the copper losses of inductor L_{f2}, and C_f is the filter capacitance. The inductor L_g and resistance R_g are the grid side inductance and resistance seen from the terminals of the transformer. The collector network is modelled by a lumped

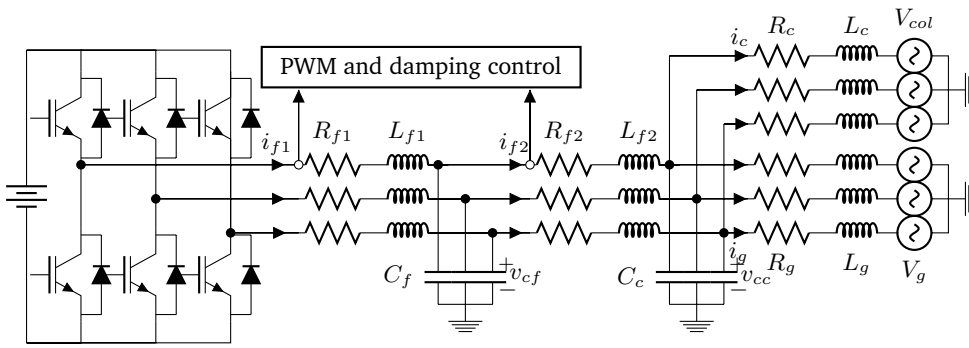

Figure C.3: Three-phase VSI with LCL filter connected to grid and transmission network.

capacitance C_c, a resistance R_c and an inductance L_c. The grid voltage is v_g; the capacitor voltage is v_{cf}; i_{f1}, i_{f2} and i_g represents the inverter output currents and the injected transformer current respectively, and the voltage at the inverter output terminals is v_i. The total inductance seen from the terminals of the capacitors is given by $L_t = L_{f2} + L_g$ and the resistance $R_t = R_{f2} + R_g$. The collector network is modeled as a controlled voltage source and an equivalent impedance using the NREL aggregation method, taking into account each element upstream of the VSI [185],[186]. The collector system is based on the London Array project and uses string 12 on substation 2 as a standard reference for connecting m identical strings to the busbar. Each string consists of n_1 wind turbines 650m apart connected by underground cable. The cables are of type $500mm^2(t_2)$ for the first n_2 WTs in the string and type $150mm^2(t_1)$ for the remaining. The aggregated impedance of one string equals,

$$\boldsymbol{Z_s} = \frac{\sum_{k=1}^{n_1-n_2} k^2 Z_k^{t_1}}{(n_1-n_2)^2} + \frac{\sum_{k=(n_1-n_2+1)}^{n_1} k^2 Z_k^{t_2}}{n_2^2}, \tag{C.2}$$

and the parallel connection of the aggregated strings to the busbar is,

$$\boldsymbol{Z_c} = \frac{\sum_{k=1}^{m}(n_k^2 Z_s^k)}{(\sum_{k=1}^{m} n_k)^2} = \frac{mn_1^2 \boldsymbol{Z_s}}{(mn_1)^2}, \tag{C.3}$$

as the strings are assumed identical. The capacitance in the cables are represented in the system as,

$$\boldsymbol{C_c} = \sum_{k=1}^{m}\left(\sum_{h=1}^{n_1-n_2} C_h^{t_1} + \sum_{h=n_1-n_2+1}^{n_1} C_h^{t_2}\right). \tag{C.4}$$

The aggregated system is uncertain in its parameters. The uncertainties in the collector cables, grid and internal filter are listed in Table C.1. Space vector transformation and measurement of the line voltage enables the transformation of the system equations into Park's d-q frame rotating synchronously with the grid

Table C.1: Relative uncertainty in system parameters

Potential	**Structure**	**Element**	**Uncertainty** $\pm$
$0.69kV$ LV	LCL Filter	C_f, Z_{f1} Z_{f1}, Z_{f2}	15%
$33kV$ HV	Collector Grid	C_c, L_c , R_c L_g, R_g	75%

angular speed. Assuming that the mutual capacitance and inductance between the phases are zero, the dynamics of the inverter is transformed to,

$$\begin{aligned}
\boldsymbol{L_{f1}}\frac{\boldsymbol{di_{f1}^{dq}}}{dt} + \boldsymbol{R_{f1}i_{f1}^{dq}} &= \boldsymbol{v_{inv}^{dq}} - \boldsymbol{v_{cf}^{dq}} - \boldsymbol{v_d^{dq}} + \boldsymbol{DL_{f1}D\omega i_{f1}^{dq}} \\
\boldsymbol{L_{f2}}\frac{\boldsymbol{di_{f2}^{dq}}}{dt} + \boldsymbol{R_{f2}i_{f2}^{dq}} &= a\boldsymbol{v_{cc}^{dq}} - \boldsymbol{v_{cf}^{dq}} - \boldsymbol{v_d^{dq}} + \boldsymbol{DL_{f2}D\omega i_{f2}^{dq}} \\
\boldsymbol{L_c}\frac{\boldsymbol{di_c^{dq}}}{dt} + \boldsymbol{R_c i_c^{dq}} &= a^2\boldsymbol{v_{cc}^{dq}} - a^2\boldsymbol{v_{col}^{dq}} + \boldsymbol{DL_c D\omega i_c^{dq}} \\
\boldsymbol{L_g}\frac{\boldsymbol{di_g^{dq}}}{dt} + \boldsymbol{R_g i_g^{dq}} &= a^2\boldsymbol{v_g^{dq}} - a^2\boldsymbol{v_{cc}^{dq}} + \boldsymbol{DL_t D\omega i_g^{dq}} \\
\boldsymbol{C_f}\frac{\boldsymbol{dv_{cf}^{dq}}}{dt} &= \boldsymbol{i_{f1}^{dq}} + \boldsymbol{i_{f2}^{dq}} + \boldsymbol{DC_f D\omega v_c^{dq}} \\
\boldsymbol{C_c}\frac{\boldsymbol{dv_{cc}^{dq}}}{dt} &= (1/a^2)(\boldsymbol{i_g^{dq}} - \boldsymbol{i_c^{dq}}) - (1/a)i_{f2}^{dq} + \boldsymbol{DC_c D\omega v_c^{dq}},
\end{aligned} \tag{C.5}$$

where,

$$\boldsymbol{\omega} = \begin{bmatrix} 0 & \omega_g \\ -\omega_g & 0 \end{bmatrix} \quad \boldsymbol{D} = \begin{bmatrix} 0 & 1 \\ 1 & 0 \end{bmatrix}, \tag{C.6}$$

and $\boldsymbol{L_{f1}}, \boldsymbol{L_{f2}}, \boldsymbol{L_c}, \boldsymbol{L_g}, \boldsymbol{R_{f1}}, \boldsymbol{R_{f2}}, \boldsymbol{R_c}, \boldsymbol{R_g}, \boldsymbol{C_f}$ and $\boldsymbol{C_c}$ are diagonal matrices with the dimensions $2 \times 2 \in \Re^+$ composed of the nominal values of the components in the dq frame projected to the primary side of the transformer, a is the pad-mounted transformer ratio given by $0.69kV/33kV$ and $\boldsymbol{v_d^{dq}}$ is the potential difference across a virtual damping resistor. The nominal system component values are frequency dependent. This frequency dependence is comprised in the system uncertainty description. The system frequency ω_g is assumed to be constant. The model is bounded by the limits of the physical system given by the switching technology used in the VSI. The injected current is limited by the maximum current rating of the inverter, and the load voltage at the terminals is limited to the maximum output voltage of the inverter. The LCL filter added to the system to attenuate the switching harmonics has an unwanted resonance frequency that should be damped to enable the design of a high-bandwidth current controller and mitigate the grid-inducted distortion. The LCL filter resonance can be damped by injecting a damping voltage proportional to the capacitor current in the filter [46]. The injected damping voltage

is introduced by defining the damping resistance R_d and the decoupling voltage,

$$\boldsymbol{v_d^{dq}} = \boldsymbol{R_d}(\boldsymbol{i_{f1}^{dq}} + \boldsymbol{i_{f2}^{dq}}). \tag{C.7}$$

It should be noted that the use of a directly measured capacitor current could inject noise into the system, and one could use a low-pass filtered signal to overcome this issue. Assuming that the system in (C.5) is decoupled by feedback and no collector system present, the damping properties of the system wrt. the choice of damping resistor R_d can be investigated. The nominal value of the resistor is [183],

$$R_d = \frac{1}{3\omega_{res}C_f}. \tag{C.8}$$

Given that the virtual resistance is calculated from the nominal resonant frequency of the LCL filter, the damping properties of the chosen resistance will change with parametric uncertainty of the grid inductance. Addtive uncertainty on L_g is introduced as,

$$L_g = L_{gn}(1+\delta). \tag{C.9}$$

The change of the resonant frequency of the LCL filter as a function of the uncertainty parameter δ and the nominal frequency is found to be,

$$\omega_{res}(\delta)^2 = \frac{(L_{gn}+L_{f2})(L_{gn}(1+\delta)+L_{f1}+L_{f2})}{(L_{gn}(1+\delta)+L_{f2})(L_{f1}+L_{f2}+L_{gn})}\omega_{res}^2|_{\delta=0}. \tag{C.10}$$

The virtual resistance was determined from the nominal resonant frequency and its attenuation properties from inverter voltage to grid current $H(s)$, will change as

$$\left|\frac{H(\omega_{res})|_{\delta=\delta}}{H(\omega_{res})|_{\delta=0}}\right| = \frac{L_{gn}+L_t}{L_{gn}(1+\delta)+L_{f1}+L_{f2}}. \tag{C.11}$$

Equation (C.11) shows that the attenuation of the resonant peak at the perturbed resonant frequency will decrease with increased δ. The magnitude of the change is a function of the relation between the inverter side inductance and the grid side inductance. Minimization of costs opts for lower values of L_{f1} which then increases the effect of a change in the uncertain parameter L_g, which determines the control requirements needed for operation in an uncertain grid.

C.4.1 Uncertain Continuous Time State-Space Model

External voltage disturbances and uncertainty in the system parameters wrt. both cross coupling and active damping requires an uncertain formulation of the system dynamics. The uncertainty of parameters should be included in the system model in addition to possible unmodelled internal dynamics and time delays. The system can be formulated as a nominal system with dynamic disturbances and perturbations of the parameters.

$$\begin{aligned}\frac{d\boldsymbol{x}(t)}{dt} &= \boldsymbol{A_0}\boldsymbol{x}(t) + \boldsymbol{B_0}\boldsymbol{u}(t) + \boldsymbol{E_0}\boldsymbol{d}(t) + \boldsymbol{W_0}\boldsymbol{x}(t)\\ y(t) &= \boldsymbol{C}\boldsymbol{x}(t),\end{aligned} \tag{C.12}$$

where

$$\begin{aligned} \boldsymbol{x(t)} &= \begin{bmatrix} \boldsymbol{i_{f1}^{dq}} & \boldsymbol{i_{f2}^{dq}} & \boldsymbol{i_{c}^{dq}} & \boldsymbol{i_{g}^{dq}} & \boldsymbol{v_{cf}^{dq}} & \boldsymbol{i_{cc}^{dq}} \end{bmatrix}^{\intercal} \\ \boldsymbol{u(t)} &= \begin{bmatrix} \boldsymbol{v_{inv}^{dq}} \end{bmatrix}^{\intercal},\ \boldsymbol{d(t)} = \begin{bmatrix} \boldsymbol{v_{col}^{dq}} & \boldsymbol{v_{g}^{dq}} \end{bmatrix}, \end{aligned} \tag{C.13}$$

with $\boldsymbol{C} = \boldsymbol{I}$ and $\boldsymbol{A_0}$, $\boldsymbol{B_0}$, $\boldsymbol{E_0}$ and $\boldsymbol{W_0}$ as shown in (C.14).

$$\boldsymbol{A_0} = \begin{bmatrix} -(\boldsymbol{R_{f1}} + \boldsymbol{R_d})\boldsymbol{L_{f1}^{-1}} & -\boldsymbol{R_d}\boldsymbol{L_{f1}^{-1}} & \boldsymbol{O_{2x2}} & \boldsymbol{O_{2x2}} & -\boldsymbol{L_{f1}^{-1}} & \boldsymbol{O_{2x2}} \\ -\boldsymbol{R_d}\boldsymbol{L_{f2}^{-1}} & -(\boldsymbol{R_{f2}} + \boldsymbol{R_d})L_{f2}^{-1} & \boldsymbol{O_{2x2}} & \boldsymbol{O_{2x2}} & -\boldsymbol{L_{f2}^{-1}} & a\boldsymbol{L_{f2}^{-1}} \\ \boldsymbol{O_{2x2}} & \boldsymbol{O_{2x2}} & -\boldsymbol{R_c}\boldsymbol{L_c^{-1}}\boldsymbol{O_{2x2}} & \boldsymbol{O_{2x2}} & a^2\boldsymbol{L_c^{-1}} & \\ \boldsymbol{O_{2x2}} & \boldsymbol{O_{2x2}} & \boldsymbol{O_{2x2}} & \boldsymbol{R_g}\boldsymbol{L_g^{-1}} & \boldsymbol{O_{2x2}} & -a^2\boldsymbol{L_g^{-1}} \\ \boldsymbol{C_f^{-1}} & \boldsymbol{C_f^{-1}} & \boldsymbol{O_{2x2}} & \boldsymbol{O_{2x2}} & \boldsymbol{O_{2x2}} & \boldsymbol{O_{2x2}} \\ \boldsymbol{O_{2x2}} & -(a\boldsymbol{C_c^{-1}}) & -(a^2\boldsymbol{C_c^{-1}}) & a^2\boldsymbol{C_c^{-1}} & \boldsymbol{O_{2x2}} & \boldsymbol{O_{2x2}} \end{bmatrix}$$

$$\boldsymbol{B_0} = \begin{bmatrix} \boldsymbol{L_{f1}^{-1}}\boldsymbol{O_{10x2}} \end{bmatrix}^{\intercal} \boldsymbol{E_0} = \begin{bmatrix} \boldsymbol{O_{4x6}} \\ \boldsymbol{O_{2x2}} & -a^2\boldsymbol{L_c^{-1}} & \boldsymbol{O_{2x2}} \\ \boldsymbol{O_{2x2}} & \boldsymbol{O_{2x2}} & a^2\boldsymbol{L_g^{-1}} \\ \boldsymbol{O_{4x6}} \end{bmatrix}^{\intercal} \boldsymbol{W_0} = \begin{bmatrix} \boldsymbol{\omega_g} & & \\ & \ddots & \\ & & \boldsymbol{\omega_g} \end{bmatrix} \tag{C.14}$$

The uncertainty is represented by the uncertain time delay of the actuator and parametric uncertainty on each of the electrical elements of the system listed in Table C.1. The general parameter α is with added uncertainty given as $\alpha = \alpha_0 + \delta_\alpha$, which results in the uncertain state-space representation,

$$\begin{aligned} \frac{d\boldsymbol{x}(t)}{dt} &= (\boldsymbol{A_0} + \boldsymbol{A_u})\boldsymbol{x}(t) + (\boldsymbol{B_0} + \boldsymbol{B_u})\boldsymbol{u_u}(t) \\ &\quad + (\boldsymbol{E_0} + \boldsymbol{E_u})\boldsymbol{d}(t) + \boldsymbol{W_0}\boldsymbol{x(t)} \\ \boldsymbol{u_u}(t) &= \boldsymbol{F(s)}\boldsymbol{u}(t),\ y(t) = \boldsymbol{C}\boldsymbol{x}(t), \end{aligned} \tag{C.15}$$

where the subscript 0 denotes the nominal system parameters, and u is the uncertain perturbations. $\boldsymbol{F(s)}$ is the actuator transfer function matrix and is included as an uncertain time delay. The set of possible plants is illustrated in Figure C.4. The linear system with uncertainty in (C.15) can be rewritten as two identical decoupled SISO systems with multiplicative uncertainty in the Laplace domain by introducing frequency dependent uncertainty regions. Component uncertainty with respect to values and frequency dependency is contained in the uncertainty regions. The output of such system with uncertainty weight $W_O(s)$ and $0 \leq \Delta \leq 1$ is given as,

$$y(s) = \begin{bmatrix} (1 + W_O(s)\Delta)G_{i_{f2}v_{inv}}(s) \\ G_{i_{f2}v_g}(s) \\ G_{i_{f2}v_{col}}(s) \end{bmatrix}^{\intercal} \begin{bmatrix} v_{inv}(s) \\ v_g(s) \\ v_{col}(s) \end{bmatrix}, \tag{C.16}$$

where $\Delta = 1$ would represent 100% uncertainty. Omitting the Laplace operator, the closed-loop system output is,

$$y = \underbrace{\frac{GK}{I + GK}}_{T} r + \underbrace{\frac{1}{I + GK}}_{S} G_d d - \underbrace{\frac{GK}{I + GK}}_{T} n \tag{C.17}$$

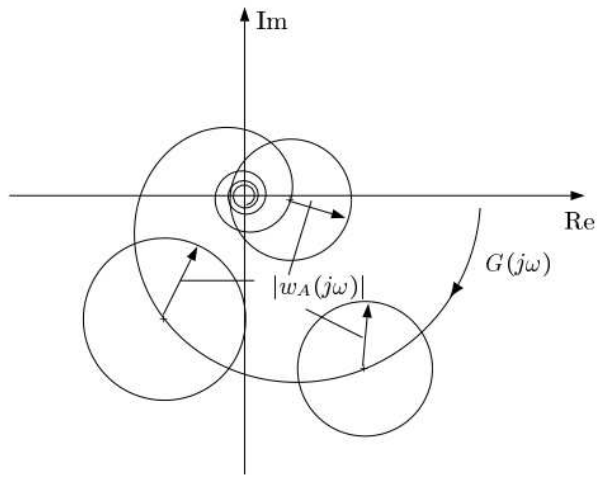

Figure C.4: Disc-shaped uncertainty regions of $G(j\omega)$ generated by complex uncertainty. The set of plants G_Π at each frequency is governed by the magnitude of the weighting function $w_A(j\omega)$ determined by Monte-Carlo simulation with varying parameters. [50]

where $G = (1 + W_O(s)\Delta)G_{i_{f2}}$ and K is the controller. System theory states that $S + T = 1$, which shows that ideal fulfillment of objective one in section C.3 would provide perfect noise rejection. The system setup is further described in section C.5.4.

C.5 VSI Controller Design

The PI controller is the best candidate for regulating DC values with zero steady state error due to its infinite DC gain. PR control and RC are not able to guarantee a closed-loop unity attenuation of power system harmonics. The PI control is therefore used as comparison to the $\mathcal{H}_\infty$ controller. The filter capacitor can be neglected with the approximation that the LCL-filter converges to a simple L filter at low frequencies [43]. Generalized parameter estimation techniques such as symmetrical optimum (SO) or magnitude optimum (MO) are traditionally used for control design [187]. Requirements for the control system are bandwidth and overshoot [51]. Internal mode control (IMC) is considered as a closed loop systematic approach for parameter specification [188]. A major disadvantage of the PI control design is the inability to shape the disturbance rejection loop at the harmonic frequencies. The PI control law for the VSI system is given by,

$$\boldsymbol{u}(t) = \boldsymbol{L}_{\sum}\boldsymbol{\omega_g}\begin{bmatrix} i_{f2}^{d} \\ i_{f2}^{q} \end{bmatrix} + \boldsymbol{K_p}\boldsymbol{e_{f2}^{dq}} + \boldsymbol{K_i}\int \boldsymbol{e_{f2}^{dq}}dt, \tag{C.18}$$

where the error signal $\boldsymbol{e_{f2}^{dq}} = \boldsymbol{r_{f2}^{dq}} - \boldsymbol{i_{f2}^{dq}}$ and

$$\boldsymbol{L_{\sum}} = \boldsymbol{L_{f1}} + \boldsymbol{L_{f2}} + a\boldsymbol{L_g}. \tag{C.19}$$

K_p and K_i are found for SO, MO and IMC given equal performance criteria defined in section C.3.

C.5.1 Magnitude Optimum

Low order plants without time delay and one dominant time constant is often tuned using the magnitude optimum criteria. For a general second order system,

$$G(s) = (1 + \tau_1 s)/(1 + \sigma s)K^{-1} \tag{C.20}$$

where σ is the sum of parasitic time constants smaller that τ_1, it has the solution [189],

$$K_i = \frac{1}{2K}(\frac{1}{\sigma} + \frac{1}{\tau_1} - \frac{1}{\tau_1 + \sigma}),\ K_p = \frac{1}{2K}(\frac{\tau_1}{\sigma} + \frac{\sigma}{\tau_1}) \tag{C.21}$$

which if $\sigma << T_1$ provides full cancellation of the plant pole by the controller zero.

C.5.2 Symmetrical Optimum

The *symmetrical optimum* method aims at shaping both disturbance rejection and reference tracking by optimizing their common characteristic equation. The loop transfer function is shaped to be in the form $\omega_0^2(2s + \omega_0)/s^2(s + 2\omega_0)$. A system in the form of (C.20) with $\tau_1 >> \sigma$ has the solution [190],

$$K_p = \frac{\tau_1}{\alpha K \sigma}, \qquad K_i = \frac{\tau_1}{\alpha^3 K \sigma^2} \tag{C.22}$$

with typically $2 \leq \alpha \leq 3$ [191]. The closed-loop response of the system (C.22) has a large overshoot and a pre-filter is usually designed to shape the reference input [192].

C.5.3 Internal Mode Control

IMC encapsulates that control can be achieved if the control system contains some representation of the process to be controlled. For the PI-control, the system must be approximated by a first order system. Using the *half-rule* [50], a second order system is approximated as,

$$G(s) = \frac{k}{(\tau_1 + \sigma/2)s + 1} e^{-(\sigma/2)s} \tag{C.23}$$

and the PI parameters are given by,

$$K_p = \frac{1}{k}\frac{\tau_1 + \sigma/2}{\tau_c + \sigma/2} \quad \tau_I = min(\tau_1 + \sigma/2, 4(\tau_c + \sigma/2) \tag{C.24}$$

where τ_c is a tunable parameter adjusting the tradeoff between tracking performance and input usage.

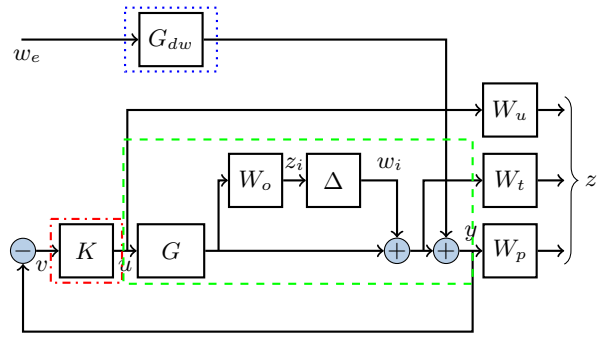

Figure C.5: Standard control configuration for $\mathcal{H}_\infty$ synthesis with multiplicative output uncertainty $W_o\Delta$, error signals z shaped by weighting functions W_u, W_t and W_p, and the exogenous inputs w_e.The nominal control diagram of closed loop VSI control and its translation into the standard control configuration is marked as: Control($dashdot$), plant($stipple$) and disturbances($dotted$). Note that the reference signal i^*_{f2} is part of G_{dw}.

C.5.4 $\mathcal{H}_\infty$ Controller Design

The system is cast as an output disturbance problem and formulated using the generalized P control structure. The dynamics of the VSI system is cast into the generalized plant representation shown in Figure C.5a where v is the measured signal, u is the controlled input, w_e and w_i are the exogenous and internal inputs and z is the error signals to minimize. The set of models G_Π is characterized by a matrix Δ which can either be a full matrix or a block matrix including all possible perturbations representing uncertainty in the system, given in Table C.1. The uncertainty is represented in the frequency domain using unstructured multiplicative output uncertainty representing the set of plants G_Π in an uncertainty region. The frequency domain representation is conservative as the set includes additional plants which are not specified by the direct uncertainty in the parameters. Considering the goal is to provide robust non-interacting controllers, a conservative approach is deemed as suitable. Given the nominal plant G_0, the set of plants are given by,

$$G_\Pi = (I + L_O)G_0, \quad L_O = W_o\Delta. \tag{C.25}$$

The perturbation L_O is measured in terms of a bound on $\overline{\sigma}(L)$,

$$\begin{aligned} \overline{\sigma}(L) &\leq W_o(\omega) \quad \forall\omega \\ W_o(\omega) &= \underset{G\in G_\Pi}{max}\,\overline{\sigma}(L), \end{aligned} \tag{C.26}$$

such that W_o covers the entire set of possible plants as shown in Figure C.6. With W_u, W_t and W_p being weighting functions specifying the requirements from section C.3,

the system dynamics are,

$$\begin{bmatrix} z \\ v \end{bmatrix} = \boldsymbol{P(s)} \begin{bmatrix} w \\ u \end{bmatrix} = \left[\begin{array}{c|c} P_{11}(s) & P_{12}(s) \\ \hline P_{21}(s) & P_{22}(s) \end{array}\right] \begin{bmatrix} w \\ u \end{bmatrix} \qquad \text{(C.27)}$$
$$u = K(s)v,$$

with the matrix $P(s)$

$$P(s) = \left[\begin{array}{cccc|c} 0 & 0 & 0 & 0 & H_{i_{f2}v_i}W_o \\ W_p & W_pG_{i_{f2}v_c} & W_pG_{i_{f2}v_g} & -W_p & W_pG_{i_{f2}v_i} \\ 0 & 0 & 0 & 0 & W_u \\ W_t & 0 & 0 & 0 & W_tG_{i_{f2}v_i} \\ \hline -I & -G_{i_{f2}v_c} & -G_{i_{f2}v_g} & 1 & -G_{i_{f2}v_i} \end{array}\right]. \qquad \text{(C.28)}$$

The $\mathcal{H}_\infty$ controller design opts to minimize the $\mathcal{H}_\infty$-norm of the lower fractional transformation of P and K,

$$N = F_l(P,K) = P_{11} + P_{12}K(I - P_{22}K)^{-1}P_{21}, \qquad \text{(C.29)}$$

which is the transfer function matrix from exogenous signals w to performance signals z. The uncertainty is included as an internal exogenous input, w_i, and a performance signal z_i. The external exogenous signals included are the current reference i^*_{f2}, the grid disturbance v_g and the network disturbance v_c. The disturbance transfer function matrix G_{dw} maps the exogenous signals to the output current i_{f2}. The disturbance dynamics are specified in the $P(s)$ matrix and provides the relation between the exogenous inputs w and the performance signals z. The complex uncertainty description W_o is lumped using a third order filter that covers the set of plants in G_Π as shown in Figure C.6. It is possible to include neglected series and parallel resonances and specific frequency dependent components in the uncertainty description by increasing the order of W_O. Higher order filter results in a higher order controller and a conservative design. The parametric uncertainty is assumed to be sufficient to cover the frequency dependency within the controller bandwidth.

C.5.5 Weighting Functions

The weighting functions specify the relative weight on signal frequency characteristics and should reflect the design criteria set in section C.3.

W_p specifies the tracking performance of the system by bounding the sensitivity below the wanted bandwidth, ω_{bi}, of the system and decrease at high frequencies. The high-pass filter specifies a minimum bandwidth and approximate integral action. The performance weight is found as,

$$W_p(s) = \frac{s/A_p + \omega_{ph}}{s + \omega_{pl}\tau_i} \prod_{k=1}^{n} \left(1/(\frac{s^2 + 2kg_p\omega_{bn}\omega_0 s + (\omega_0 k)^2}{s^2 + 2k\omega_{bn}\omega_0 s + (\omega_0 k)^2}) \right), \qquad \text{(C.30)}$$

where ω_{bn} is the bandwidth of the non-ideal notch filter, g_k is the gain of the k'th notch filter and τ_i provides approximate integral action. The performance will be

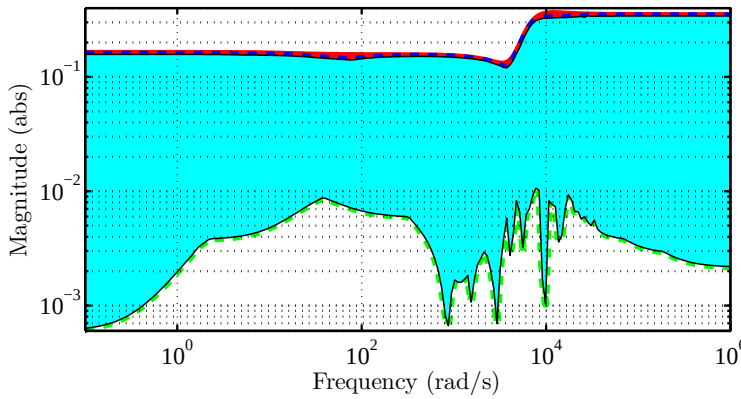

Figure C.6: Relative error L_O of G_Π and uncertainty filter W_O with $|\Delta| < 1$ for 200 samples of G_Π representing the relative uncertainty as $G_\Pi = (I + W_o\Delta)G_0$. Weighting filter$W_o(s)(r-)$, worst case uncertainty$(stipple)$, best case uncertainty$(dastdot)$, relative error area $(shaded)$.

dictated by W_p for $\omega < \omega_{bi}$ and by W_t for $\omega > \omega_{bi}$ ensuring fulfillment of the second and third requirement. The notch filters are inversely included in the selection of W_p to satisfy (C.33).

The control signal weight, W_u, is designed to allow for sufficient control effort while realizing the fourth requirement. W_u is implemented as a second order weight to increase roll off,

$$W_u(s) = \frac{(s/g_u^{1/2} + \omega_h)^2}{(s + \omega_l)^2}, \tag{C.31}$$

where g_u is a tuning parameter to select the attenuation of the filter.

The weighting function on the complementary sensitivity function W_t is designed for low attenuation in a narrow band around the n significant harmonics to fulfill the first requirement. It is the upper bound on T, and is additionally shaped for high-frequency roll-off and force $T \to \epsilon$ for all $\omega \in \omega_h$,

$$W_t(s) = \frac{s/A_t + \omega_{th}}{s + \omega_{tl}} \prod_{k=1}^{n} \left(\frac{s^2 + 2kg_t\omega_{bn}\omega_0 s + (\omega_0 k)^2}{s^2 + 2k\omega_{bn}\omega_0 s + (\omega_0 k)^2} \right). \tag{C.32}$$

The parameters are listed in Table C.2. Picking $A_p > 1$ provides room for $S > 1$ when $u(s)/r(s) > 1$, and is necessary to comply with the robust performance bound,

$$||W_p(s)S(s)||_\infty + ||W_o(s)T(s)||_\infty < 1 \tag{C.33}$$

and the robust stability bound,

$$||T(s)||_\infty < ||1/W_o(s)||_\infty. \tag{C.34}$$

Table C.2: Weighting function parameters

W_p		W_t		W_u	
τ_i	$5e^{-3}$	A_s	1.65	g_u	1/9
A_p	2	A_t	1		
g_{p1}	1.60	g_{t1}	7.12		
g_{p2}	1.44	g_{t2}	7.64		
g_{p3}	0.72	g_{t3}	7.93		
g_{p4}	0.01	g_{t4}	7.51		
ω_{pl}	20 Hz	ω_{tl}	400 Hz	ω_{uh}	3900 Hz
ω_{ph}	140 Hz	ω_{th}	1000 Hz	ω_{ul}	470 Hz

The closed-loop system includes modes associated with the notch filters and thus have an oscillatory impulse response with frequency and damping selected in W_t. The controller specification designates a $1Hz$ bandwidth of the notch filter which equates a notch filter damping of $\zeta = 0.001$. Excitation of notch filter dynamics when tracking the current reference is avoided by inclusion of filter $C(s)$ on the reference signal $r(s)$,

$$r(s)^* = C(s)r(s) = \left(\prod_{k=1}^{n}\left(\frac{z_n}{p_n}\right)\right) r(s), \tag{C.35}$$

where z_n and p_n are the zero and pole pair of the n'th notch filter in the closed loop, identified by their damping properties. In addition to designing a prefilter, the controller K is reduced from a 77 order design to a 14 order using Hankel optimal model reduction while conserving the notch filter dynamics.

C.6 Performance Evaluation

The closed loop sensitivity function with uncertainty is illustrated in Figure C.7. The Figure shows the integral action and limitations of the PI design as the closed-loop system disturbance rejection cannot be shaped at the power system harmonics. The complementary sensitivity function $T = 1 - S$ obtains a bandwidth of $0.4kHz$ as seen in Figure C.7, but cannot guarantee nominal performance for all system perturbations. To asses the performance and quality in regards to the specifications, quantitative metrics J_{d1} and J_{d2} are introduced to measure the control effort and sensitivity attenuation at ω_h. With S_{v_g} being the spectrum of the harmonics,

$$\begin{aligned} J_{d1}(\omega_h) &= \frac{1}{2}\int_{\omega=\omega_h-\omega_d}^{\omega_h+\omega_d} \left(|H_{i_{v_{inv}}v_g}(\omega)|^2\right) S_{v_g} d\omega \\ J_{d2}(\omega_h) &= \frac{1}{2}\int_{\omega=\omega_h-\omega_d}^{\omega_h+\omega_d} \left(|1-|H_{i_{f2}v_g}(\omega)||^2\right) S_{v_g} d\omega. \end{aligned} \tag{C.36}$$

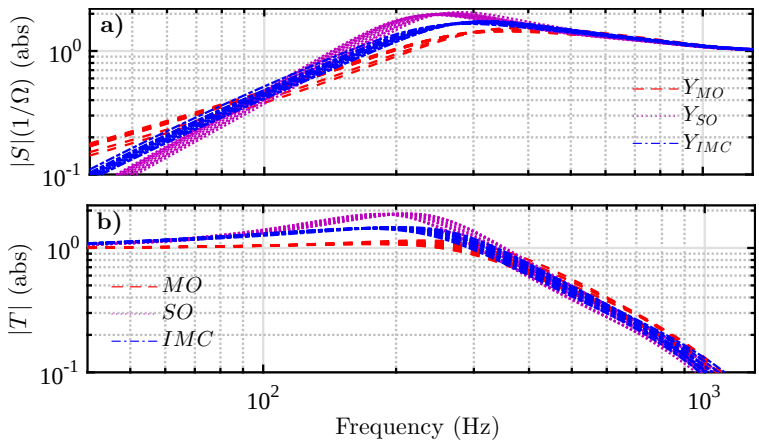

Figure C.7: **a)** Variation of perturbation bodeplot of closed loop harmonic admittance($|S|$) at terminals. MO shows least integral action while IMC and SO are comparable. **b)** Bode plot of closed-loop T. The closed loop performance of the PI loop shaping controllers achieves $|T| > -3dB$ for $\omega < \omega_{bi}$, but both IMC and SO have resonance peaks $|T| > 1$ which leads to overshoot.

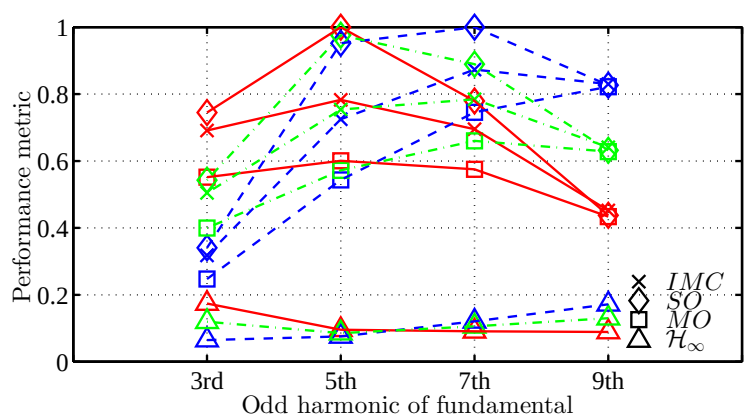

Figure C.8: Normalized $J_d(\omega_h)/|(J_d(\omega_h))|_\infty$, performance metric $J_d(\omega_h)$ for IMC, SO, MO and $\mathcal{H}_\infty$ controllers. Disturbance to control input $J_{d1}(solid)$, sensitivity $J_{d2}(stipple)$ and combined $J_d(dashdot)$.

The normalized worst case gain of the system to output disturbance with respect to both output current and inverter switching is shown in Figure C.8. The duality of the measured metrics and the limitation of the first order compensator with respect to disturbance attenuation and control system limits is clear, as no PI-controller is significantly better at the selected harmonics.

C.7 Simulation

The system is evaluated using the performance metric from (C.36) under worst case uncertainty criteria. The $\mathcal{H}_\infty$ optimal design guarantees internal stability of the closed-loop system when $F_l(P,K) < 1 \; \forall \; \omega$. The robust performance and stability is shown in Figure C.10 and the system is stable and performing to specifications for all plants in G_Π. The challenge of tuning the system using notch filters is evident due to the simultaneous increase in amplitude of W_p and W_t. Time domain simulations are performed in an SimPower Systems model of the London Array wind park using an (N+1) model shown in Figure C.9. Tracking results are shown in Figure C.11a for a doublet step reference change, and the system obtains a rise-time of $1.3ms$ which corresponds to a bandwidth of $0.27kHz$ which is lower than the specification. The rise-time is a consequence of the conservatism introduced and having no overshoot, which results in an improved settling time compared to the PI-controllers. The control effort associated with the reference tracking is shown in Figure C.11b and the $\mathcal{H}_\infty$ controller has 25% less effort compared to the best PI control.

Figure C.12 shows the output response to a disturbance on grid voltage and measurements containing power system harmonics. In Figure C.12a, the controller ensures almost unity sensitivity for the harmonic frequencies and complements the designed filters compared to the phase-lag and amplification of the best PI-controller. Figure C.12b shows an average attenuation of 90% from noise to output. The fact that noise is rejected when sensitivity is forced towards unity is a fundamental property of control theory and shows how this design methodology can be used to complement the effect of existing filters.

The performance metric from section C.6 for the $\mathcal{H}_\infty$ design in Figure C.8 shows the notch filter design efficiency in obtaining a closed-loop sensitivity $\epsilon \in [0.8; 1]$. J_d is close to 0.1 for all $\omega_h \pm \omega_d$ and improving J_{d1} and J_{d2} by minimum 75%.

Robust stability and performance is demonstrated by the multiplicative uncertainty implemented. Uncertainty caused by frequency dependence of components could be represented by using an uncertainty extending throughout a wide range of frequencies. Any additional uncertainty or neglected dynamics could be obtained by using a weighting function of higher order [50]. In systems with low frequency series and parallel grid resonances, a more aggressive choice of uncertainty region could be used to ensure robust stability. Such change would affect the controller synthesis towards a conservative design and by an increase of controller order. The extension of the uncertainty region is decided from the uncertainty in wind-park layout. Variations of cable length, placement, specifications and grid strength all contribute to the combined uncertainty. For wind-farms where the relative uncer-

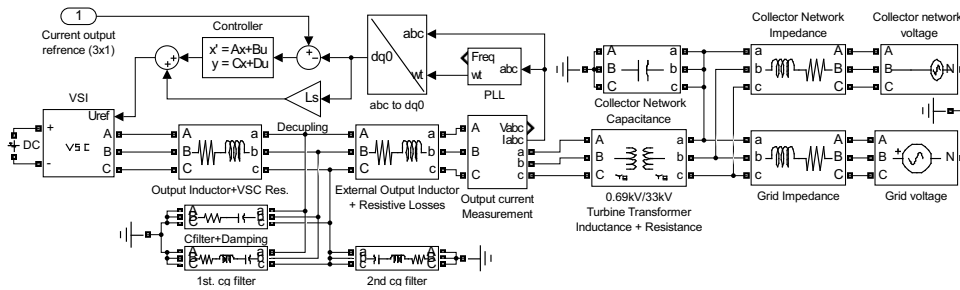

Figure C.9: N+1 model of London Array wind park with generic controller implementation and constant VSI DC-link voltage. The system is balanced and the PLL synchronized with grid voltage vector. Carrier group trap filters are included and tuned to 1^{st} and 2^{nd} harmonic of the switching frequency. Weak PCC/Grid system with an SCR of 20 to emphasize collector network parameter perturbation.

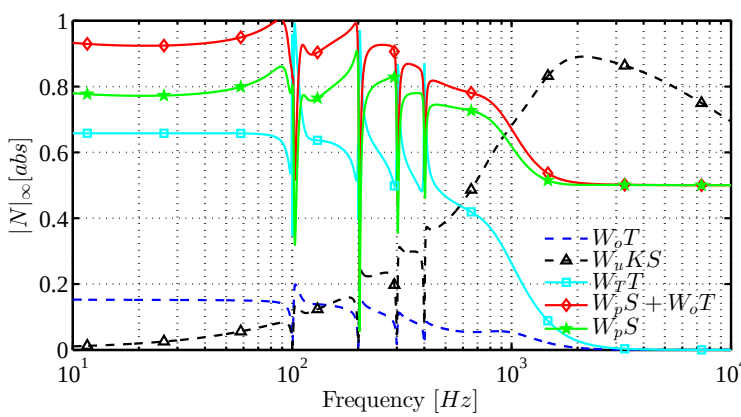

Figure C.10: $\mathcal{H}_\infty$ closed loop worst case singular values. $|T_{zw}|_\infty < 1$ is obtained and conforms with robust performance (C.33) and robust stability (C.34) criteria.

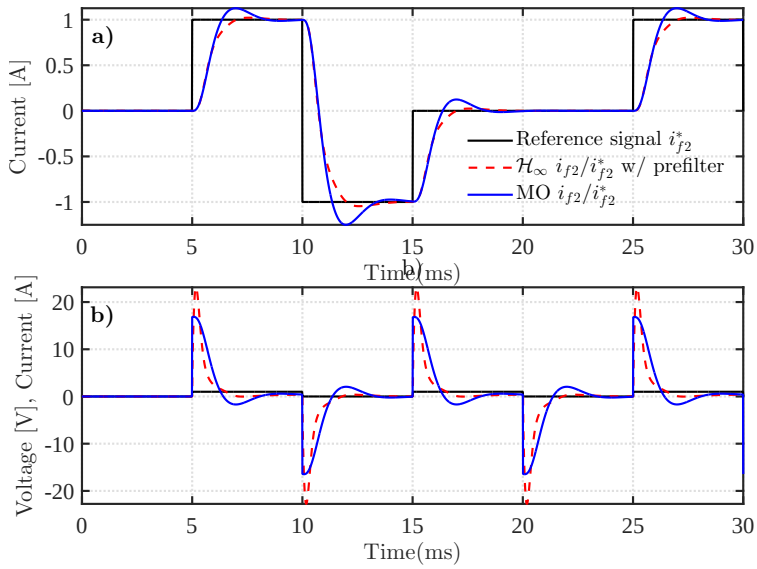

Figure C.11: Reference tracking. **a)** Output current, $\mathcal{H}_\infty$ compared to best PI controller. $\mathcal{H}_\infty$ shows faster tracking with no overshoot and within specifications. **b)** Control effort. $\mathcal{H}_\infty$ has a larger initial effort but avoids overshoot and obtains a 25% reduction compared to PI.

tainty is known, the fixed parameter robust controller instantaneously provides its designed characteristics while additional algorithms in the loop and an adaptation transient is present for adaptive control. If the performance cannot be achieved by robust control, adaptive control should be considered [193].

A high order controller in a real-world discrete control structure puts requirements on the computing power needed. Modern WTs are equipped with powerful processors, fiber cables for communication and high frequency measurement equipment. In practice the probable challenges that can arise in implementation are associated with the effects of unmodelled external systems such as the PLL.

C.8 Conclusion

Inverter control is a challenging part of designing the output stage of a type-4 wind turbine. In this paper, traditional loop shaping methods were compared to an $\mathcal{H}_\infty$ optimal design with focus on minimizing disturbance rejection for use in inner loop system current control schemes. The $\mathcal{H}_\infty$ design using notch filters tuned at the odd harmonic frequencies combined with approximate integral action showed a considerable improvement in performance concerning overshoot, control effort and specific output disturbance rejection. Robust performance and stability

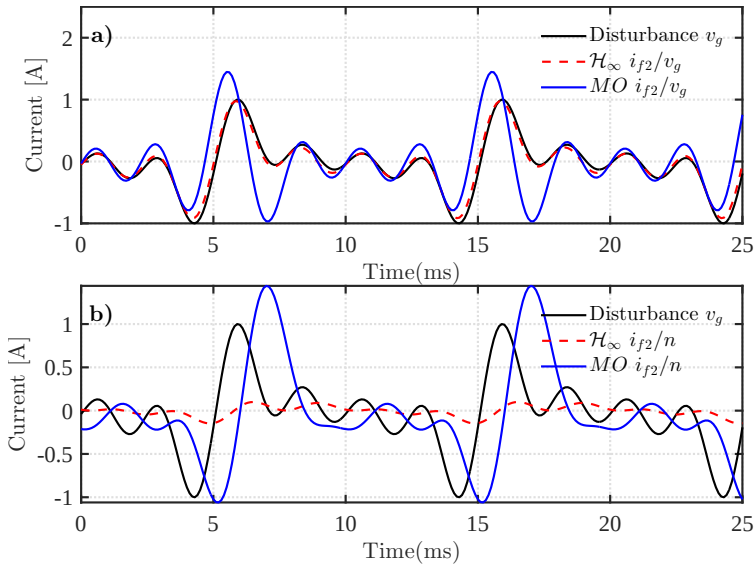

Figure C.12: Disturbance v_g and i_{f2} measurement noise composed of normalized harmonic signal, $\omega = [100Hz, 200Hz, 300Hz, 400Hz]$ **a)** Disturbance attenuation. Output current, $\mathcal{H}_\infty$ compared to best PI controller for harmonic grid disturbance. $\mathcal{H}_\infty$ shows compliance within specifications and ensures a sensitivity of unity, while the PI-controller amplifies the disturbance. **b)** Noise rejection. The controller attenuates power system harmonic noise on the transformer current measurements used in feedback according to the notch filter dynamics.

was achieved with a uncertainty span equivalent to a collector system with one to multiple connected turbines.

Acknowledgment

DONG Energy and The Danish Council for Technology and Innovation are gratefully acknowledged for funding of this research.

Appendix D

Stability Boundaries and Robust Design for Offshore Wind Park Distributed Voltage Control[1]

Mikkel Gryning[2], Qiuwei Wu[3], Łukasz Kocewiak[4], Mogens Blanke[3], Hans Henrik Niemann[3] and Karsten P.H. Andersen[4]

D.1 Abstract

In order to identify mechanisms giving rise to slow reactive power oscillations that were observed in an existing offshore wind park, and be able to avoid similar events in the future, voltage control is scrutinized in this paper for a wind park with a STATCOM, type-4 wind-turbines and a park pilot control. Using data from the actual wind power plant, all stabilizing subsystem voltage proportional-integral (PI) controller parameters are first characterized based on their Hurwitz signature. Inner loop current control is then designed using Internal Mode Control principles and guidelines for feed forward filter design are given to obtain required disturbance rejection properties. The paper contributes by providing analytical relations between power plant control (PPC), droop, sampling time, electrical parameters and inner loop voltage control characteristics, and by assessing frequencies and damping of reactive power modes over a realistic envelope of electrical impedances and control parameters.

[1]Submitted to IEEE Transactions on Control Systems Technology— 2015

[2]M. Gryning is with DONG Energy and Department of Electrical Engineering, Technical University of Denmark, e-mail: migry@dongenergy.dk

[3]Q. Wu, M. Blanke and H.H. Niemann are with Department of Electrical Engineering, Technical University of Denmark, 2800 Kgs. Lyngby, Denmark, e-mail: qw@elektro.dtu.dk, mb@elektro.dtu.dk and hhn@elektro.dtu.dk

[4]Ł. Kocewiak and K. Andersen are with DONG Energy, 2820 Gentofte, Denmark, e-mail: lukko@dongenergy.dk and kahan@dongenergy.dk

D.2 Introduction

Full-scale back-to-back converters are used in large wind-turbines(WTs) to control active and reactive power [194]. Power electronic devices (PEDs) enable fast and independent control at the cost of increased complexity of the wind power plant (WPP) and the associated control systems [195]. Offshore turbines are connected to the transmission system through a medium-voltage (MV) sub sea cable network and a high voltage (HV) network from the point of common coupling (PCC). The WT control system design is complicated by limited knowledge of the transmission system characteristic. Depending on the system topology, the uncertain interconnection dynamics between distributed voltage controllers poses a threat to the overall system stability.

Dynamic voltage control at the PCC is achieved by adjusting the injection of reactive power from the WTs and the SC connected at the HV network transformer. FigureD.1 shows a generalized voltage control scheme. The voltage control is governed by two distributed controllers; local voltage control at the WT LV terminals combined with local voltage control at the PCC using the STATCOM. The reference point of the automatic voltage regulator is the transmission interface point (TIP) at the HV transformer. The PPC dispatches a voltage reference to the local WT voltage controller based on the measurements at the TIP, while the STATCOM tries to fulfill a similar objective. Similar objective at different points of coupling could lead to unwanted interaction if the system parameters are not aligned.

Matrix and back-to-back converters are the prevalent technologies used to control reactive power output [196]. The WPP dynamic voltage stability requires fast distributed reactive sources [197]. Reactive power capability is a function of active power output [198]. Combined power optimization and reactive power control is presented in [199]. The provision of reactive power by decentralized generation

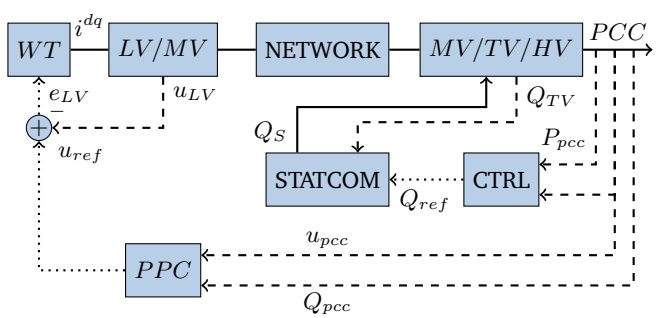

Figure D.1: Schematic wind farm voltage control. Plants *WT* and *STATCOM* include current controllers in the blocks. − − − Measurement, ⋯ Command, → Physical connection

system is studied in [200]. An analysis of local regulation of voltage profiles in distributed systems considering WT capability curves and its impact on stability is shown in [201]. A centralized PPC design is limited by unknown network parameters and system dynamics [201]. Perturbation of system parameters with local voltage profile regulation can lead to reactive power oscillations [202]. Local voltage control influences voltage flicker, and the parameter space of individual control systems should be evaluated [203],[204]. The Complex Hurwitz test is used by [205] to achieve a stabilizing envelope of parameters for a current controlled generator. Assessment of static voltage stability of a power system considering all power controls using singular values is presented in [93]. Grid voltage feed forward in current control is used to improve disturbance rejection and was shown to increase d- and q-components of the converter output impedance [206]. The feed forward low pass filter reflects a tradeoff between noise, over current protection and stability [207]. Multiple converter systems in a network affect the stabilizing set of parameters, and can cause instability [15].

The origins of reactive power oscillations in an existing WPP is investigated in this paper. Section two introduces the gathered data and proposes two possible causes. Section three focuses on tuning of the WT VSI control. The internal mode control design technique establishes a baseline current controller for the WT in compliance with bandwidth and gain limits of over-current protection and switching devices [208]. The filtered feed forward of grid voltage is shown to be bandwidth limited by the choice of disturbance transient peak time versus current magnitude. PI controller parameter separation analytically defines the outer voltage controller stability envelope as a function of component values. The numerical solution of the stabilizing set and the root-locus analysis are used to validate the analytical result. The relation between the PPC sampling time and the cascade voltage control is shown to provide limits for droop and PI parameters. A commissioning procedure is proposed from the results of section three. Section four uses the results from section three for the STATCOM control and the stabilizing set is found for the voltage control. Section five introduces the effect of information propagation in cables and section six presents the effect of parameter variation for reactive power oscillations. Finally section seven discuss the contributory causes to the observed oscillation followed by conclusions. The oscillations are recreated by varying the electrical distance and controller parameters in their respective stabilizing sets.

D.3 Problem Formulation

The reactive power requirement at the PCC in normal operation is a function of active power and voltage [198]. The reactive power is supplied by the WT(s), STATCOM and a manually switched reactor(MSR). In steady state operation, the WT(s) compensate for the reactive power consumption. The STATCOM is used for additional compensation or in case of lacking WT reactive power capability. As shown in Figure D.1, the PPC generates a WT voltage reference according to the PCC voltage

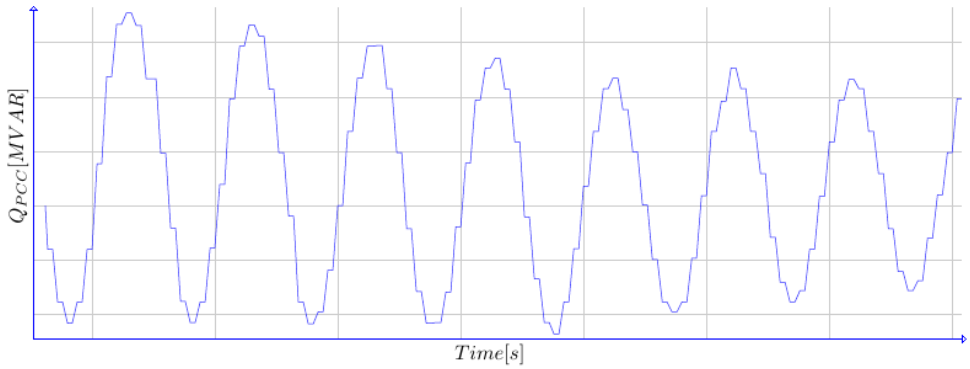

Figure D.2: Oscillations of reactive power measurements at PCC from operational WPP with period in a timescale of seconds.

error. The turbine voltage controller injects or absorbs reactive power to track the external reference. Fast centralized control is a challenging task and the controller is operated at a low bandwidth [90]. Fast voltage control at the PCC is thus dependent on the STATCOM which injects reactive power directly at the tertiary winding of the HV transformer.

Recent observations indicate a problem with the initial tuning of voltage controllers in modern WPPs. An incident showed an unacceptable reactive power oscillation pattern. The phenomenon appeared as poorly damped oscillations at the PCC shown in Figure D.2. The phenomena was also observed at the WT and STATCOM with different phases. Disconnecting WTs from the PPC attenuated the oscillation amplitude and iterative adjustment of controller gains partly remedied the problem. The origin was never clarified. Possible causes are either hunting or controller interaction. To ensure proper operation for all future plants employing similar voltage control strategies, guidelines for power plant (PP), STATCOM and WT voltage control tuning must be identified as a function of system parameters.

Consider a WPP with the voltage control scheme shown in FigureD.1, the identified oscillations can originate from:

- Proposition 1: Inadequate controller bandwidth separation in WT cascade voltage control configuration and interaction with grid dynamics, shown in Figure D.3.

- Proposition 2: PPC and STATCOM similar regulation objective using one feedback signal.

An analysis of the voltage control scheme limitations is used to confirm or disprove

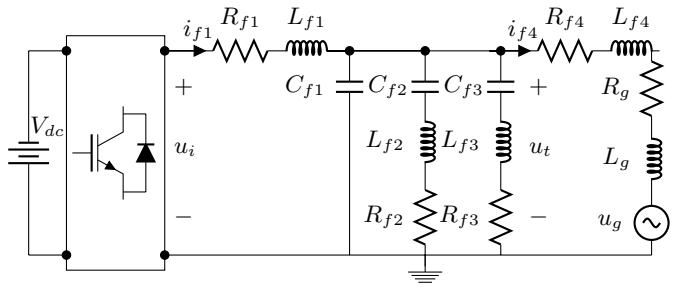

Figure D.3: Single line diagram of VSI with LCL and trap filters for 1^{st} and 2^{nd} carrier group connected to grid.

the propositions. The investigation is extended to include the PPC and the impact of internal dynamics on controller comparability.

D.4 Proposition 1: Limitations In VSI control

The fundamental terminal voltage u_i of a VSI is proportional to the DC-side voltage $u_{dc}(t)$ as,

$$u_i(t) = mu_{dc}(t), \tag{D.1}$$

where m is a controllable modulation index of the converter. The modulation and switching is modeled by an average model of one switching cycle delay τ_s,

$$u_i(s) = U(s)u_{dc}(s) = \frac{1}{\tau_s s + 1}u_{dc}(s), \tag{D.2}$$

which is adequate for controller analysis [209]. The VSI control tracks the active power output while providing reactive power to sustain the active power level. Expressing the sinusoidal reference signals in the *dq* reference frame (RRF) synchronized with the grid frequency enables PI control tracking. Instantaneous active and reactive power are expressed in the RRF as,

$$P = \frac{3}{2}(u_t^d i_f^d + u_t^q i_f^q), \quad Q = \frac{3}{2}(-u_t^d i_f^q + u_t^q i_f^d). \tag{D.3}$$

Currents i_f^d and i_f^q independently control active and reactive power if the reference of the RRF is selected such that u_t^q is negligible. The output current i_f^q is regulated to achieve a change in transformer terminal voltage u_t, providing distributed reactive power support at the PCC.

D.4.1 WT VSI Model

A single line diagram of the VSI with inductor-capacitor-inductor (LCL) and trap filters tuned at carrier group frequencies is shown in FigureD.3. The filter and LV

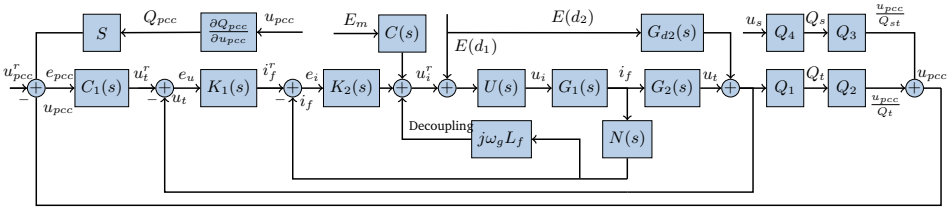

Figure D.4: Cascade voltage control structure of the VSI. The PI-controller $K_2(s)$, actuator $U(s)$ and plant $G_1(s) = i_{f4}/u_i$ constitute the inner current control loop with output disturbance $G_d(s) = i_{f4}/u_g$. The outer loop consists of PI-controller $K_1(s)$, the inner loop and $G_2(s) = u_t/i_{f4}$.

side of the transformer make up the dynamics of the plant $G_1(s)$, while the grid and HV side of the transformer constitute the disturbance dynamics $G_d(s)$. The filter capacitor(s) are neglected by approximating the LCL-filter with an inductor filter for low frequencies [43]. The inner current loop dynamics are given by,

$$\boldsymbol{L_f}\frac{\boldsymbol{di_f^{dq}}}{dt} + \boldsymbol{R_f i_f^{dq}} = \boldsymbol{u_i^{dq}} - \boldsymbol{E^{dq}} + \boldsymbol{DL_f D\omega_g i_f^{dq}}, \tag{D.4}$$

where,

$$\boldsymbol{\omega_g} = \begin{bmatrix} 0 & \omega_g \\ -\omega_g & 0 \end{bmatrix}, \quad \boldsymbol{D} = \begin{bmatrix} 0 & 1 \\ 1 & 0 \end{bmatrix}, \tag{D.5}$$

$$\boldsymbol{L_f} = \boldsymbol{L_{f1}} + \boldsymbol{L_{f4}} + \boldsymbol{L_g}, \quad \boldsymbol{R_f} = \boldsymbol{R_{f1}} + \boldsymbol{R_{f4}} + \boldsymbol{R_g}. \tag{D.6}$$

The modified control variable $\boldsymbol{u_{i*}^{dq}}$ is introduced in the VSI voltage reference to provide axis decoupling and feed forward of the measured grid voltage,

$$\boldsymbol{u_{i*}^{dq}} = \boldsymbol{u_i^{dq}} - \boldsymbol{C(s)E_m^{dq}}, \tag{D.7}$$

where subscript m indicates measurement. $\boldsymbol{C(s)}$ is the low-pass filter,

$$C(s) = \alpha_f/(s + \alpha_f), \tag{D.8}$$

$\boldsymbol{u_i}$ is the voltage at VSI terminals, $\boldsymbol{E}$ is the grid voltage vector, ω_g is the angular frequency of the grid and α_f is the filter tuning variable. The low frequency resonance characteristic is damped using the virtual resistor principle [210],

$$\boldsymbol{u_{i'}^{dq}} = \boldsymbol{u_{i*}^{dq}} + \boldsymbol{R_d}(\boldsymbol{i_f^{dq}} - \boldsymbol{i_{f1}^{dq}}). \tag{D.9}$$

where $R_d = 1/(3\omega_r C_{f1})$ and ω_r is the resonance frequency. Given a bounded reference trajectory $u_i^r(t)$, the computational- and switching delay is modeled as a dead time τ_s,

$$u_i(t) = e^{-s\tau_s} u_i^r(t), \tag{D.10}$$

and the system is cast as two identical single input-output systems. In the Laplace domain,

$$u_i(s) = \frac{u_i^r(s)}{\tau_s s + 1}, i_f(s) = \frac{u_i(s) - E(s)}{L_f s + R_f}. \tag{D.11}$$

The voltage at the LV terminals of the WT transformer $u_t(s)$ as a function of output current $i_f(s)$ and grid voltage $E(s)$ with scaling variable λ to account for losses in the filter,

$$u_t(s) = \frac{(L_v s + R_v) i_f(s) + E(s)}{C_p L_v s^2 + C_p(R_v + (R_d/\lambda))s + 1}, \tag{D.12}$$

where $L_v = L_f - L_{f1}$ and $C_p = C_{f1} + C_{f2} + C_{f3}$.

D.4.2 Current Control Design

The cascade control scheme of a VSI is shown in Figure D.4. The current control structure consists of a PI controller for zero steady state error, and a notch filter, $N(s)$, tuned to 2^{nd} order power system harmonic for unbalanced operation in the RRF. The reference voltage is,

$$u_i^r = (k_p + \frac{k_i}{s})(i_f^r - i_f N(s)) + C(s)E \pm j\omega_g L_f i_f \tag{D.13}$$

$$N(s) = \frac{s^2 + (\omega_N/Q_n)s + \omega_N^2}{s^2 + (\omega_N/Q_d)s + \omega_N^2}, \tag{D.14}$$

where ω_N is the tuned frequency, Q_n and Q_d are the quality factors of the filter. The closed loop transfer functions from reference $i_f^r(s)$ to output $i_f(s)$ and from disturbance $E(s)$ to $i_f(s)$ are given by,

$$\begin{aligned} i_f(s) &= \frac{(k_p s + k_i) i_f^r(s)}{D(s)} - \frac{(s\tau_s + 1)s^2 E(s)}{(s + \alpha_f)D(s)}, \\ D(s) &= L_f \tau_s s^3 + (R_f \tau_s + L_f)s^2 + (N k_p + R_f)s + N k_i. \end{aligned} \tag{D.15}$$

The disturbance $E(s)$ contains power system harmonics, series resonances and parallel resonances [16]. Power system harmonics exist in the control bandwidth and are filtered by $N(s)$. The system bandwidth is limited by the voltage modulator switching frequency f_s. Proper attenuation of carrier harmonics limits the bandwidth to $f_b = 0.2 f_s$ [119]. The system for control synthesis is represented as a first-order plus time delay model,

$$\widetilde{G_1}(s) = \frac{1}{R_f} \frac{1}{(L_f/R_f + \tau_s/2)s + 1} e^{-\tau_s/2s}. \tag{D.16}$$

By process inversion design, the controller parameters are given as [50],

$$k_p = \frac{L_f + R_f(\tau_s/2)}{\tau_c + \tau_s/2}, \tag{D.17}$$

$$k_i = \frac{k_p}{\min\left(L_f/R_f + \tau_s/2, 4(\tau_c + \tau_s/2)\right)}, \tag{D.18}$$

where τ_c is a tuning parameter for trade-off between output performance and robustness.

Parameter Bounds

Physical limitations of the VSI and the maximum bandwidth of the closed-loop system bounds the proportional gain. Assuming small k_i, (D.17) and the bandwidth specification of $\widetilde{G_1}(s)$ lower bounds τ_c for performance,

$$\tau_c \geq \begin{cases} \dfrac{-50(\kappa_2 + L_f)R_f - \tau_s\kappa_1 + 5\kappa_2\kappa_3 + 10L_f\kappa_3}{50R_f^2 + 2\kappa_1}, \omega_b \leq \omega_s/5 \\ \dfrac{(\tau_s/2)(R_f - K_{max}) + L_f}{K_{max}}, k_p \leq K_{max}, \end{cases} \tag{D.19}$$

where κ are strictly positive functions given in the appendix. Assuming zero filter resistance and dead time, the proportional gain can be determined as $k_p = \omega_b L_f$, where ω_b is the desired bandwidth [211],[212]. In fact, insertion in (D.17),

$$\tau_c = \frac{1}{\omega_b} + \frac{R_f\tau_s/2}{\omega_b L_f} - \frac{\tau_s}{2} \approx \frac{1}{\omega_b}, \tag{D.20}$$

shows conformity with (D.19) for $R_f = 0$ and $\tau_s = 0$. Selecting τ_c from bandwidth limitation of k_p gives an upper bound on k_i,

$$k_i \leq \frac{(25R_f^2 + \kappa_1)^2}{50(\kappa_3 - 5R_f)^2(\kappa_2 + 2L_f)}. \tag{D.21}$$

Disturbance Rejection

The choice of low-pass filter coefficient α_f determines the bandwidth. Converter over current protection requires small $|i_f^{max}|$ for network disturbances [213]. This is achieved for large α_f. Parameters α_f and k_p are respectively lower and upper bounded by bandwidth limitations. For sufficiently small $\tau_s < 1ms$, the roots of $D(s)$ are governed by,

$$\boldsymbol{z_p} \in \mathbb{R},\ k_i < (R_f^2 + k_p^2 + 2R_f k_p)(4L_f)^{-1}, \tag{D.22}$$

$$\boldsymbol{z_p} \in \mathbb{C},\ k_i > (R_f^2 + k_p^2 + 2R_f k_p)(4L_f)^{-1}. \tag{D.23}$$

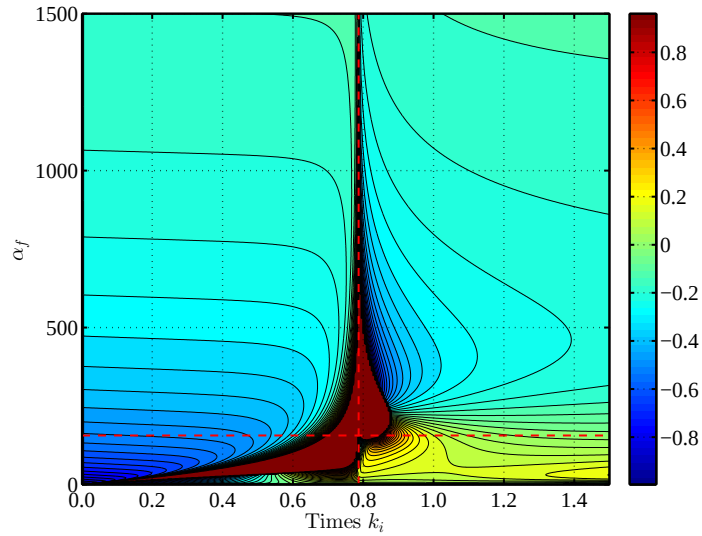

Figure D.5: Countourplot of $i(t_{max})$ for $k_i \in [0; 1.2k_i]$ and $k_p = 1$. The vertical dotted line is the transition from real to complex poles and the horizontal is the bound on α_f for assumption (D.4.2). *Note: The limit of $i(t_{max})$ is bounded to 1 to enhance the illustration.*

Bounding k_i by (D.22) guarantees a damping of unity on all modes. The system response to a grid voltage step disturbance as a function of PI parameters and α_f is,

$$i(t) = \frac{((\kappa_9 - \kappa_8)\mathrm{e}^{2\kappa_7 t} + \kappa_9 + \kappa_8)\mathrm{e}^{-t(\kappa_4+\kappa_7)} - 2\mathrm{e}^{-t\alpha_f}\kappa_9}{-L_f^{-1}\kappa_6}. \tag{D.24}$$

For large α_f, the local maximum of $\partial i(t)/\partial t$ is dominated by terms I_2 and I_3,

$$\underbrace{|(\kappa_3 + \kappa_2)\mathrm{e}^{(\kappa_7-\kappa_4)t}|}_{I_1} \ll \underbrace{|\kappa_5\mathrm{e}^{-\alpha_f t}|}_{I_2} < \underbrace{|(\kappa_3 - \kappa_2)\mathrm{e}^{-(\kappa_7+\kappa_4)t}|}_{I_3}.$$

The response thus has a global maximum at,

$$t_{max} = \ln(\frac{-2\kappa_5}{\kappa_2 - \kappa_3})/\left(\alpha_f - \kappa_4 - \kappa_7\right). \tag{D.25}$$

The contourplot of Figure D.5 illustrates $i(t_{max})$ from (D.25) and (D.24) bounded by (D.23). If restrictions on t_{max} or $|i_f^{max}|$ exist, α_f should be selected from (D.25) or Figure D.5.

D.4.3 Voltage Control Design

The structure of $K_1(s)$ is a PI-controller. The reference signal is,

$$i_f^r(s) = K_1(s)(v_t^r(s) - v_t(s)) \pm j\omega_g C_p u_t. \tag{D.26}$$

The signature of the polynomial function (D.12) with a fixed-structure controller is used to find parameter stability bounds. The Hurwitz signature of a rational polynomial with real coefficients $Q(j\omega) = N(j\omega)/D(j\omega)$ with $N(j\omega)$ having no zeroes on the $j\omega$ axis is [60],

$$\sigma(Q) = \left(\sum_{j=1}^{l-1} (-1)^{l-1-j} sgn[Q_r(\omega_j)] \right) sgn[Q_i(\infty^-)], \tag{D.27}$$

where,

$$Q(j\omega) = Q_r(\omega) + jQ_i(\omega). \tag{D.28}$$

Defining $deg[D(s)] = n$, $deg[N(s)] = m \leq n$ and $K_1(s) = k_{pv} + k_{iv}/s$, closed loop stability of the feedback interconnection $Q(s), K_1(s)$ is equivalent to having $n+1$ zeroes of the characteristic polynomial,

$$\delta(s) = D(s)s + (k_p s + k_i)N(s), \tag{D.29}$$

in the open LHP. The polynomial $\nu(s) = \delta(s)N(-s)$ is formed and exhibits the parameter separation property such that [60],

$$\nu(s) = \nu_{even}(s^2, k_{iv}) + s\nu_{odd}(s^2, k_{pv}), \tag{D.30}$$

$$\nu(j\omega) = (p_1(\omega) + k_{iv}p_2(\omega)) + j(q_1(\omega) + k_{pv}q_2(\omega)). \tag{D.31}$$

The stability requirement on $\delta(s)$ is rewritten,

$$\sigma(\nu) = (n-m) + 1 + 2z^+, \tag{D.32}$$

where z^+ denotes the number of RHP zeroes of $Q(s)$. For even degree $\nu(s)$, (D.32) is satisfied for,

$$\sigma(\nu) = j(i_0 - 2i_1 + \cdots + (-1)^l 2i_l + (-1)^{l+1} i_{l+1}), \tag{D.33}$$

$$j = sign(\nu_{odd}(0^+, k_p^*)), \tag{D.34}$$

where k_p^* is in the stabilizing set $\mathbf{\Omega}(k_{pv}, k_{iv})$ and $\mathbf{\Gamma}$ is distinct strings of integers $\{i_0, i_1, \ldots, i_{l+1}\}$ satisfying (D.33). The minimum number of distinct non-negative roots l needed to satisfy (D.33) is,

$$l \geq (n - m + 1)/2 - 1. \tag{D.35}$$

The number of distinct non-negative real roots l in an univariate polynomial in the interval $[0, \infty]$ can be determined by the number of sign changes in the Sturm sequence evaluated at the end points of the interval [214]. Let p_1 be the number of sign changes at $\omega_0 \triangleq 0$ and p_2 at $\omega_{l+1} \triangleq \infty$, the number of distinct non-negative real roots are $l = p_1 - p_2$ [215]. The separation property of $\nu(s)$ with the free parameter k_p in the Sturm sequence satisfying (D.35) thus determines the allowable range on $k_p^* \in \mathbf{\Omega}(k_{pv}, k_{iv})$.

The closed loop system $P_2(s)$ defined by (D.12) and (D.15) with input (D.26) has $n = 5$ and $m = 2$ which satisfies (D.35) for $l \geq 1$. The signs of the Sturm sequence $sm(\omega)$ of $\nu_{odd}(\omega_0, k_{pv})$ are determined by,

$$sm(\omega_0, k_p) = \{\alpha_0, -\alpha_0, \alpha_0, -\alpha_0\}, \tag{D.36}$$

$$\alpha_0 = sign(k_{pv} + 1/R_v), \tag{D.37}$$

which shows $p_1 = 3 \,\forall\, k_{pv} \in \mathbb{R}\backslash\{-1/R_v\}$. The Sturm sequence of $\nu_{odd}(\infty, k_{pv})$ is,

$$sm(\omega_{l+1}, k_{pv}) = \{\alpha_1, \alpha_1, \alpha_3, \alpha_3, \alpha_5, \alpha_5, \alpha_0\}, \tag{D.38}$$

where α_1, α_3, and α_5 are functions of system component parameters and inner loop tuning given in the appendix. Minimizing the amount of subsequent sign changes in the sequence maximizes the number of non-negative roots [214]. Over-constraining k_{pv} results in $\mathbf{\Omega} = \emptyset$ and the bounding should be chosen such that $p_1 - p_2 = l$. The controller from section D.4.2 ensures $k_{pc} > k_{ic}$ which implies $|(R_f\tau_s + L_f)k_{pc}| > |L_f\tau_s k_{ic}|$ for $\tau_s \leq 1$ and it follows that the sign of α_1 is negative. The lower bound on k_{pv} follows from α_3 and α_5 ensuring $l = 1$,

$$k_{pv} > \frac{k_{ic}(L_f R_v - L_v R_f) - k_{pc}(R_v(R_f + k_{pc}))}{k_{ic}^2 L_v^2 + k_{pc}^2 R_v^2}. \tag{D.39}$$

The rational polynomial $Q_i(\omega)$ of order $n+1$ is consequently guaranteed to have one real root, ω_1. Substituting $\omega^2 = w$ in $Q_i(\omega)$ and factoring the expression,

$$(w + \frac{\beta_2}{\beta_1})(w^2 + \frac{\beta_3}{\beta_2}w + \frac{\beta_4}{\beta_2}) \approx \beta_1 w^3 + \beta_2 w^2 + \beta_3 w + \beta_4, \tag{D.40}$$

provides a good approximation of ω_1 for $\beta_1 \ll \beta_2$. The root is located at,

$$\omega_1^2 = \frac{-\beta_2}{\beta_1} \approx \frac{-k_{pc}(L_v k_{pc} k_{pv} + L_f)}{L_v C_p(-k_{pc}(L_f + R_f\tau_s) + L_f\tau_s k_{ic}}. \tag{D.41}$$

From the Hurwitz signature (D.34), every admissible string for $l = 1$, $\mathbf{\Gamma} = \{i_0, i_1, i_2\}$, must satisfy,

$$sign(\nu_{odd}(0, k_{pv}))(i_0 - 2i_1 - i_{l+1}) = n - m + 1, \tag{D.42}$$

for all $k_p^* \in \mathbf{\Omega}(k_{pv}, k_{iv})$. The sign of $\nu_{odd}(\omega_0, k_{pv})$ is strictly positive as,

$$\nu_{odd}(\omega_0, k_{pv}) > 0 \,\forall\, k_{pv} > -1/R_v, \tag{D.43}$$

and the magnitude of the bound in (D.39) $\ll$ (D.43). Hence the only admissible string is $\mathbf{\Gamma}_1 = \{1, -1, -1\}$. The stabilizing pair k_{pv} and k_{iv} must satisfy the constraints,

$$p_1(\omega_0) + k_{iv}p_2(\omega_0) > 0 \Rightarrow k_{iv} > 0, \tag{D.44}$$

$$p_1(\omega_{l+1}) + k_{iv}p_2(\omega_{l+1}) < 0 \Rightarrow k_{iv} < \infty, \tag{D.45}$$

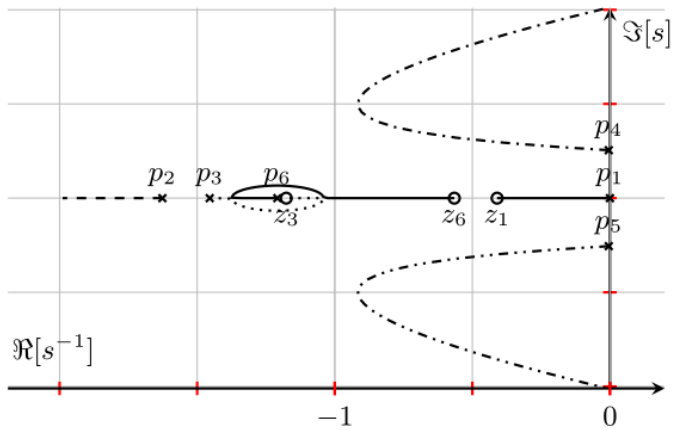

Figure D.6: Scaled root locus diagram of the open-loop plant $P_2(s)$ for $k_{pv} \in \mathbf{\Omega}(k_{pv}, k_{iv})$. The left-most pole is stopped at z_2 for clarity in the central region.

and the non-trivial constraint for $\omega_1(k_{pv})$,

$$p_1(\omega_1) + k_{iv} p_2(\omega_1) < 0. \tag{D.46}$$

Insertion of $\omega_1(k_{pv})$ in (D.46) further bounds k_{pv} for $k_{iv} = 0$ as the solution to the polynomial,

$$\gamma_1 k_{pv}^2 + \gamma_2 k_{pv} + \gamma_3 = 0, \tag{D.47}$$

where γ_1 to γ_3 are functions of system parameters given in appendix. The stabilizing set $\mathbf{\Omega}(k_{pv}, k_{iv})$ is the area,

$$k_{iv} < \frac{-p_1(k_{pv})}{p_2(k_{pv})}, k_{pv} \in \mathbf{\Omega}(k_{pv}, k_{iv}), \tag{D.48}$$

for k_{pv} lower bounded by the intersection of (D.47) and (D.39), and upper bounded by (D.47). The system parameters yields the full stabilizing set $\mathbf{\Omega}(k_{pv}, k_{iv})$ as shown in Figure D.7.

D.4.4 Stability Considerations

Increasing the proportional gain k_{pv} moves the closed-loop poles from the open loop poles toward the open loop zeroes. Non pole-zero pairs for $n > m$ goes toward infinity. The sum of the real parts is constant and the complex poles move to the right half plane as the left-most pole goes to infinity as shown in Figure D.6. This movement limits k_{pv} in accordance with Figure D.7 and highlights the importance of including $U(s)$ in the system dynamic description. Increasing k_{iv} shifts the zero

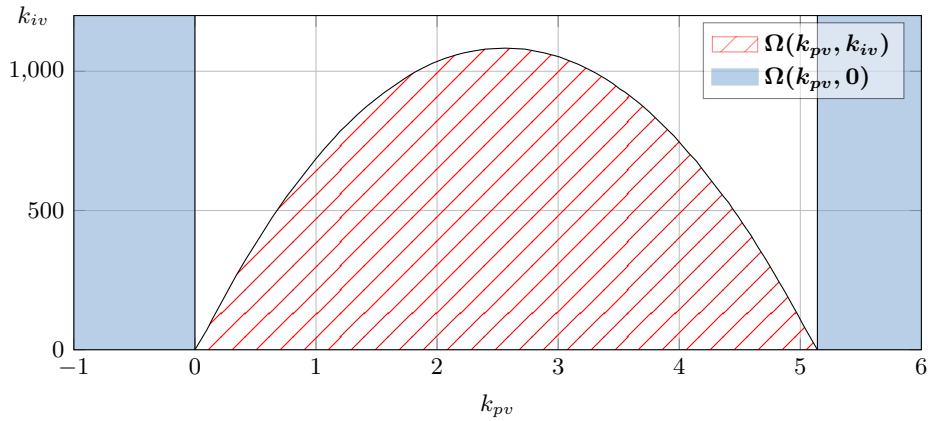

Figure D.7: Stabilizing set $\boldsymbol{\Omega}(k_{pv}, k_{iv})$.

z_1 into the left half plane rendering $\mathbb{R}(p_{4,5})$ smaller. The locus of $p_{4,5}$ shows that a desired damping can obtained by two values of k_{pv}. Poles $p_{3,6}$ originate from the inner loop and stay in the LHP for all k_{pv} and k_{iv}. The k_{pv} needed to obtain the desired damping of $p_{4,5}$ can be lowered by increasing R_d. Increasing k_{pc} in violation with (D.23) produces a complex pole pair that enlarge $\mathbb{R}(p_{4,5})$, extending the stabilizing set $\boldsymbol{\Omega}(k_{pv}, k_{iv})$. The likelihood of the observed oscillations originating from inadequate tuning of VSI control is possible for low values of k_{iv} and high k_{pv} resulting in poorly damped oscillations in the time range of seconds.

D.4.5 Commissioning Algorithm

Sections D.4.2 to D.4.4 provide performance and disturbance rejection guidelines to guarantee stability. For commissioning of a type-4 WT, the following algorithm is proposed:

1: **procedure** COMMISSIONING
2: Refer systems $G_1(s)$ and $G_2(s)$ to WTG-LV side.
3: Check damping resistance $R_d \geq 1/(3\omega_r C_p)$.
4: Compute k_{pc} and k_{ic} performance bounds - (D.19).
5: Check k_{ic} for real poles - (D.23)
6: Compute α_f from t_{max} - (D.25).
7: Check $i(t_{max}) \leq i_{max}$ - (D.24).
8: Compute $\nu(j\omega)$ - (D.31).
9: Check k_{pv} compliance with (D.39) and (D.47).
10: Plot $\boldsymbol{\Omega}(k_{pv}, k_{iv})$ as $-p_1(k_{pv}/p_2(k_{pv}))$.
11: Check $k_{iv} \in \boldsymbol{\Omega}(k_{pv}, k_{iv})$.
12: **end procedure**

D.5 Proposition 2

The WPP voltage control philosophy is shown in Figure D.8. Injection of reactive

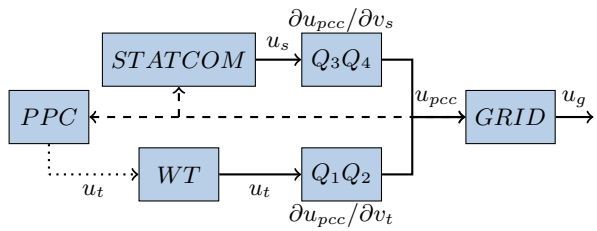

Figure D.8: Conceptional diagram of the park level voltage control. STATCOM and WT represents structures as Figure D.4. $- - -$ Measurement, $\cdots$ Command, $\rightarrow$ Physical connection

power from the WTs and STATCOM regulates the PCC voltage. The STATCOM injects reactive power at the tertiary winding of the substation transformer while the WTs inject reactive power into the sub-sea network. The PPC uses the WT local voltage control as actuator, and constitutes a cascaded closed loop control. The power flow in Figure D.8 is modeled as two Π realizations plus local transformer impedance [216],

$$Q_{pcc} = \sum Q - (X_{t1} + X_{t2})\frac{P_t^2 + Q_t^2}{u_{pcc}^2} - (X_{s1} + X_{s2})\frac{Q_s}{u_{pcc}^2} + B_p u_{pcc}^2 + B_t u_t^2 + B_s u_s^2, \tag{D.49}$$

$$P_{pcc} = \sum P - (R_{t1} + R_{t2})\frac{P_t^2 + Q_t^2}{u_{pcc}^2} - (R_{s1} + R_{s2})\frac{Q_s}{u_{pcc}^2} - G_p u_{pcc}^2 - G_t u_t^2 - G_s u_s^2, \tag{D.50}$$

where $Z_{s,t} = R_{s,t} + jX_{s,t}$ and $Y_{s,t} = G_{s,t} + jB_{s,t}$ are the sending and receiving end impedance and admittance. B_p and G_p are the PCC side susceptance and conductance, subscript s,t,l and n denotes STATCOM, WT, local and network respectively. The reactive power flow equation is linearized as,

$$\frac{\partial Q_{pcc}}{\partial u_{pcc}} = f_u(Q_1, Q_2, Q_3, Q_4, Z_{s,t}, Y_{s,t})\big|_{u_{pcc}=u_0}, \tag{D.51}$$

where the voltage sensitivities Q_1,Q_2,Q_3 and Q_4 are estimated by neglecting the weak coupling between reactive power Q and load angle θ [27]. The voltage sensitivities

$\partial Q_{s,t}/\partial u_{pcc}$ are estimated for the system,

$$\frac{\partial Q_t}{\partial u_{pcc}} = u_t f_q(Z_{t1}, Z_{t2}, 1/Y_t) = Q_2^{-1},\ u_t \approx 1pu, \tag{D.52}$$

$$\frac{\partial Q_s}{\partial u_{pcc}} = u_s f_q(Z_{s1}, Z_{s2}, 1/Y_s) = Q_3^{-1},\ u_s \approx 1pu, \tag{D.53}$$

$$\frac{\partial Q_t}{\partial u_t} = Q_1,\ \frac{\partial Q_s}{\partial u_s} = Q_4, \tag{D.54}$$

where $f_q(Z_1, Z_2, Z_3)$ is a frequency dependent function given in the appendix. At fundamental frequency assuming voltages u_t and u_s limited to $\pm 5\%$ deviation, $\partial Q_{s,t}/\partial u_{pcc}$ are considered constants [27]. Q_t/u_t, Q_t/u_{pcc} and Q_s/u_{pcc} can be obtained with extended precision as elements of $-\Im(\boldsymbol{Y_{bus}})$ used in Load-Flow methods, such as FDLF [27].

D.5.1 Power Plant Control

The PPC provides a voltage reference to the WT control from the PCC voltage error. The voltage magnitude is controlled by the d-axis voltage. The error signal provided to the PI controller is,

$$u_{pcc}^{d_e} = u_{pcc}^{d_*} - u_{pcc}^{d} - (3SQ_{pcc})/(2nQ_{max}), \tag{D.55}$$

where S is the desired slope of the droop control, n is the amount of turbines connected and Q_{max} is the reactive power capability of one turbine. The PPC is a digital PI controller with sample time $T_s > 100ms$. The electrical subsystem seen from the controller is considered a fast first order system. The impact of $Q_t(s)$ on $u_{pcc}(s)$ is given by (D.52) for the fundamental frequency. The reactive power error at the PCC and the output of the WT are [217],

$$Q_{pcc}^{e} = (3/2)(-u_{pcc}^{d_e} i_{pcc}^{q}),\ Q_{wt} = (3/2)(-u_t^d i_{wt}^q). \tag{D.56}$$

The used voltage philosophy dictates even distribution of reactive power. Equating Q_{wt} to $(1/n)Q_{pcc}^{e}$ and adding the integration parameter γ,

$$C_3(s) = k_{pu} + \frac{k_{iu}}{s} = \frac{i_{pcc}^q}{n i_{wt}^q} u_{pcc}^{d_e} + \frac{\gamma}{s}, \tag{D.57}$$

where the currents are the rated values. The discrete zero order hold plus sampler system is modeled in the continuous domain as,

$$T(s) = (1 - e^{-sT_s})/(T_s s) \tag{D.58}$$

and the output $u_{pcc}(s)$ of the closed loop system is given by,

$$\begin{aligned} u_{pcc}(s) &= \frac{Q_s(s)Q_3 + Q_1Q_2P_2(s)C_1(s)T(s)u^r_{pcc}}{1 + Q_1Q_2P_2(s)C_1(s)T(s)(1+SQ_4)}, \\ P_1(s) &= \frac{i^r_f(s)}{i_f(s)} = \frac{U(s)G_1(s)K_2(s)}{1 + N(s)U(s)G_1(s)K_2(s)}, \\ P_2(s) &= \frac{u^r_t(s)}{u_t(s)} = \frac{K_1(s)P_1(s)}{1 + K_1(s)P_1(s)} \approx \frac{1}{T_vs+1}, \end{aligned} \tag{D.59}$$

where T_v is the effective rise-time of the inner processes. Setting $Q_c = Q_1Q_2$, using a first order Padé time delay approximation and introducing $\alpha = T_s/T_v$ as the response time ratio, the open-loop response is,

$$u_{pcc}(s) = Q_c/\left((T_vs+1)(\alpha T_v/2s+1)\right). \tag{D.60}$$

Using the Hurwitz signature and separating the control parameters as (D.31), the number of distinctive non negative real roots l needed to satisfy (D.34) to guarantee stability is $l \geq 1$ for $n = 2$ and $m = 0$. The maximum number of non-negative real roots for the Sturm sequence given $\nu_{odd}(\omega_0, k_{pu})$ and $\nu_{odd}(\infty, k_{pu})$ is achieved for,

$$k_{pu} \geq -\frac{1}{Q_c(SQ_4+1)},\ 2Q_c^2(SQ_4+1) > 0. \tag{D.61}$$

The root is located at,

$$\omega_{1u} = \sqrt{2}\sqrt{\alpha(1 + k_{pu}(SQ_4+1)Q_c)}/(\alpha T_v). \tag{D.62}$$

Every admissible string for $l = 1$, $\mathbf{\Gamma} = \{i_0, i_1\}$, must satisfy,

$$sign(\nu_{odd}(0^+, k_{pu}))(i_0 - 2i_1) = n - m + 1, \tag{D.63}$$

where $sign(\nu_{odd}(0, k_{pu}))$ is strictly positive given (D.61). The only admissible string is $\mathbf{\Gamma}_2 = \{1, -1\}$, imposing the non-trivial constraint for $\omega_{1u}(k_{pu})$,

$$p_1(\omega_{1u}) + k_{iu}p_2(\omega_{1u}) < 0, \tag{D.64}$$

and by insertion of (D.62) in (D.64),

$$k_{iu} < \underbrace{\frac{\alpha+2}{\alpha T_v}}_{a_k} k_{pu} + \underbrace{\frac{\alpha+2}{\alpha T_v}\frac{1}{Q_c(SQ_4+1)}}_{b_k}, \tag{D.65}$$

which defines the set $\mathbf{\Omega}_{\boldsymbol{H}}(k_{pu}, k_{iu})$. Inequality (D.65) shows $a_k \to 1/T_v$ for $\alpha \to \infty$ due to increased separation of control and plant bandwidth. An increase of integration gain is needed to guarantee stability as $a_k \to \infty$ for $\alpha \to 0$. Increasing the sensitivity to reactive power change, Q_1 to Q_4, or the droop S decreases the constant factor b_k.

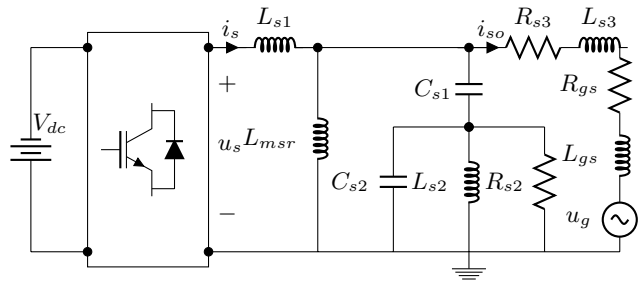

Figure D.9: SLD of grid connected STATCOM with MSR reactor and filter.

D.5.2 Dynamic Reactive Power Compensation

The STATCOM provides reactive power support at the PCC. The physical structure shown in Figure D.9 consists of a MSR and an output filter.

The STATCOM is Δ-connected to the onshore transformer, represented by R_{s3} and L_{s3}. The Δ-connection is converted to star for analysis [218]. A droop plus PI controller regulates the PCC voltage by modifying the STATCOM output current, $i_{so}(s)$ similar to the VSI in subsection D.4.1 with an additional reactor. Decoupling the RRF axes and neglecting high frequency filter components,

$$i_{so}(s) = \frac{L_{msr}u_i(s) - L_d E(s)}{L_s s + R_s L_d}, \tag{D.66}$$

where $u_i(s)$ is the terminal voltage, $E(s)$ is the grid voltage and

$$L_s = L_{msr}(L_{s3} + L_{gs} + L_{s1}) + (L_{s3} + L_{gs})L_{s1}, \tag{D.67}$$
$$L_d = L_{s1} + L_{msr},\ R_s = R_{gs} + R_{s3}, \tag{D.68}$$

are constants. The system (D.66) is similar to (D.11) with,

$$L_f = L_s/L_{msr},\ R_f = R_s L_d/L_{msr}. \tag{D.69}$$

The output filter is modelled with output current $i_{so}(s)$ and converter voltage $u_i(s)$ as inputs and the voltage at the LV side of STATCOM transformer terminal $u_{st}(s)$ as output,

$$u_{st}(s) = \frac{(n_1 s + n_2)L_{msr}(u_i(s) - L_{s1} i_{so}(s))}{d_1 s^4 + d_2 s^3 + d_3 s^2 + d_4 s + d_5}, \tag{D.70}$$

with the control law,

$$i^r_{so}(s) = K_3(s)(u^r_{st}(s) - u_{st}(s)) \pm j\omega_g C_{p2} u_{st}(s), \tag{D.71}$$
$$C_{p2} = C_{s1}C_{s2}/(C_{s1} + C_{s2}). \tag{D.72}$$

Following the parameter separation method with k_{psi} and k_{isi} being the current controller parameters, the Sturm sequence given $\nu_{odd}(\omega_0, k_{psv})$ for the closed loop system is,

$$sm(\omega_0, k_{psv}) = \{l_0, 0, -l_0, 0, l_0, 0, -l_0\}, \tag{D.73}$$

where the sequence is alternating with l_0 as a function of k_{psv} if,

$$k_{psv} \in \mathbb{R} \backslash \frac{L_{msr}(n_2 d_3 - n_1 d_4)k_{isi} + L_d R_s n_2 d_4}{L_{msr} k_{isi} n_2^2} \triangleq l_\alpha. \tag{D.74}$$

The sequence for $\nu_{odd}(\infty, k_{psv})$ is given by,

$$sm(\infty, k_{psv}) = \{\alpha_7, \alpha_7, \alpha_8, \alpha_9, \alpha_9, \alpha_{10}, \alpha_{11}, 0\}, \tag{D.75}$$

where α_7, α_8 and α_9 are given in the appendix. The sign of α_7 is negative for $k_{isi} > 0$ and $k_{psi} > 0$, and α_8 is positive for $k_{psv} > 0$. α_9 is positive for $k_{psv} \leq \gamma_2$, α_{10} is positive for $k_{psv} \leq \gamma_3$ and α_{11} is positive for $k_{psv} > l_\alpha$. To guarantee stability for $n = 6$ and $m = 3$, $l \geq 1$ to satisfy (D.34), and $l = 2$ for $k_{psv} > l_\alpha$ and $k_{psv} < \gamma_3 < \gamma_2$. The Hurwitz signature for even $\nu(s)$ is given in (D.33) and is satisfied for $\mathbf{\Gamma}_3 = \{1, -1, 1, 1\}$ and $\mathbf{\Gamma}_4 = \{-1, -1, 1, -1\}$, imposing the non-trival constraints,

$$S_1 : p_1(\omega_2(k_{psv}) + k_{isv} p_2(\omega_2(k_{psv})) > 0, \tag{D.76}$$

$$S_2 : p_1(\omega_3(k_{psv}) + k_{isv} p_2(\omega_3(k_{psv})) < 0, \tag{D.77}$$

where $\omega_2(k_{psv})$ and $\omega_3(k_{psv})$ are the solutions to the factorization as (D.40). The envelope of stability for the STATCOM control, $\mathbf{\Omega_s}(k_{psv}, k_{isv}) = S_1 \cup S_2$, is shown in Figure D.10 using the parameters listed in Table D.1.

Table D.1: WYE STATCOM Filter parameters referred to WT LV side

L_{s1}	L_{s2}	L_{s3}	L_{msr}	L_{gs}	τ_s
$7.39\mu H$	$1.07\mu H$	$21.29nH$	$28.09\mu H$	$4.55\mu H$	$0.1ms$
C_{s1}	C_{s2}	R_{s2}	R_{s3}	R_{gs}	L_0
$5.68mF$	$1.46mF$	$12.32m\Omega$	$42.58n\Omega$	$8.00\mu\Omega$	$48km$

The droop controller S_2 acts as a simple proportional gain, and an initial value is the inverse of $Q_3 Q_4$. The designs and stability envelopes are found based on lumped system models, however the timing of a change in terminal voltage to a similar change in grid voltage is delayed by the group velocity waveforms in the array cables, which has an effect on the combined system stability.

D.6 Group Velocity Effects on System Stability in MISO Systems with Long Transmission Cables

Reactive power output is primarily determined by potential magnitude difference. Figure D.8 shows the multi input single output (MISO) voltage control system,

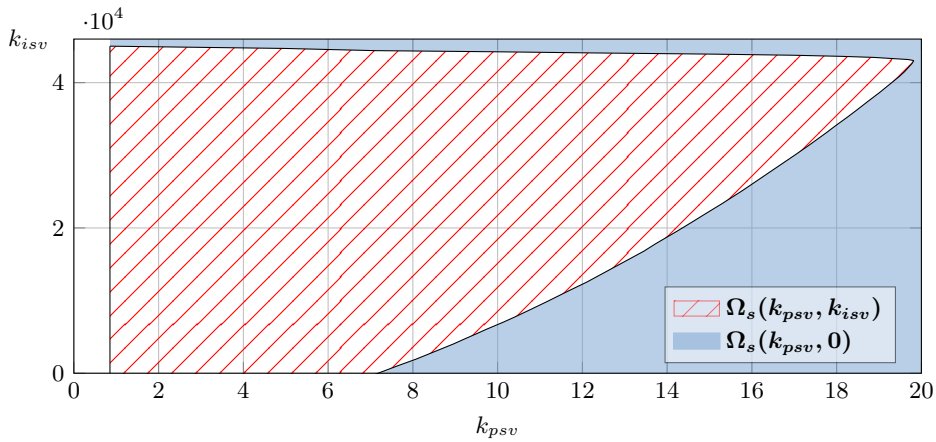

Figure D.10: Stabilizing set $\Omega_s(k_{psv}, k_{isv})$ for parameters in Table D.1. White area $\gamma_3 < k_{psv} < l_{alpha}$ less than two real roots of $\nu(s)$. Hatched area $\Omega_s(k_{psv}, k_{isv})$ and blue area $\Omega_s(l_{psv}, 0)$.

and it is evident that the WT local voltage change must propagate through a long transmission cable, while the STATCOM is directly connected to the transformer. The phase velocity of a wave is provided by cable manufactures, typically $150 - 200m/\mu s$. However, information is propagated at the group velocity given for a lumped transmission line model as,

$$v_c = 1/\sqrt{L'C'},\ G' \ll j\omega C', R' \ll j\omega L', \tag{D.78}$$

where L' and C' are cable unit length inductance and capacitance. A typical sub-sea transmission cable used in the OWPP has $v_c \approx 0.1m/\mu s$, a factor of 1500 slower.

The combined export and substation transmission lines span 52 km, thus causes a maximum delay of, $t_{delay} = 150ms$. RMS based analysis does not consider this effect, but it needs to be included in the nodal matrix formulation for long transmission lines. The effect of group velocity propagation delay on the PCC voltage stability is illustrated in Figure D.11, which shows the movement of system poles as a function on the delay. The dominating pole pair p_1 and p_2 for the cascade configuration move into the RHP for $t_{delay} > 250ms$. The phase shift of the time delay can cause the observed oscillations within the entire PP, STATCOM, WT voltage control system.

D.7 Inter-area Parameter Effect Simulation

The nonlinear inter-area effects on reactive power oscillations at the PCC are studied by simulation. The parameters k_{pv}, k_{iv}, k_{pu}, k_{iu}, k_{psv} and k_{isv} are varied in the joint stabilizing set $\boldsymbol{\Omega_M(\cdot) = \Omega(k_{pv}, k_{iv}) \cup \Omega_S(k_{psv}, k_{isv}) \cup \Omega_H(k_{pu}, k_{iu})}$. The cable lengths are varied in the set L_Ω which spans $0.1L_0$ to $3L_0$. For each vector

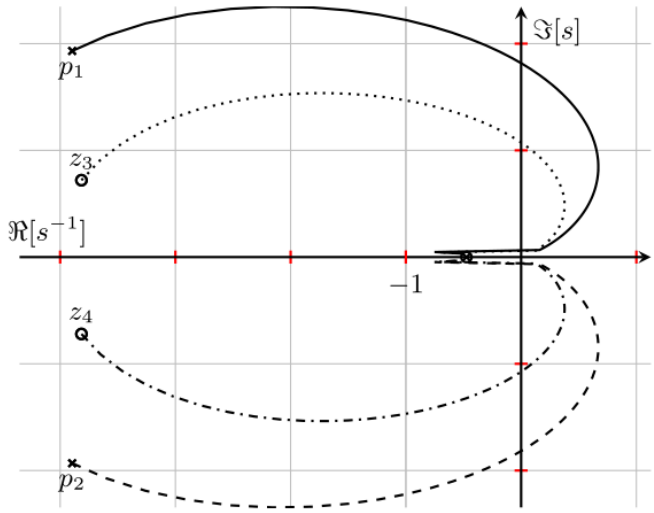

Figure D.11: Pole-zero transition plot for variation of T_{delay}. The group velocity delay is approximated by a 10^{th} order Padé model.

$\boldsymbol{\Psi_i}$ in $\boldsymbol{\Omega_M}$ the system is subjected to a step in $E(s)$. The dominating frequencies are identified from peaks in the estimated spectral density of the response. The damping of the identified modes are found by time shifting and applying the moving block method [219]. The i'th frequency, maximum peak and damping matrix $[\boldsymbol{f_i}, \boldsymbol{A_i}, \boldsymbol{\zeta_i}]$ is sorted descending with respect to maximum peak, and the simulation is represented by two scalars,

$$f_{m,i} = \sum_{j=1}^{n}(f_{i,j}A_{i,j})/A_{i,avg}, \tag{D.79}$$

$$\zeta_{m,i} = \sum_{j=1}^{n}(\zeta_{i,j}A_{i,j})/A_{i,avg}, \tag{D.80}$$

where $A_{i,avg} = \sum_{j=1}^{n}(A_{i,j})$. The amplitude weighted change in frequency and damping for variation of voltage sensitivity and controller parameters are shown in Figure D.13 and Figure D.14. Figure D.13 shows an inter-area network frequency component around $2Hz$. A distinct effect on the PCC reactive power by varying the turbine local voltage integration constant for different cable lengths is observed. A short cable coupled with fast local voltage control removes all oscillations. Increasing the cable length and thus the impedance seen from the controller viewpoint, the integration constant must follow proportionally to reduce oscillation and increase damping. Nearing the edge of the nominal operational envelope, it is evident that increasing cable length additionally causes unwanted oscillation with low damping at the PCC. Variation of the STATCOM integral constant reveals an area in the stability region with increased frequency and reduced damping, similar to the movement of poles in Figure D.6. The linear relation between voltage sensitivity and integral

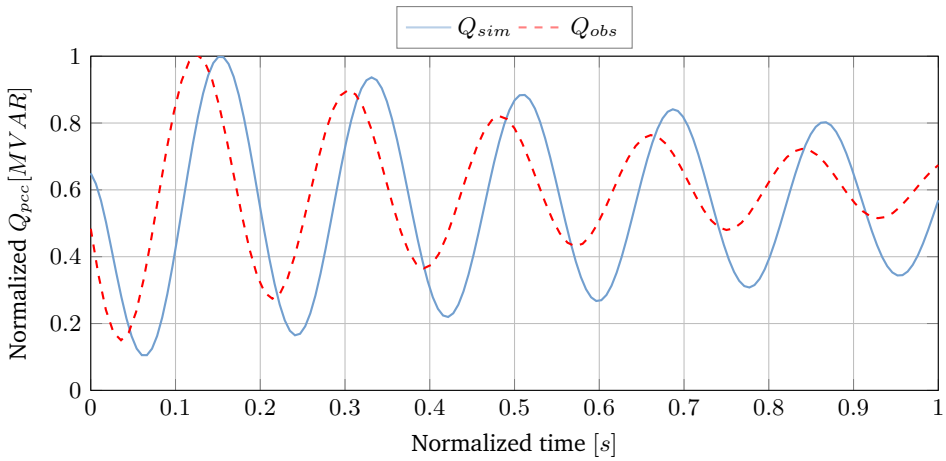

Figure D.12: Reactive power oscillations at PCC with long cable and large PPC integral gain.

constant as (D.65) is reflected in Figure D.14 and shows the effect on the overall system damping.

D.8 Possible Causes For Observed Reactive Power Oscillation

The WT and STATCOM stability criteria show the possibility of a local reactive power oscillation presence. Aligning the results of section D.4 with proposition one shows probable cause. Assuming a well-defined current control design, flawed tuning of the local voltage control was shown to be able to provoke poorly damped local oscillations, as illustrated in in Figure D.6. Furthermore, an increase in outer loop voltage control bandwidth could destabilize the cascade if the inner current control could not track its reference. The resulting damped oscillation was plotted in Figures D.13 and D.14. As the system employs rate and output limits, this could lead to limit cycles. An insinuation of this being a contributing mechanism is that the oscillations shown in Figure D.2 were attenuated when WTs were disconnected from the PPC.

Reactive power transfer is proportional to the difference in voltage magnitude between terminals. The electrical distance separating the WTs and STATCOM complicates the local control explanation. The PPC tuning bounds of section D.5.1 show a correlation between local voltage control performance and PPC sampling time. Aggressive local voltage control and neglected group transmission delay in the PPC tuning can combined cause the PPC-WT cascade to show oscillatory behavior. In line with proposition two, the analytical stability bounds show dependence on grid impedance and are subject to uncertainty. If the WT and STATCOM voltage control is tuned according to the most aggressive grid code [220], the impact of the system

impedance variation with control parameter perturbation shows an possible explanation for the observed phenomena.

The grid code specifies both settling- and rise time for the reactive power response at the PCC during a voltage decrease. One method to meet the specification is a large PPC integrator gain. The PPC response in turn is dependent on the impedance and, on WPPs with long array-, export- and substation cables, oscillatory behavior can be the result, as we have shown above. The cable length in the particular is very long for the WPP case referred to in Figure D.2. Figure D.12 shows these observed oscillations compared to a simulation of a WPP with very long cables and a PPC integral gain increased to fulfill the grid code rise time parameter. It is thus plausible that the observed oscillations are caused by the mechanism described and that they can be very poorly damped when having long cables. The grid code specification may therefore be difficult to achieve with the commonly applied strategy for voltage control. The main-result of the investigation is that given a stable combination of WT and STATCOM cascade control, the most likely cause of the oscillations is, according to proposition two, a too aggressive PPC setting for the system at hand.

D.9 Conclusion

The reactive power oscillations encountered when energizing the WPP caused quite a bit of concern as they could not be replicated by simulation software. Identification of problem causes in systems with multiple controllers pose many challenges. Without direct access to the implicated systems, a bottom-up approach was necessary. This paper ties analytical properties of WT and STATCOM current control design to a generalized filter setup achieving the performance and disturbance rejection requirements. The voltage control parameter stability envelopes of WT and STATCOM were derived as a function of current control and system parameters based on their Hurwitz signature. Based on the results for WT and STATCOM voltage control, stability guidelines for the PPC was proposed to ensure proper cooperation between STATCOM and WT control as a function of sample time, droop and network voltage sensitivity. The investigation of isolated systems showed probable cause given a discrepancy between current and voltage control bandwidth leading to signal truncation. The voltage control structure of the WPP was shown to include two joint cascade control systems, modeled as a MISO system. Using the proposed guidelines for WT, STATCOM and PPC design, the WPP system was simulated over a realistic envelope of electrical impedances and stabilizing control parameters. The observed oscillations were reproduced using perturbed WT voltage control integral constant and park pilot integral constant. Achieving oscillations similar to the data does not prove causality, but the process contributes by identifying possible risks and methods to guarantee stability. This work seeks to highlight an ongoing trend of using similar controllers for every park without taking the topology into account, and tries encourage additional testing of controllers in WPP - both before and after deployment.

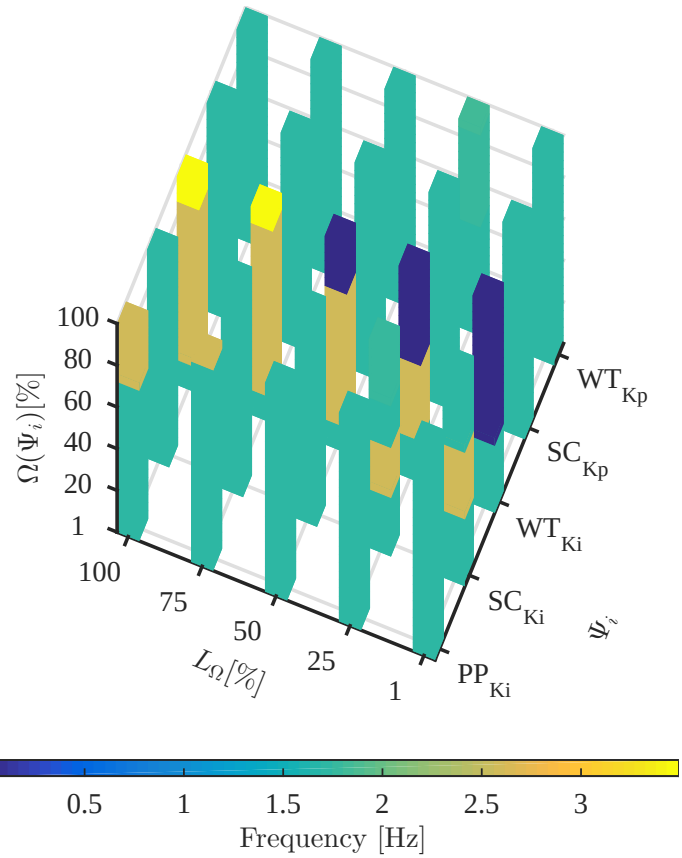

Figure D.13: Amplitude weighted mode frequency from variation of cable length versus controller parameters.

Acknowledgment

The authors would like to thank DONG Energy and The Danish Council for Technology and Innovation for funding the research project.

Appendix

$$
\begin{aligned}
R_x &= R_1^2 + X_1^2 \\
R_{n1} &= (R_x {R_3}^2 + 2R_1R_3 + 1 + R_x + {X_1}^2){X_3}^2 - 2X_1X_3) \\
R_{n2} &= (-2{R_3}^2X_1 - 2X_1{X_3}^2 + 2X_3)
\end{aligned}
$$

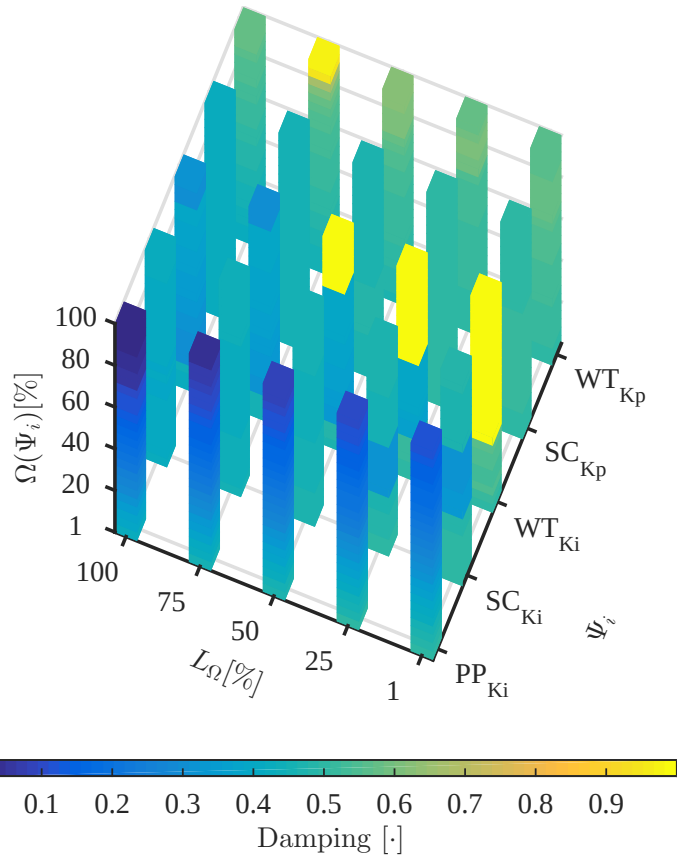

Figure D.14: Amplitude weighed damping from variation of cable length versus controller parameters.

$$
\begin{aligned}
R_{n3} &= ({R_2}^2{X_1}^2 + (R_1R_2+1)^2)\\
R_{n4} &= (2R_1{R_2}^2 + 2R_2)\\
R_{n5} &= ({R_2}^2{X_1}^2 + (R_1R_2+1)^2)\\
n_1 &= L_{s2}R_{s2}(C_{s1}+C_{s2}),\ n_2 = L_{s2},\ n_3 = R_{s2}\\
d_1 &= C_{s1}C_{s2}L_{s2}L_{msr}L_{s2}R_{s2},\ d_2 = C_{s1}L_{s2}L_{msr}L_{s2}\\
d_3 &= R_{s2}((L_{msr}+L_{s2})(C_{s1}+C_{s2})L_{s2} + C_{s1}L_{msr}L_{s2})\\
d_4 &= L_{s2}(L_{msr}+L_{s2}),\ d_5 = R_{s2}(L_{msr}+L_{s2})\\
\kappa_1 &\triangleq L_f^2\omega_s^2,\ \kappa_2 \triangleq R_f\tau_s,\ \kappa_3 \triangleq \sqrt{50R_f^2+\kappa_1}\\
\beta_1 &= L_v^2C_p(k_{pc}(-R_f\tau_s - L_f) + k_{ic}L_f\tau_s)\\
\beta_2 &= \beta_1 + L_v^2k_{pc}^2k_{pv} + k_{pc}((R_f\tau_s+L_f)L_v
\end{aligned}
$$

$$
\begin{aligned}
&- L_f R_v(C_p R_v + \tau_s)) - L_v k_{ic}(C_p L_v R_f + L_f \tau_s) \\
\beta_3 &= R_v^2(k_{pc}^2 k_{pv} - C_p R_f k_{ic}) + R_v(k_{pc}(R_f + k_{pc}) \\
&+ k_{ic}(-L_f - R_f \tau_s)) + k_{ic} L_v(L_v k_{ic} k_{pv} + R_f) \\
\beta_4 &= k_{ic}^2 R_v(R_v k_{pv} + 1) \\
\gamma_d &= C_p \left(L_f \tau_s k_{ic} - k_{pc}\left(R_f \tau_s + L_f\right)\right)^2 \\
\gamma_1 &= L_f \tau_s k_{pc}^5 L_v^2 k_{pv}^2 / \gamma_d \\
\gamma_2 &= 2{L_f}^2 \tau_s {k_{pc}}^4 L_v / \gamma_d \\
&+ \left(C_p\left(\left(-R_f \tau_s - L_f\right) k_{ic} + k_{pc}\left(R_f + k_{pc}\right)\right) {L_v}^2\right) / \sqrt{\gamma_d} \\
&+ \left(k_{pc} L_f L_v \tau_s - k_{pc} C_p L_f {R_v}^2 \tau_s\right) {k_{pc}}^2 / \sqrt{\gamma_d} \\
\gamma_3 &= \left(R_f k_{pc} + {k_{pc}}^2 - \left(R_f \tau_s + L_f\right) k_{ic}\right) L_v \\
&+ (C_p(-R_f k_{pc} - {k_{pc}}^2 + (R_f \tau_s + L_f) k_{ic}) \\
&\times R_v(-R_f \tau_s - L_f) k_{pc}) + L_f \tau_s k_{ic} R_v + {L_f}^3 \tau_s {k_{pc}}^3 / \gamma_d \\
&+ (C_p((-R_f \tau_s - L_f) k_{ic} + k_{pc}(R_f + k_{pc})) {L_v}^2 \\
&+ k_{pc} L_f L_v \tau_s - k_{pc} C_p L_f {R_v}^2 \tau_s) k_{pc} L_f / (\gamma_d L_v) \\
t_1 &= (k_{pc} L_f((C_p R_v^2 + R_v \tau_s - L_v) + R_f \tau_s (C_p R_v^2 - L_v)) \\
&- k_{ic}(\tau_s (C_p R_v^2 - L_v) L_f - C_p L_v^2 R_f)) / (L_v^2 k_{pc}^2) \\
t_2 &= k_{ic}(L_f R_v - L_v R_f) - k_{pc}(R_v(R_f + k_{pc})) \\
&\times (k_{ic}^2 L_v^2 + k_{pc}^2 R_v^2)^{-1} \\
t_3 &= L_{msr}(-k_{isi} n_1 d_1 \tau_s L_s + k_{psi}(\tau_s n_1 d_1 R_s L_d \\
&+ L_s(\tau_s n_1 d_2 + d_1(n_1 - n_2 \tau_s))) \\
t_4 &= (-L_{msr}(d_1 n_2 - d_2 n_1) {k_{psi}}^2 + ((R_s(d_3 \tau_s + d_2) L_d \\
&+ L_s(d_4 \tau_s + d_3)) n_1 - (R_s(d_2 \tau_s + d_1) L_d \\
&+ L_s(d_3 \tau_s + d_2)) n_2) k_{psi} + (((-d_3 \tau_s - d_2) L_s \\
&- R_s(d_2 \tau_s + d_1) L_d) n_1 + (L_d R_s d_1 \tau_s + L_s(d_2 \tau_s + d_1)) \\
&\times n_2) k_{isi}) / (L_{msr} {n_1}^2 {k_{psi}}^2) \\
\alpha_0 &= [+, k_{pv} < -1/R_v,\ -, k_{pv} > -1/R_v] \\
\alpha_1 &= \alpha_2 = sign[\beta_1],\ \alpha_3 = \alpha_4 = [-, k_{pv} > t_1,\ +, k_{pv} < t_1] \\
\alpha_5 &= \alpha_6 = [+, k_{pv} > t_2,\ -, k_{pv} < t_2] \\
\alpha_7 &= -sign[t_3] \\
\alpha_8 &= [+, k_{psv} > t_4,\ -, k_{psv} < t_4] \\
\alpha_9 &= [-, k_{psv} > l_\alpha \text{(D.74)},\ +, k_{psv} < l_\alpha] \\
f_q(\cdot) &= ((R_x {R_3}^2 - R_1 R_3 + R_x {X_3}^2 + X_1 X_3) X_2 \\
&+ R_1 R_2 X_3 + R_2 R_3 X_1 + {R_3}^2 X_1 + X_1 {X_3}^2)
\end{aligned}
$$

$$\times (R_{n1}{X_2}^2 + R_{n2}X_2 + R_{n3}{R_3}^2 + R_{n4}R_3 + R_{n5}{X_3}^2 - 2{R_2}^2X_1X_3 + {R_2}^2)^{-1}$$

www.elektro.dtu.dk
Department of Electrical Engineering
Automation and Control (AUT)
Technical University of Denmark
Elektrovej
Building 326
DK-2800, Kgs. Lyngby
Denmark
Tel: (+45) 45 25 35 76
Email: info@elektro.dtu.dk